ENVIRONMENTAL SPECIATION, CHEMISTRY, STABILITY AND

KINETICS OF NICKEL IN SOILS, MINERAL SYSTEMS AND PLANTS

by

Matthew G. Siebecker

A dissertation submitted to the Faculty of the University of Delaware in partial fulfillment of the requirements for the degree of Doctor of Philosophy in Plant and Soil Sciences

Fall 2013

UMI Number: 3613064

UMI®
Dissertation Publishing

UMI 3613064

ProQuest®

ENVIRONMENTAL SPECIATION, CHEMISTRY, STABILITY AND

KINETICS OF NICKEL IN SOILS, MINERAL SYSTEMS AND PLANTS

by

Matthew G. Siebecker

Approved: _____
Blake C. Meyers, Ph.D.
Chair of the Department of Plant and Soil Sciences

Approved: _____
Mark Rieger, Ph.D.
Dean of the College of Agriculture and Natural Resources

Approved: _____
James G. Richards, Ph.D.
Vice Provost for Graduate and Professional Education

I certify that I have read this dissertation and that in my opinion it meets the academic and professional standard required by the University as a dissertation for the degree of Doctor of Philosophy.

Signed: _____

Donald L. Sparks, Ph.D.
Professor in charge of dissertation

I certify that I have read this dissertation and that in my opinion it meets the academic and professional standard required by the University as a dissertation for the degree of Doctor of Philosophy.

Signed: _____

Rufus L. Chaney, Ph.D.
Member of dissertation committee

I certify that I have read this dissertation and that in my opinion it meets the academic and professional standard required by the University as a dissertation for the degree of Doctor of Philosophy.

Signed: _____

Syed Khalid, Ph.D.
Member of dissertation committee

I certify that I have read this dissertation and that in my opinion it meets the academic and professional standard required by the University as a dissertation for the degree of Doctor of Philosophy.

Signed: _____

James D. Kubicki, Ph.D.
Member of dissertation committee

ACKNOWLEDGMENTS

Kathy. The following people were extremely helpful during the past 6.5 years: Caroline Golt, the UD Soil Testing Lab (especially Cathy Olsen), Dr. Ryan Tappero, Dr. Sam Webb, Dr. Kaumudi Pandya, Brian McCandless, Dr. Tiziana Centofanti, Dr. Antonio Lanzirotti, Dr. Clara Chan, Dr. Chris Oze, Dr. Michael Mrozik, Karol Miaskiewicz, and John Hanson the X18B beamline staff.

Dalton Abdala is a great friend to me and a wonderful addition to my family. Wei Li has provided me with much help and is a great colleague. I wish to acknowledge Matt Ginder-Vogel, Sanjay Parikh, Brandon Lafferty, Mike Zhu, Ted Peltier, Yuji Arai, and Maarten Nachtegaal. In Environmental Soil Chemistry group, I have also had the pleasure of working with wonderful colleagues from around the world, including Brazil, China, France, Russia, Thailand, the United States and Delaware.

I have some advice for those wishing to pursue higher education. There is no substitute for hard work. Time and perseverance are critical. However, suffering is a part of earning the Ph.D. To learn from your mistakes you must first recognize you made one, so be open minded and write down everything in your lab notebook. "It pays to be naïve. If I had understood the magnitude of what I'd taken on, I might not ever have done it." – Lyn Evans. When looking for direction, ask yourself: what do I want to learn about next? And lastly, even though you or others may put you down, or you have doubts about your knowledge, research interests or experimental methodology, recognize and have the self confidence in your ability *to learn*.

TABLE OF CONTENTS

Appendices

LIST OF TABLES

LIST OF FIGURES

ABSTRACT

Soil chemistry is a branch of research stemming from soil science and was mostly geared towards research for agriculture and farming. However, because of increased awareness about the environment, soil chemistry now largely focuses on the chemical processes in contaminated soils. The chemical processes in soil occur at the interfaces between soil components such as minerals, humic substances, microbes, fungi, plants and water, and they control contaminant mobility. In this dissertation four projects were carried out to study the soil chemical processes of nickel. Nickel is a common contaminant in soils polluted with "heavy metals" and a model element to study because other transition metals undergo similar chemical reactions.   We find that nickel can transform rapidly at the mineral-water interface into newly formed Ni-Al LDH precipitates in tens of minutes, and we illustrate for the first time these fast reaction kinetics in a "live" sorption reaction. Additionally, nickel hyperaccumulating plants have no specific mechanism to preferentially remove nickel from minerals for transport into their leaves, which was contrary to our hypothesis that the plants had some preferential mechanism for nickel uptake. Lastly, we find that nickel is heterogeneously distributed in ultramafic soils amongst iron and manganese oxides and in the silicate minerals of primary and secondary ultramafic rocks and serpentinite, which illustrates the importance of climate on weathering processes in soils, and that hyperaccumulating plants can remove nickel from a variety of nickel mineral species.

xix

Chapter 1

INTRODUCTION

Environmental Soil Chemistry

Research in environmental soil chemistry revolves around interfaces, more specifically, the interfaces in soils and sediments where surfaces of solids and water meet. The reason for this is because the chemical reactions that control contaminant mobility (e.g., dissolution, sorption, precipitation) occur at interfaces. The "solid" can take many forms, and may be an inorganic mineral, like quartz or mica. Importantly, though, is the distinction of particle size, for a sand-size grain of quartz has a much smaller reactive surface area than its weight equivalent in the clay-size fraction. The solid could also be a humic substance (e.g., organic matter or detritus). Additionally, a solid could be a living organism, like a plant root, bacterial cell wall, or fungi. All of these solids react differently with the elements dissolved in the soil pore water, and all play a role in contaminant mobility and bioavailability.

What sets environmental soil chemistry apart from other, perhaps similar, research fields (e.g., low temperature interfacial geochemistry or environmental engineering of soils and sediments) is its flexibility to cover a range of interdisciplinary research topics. Not only can research in environmental soil chemistry be strictly about the inorganic chemical reactions that take place at the mineral-water interface, but it is possible (and important) to incorporate all the important biotic and environmental factors

1

that are relevant to the natural environment. Additionally, environmental soil chemistry's history in agriculture and soil science puts food production and nutrient management also under its research umbrella. Agriculturally important nutrients like nitrogen and phosphorous and biocides commonly applied to crops are also studied in soil chemistry.

A range of environmentally important elements and molecules, including light elements, to transition and heavy metals and metalloids, to radionuclides are studied in environmental soil chemistry. Organic contaminants, such as petroleum based hydrocarbons, are also common soil contaminants. Even research on global climate change and carbon dioxide cycling are areas of intense research in soil science because soils act as sinks for carbon dioxide. This range of research topics makes environmental soil science and chemistry a highly interdisciplinary research field and sets it apart from more traditionally defined academic roles.

Nickel in Soil

Nickel is a model element to study because it behaves similarly to other transition metals in soils by forming mixed metal hydrotalcite-type layered double metal hydroxides (LDHs). Other metals found to form LDHs on soil clay minerals include iron, cobalt, nickel, and zinc (Elzinga, 2012; Nachtegaal et al., 2005; O'Day et al., 1994; Scheidegger et al., 1997). Nickel in soil comes from two sources: human activities (anthropogenic) and natural materials (geogenic). These sources yield chemical forms (species) of nickel with different solubilities, which in turn affect nickel mobility in soils.

Anthropogenic sources of nickel include municipal and industrial waste, disposal of household garbage and incineration, batteries, stainless steel production, coal combustion, fertilizer applications, nickel refinery emissions, the metallurgical and electroplating industries, and catalysts in the chemical and food industries (Alloway, 1995; Bacon et al., 2002; Denkhaus and Salnikow, 2002; Easton et al., 1992; Salt et al., 2000; Yusuf et al., 2011). Nickel is a component of stainless steel, coins and jewelry. The production, refining, recycling and disposal of nickel containing products contribute to nickel release into the environment. The most common anthropogenic nickel species include oxides, sulfides, silicates, soluble compounds, and metallic Ni. The use of fossil fuels contributes most of the nickel found in ambient air (Denkhaus and Salnikow, 2002; Merian, 1984). Divalent nickel is the most common oxidation state of nickel in aquatic environments (Förstner and Wittmann, 1981).

Geogenic sources of nickel include magmatic sulfide ores and additionally lateritic silicates and iron oxides found in serpentine soils. Geochemical weathering alters ultramafic bedrock into Ni-rich serpentine soil. In ultramafic bedrock (e.g., peridotite), nickel is substituted for magnesium in silicate minerals (e.g. olivine). Nickel is present in serpentine minerals (e.g., lizardite) and accumulates with iron oxides as primary silicate minerals weather (Alexander et al., 2007). Nickel hyperaccumulator plants are native to ultramafic soils and can accumulate up to 3% weight nickel in their above ground biomass. This high amount of nickel in the plant leaves makes them good candidates for phytomining, where the dry plant material can be sold and economically profitable (Chaney et al., 2007; Reeves et al., 1983).

3

People may be exposed to nickel by air, skin contact with soil, or metals containing nickel; however, the major source of exposure to nickel is food (ATSDR, 2005). Nickel release can be a serious hazard to human health (Denkhaus and Salnikow, 2002), and low levels of nickel are ubiquitous in the environment and unavoidable to humans. Nickel mining, smelting and refinery workers are among the most susceptible to lung and nasal cancer caused by nickel exposure. Nickel refinery dust is carcinogenic to humans (ATSDR, 2005).

Research Hypotheses and Objectives

This dissertation is composed of four research projects. Each project uses different research methods to study nickel in soils and plants. The first research project aims to understand the fast sorption kinetics of nickel to clay minerals. Nickel can transform chemically in soils and on clay minerals to new, insoluble solid phases, such as Ni-Al LDHs. We hypothesize that nickel can form these new phases in tens of minutes and will carry out research to prove such. The second project characterizes the molecular stability of LDHs using molecular modeling, with the goal of understanding how aluminum substitution affects LDH stability. Ni-Al LDHs are important sinks for nickel in contaminated soils. We hypothesize that changing the aluminum content of LDH will significantly affect LDH stability, and hope to identify what aluminum content yields the most stable LDH. The third project aims to identify the types of nickel minerals that are most susceptible to hyperaccumulation by a specific plant. We hypothesize that certain nickel minerals are more susceptible to hyperaccumulation than others. Nickel

hyperaccumulator plants are important for use in phytomining and are unique because they accumulate large amounts of what would be toxic levels of nickel in other plants. The fourth and final project will analyze several ultramafic soils to study nickel speciation and distribution. Little research is available using direct methods (i.e., synchrotron techniques) to analyze ultramafic topsoils, which are naturally high in nickel. We hypothesize that nickel is heterogeneously distributed with iron and manganese oxides in addition to being a part of primary and secondary minerals in ultramafic ophiolites and serpentinite (e.g., olivine and lizardite).

REFERENCES

Alexander, E.B., R.G. Coleman, T. Keeler-Wolf, and S.P. Harrison. 2007. Serpentine geoecology of western North America: soils, geology, and vegetation. Oxford University Press.

Alloway, B.J. 1995. p. 25-34, In A. B.J., ed. Heavy metals in soils. Blackie Academic and Professional, London.

ATSDR. 2005. Toxicological profile for nickel. U.S. Department of Health and Human Services.

Bacon, W.G., A.D. Dalvi, B.A. Rochon, and M. Selby. 2002. Nickel outlook - 2000 to 2010. Cim Bulletin 95:47-52.

Chaney, R.L., J.S. Angle, C.L. Broadhurst, C.A. Peters, R.V. Tappero, and D.L. Sparks. 2007. Improved understanding of hyperaccumulation yields commercial phytoextraction and phytomining technologies. Journal of Environmental Quality 36:1429-1443.

Denkhaus, E., and K. Salnikow. 2002. Nickel essentiality, toxicity, and carcinogenicity. Critical Reviews in Oncology Hematology 42:35-56.

Easton, D.F., J. Peto, L.G. Morgan, and e. al. 1992. Respiratory cancer mortality in Welsh nickel refiners: which nickel compounds are responsible., p. 603-619, In E. Nieboer and J. O. Nriagu, eds. Nickel and Human Health: Current Perspectives. John Wiley & Sons, New York.

Elzinga, E.J. 2012. Formation of layered Fe(II)-Al(III)-hydroxides during reaction of Fe(II) with aluminum oxide. Environmental Science & Technology 46:4894-4901.

Förstner, U., and G.T.W. Wittmann. 1981. Metal pollution in the aquatic environment. 2 ed. Springer-Verlag, New York.

Merian, E. 1984. Introduction on environmental chemistry and global cycles of chromium, nickel, cobalt, beryllium, arsenic, cadmium and selenium, and their derivatives. Toxicological and Environmental Chemistry 8:9-38.

Nachtegaal, M., M.A. Marcus, J.E. Sonke, J. Vangronsveld, K.J.T. Livi, D. Van der Lelie, and D.L. Sparks. 2005. Effects of in situ remediation on the speciation and bioavailability of zinc in a smelter contaminated soil. Geochimica et Cosmochimica Acta 69:4649-4664.

O'Day, P.A., G.E. Brown, Jr., and G.A. Parks. 1994. X-ray absorption spectroscopy of cobalt(II) multinuclear surface complexes and surface precipitates on kaolinite. Journal of Colloid and Interface Science 165:269-289.

Reeves, R.D., R.R. Brooks, and T.R. Dudley. 1983. Uptake of nickel by species of *Alyssum, Bornmuellera*, and other genera of old-world *Tribus Alysseae*. Taxon 32:184-192.

Salt, D.E., N. Kato, U. Kramer, R.D. Smith, and I. Raskin. 2000. The role of root exudates in nickel hyperaccumulation and tolerance in accumulator and non-accumulator species of *Thlaspi*, p. 189–200, In N. Terry and G. Banuelos, eds. Phytoremediation of contaminated soil and water. CRS Press LLC, London.

Scheidegger, A.M., G.M. Lamble, and D.L. Sparks. 1997. Spectroscopic evidence for the formation of mixed-cation hydroxide phases upon metal sorption on clays and aluminum oxides. Journal of Colloid and Interface Science 186:118-128.

Yusuf, M., Q. Fariduddin, S. Hayat, and A. Ahmad. 2011. Nickel: An overview of uptake, essentiality and toxicity in plants. Bulletin of Environmental Contamination and Toxicology 86:1-17.

Chapter 2

**RAPID FORMATION OF LAYERED DOUBLE HYDROXIDES REVEALED BY
QUICK-EXAFS SPECTROSCOPY**

Abstract

Sorption reactions at the mineral-water interface between trace metals and clay minerals are extensively studied to understand trace metal fate, transport, toxicity and bioavailability in the environment. Some trace metals in soils, such as cobalt, nickel and zinc, transform into mixed metal layered double hydroxides (LDHs) and effectively immobilize those trace metals as newly formed solid phases. However, no studies have identified the rapid kinetics of LDHs formation in real time on mineral surfaces. Using novel quick-scanning extended X-ray absorption fine structure (EXAFS) spectroscopy, we demonstrate that Ni-Al LDHs form in mineral systems flow environments in about 30-40 minutes. This finding provides the first direct, in situ, real time evidence that metal adsorption and precipitation at the mineral-water interface can take place on the same time scale and establishes a new precedent for measuring and modeling the rapid kinetics of adsorption and surface precipitation.

One Sentence Summary

QXAS reveals adsorption and precipitation of trace metals at the mineral-water interface can occur on the same time scale.

Introduction

Adsorption Models

Equilibrium based adsorption models, such as the Freundlich and Langmuir equations, and electric double layer and surface complexation models have been commonly used to describe sorption reactions of trace metals at the mineral-water interface. They are useful for comparative descriptions of macroscopic data but do not prove reaction mechanisms and have also been criticized for their core assumptions when applied to the chemical reactions at the mineral-water interface under environmental conditions, such as in soils (Sparks, 2002). Additionally, these models do not include several other processes important under environmental conditions. Specifically, clay mineral size is not accounted for in the models, yet it heavily influences geochemical reactions and kinetics (Hochella et al., 2008). Also, minerals (adsorbents) themselves are dynamic and dissolve, thereby impacting sorption reactions of trace metals (adsorptives) at their surfaces, often incorporating trace metals into newly formed precipitates (Charlet and Manceau, 1994; Delacaillerie et al., 1995; Li et al., 2012; Scheidegger et al., 1997; Scheinost and Sparks, 2000). Lastly, because the models are equilibrium based they do not take into account the kinetics of sorption reactions, which vary from microseconds to years and also heavily influence reaction products (Sparks, 2002). Given these limitations in sorption models, it is desirable to investigate empirically the sorption kinetic reactions at the mineral-water interface using direct, in situ methods, such as synchrotron-based X-ray absorption spectroscopy (XAS).

Layered Double Hydroxides in Soils

Elevated levels of trace metals in soils and sediments pose environmental hazards to plants, animals and humans, and the chemical form (species) of trace metals is directly related to its mobility and bioavailability. To analyze environmental soils and sediments and identify metal species at the mineral-water interface, direct methods, such as X-ray absorption spectroscopy (XAS), are commonly used. Using XAS, the formation of metal rich precipitates, such as hydrotalcite-type LDHs, on clay minerals has been identified for reactions with iron(II) (Fe^{2+}), cobalt (Co), nickel (Ni), and zinc (Zn) (Charlet and Manceau, 1994; Delacaillerie et al., 1995; Elzinga, 2012; Scheidegger et al., 1997; Thompson et al., 1999; Towle et al., 1997; Trainor et al., 2000). LDHs can serve as important neoformed minerals for trace metal immobilization in contaminated soils and sediments (Sparks, 2002). LDHs appear to form rapidly on clay minerals (Scheidegger et al., 1998), and when silicon is present in the adsorbent they tend to be amorphous (Livi et al., 2009). Lack of Si in the adsorbent can result in crystalline LDH products much larger in size than the adsorbent itself (Li et al., 2012). Silication of the LDH interlayer, where $SiO_{2(aq)}$ enters the interlayer space, is thermodynamically favorable (Peltier et al., 2006), and silicated-LDHs are similar to precursor phyllosilicates with mixed metal hydroxide sheets (Charlet and Manceau, 1994; Ford et al., 1999; Sparks, 2002).

Limitations of Past Methodology

Although it has been shown that LDHs may form rapidly, previous methodology has been limited because of the batch technique typically used in sorption reaction

10

experiments in addition to the XAS hardware and software available at the time. Of the literature on LDHs formation, most have employed at some point batch techniques and XAS. Several studies have carried out time-resolved research [e.g., (Livi et al., 2009; Scheidegger et al., 1998; Scheinost and Sparks, 2000)] via batch technique; however, as such, all XAS measurements are not actually taken in real time and in situ of the chemical reaction during LDH precipitation. XAS spectra collected from samples reacted in batch mode are taken ex-situ of and posterior to the LDH precipitation reaction. Regardless, from the literature, it has been concluded that there is often a continuum between adsorption and precipitation (Sparks, 2002). This conclusion is based on indirect evidence from batch studies of samples taken at discrete time frames.

Apart from the limitations of the batch methodology, XAS for most geochemical reactions has been limited, until recently, to long scan times (e.g., 30 minutes to 1 hour per scan) to obtain the extended x-ray absorption fine structure (EXAFS) spectra with reasonable signal to noise ratios. To overcome these limitations, we combined a custom built flow cell and Quick-Scanning XAS (QXAS) (Khalid et al., 2010). This setup allows for the rapid acquisition of XAS data during the initial sorption phases of the reaction (i.e., the first several minutes), which in turn permits the identification of a continuum of trace metal chemical species in real time and in situ. The Q-XAS scan time has been dramatically decreased in some cases to less than 1 second per scan (Khalid et al., 2010). For environmental soil chemical reactions, Q-XAS has been used only in analysis of the near edge structure (Ginder-Vogel et al., 2009; Landrot et al., 2010). Here we apply the technique to the entire EXAFS range. Batch techniques and XAS beamline

hardware were two limitations for the study of kinetic reactions at the mineral-water interface. Additionally, improvements in XAS data analysis software such as Athena/Artemis and Sixpack (Ravel and Newville, 2005; Webb, 2005), have greatly enhanced the users' ability to process data more quickly and accurately.

Objectives

Realizing the limitations in models and methodology and the recent advances in Q-XAS, the specific scope and objective of our research was to determine in real-time, in situ, and at the molecular scale for the first time the kinetics of trace metal rich LDH precipitate formation on clay minerals. We designed a flow-cell to carry out the reactions in situ by placing the flow-cell in the path of the incident x-ray beam, which rapidly scans through the EXAFS range at about 1 scan per second, to monitor changes in metal sorption and speciation over time.

Materials and Methods

Overview of Experimental Methods

This study overcomes prior research limitations to determine the rapid kinetics of LDH formation on clay minerals by employing a novel approach that combines a flow cell and Q-XAS. First, a flow-cell was designed to carry out the reactions in a flow environment. A flow environment has the benefit of removing non-sorbed products from the reaction versus a batch reaction where desorbed products and reactions are still able to resorb to the surface (Sparks, 2002). Second, the flow cell is used in conjunction with

12

Q-EXAFS spectroscopy (Khalid et al., 2010), which is a technique recently proven to be useful in identifying the fast kinetics of environmentally important soil chemical reactions (Ginder-Vogel et al., 2009; Landrot et al., 2010). The flow cell was packed with a homogeneous mixture of pyrophyllite clay and glass beads. It was placed in the x-ray path and solution containing nickel was pumped through the cell. In this setup, under incident X-rays at the nickel K edge, the nickel that sorbs and accumulates at the clay mineral surface fluoresces. The fluorescence was measured with a PIPS detector and analyzed to determine the chemical form of nickel accumulating in real time on the mineral surface. At the end of the reaction time, the flow was stopped. While stopped, data were continuously collected on the non-flowing (NF) sample to measure further changes under stagnant conditions over time. For Run 1, the reaction was run for 12.5 hours and then fluorescence data were obtained on a NF cell over 15 minutes. For Run 2 the reaction was run for about 5 hours and 20 minutes, and then the NF data were collected over 40 minutes about 8 hours after the flow was stopped. For Run 3, the reaction was run for 74 minutes and flow was stopped, and NF data were collected immediately. For Runs 4 and 5, the reactions ran for 4 hours before flow was stopped and NF data were acquired immediately.

Preparation of Pyrophyllite Mineral

The sub-0.2 micrometer fraction of several different sources of naturally occurring pyrophyllite (from Ward's Science) was obtained by centrifugation in water at room temperature, assuming a particle density of 2.65g/cc and taking into account the

initial and final settlement radii, r1 and r2, respectively. 50 mL conical centrifuge tubes were used in a swing-bucket centrifuge. X-ray diffraction confirmed the major mineral to be pyrophyllite in all samples with minor impurities of quartz. The clays were washed once with 0.5M $NaNO_3$ and then three times with RO water. Lastly, they were freeze dried.

Experimental Details

The experiments were carried out at beamline X18B of the National Synchrotron Light Source (Khalid et al., 2010). The solution influent varied slightly from pH 7.5 ±0.1, 3 mM nickel buffered with 40 mM HEPES and 100 mM NaNO3 for Runs 1 & 2 to pH 7.5 ±0.1, 3 mM nickel buffered with 50 mM HEPES for Runs 3, 4 & 5 (Ford et al., 1999; Scheidegger et al., 1997). The HEPES buffer was necessary to counter the pH decrease of the LDH hydrolysis reaction occurring in the flow cell and to maintain the pH of 7.5 of the influent in the bottle open to the ambient air. The minimum amount of buffer necessary was used. The influent solution was pumped via a peristaltic pump at a rate of about 0.51 mL/min. The bulk density of the clay/glass bead mixture was 1.59 g/cc on average. The <0.2 or <2 micrometer fraction of several different sources of naturally occurring pyrophyllite (Scheidegger et al., 1996) was obtained by centrifugation in water at room temperature, assuming a particle density of 2.65g cc^{-1} and taking into account the initial and final settlement radii, r1 and r2, respectively. X-ray diffraction confirmed the major mineral to be pyrophyllite in all samples with minor impurities of quartz and kaolinite.

The solution flowed from the influent bottle through tubing connected to the flow cell. A 0.2 micrometer nylon syringe filter was placed at the exit of the flow cell. The solution effluent flowed through filter and then through tubing to a fraction collector where it was collected over two minute intervals throughout the reaction of several hours.

The material inside the flow cell consisted of a homogenous mixture of 4% or 8% pyrophyllite clay with inert solid glass beads. Run 1 had 4% while Runs 2, 3, 4, and 5 had 8%. The glass beads were 250-300 micrometers in diameter, or $\geq$1250-1500 times larger than the pyrophyllite clay mineral. Additionally, glass beads low in trace metals, specifically iron, were obtained in order to minimize any interference of trace metal fluorescence from the beads into the PIPS detector during the EXAFS experiments. Trace metal free solid glass beads 200-300 μm in diameter proved difficult to obtain. Glass beads made of "soda lime" can have up to several thousand ppm of iron, which can interfere with the nickel fluorescence. However, we found borosilicate glass beads that were low in trace metals from Mo-Sci Specialty products, L.L.C., product number GL0179B5/250-300.   We were unable to fine "fused quartz" glass beads but did find fused quartz chips. However, preliminary experiments showed that the flow through a mix of quartz chips and pyrophyllite was not as homogeneous as with glass beads. Control experiments run with no pyrophyllite (i.e., just glass beads) showed no increase in edge jump over time and an edge jump 3.6% in size to those at the end of other experimental runs, indicating little nickel sorption and no increase in sorption to the glass beads over time.

All XAS experiments were carried out at the National Synchrotron Light Source (NSLS) beamline X18B under QXAS mode (Khalid et al., 2010). The monochromator was detuned approximately 30% and oscillated at approximately 0.5Hz. This frequency combined with the rapid data collection software available at X18B yields about 4000 data points per EXAFS scan per second. To minimize the effects of the glitches caused by the monochromator, the monochromator was rotated in the chi direction, which dramatically decreased the glitch intensity and separated one large glitch into several smaller ones. The smaller glitches moved up to higher energy as well, c.a. 11.5 Å^{-1}, where they were excluded from the FT window. It was determined through trial-and-error that to obtain clean fluorescence EXAFS data that could produce meaningful fitting parameters, data from about 5-10 minutes of scanning could be merged together. Less amounts of time yielded data too noisy to carry out shell-by-shell fitting. Current to voltage amplifiers were set to a filter time of 1millisecond. If amplifier filters were set to longer times, e.g. 3 ms, the glitch spread out over more data points and was more difficult to remove.

Q-XAS Data Processing

To process the QXAS data, multiple steps are necessary prior to background subtraction and normalization because data are continuously collected both up and down in energy. An encoder is used to measure the monochromator angle and nickel foil scans are used to convert the encoder angle to energy (eV) using the first derivative of the foil (8333 eV). The continuous up and down scans must be cut at high and low energies to

separate individual scans. This procedure was carried out using custom software available at X18B. Subsequently, the software packages Athena and Artemis (Ravel and Newville, 2005) were used for normalization and background subtraction, deglitching where appropriate and shell fitting analysis. Due to a glitch in the monochromator, it was necessary to remove in general 4-5 consecutive data points in the EXAFS spectrum at longer stages of the reaction and occasionally up to 8-9 points at beginning reaction times. The amplifier filter set to 1 or 3 ms caused the glitch to spread out in energy and only those points affected were removed. Generally up to a 0.15 Å^{-1} gap in data points is allowed, or 3 points on a 0.05 Å^{-1} grid, for deglitching (Kelly et al., 2008). For all spectra, the FT was carried out on a k-range of 3-11.3 with a k weighting of 3. Hanning windows with widths of 1 and 0.3 were used for the forward and back FT, respectively. FEFF6L (Zabinsky et al., 1995) was used to calculate theoretical scattering paths of Ni-O, Ni-Ni, Ni-Al, and Ni-Si based on the structure of lizardite (Mellini and Viti, 1994). In the lizardite structure, nickel and aluminum were substituted for magnesium. All spectra were analyzed with a k weighting of 3. Amplitude reduction factors of 0.99 or 0.91 were determined from aqueous nickel and nickel hydroxide standards for the filter times of 1 ms or 3 ms where appropriate and then applied to all fitting paths (Table 2.2). An amplitude reduction factor for standards of Ni-Al LDH and nickel hydroxide from Scheinost and Sparks (2000) was set to 0.85.

Testing Different Structural Models

Several fitting models were tested to determine the most reasonable method to fit the EXAFS data, including an isostructural fitting model. This model has several assumptions (Kelly et. al., 2008). One of which is that the Ni-Al distance is the same (Delacaillerie et al., 1995; Peltier et al., 2006). This assumption, however, may be inaccurate as the ionic radius of Al is less than that of nickel, which is what causes the contraction of the M-M distance in the Ni-Al LDH versus the $Ni(OH)_2$ (Delacaillerie et al., 1995). Perhaps a more reasonable fitting model would restrict Al distances to less than those of Ni by 0.03 Å. Regardless, such small differences are on the borderline of the detection limits for XAFS (O'Day 1994). Additionally, because of the impurities of these systems (e.g., Si, NO_3^-, and vacancy sites) it is difficult to decide with certainty which atoms, apart from nickel, belong to the second shell using just structural fitting models. Moreover, the Reduced Chi Square (RCS) values are significantly reduced in the longer reacted samples with the inclusion of silicon into the fit. A reduction of ~2x in RCS is considered to be significant improvement in the fit (Kelly et al., 2008). Additionally, this improvement was accomplished without adding more fitting variables (i.e., no increase in the degrees of freedom).

Another fitting model allowed the silicon atom to drift in R. Here we found with one more degree of freedom the Ni-Al distance contracted even more while the Ni-Si distance expanded further. This type of fitting could perhaps even more accurately portray the neoformed silicated LDH by indicating a non-fully formed silicate layer

partially detached from the hydroxide sheet and therefore at a slightly longer distance than that generally found in a phyllosilicate mineral.

Wavelet Transformation

Wavelet transformation analysis was carried out with the HAMA program written for IGORpro (Funke et al., 2007). WT was carried out on r and k ranges from approximately 2.3-3.3 Å and 3-11 k with a k-weighting of 3. The product of the WT parameters sigma and kappa were set to equal twice the distance of the second shell uncorrected for phase shift. The distance is circa 2.7 Å and therefore sigma and kappa were set to 1 and 5.4, respectively.

Results and Discussion

Figure 2.1 provides a direct comparison of two isostructural synthetic standards, an alpha-$Ni(OH)_2$ and a Ni-Al LDH with a Ni/Al ratio of 1.3 (Scheinost and Sparks, 2000) to Run 3 at 50-60 minutes of the reaction. The LDH and sample peaks at ~8.2 $Å^{-1}$ are truncated compared to the peak of the nickel hydroxide, which has higher, slender amplitude and ends with an acute point at ~8.4 $Å^{-1}$ (Scheidegger et al., 2000).

Figure 2.2 is the EXAFS data of all sample runs. Among all the runs, several common features are indicated by arrows 1, 2, and 3. At ~5.3 $Å^{-1}$, arrow 1 indicates a shoulder forming during the reaction. This shoulder results from focused multiple scattering that occurs in the planar hydroxide layers and is common to many layered single and double metal hydroxides and silicates (Charlet and Manceau, 1994; Delacaillerie et al., 1995; Scheinost and Sparks, 2000; Yamaguchi et al., 2002).

19

Additionally, between 7-9 Å^{-1} a separation from one peak into two occurs over time in all sample runs. Initially one peak is present and over the first hour in all samples two peaks form.

Figure 2.2 also contains the Fourier Transformation (FT) of the EXAFS data into radial structure functions (RSF), uncorrected for phase shift. Over the course of the reaction, the amplitude of the first shell at ~1.6 Å remains constant while that of the second shell at ~2.65 Å increases. The second shell is dynamic over time in all samples, increasing in amplitude and changing slightly in distance and backscatterer CN (Table 2.2). At the beginning of each run, the second shell is small and continues to increase in size over time as nickel accumulates on the pyrophyllite surface and precipitates begin to form. The changes in amplitude, distance, and CN indicate shifts in the local atomic environment surrounding the central nickel atom. Shells at ~4.9 Å and ~5.6 Å present in all samples are the 2nd and 3rd metal coordination shells and also increase in height with reaction time. They result from focused multiple scattering in the hydroxide layer and are most prominent at the end of the reaction time (Funke et al., 2007; O'Day et al., 1994; Scheinost and Sparks, 2000).

Table 2.2 gives the structural fitting results for all sample runs. The first shell results from the oxygen atoms that surround nickel, and coordination numbers (CN) of 5.6-6.4 remain constant throughout the reaction for all runs. In all runs, the Ni-O distances were determined to be between 2.05-2.08 Å, with 2.06 Å being the most common distance. The second shell of Ni-Ni ranged from 3.10-3.07 Å with CN of nickel ranging from 0.5 to 4. Distances of 3.07 Å to 3.08 Å for Ni-Ni in the second shell are the

most common. 3.07 Å is slightly reduced compared to the Ni-Ni distances of the alpha

nickel hydroxide standard 3.09 Å. However, Ni-Ni distances in alpha nickel hydroxide

can range from 3.07-3.09 Å (Pandya et al., 1990). The incorporation of aluminum into

the hydroxide layer decreases the metal-metal distance (Delacaillerie et al., 1995;

Scheinost and Sparks, 2000); regardless differences of 0.02 Å are still within the

experimental error (O'Day et al., 1994).

Analysis of the second shell is complicated by the contribution of several different

atomic backscatters at different distances from the central absorbing nickel atom. In

silicated mixed metal hydroxides, e.g., a silicated-Ni-Al-LDH, aluminum substitution for

nickel in the octahedral layer and silicon present in a tetrahedral layer simultaneously

produce two different backscattered photoelectric waves that are partially destructive and

constructive, respectively, with the photoelectric wave produced by nickel in the

octahedral layer (Delacaillerie et al., 1995; Manceau, 1990; Manceau and Calas, 1986;

Scheinost and Sparks, 2000). The Ni-Ni and Ni-Al photoelectric waves produced from

those atom pairs at ~3.06 Å are partially destructive; however partially constructive

interference occurs between Ni and Si when the Si atoms are further away from the

absorbing Ni atom and located in a tetrahedral sheet at e.g., 3.21 Å (Manceau and Calas,

1986). Additionally, because of the impurities of these systems (e.g., covalently bonded

NO_3^- to the hydroxide layer and vacancy sites) it is challenging to decide with any degree

of certainty which atoms apart from nickel belong to the second shell using the statistics

of structural fitting models alone. This is one reason why Table 2.2 mainly consists of

Ni-Ni for second shell fits. Another reason is to avoid any false positive results for

aluminum or silicon scattering paths. For example, the Reduced Chi Square (RCS)

values are significantly reduced in the longer reacted samples with the inclusion of

silicon and aluminum into the fit (Table 2.2, all samples at the end of their runs). A

reduction in RCS of about two is considered to be significant improvement in the fit

(Kelly et al., 2008). Additionally, this improvement was accomplished without adding

more fitting variables (i.e., no increase in the degrees of freedom). It is reasonable for

nickel to share σ^2 and ΔR values with aluminum and silicon because when those variables

are fit independently, their error bars overlap with those of Ni and so they can be shared

(Kelly et al., 2008). Additionally, using an isotropic expansion–contraction fitting model

is reasonable to help reduce the number of independent fitting variables (Kelly et al.,

2008).

However, when silicon is added to the nickel hydroxide standard, the RCS value

also decreases by more than twice (Table 2.2). Perhaps this is due to similar

backscattering amplitudes and frequencies of silicon and nitrate groups commonly found

covalently bonded in single layered hydroxides (Delacaillerie et al., 1995; Scheinost and

Sparks, 2000). The standard is known to have no silicon in the interlayer according to the

FITR spectra (Scheinost and Sparks, 2000); however because silicon can increase the fit

of the silicon-free nickel hydroxide standard, there is no confidence to place silicon as a

scattering path into unknown samples.

In Table 2.2, the choice to only show Ni-Ni distances for the majority of the

reactions was deliberate. At the end of all sample runs, both fitting models A and B are

shown for comparison to prove that other scattering paths do improve the fit by lowering

22

the RCS value by more than a factor of two without adding additional fitting parameters. We choose not to include fitting model B into the earlier portions of sample runs because even though the RCS values do decrease, they do not decrease by a factor of two until later in the reactions. Adding aluminum and/or silicon in model B did not change the Ni-Ni distance significantly, so it is reasonable to only consider model A for interatomic distances. Even when aluminum is included in the fit for the Ni-Al LDH standard, the RCS value decreases but not significantly. The presence of aluminum, however, is indisputable because of the beat pattern and truncation at ~8.2 Å^{-1}.

Regardless of these interferences and statistical comparisons, the beat pattern present at ~8.2 Å^{-1} (Figures 2.1 and 2.2, arrow 3) can be used to unequivocally distinguish LDHs from hydroxides (Scheinost and Sparks, 2000). In Figure 2.2 the peak height at ~7.5 Å^{-1} (arrow 2) is equal to that of the adjacent peak at ~8.2 Å^{-1} (arrow 3). The equal peak heights at arrows 2 & 3, i.e., a truncated peak at arrow 3, are apparent in some sample runs (e.g. Run 3) starting at 31-40 minutes and throughout the rest of the reaction. Based on this truncated peak height and beat pattern of Ni-Al LDHs, we conclude that LDH precipitates form over short time scales in real time, *in situ,* flowing reactions and provide the first direct evidence that adsorption and precipitation can occur on the same time scale.

The rapid formation of LDHs identified here in an *in situ,* flowing environment has many implications for fate, transport, toxicity, and bioavailability of trace metals in the environment because those processes are related to the kinetics of trace metal precipitation in soils. These rapid precipitation mechanisms can be used to improve

23

modeling efforts so models more accurately depict the natural environment. For example, modeling of trace and toxic metals in the environment heavily depends on their sorption affinities to soil minerals and oxides, the rates at which new precipitates form, and the mineral solubilities. Software programs used in modeling, like MINTEQ (Zelmy et al., 1984) or TICKET (Farley et al., 2011), often use equilibrium constants of pure minerals, however, because these mixed metal LDH phases are only recently being characterized (Peltier et al., 2006) their inclusion into these data bases are limited. They are not accounted for in speciation/solubility diagrams because they are impure, and up to this point not considered to form rapidly. However, LDHs are thermodynamically stable over pure single metal phases; for example, Ni-Al LDH is more stable than nickel hydroxide (Peltier, et al., 2006).

Never has a molecular scale study been carried out under these conditions to show the rapid formation of metal rich precipitates in real time. Showing that precipitates can form on the same time scale as adsorption establishes a new precedent for the way we consider the kinetics of adsorption and surface precipitation. In environmental soil chemistry and low temperature surface geochemistry this finding challenges the long held belief that precipitation in soils occurs on long time scales. But now we have shown for the first time how LDHs can form in a live reaction in tens of minutes to immobilize trace metals. The kinetics of formation are so rapid in a live reaction, we propose that a new perspective on mixed metal phases in the environment should be realized and accounted for in modeling and predicting transport of trace metals to truly capture the heterogeneity of environmental systems.

Wavelet Transformation of LSHs and LDHs

Apart from the qualitative comparison of EXAFS data, interference between distinct backscattering waves in a mixed metal shell significantly complicates EXAFS modeling. To separate backscattering waves that compose a single shell in r-space, it is helpful to resolve the data in both k- and r-space using wavelet transformation (WT). WT can identify if more than one type of backscatterer (either from an atom or multiple scattering) is contributing to the EXAFS data (Funke et al., 2007). Figure 2.8 shows the WT plots of Run 3 and of the reference alpha-nickel hydroxide phase from Scheinost and Sparks (2000). The WT was carried out on the 2nd and 3rd metal peaks between ~4.6-6.4 Å, which result from the focused multiple scattering in the hydroxide sheet (Funke et al., 2007). What was thought to be the presence of a light and heavy backscatterer in the hydroxide sheet of Run 3 is indicated by the separate red maxima at different wavenumbers. The maxima for the nickel hydroxide sample are at the same wave number, indicating the 2nd and 3rd peaks are of the same composition, i.e., nickel atoms (Aimoz et al., 2012). Upon further examination, it has been determined that identical sigma and kappa values for the WT must be used in order to make any conclusions. By shifting the kappa values, the shapes of the WT plots change drastically as is also noted in Figure 2.8. When Run 3 is transformed using a kappa value of 30, the two peaks merge into one and a conclusion about light and heavy elements occupying the 2nd and 3rd metal shells is incorrect. Upon further examination of the supplemental information in Aimoz et al. (2012), it is shown that the LDH must have a significant amount of light elements in the 2nd and 3rd metal shells to observe changes in k-space for peak maxima.

Many LDHs still show two maxima at similar k values, making the WT plot by itself a difficult tool to use distinguish LDH from a single metal hydroxide.

Wavelet Transformation of Alpha and Beta Nickel Hydroxides

The purpose of focusing on the second and third metal shells is that they result from the focused multiple scattering in the hydroxide sheet (Funke et al., 2007). So ideally Ni and Al should appear at different k values, but the sensitivity of WT analysis along with a lack of long range order in precipitated Ni-Al LDHs many times do not allow for this. It would be preferred to analyze the second shell of an LDH in order to separate out the Ni and Al phases, however, as described below, several other problems arise.

Figure 2.9A,B, and D illustrate the problem. Alpha and beta nickel hydroxides have the same WT plots as two different Ni/Al LDHs and a nickel phyllosilicate. Perhaps silica is a contaminant in the nickel hydroxide interlayer (see discussion below), or perhaps a triangular Ni-O-O-Ni MS path could cause the same effect in the WT plot. Both of these hypotheses produce statistically improved fits over just Ni in the second shell of single metal nickel hydroxides. The problem is that in the literature, researchers never use MS paths to fit nickel hydroxides and other articles state that molecules do not intercalate the b-nickel hydroxide layers. However, a silicon tetrahedron could theoretically fit in the interlayer.

In using wavelet transformation software HAMA (the Fortran version), performing the WT of the second shell of several alpha or beta nickel hydroxide samples

26

yields two distinct regions in the WT plot. This pattern, as discussed in the literature, generally indicates two types of backscatterers, one low Z and one high Z, that contribute to the EXAFS spectra at different regions of chi. In fact, these nickel hydroxide samples produce similar WT to those of Ni/Al LDH. This is problematic for using WT to identify LDH because nickel hydroxide should only have 1 type of backscatter dominant in chi, i.e., nickel. Several hypotheses as to why nickel hydroxide and Ni/Al LDH produce similar WT plots are presented: 1) Ni-O multiple scattering paths in the single metal hydroxide could significantly contribute to chi at low k, or 2) there is silicon contamination in the nickel hydroxide interlayer [e.g., adding a Si path to the shell fit (not shown in the attachment) gives Si at about 3.29A, which is indicative of a tetrahedral silicate sheet adjacent to the octahedral metal sheet.

Delacaillerie et al. (1995) states that (1) the basic nickel nitrate salt $[Ni(N0_3)_2*2Ni(OH)_2]$ is indistinguishable from alpha-$Ni(OH)_2$ by EXAFS observation only, and (2) the basic nitrate salt has nitrato groups covalently bonded to the hydroxide layer. Additionally, nitrate or carbonate ions may remain adsorbed to the alpha-hydroxide due to air contamination or insufficient washing.

Although Delacaillerie et al. (1995) states that the spectra of a basic nickel nitrate salt and that of alpha nickel hydroxide are indistinguishable, the bound nitrato groups seem to slightly dampen the EXAFS signal amplitude, throughout all parts, as compared to the pure alpha nickel hydroxide. Perhaps this dampening from covalently bonded nitrato or carbonate groups appears in the WT plots. Essentially, they dampen the oscillations of the basic salt EXAFS spectra compared to those of the pure alpha-

hydroxide spectra. Then, in the WT plots they appear as a lighter Z element, similar to the effect that aluminum has in the WT plot. The major difference, however, between the nitrato groups and Al is that Al in the hydroxide layer produces a very noticeable beat pattern in the chi spectrum at 8 Å^{-1}.

It is quite deceiving when one is looking for another maximum at lower k values in the LDH and then they also appear in the pure mineral single metal hydroxides. So it would be important to wash samples thoroughly so as to remove as much basic nitrate anions as possible. See Figure 2.9A,B, & B where the basic nickel nitrate salt hydroxides have very similar EXAFS spectra to the alpha nickel hydroxides. The good news is that the characteristic beat pattern and dampening of the oscillation at about 8 Å^{-1} is not affected by the adsorbed basic salts. After working with many samples, I've come to the conclusion that many of our nickel hydroxides are contaminated with nitrate/nitrato groups bonded to the hydroxide layer and are not pure single metal hydroxide standards, as seen in the WT plots of Figure 2.9A,B & C.

Using Different Structural Fitting Models

In order to determine the best structural model to use when fitting the EXAFS data, several fitting models were used and the results are described below. Run 3 was reacted in the flow cell for 74 minutes. During that time, 3 mM nickel constantly flowed through the cell at 0.5 mL/min. The sample was then allowed to rest for an additional 70 minutes to measure any changes in nickel speciation without flow (i.e., under non-flowing "NF" conditions). Information presented in Figures 2.10 and Table 2.3

represents the analysis of EXAFS data collected over a period of 5 minutes at the end of that resting period.

Shell fitting analysis was carried out on the first two shells of the Fourier Transformed (FT) k^3-weighed EXAFS data. Extraction of the EXAFS data from the raw spectrum was carried out using Athena, while shell fitting analysis was carried out using Artemis (Ravel and Newville, 2005). FEFF6L (Zabinsky et al., 1995) was used to calculate theoretical scattering paths of Ni-O, Ni-Ni, Ni-Al, and Ni-Si based on the structure of lizardite (Mellini and Viti, 1994). In the lizardite structure, nickel and aluminum were substituted for magnesium. Seven different fitting models (Table 2.3) were used based on the lizardite structure. Based on these results it could be determined that nickel-aluminum phyllosilicates were formed in the sample. This structure was the only one to have a minimum chi square value and physically acceptable interatomic distances. However, upon further examination of how extra fitting paths affect reference data (Table 2.2), it seems concluding a nickel-aluminum phyllosilicate has formed is somewhat premature because adding silicon to nickel hydroxide also decreases the RCS value by more than two, and there is no silicon in that sample. Realistically, based on the truncation and beat pattern at 8 Å^{-1}, a Ni-Al LDH has formed but the question of silication is still there [Figures 2.3 & 2. 7]. Although Scheinost and Sparks (2000) state the beat pattern at ~8.2 Å^{-1} unequivocally distinguishes LDHs from phyllosilicates, we additionally note that a silicated-Ni/Al-LDH will still yield a truncated peak at ~8.2 Å^{-1} , as illustrated by Ford et al. (1999)[Figure 2.7].

Of the 7 fitting models in Table 2.3, models 1, 3, 5, 6 and 7 have comparable reduced chi square values of 18, 7.5, 22, 17 and 11.5, respectively. Those values are on the order of 2x less than those for fit models 2 and 4, and so models 2 and 4 could be disregarded. A decrease in the reduced chi square value by a factor of 2 indicates a significant enhancement in the fit (Kelly et al., 2008). The best chi square value of 7.5 involves nickel and a Ni-O-Ni multiple scattering path. This type of path has been used to fit LDH phases (Funke et al., 2005); however, here, it requires a significant CN of 32, which is too high considering that in structures where scattering atoms are far from collinear, as is the case for the first metal shell here, MS paths are important in the EXAFS range only for interatomic distances of ≤1.6 Å, which is not the case here (Bunker and Stern, 1984). Hence fitting model 3 can be disregarded.

Fitting models 1, 5, 6, and 7 remain as possible candidates for the best model. However, several problems are identified in models 5 and 6. In model 5, the Ni-Al distance of 3.238 Å is too large to represent either nickel adsorbed to aluminum at edge sites of pyrophyllite or nickel incorporated into the hydroxide layer of a Ni-Al LDH precipitate (Scheidegger et al., 1996). However, this distance indicates that perhaps Si is present. Ni-Al distances should be 2.96-3.06 Å (Delacaillerie et al., 1995; Scheidegger et al., 1997). Fit model 6 is problematic because the Ni-Si distance of 3.137 is too short. This distance would indicate an edge sharing bidentate complex between the nickel octahedron and silicon tetrahedron; however, because of the dissimilarity between the O-O distances of nickel octahedra and silicon tetrahedra this complex is not possible (Scheidegger et al., 1996). EXAFS cannot differentiate between Al and Si because they

have nearly equal scattering factors. Additionally, if Ni is present with Al/Si at the same interatomic distance, partial destructive interference of the backscattered photoelectric wave occurs. However, constructive interference occurs between Ni and Si when the Si atoms are farther away from the absorbing atom (e.g., at 3.21 Å) (Manceau and Calas, 1986). The last fitting model number 7 uses an isotropic-expansion contraction model (Kelly et al., 2008). Here Ni, Al, and Si all share disorder terms and shifts in r. This is an acceptable assumption because their error bars overlap when fitted independently, so this allows for a reduction in fitting parameters. Here we also have a very low reduced chi square value and all the atomic distances are reasonable with reasonable disorder statistics as well. This model could also be chosen as the correct model.

In summary, by using several different fitting models, then eliminating models with statistically large reduced chi square values and models with unrealistic interatomic distances, one can choose a model that best represents the system. Here, apparently model 7 best represents the system. This indicates that the precipitation of neoformed hydrated nickel-aluminum silicates can occur within several hours of the start of the reaction. The calculated interatomic distances of Ni-O (2.056 Å), Ni-Ni and Ni-Al (3.054 Å) and Ni-Si (3.305 Å) (Table 2.2) agree well with the established values of nickel phyllosilicates. In sheet silicates, metal-Si parings near 3.2-3.3 Å is a typical distance for corner sharing of Si tetrahedra and metal octahedra, and metal-metal distances of 3.0-3.1 Å are typical of edge sharing octahedra (Charlet and Manceau, 1994; Manceau and Calas, 1986; O'day et al., 1994). However, again, one must keep in mind that adding silicon to nickel hydroxide also decreases the RCS value by more than two (Table 2.2), and there

was no silicon in that sample. In effect, we are forced to accept the most simplistic fitting

model, which was model 2 as an acceptable fit. Regardless, the truncations and beat

pattern at 8 Å^{-1} are there (Figure 2.1, 2.2, 2.3, and 2.7).

Figure 2.10 shows the graphs of the results from fitting models 2 and 7. One can

see that even though there is a decrease in RCS of more than 2, the fits themselves

visually look similar. This demonstrates the importance of how it is the responsibility of

each user to fit the data as honestly as possible so as to present results that while may not

be exactly what one expected e.g., a silicated Ni-Al LDH could be the right answer, yet

Si improves the fit of the pure nickel hydroxide standard.

Experimental Setup Improvement

Although the flow cell designed for these experiments was critical for carrying

out the reactions in situ, several improvements can be made to the design to make

duplicating the results and running experiments faster. Kapton capillary tubing could be

used to replace the flow cell. This change would make packing the flow cells much

easier and faster. Additionally, the tubes are disposable, so after the experiment is done

the tubes can be discarded or saved for future analysis. The flow cells are tedious to

clean between experiments at the beamline.

Apart from changing the flow cells to capillary tubes, it would be useful to rerun

samples to collect for aluminum and silicon concentrations in the effluent with and

without nickel addition. During these experiments, the effluent was collected, however,

because of low aluminum and silicon concentrations and fast collection times, too little

sample was collected to accurately determine the concentrations of those elements in the effluent. Running duplicate experiments with and without nickel would help to determine if nickel promotes dissolution of the sorbent mineral.

Another important modification to the experiment would be to saturate/hydrate the clay mineral prior to reaction with the influent. Generally, experiments at the mineral-water interface investigate the mineral surface that has been hydrated previous to running the experiments. In these experiments, however, the clay mineral was dry-packed in the flow cell. Unfortunately, the filter at the exit of the flow cell can become clogged when cycles of air and water pass through it. If the mineral in the flow cell is previously hydrated before pumping the influent then the filter will clog and cause leaking from the flow cell window. This could be avoided by not using a filter. However, if a capillary tube were used instead of the flow cell, pure glass beads could be used to pack the end of the tube and act as a filter. This way it may be possible to use just the clay mineral in the capillary tube and not mix the clay mineral with glass beads.

Adjusting the flow rate would also provide additional information on the kinetics of LDH formation in situ and in real time. The flow rates used in this experiment (0.51 mL/min) worked well in preliminary tests but should be looked at in more detail, for example, testing a slower or faster flow rates. Lastly, in situ desorption studies could be performed to clarify the rate of dissolution in situ.
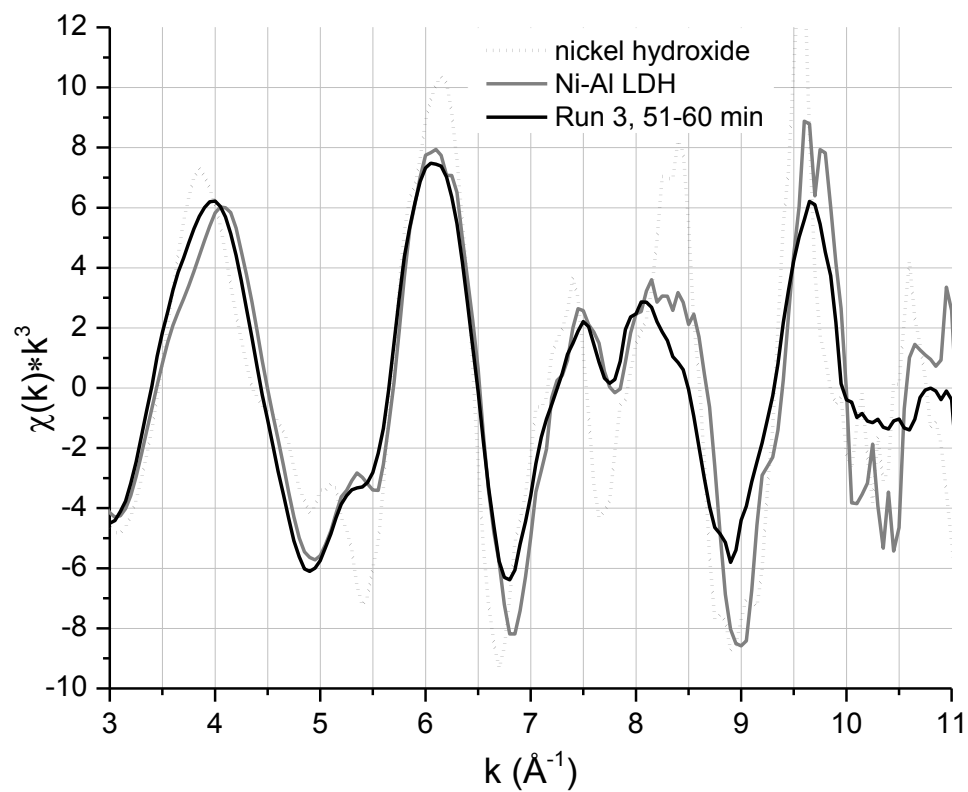
Figure 2.1   A comparison of two isostructural compounds, an alpha nickel hydroxide and Ni-Al LDH=1.3 (Scheinost and Sparks, 2000) with Run 3 at 51-60 minutes reaction time. The Ni-Al ratio in the standard is 1.3. The characteristic beat pattern and truncation at ~8.2 $Å^{-1}$ seen in the LDH is also present at the time frame in Run 3.

Run 1

Run 2

Run 3

Run 4

Run 5
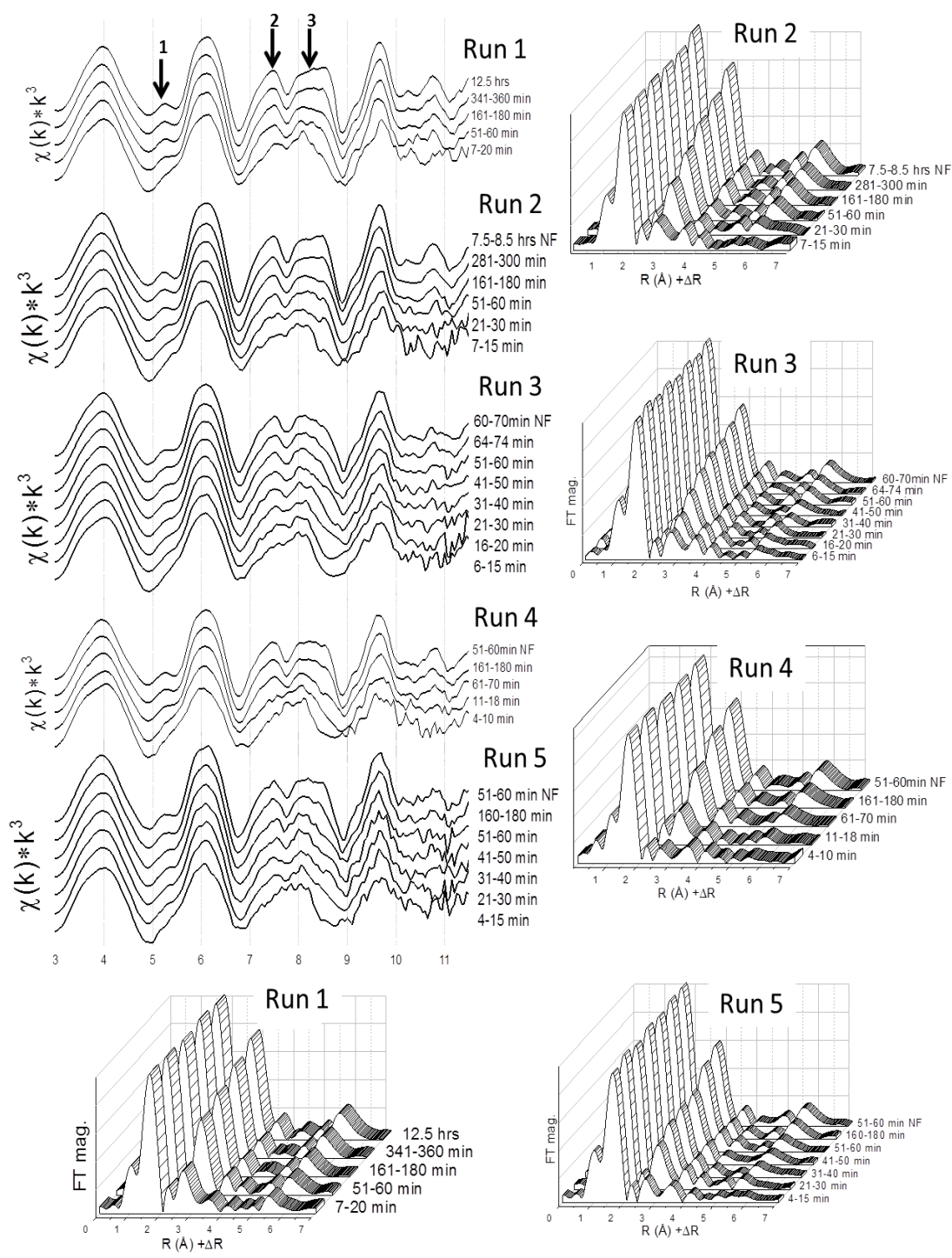
Figure 2.2   EXAFS and RSF plots of all sample runs. Arrows 1, 2, and 3 indicate similar structural changes emerging which are common to all samples over time. In all EXAFS data the samples over time develop a beat pattern at ~8.2 Å^{-1}, indicative of Ni-Al LDH (Scheinost and Sparks, 2000). In all RSF plots the first Ni-O shell remains at constant amplitude while the second shell grows with time.
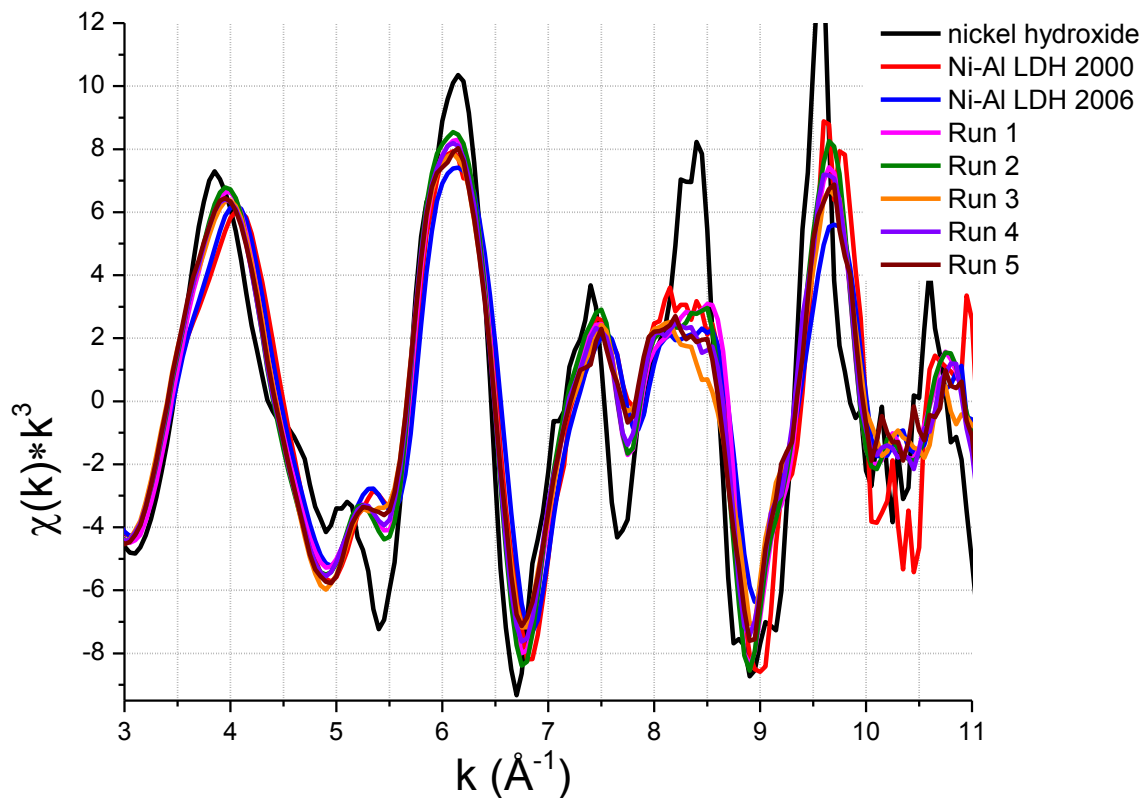
Figure 2.3   A comparison of all samples at the end of their runs to several standards.
The five runs are plotted with three standards: Ni-Al LDH =3.1 and alpha
nickel hydroxide both from Scheinost and Sparks (2000), and Ni-Al LDH-
CO_3^{2-} from Peltier et al. (2006) to illustrate how the sample runs are similar
to two Ni-Al LDH standards . The truncation at ~8.2 Å^{-1} and beat pattern are
present in all samples and in both LDH standards

Table 2.1 Shell-by-shell fitting results of all samples and standards. Structural parameters for all times during each sample run are presented along with the two standards from Scheinost and Sparks, 2000 (Ni-Al LDH 3.1 and alpha-nickel hydroxide). Fitting model A uses only nickel in the second shell while fitting model B illustrates how adding aluminum and/or silicon into the second shell affects the quality of the fit in terms of RCS value. Fitting model B is only shown where its RCS value is more than two times smaller than the RCS of model A, which generally only occurred at the end of the reaction runs.

Sample	Reaction Time	Fitting Model	R-factor	N_{idp}	N_{var}	Chi Square	Red. Chi Square	Shell #	Path	CN	R (Å)	σ^2 (Å²)	ΔE (eV)	amp	±R (Å)	$\pm\sigma^2$ (Å²)	$\pm\Delta E$ (eV)
Run 1	7-20 min	A	0.003	10.3	5	69	13	1	Ni-O	5.6	2.055	0.0056	-0.50	0.99	0.004	0.0002	0.64
								2	Ni-Ni	1.3	3.073	0.0053			0.006	0.0006	
	51-60 min	A	0.005	10.3	5	267	50	1	Ni-O	5.6	2.058	0.0059	0.24	0.99	0.005	0.0003	0.80
								2	Ni-Ni	2.6	3.078	0.0061			0.006	0.0004	
	161-180 min	A	0.002	10.3	5	498	94	1	Ni-O	5.8	2.062	0.0063	0.70	0.99	0.004	0.0003	0.56
								2	Ni-Ni	3.4	3.076	0.0075			0.004	0.0003	
	341-360 min	A	0.004	10.3	5	572	108	1	Ni-O	5.7	2.057	0.0060	0.27	0.99	0.004	0.0003	0.70
								2	Ni-Ni	3.5	3.075	0.0067			0.005	0.0003	
	341-360 min	B	0.001	10.3	5	162	31	1	Ni-O	5.6	2.053	0.0058	-0.48	0.99	0.002	0.0002	0.36
								2	Ni-Ni	3.3	3.068	0.0068			0.003	0.0002	
								2	Ni-Al	0.9	3.068	0.0068			0.003	0.0002	
								2	Ni-Si	1.5	3.274	0.0068			0.003	0.0002	
	12.5 hrs	A	0.004	10.3	5	972	183	1	Ni-O	5.8	2.053	0.0063	0.39	0.99	0.004	0.0003	0.70
								2	Ni-Ni	3.6	3.070	0.0062			0.005	0.0003	
	12.5 hrs	B	0.0004	10.3	5	105	20	1	Ni-O	5.6	2.047	0.0060	-0.71	0.99	0.001	0.0001	0.22
								2	Ni-Ni	3.6	3.058	0.0066			0.001	0.0001	
								2	Ni-Al	1.6	3.058	0.0066			0.001	0.0001	
								2	Ni-Si	1.9	3.264	0.0066			0.001	0.0001	
Run 2	7-15 min	A	0.007	10.4	5	65	12	1	Ni-O	5.5	2.058	0.0058	-0.05	0.99	0.006	0.0004	0.94
								2	Ni-Ni	1.6	3.079	0.0097			0.013	0.0014	
	21-30 min	A	0.004	10.8	5	76	13	1	Ni-O	5.8	2.055	0.0061	-0.59	0.99	0.004	0.0003	0.7
								2	Ni-Ni	2.1	3.066	0.0073			0.006	0.0005	
	50-60 min	A	0.004	10.8	5	219	38	1	Ni-O	5.8	2.055	0.0061	-0.32	0.99	0.004	0.0003	0.71
								2	Ni-Ni	2.7	3.072	0.0071			0.005	0.0004	
	161-180 min	A	0.003	10.3	5	318	60	1	Ni-O	5.6	2.065	0.0060	1.09	0.99	0.004	0.0003	0.63
								2	Ni-Ni	3.5	3.079	0.0077			0.005	0.0003	
	281-300 min	A	0.003	10.3	5	820	154	1	Ni-O	5.5	2.061	0.0058	0.68	0.99	0.004	0.0003	0.58
								2	Ni-Ni	3.5	3.077	0.0070			0.004	0.0003	
	7.5-8.5 hrs NF	A	0.003	10.3	5	976	184	1	Ni-O	6.1	2.058	0.0056	0.45	0.93	0.004	0.0003	0.66
								2	Ni-Ni	4	3.074	0.0063			0.004	0.0003	
	7.5-8.5 hrs NF	B	0.001	10.3	5	303	57	1	Ni-O	6.1	2.054	0.0056	-0.34	0.93	0.002	0.0002	0.36
								2	Ni-Ni	3.7	3.065	0.0062			0.002	0.0002	
								2	Ni-Al	1	3.065	0.0062			0.002	0.0002	
								2	Ni-Si	1.6	3.281	0.0062			0.002	0.0002	

38

Table 2.1 Continued.

Sample	Reaction Time	Fitting Model	R-factor	N_{idp}	N_{var}	Chi Square	Red. Chi Square	Shell #	Path	CN	R (Å)	σ^2 (Å²)	ΔE (eV)	amp	±R (Å)	±σ^2 (Å²)	±ΔE (eV)
Run 3	6-15 min	A	0.006	9.2	5	178	42	1	Ni-O	5.7	2.073	0.0055	1.67	0.93	0.006	0.0004	0.96
								2	Ni-Ni	1.1	3.106	0.0068			0.014	0.0016	
	16-20 min	A	0.005	9.4	5	171	39	1	Ni-O	5.2	2.075	0.0043	2.15	0.93	0.005	0.0003	0.86
								2	Ni-Ni	2.4	3.098	0.0124			0.012	0.0014	
	21-30 min	A	0.003	10.3	5	65	12	1	Ni-O	5.9	2.066	0.0058	0.85	0.93	0.004	0.0002	0.60
								2	Ni-Ni	2.2	3.080	0.0084			0.006	0.0006	
	31-40 min	A	0.003	10.3	5	87	16	1	Ni-O	5.8	2.063	0.0054	0.63	0.93	0.004	0.0003	0.63
								2	Ni-Ni	2.3	3.082	0.0071			0.005	0.0005	
	41-50 min	A	0.002	10.3	5	86	16	1	Ni-O	6	2.064	0.0060	0.61	0.93	0.003	0.0002	0.51
								2	Ni-Ni	2.8	3.075	0.0079			0.004	0.0004	
	51-60 min	A	0.003	10.3	5	116	22	1	Ni-O	5.8	2.063	0.0054	0.68	0.93	0.004	0.0003	0.61
								2	Ni-Ni	2.6	3.081	0.0071			0.005	0.0004	
	64-74 min	A	0.002	10.3	5	164	31	1	Ni-O	6	2.061	0.0060	0.35	0.93	0.003	0.0002	0.52
								2	Ni-Ni	2.7	3.073	0.0068			0.004	0.0003	
	64-74 min	B	0.001	10.3	5	113	21	1	Ni-O	5.9	2.060	0.0058			0.003	0.0002	
								2	Ni-Ni	2.4	3.072	0.0065	0.14	0.93	0.003	0.0003	0.42
								2	Ni-Al	0.2	3.072	0.0065			0.003	0.0003	
								2	Ni-Si	0.7	3.278	0.0065			0.003	0.0003	
	60-70 min NF	A	0.002	10.3	5	207	39	1	Ni-O	6	2.059	0.0057	0.23	0.93	0.003	0.0002	0.56
								2	Ni-Ni	3.2	3.072	0.0072			0.004	0.0003	
	60-70 min NF	B	0.001	10.3	5	103	19	1	Ni-O	5.9	2.056	0.0056			0.002	0.0002	
								2	Ni-Ni	3.5	3.065	0.0079	-0.28	0.93	0.003	0.0002	0.39
								2	Ni-Al	1.1	3.065	0.0079			0.003	0.0002	
								2	Ni-Si	1.1	3.271	0.0079			0.003	0.0002	
Run 4	4-10 min	A	0.007	10.3	5	53	10	1	Ni-O	6.2	2.061	0.0061	0.07	0.93	0.006	0.0004	0.95
								2	Ni-Ni	0.5	3.085	0.0072			0.029	0.0032	
	4-10 min	A	0.014	10.3	3	100	14	1	Ni-O	6.2	2.061	0.0062	0.03	0.93	0.007	0.0004	1.12
								-	-	-	-	-			-	-	
	11-18 min	A	0.004	10.3	5	76	14	1	Ni-O	6	2.057	0.0057	-0.36	0.93	0.004	0.0003	0.71
								2	Ni-Ni	1	3.081	0.0038			0.007	0.0007	
	61-70 min	A	0.003	10.3	5	205	39	1	Ni-O	6.1	2.066	0.0062	1.03	0.93	0.004	0.0002	0.57
								2	Ni-Ni	2.8	3.078	0.0079			0.005	0.0004	
	161-180 min	A	0.003	10.3	5	572	108	1	Ni-O	6.1	2.060	0.0061	0.37	0.93	0.004	0.0003	0.61
								2	Ni-Ni	3.3	3.073	0.0069			0.004	0.0003	
	161-180 min	B	0.001	10.3	5	272	51	1	Ni-O	6	2.057	0.0059			0.003	0.0002	
								2	Ni-Ni	3.1	3.067	0.0069	-0.12	0.93	0.003	0.0002	0.41
								2	Ni-Al	0.7	3.067	0.0069			0.003	0.0002	
								2	Ni-Si	1.2	3.284	0.0069			0.003	0.0002	
	51-60 min NF	A	0.003	10.3	5	206	39	1	Ni-O	6	2.058	0.0058	0.32	0.93	0.004	0.0003	0.58
								2	Ni-Ni	3.6	3.074	0.0065			0.004	0.0003	
	51-60 min NF	B	0.001	10.3	5	79	15	1	Ni-O	5.9	2.055	0.0056			0.002	0.0002	
								2	Ni-Ni	3.4	3.066	0.0065	-0.29	0.93	0.002	0.0002	0.35
								2	Ni-Al	0.9	3.066	0.0065			0.002	0.0002	
								2	Ni-Si	1.3	3.282	0.0065			0.002	0.0002	

Table 2.1 Continued.

Sample	Reaction Time	Fitting Model	R-factor	N_{idp}	N_{var}	Chi Square	Red. Chi Square	Shell #	Path	CN	R (Å)	σ^2 (Å²)	ΔE (eV)	amp	±R (Å)	±σ^2 (Å²)	±ΔE (eV)
Run 5	4-15 min	A	0.003	9.2	5	34	8	1	Ni-O	5.8	2.068	0.0061	0.83	0.93	0.005	0.0003	0.75
								2	Ni-Ni	1.5	3.088	0.0126			0.015	0.0019	
	21-30 min	A	0.002	9.3	5	57	13	1	Ni-O	6.4	2.064	0.0069	0.44	0.93	0.004	0.0003	0.59
								2	Ni-Ni	2.4	3.076	0.0090			0.006	0.0006	
	31-40 min	A	0.002	10.3	5	27	5	1	Ni-O	6.4	2.063	0.0071	0.42	0.93	0.003	0.0002	0.48
								2	Ni-Ni	2.4	3.071	0.0079			0.004	0.0004	
	41-50 min	A	0.003	10.4	5	16	3	1	Ni-O	6.1	2.059	0.0062	0.23	0.93	0.003	0.0002	0.56
								2	Ni-Ni	2.1	3.071	0.0066			0.005	0.0004	
	51-60 min	A	0.005	10.4	5	35	6	1	Ni-O	6.2	2.064	0.0065	0.69	0.93	0.005	0.0003	0.80
								2	Ni-Ni	2.7	3.084	0.0080			0.007	0.0006	
	160-180 min	A	0.003	10.4	5	78	14	1	Ni-O	6	2.058	0.0058	0.06	0.93	0.004	0.0003	0.63
								2	Ni-Ni	3	3.075	0.0068			0.005	0.0004	
	160-180 min	B	0.001	10.4	5	30	6	1	Ni-O	5.9	2.055	0.0056			0.002	0.0002	
								2	Ni-Ni	2.8	3.070	0.0069	-0.39	0.93	0.003	0.0002	0.38
								2	Ni-Al	0.6	3.070	0.0069			0.003	0.0002	
								2	Ni-Si	1.2	3.277	0.0069			0.003	0.0002	
	51-60 min NF	A	0.003	10.4	5	72	13	1	Ni-O	6.1	2.055	0.0059	-0.28	0.93	0.004	0.0003	0.66
								2	Ni-Ni	3.1	3.072	0.0063			0.005	0.0003	
	51-60 min NF	B	0.001	10.4	5	19	4	1	Ni-O	6	2.051	0.0057			0.002	0.0001	
								2	Ni-Ni	2.9	3.066	0.0064	-0.89	0.93	0.002	0.0002	0.33
								2	Ni-Al	0.8	3.066	0.0064			0.002	0.0002	
								2	Ni-Si	1.4	3.272	0.0064			0.002	0.0002	
α−Ni(OH)$_2$	standard	A	0.007	10.3	5	64	12	1	Ni-O	5.7	2.045	0.0041	0.20	0.85	0.006	0.0005	1.03
								2	Ni-Ni	6.6	3.091	0.0063			0.006	0.0003	
		B	0.003	10.3	5	25	5	1	Ni-O	5.7	2.040	0.0041			0.004	0.0003	
								2	Ni-Ni	5.2	3.086	0.0057	-0.76	0.85	0.004	0.0002	0.60
								2	Ni-Al	-	-	-			-	-	
								2	Ni-Si	2.2	3.293	0.0057			0.004	0.0002	
Ni-Al LDH	standard	A	0.006	10.3	5	38	7	1	Ni-O	5.5	2.055	0.0035	1.53	0.85	0.005	0.0003	0.88
								2	Ni-Ni	2.2	3.061	0.0020			0.005	0.0003	
		B	0.004	10.3	5	26	5	1	Ni-O	5.6	2.054	0.0037			0.004	0.0003	
								2	Ni-Ni	2.8	3.055	0.0028	1.34	0.85	0.005	0.0003	0.79
								2	Ni-Al	0.9	3.055	0.0028					
								2	Ni-Si	-	-	-			-	-	
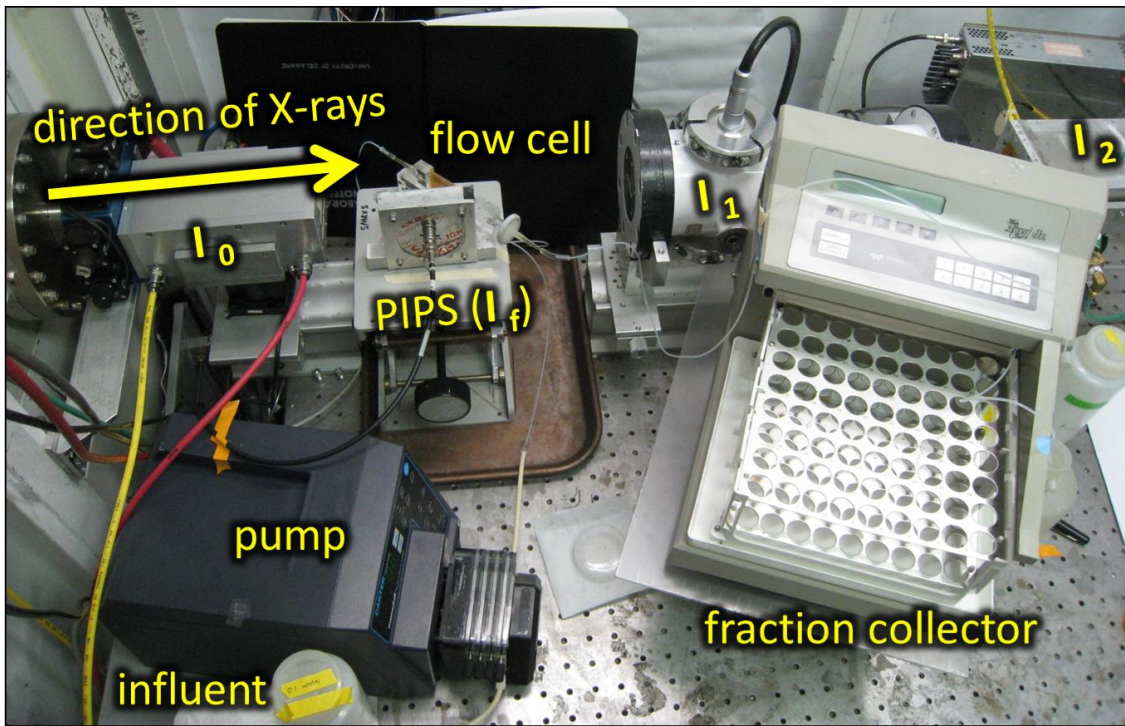
Figure 2.4   Picture of the Experimental Setup in the Hutch of Beamline X18B at the NSLS.
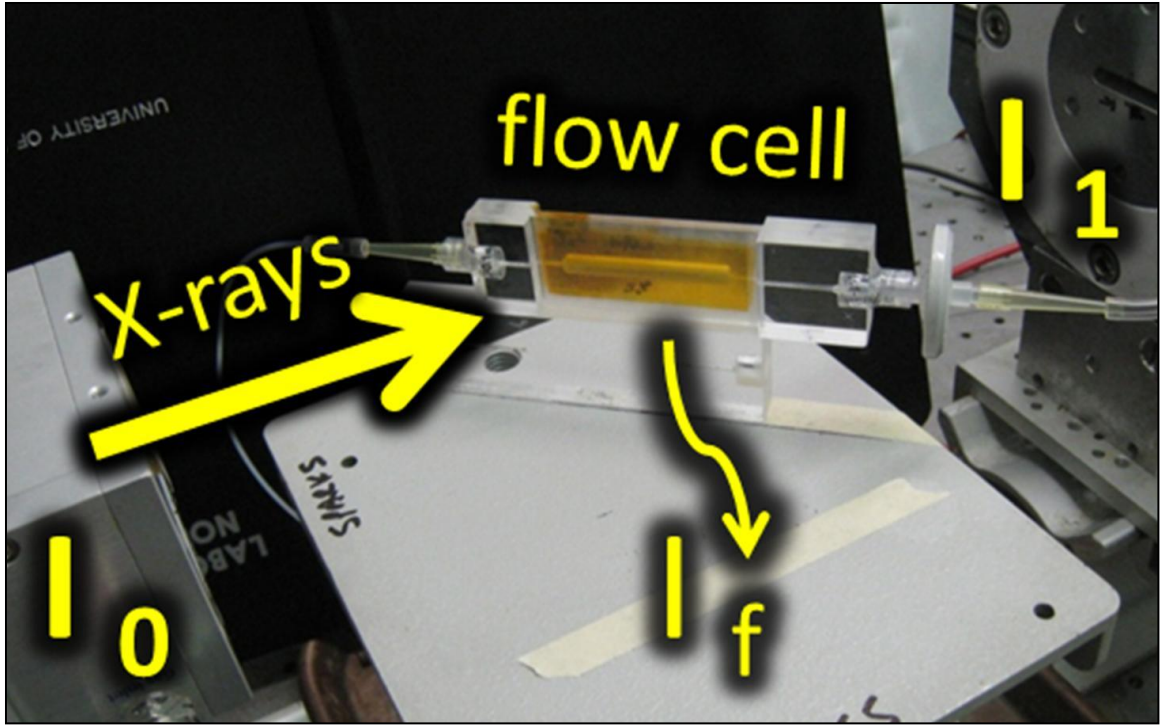
Figure 2.5   Picture of the Flow Cell in the Experimental Setup.

Design for flow cell with end fittings for syringe filters

Side view

85mm

15mm 45mm 25mm

Fitting for syringe
filter attachment (threaded)

30mm

effluent
Solution, to
fraction
collector

5mm

Window in
plastic, covered
on both sides
with kapton
tape. Sample
placed in
window with
solution flowing
thorugh

1mm diameter
hole drilled lengthwise
through plastic,
Connects window
with fitting for syringe
filter attachment

3mm

Influent
solution

Top view

85mm

15mm 45mm 25mm

3mm 6mm

Thick ends to
support filter
attachment

5mm

5mm

Figure 2.6   A Schematic Diagram of the Flow Cell.

43
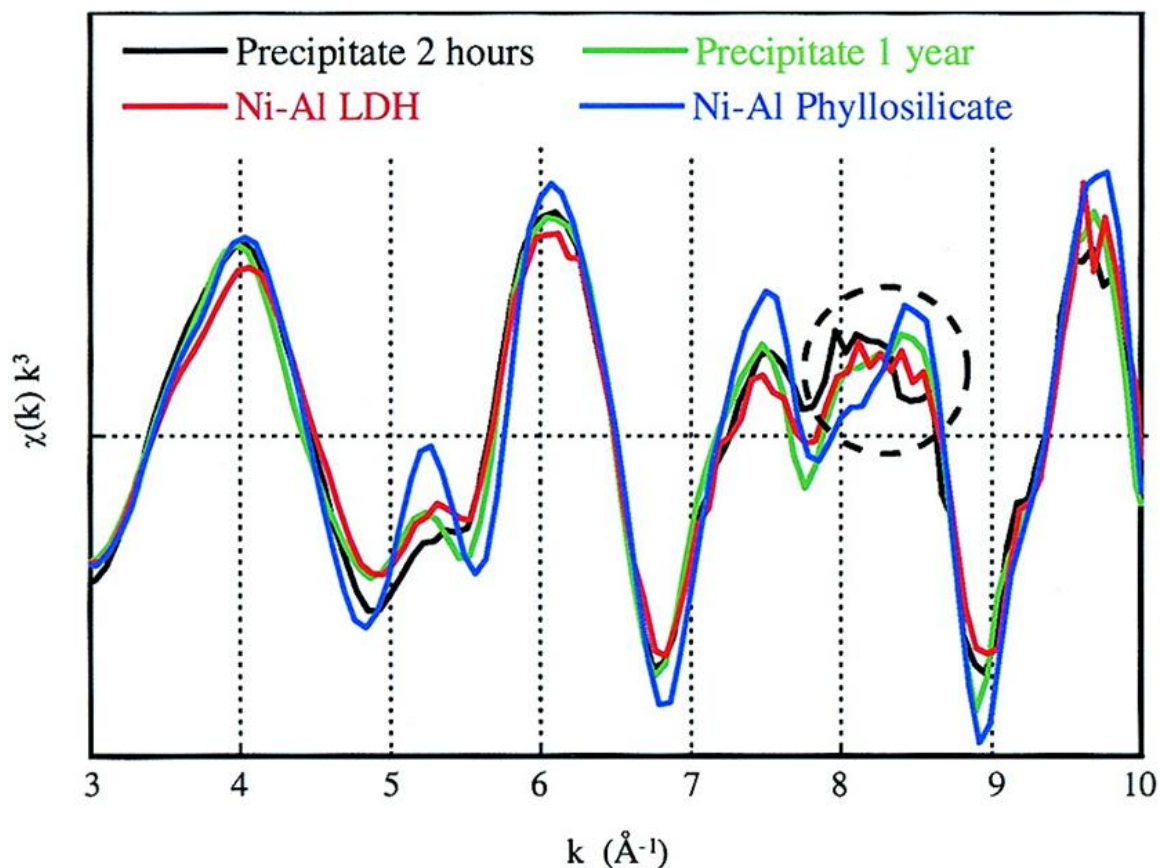
Figure 2.7   Normalized and weighted Ni K-edge EXAFS spectra, $\chi(k)k3$, for a reference Ni−Al LDH and Ni−Al phyllosilicate and the Ni surface precipitate formed on pyrophyllite at 2 h and 1 year. The characteristic oscillations between 8 and 9 $Å^{-1}$ indicate partial transformation from a Ni−Al LDH to a Ni−Al phyllosilicate. "Reprinted 2013 with permission from The Link between Clay Mineral Weathering and the Stabilization of Ni Surface Precipitates Author: Robert G. Ford, , Andreas C. Scheinost, Kirk G. Scheckel, and Donald L. Sparks. Environmental Science &Technology. Copyright (1999) American Chemical Society."
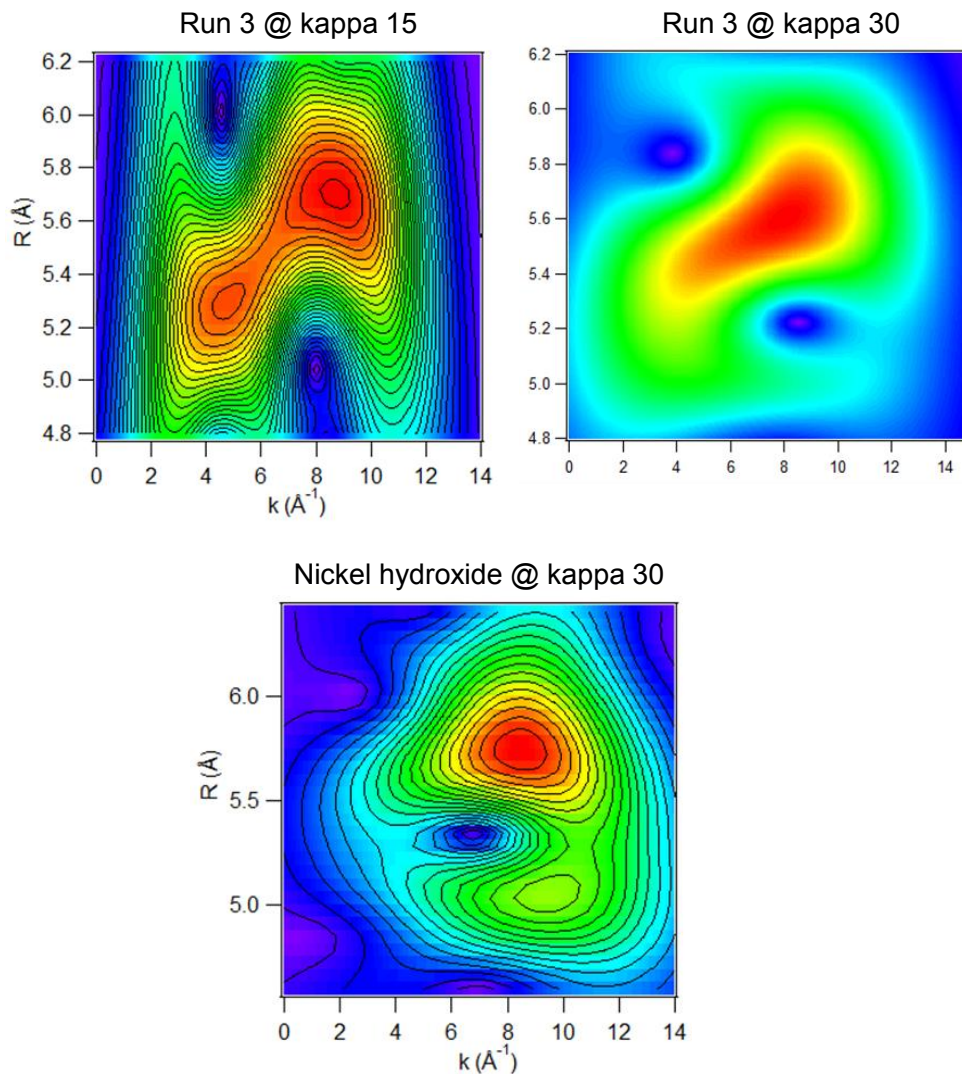
Figure 2.8   The WT plots from Run 3 at 64-74m flow. Two types of backscatterers, low (e.g., Al) and high (e.g., Ni) seemingly contribute to the EXAFS spectrum of Run 3 while 1 type of backscatter (e.g., Ni) composes the nickel hydroxide spectrum. The R-space for these WT was 4.6 or 4.8-6.2 or 6.4 Å. The k range used was 3-11.3 Å^{-1} for both samples with a k weighting of 3. The only difference between the WT processing parameters is kappa and sigma, which were 15 and 1 for Run 3 and 30 and 1 for the nickel hydroxide. However, when modifying Run 3 to kappa 30 only 1 type of backscatter is found. This demonstrates the importance of using and understanding the kappa and sigma parameters before making final conclusions.
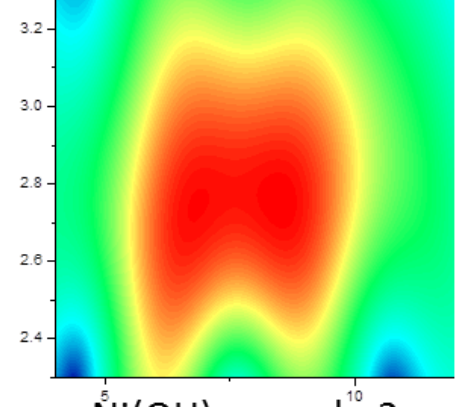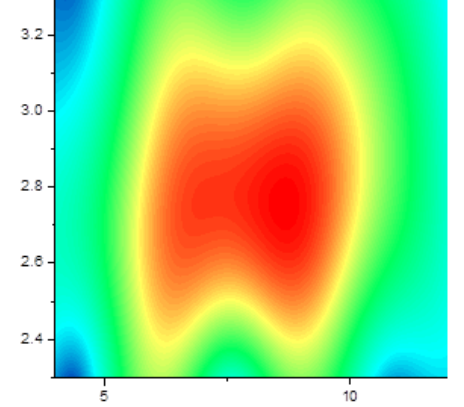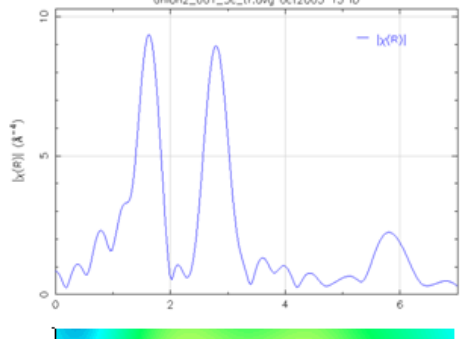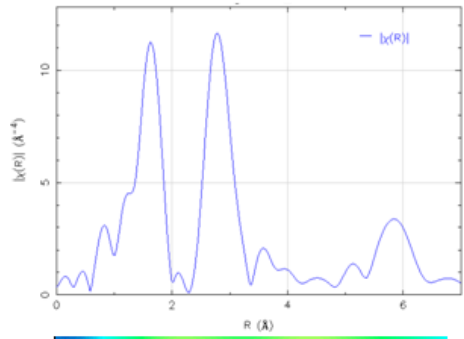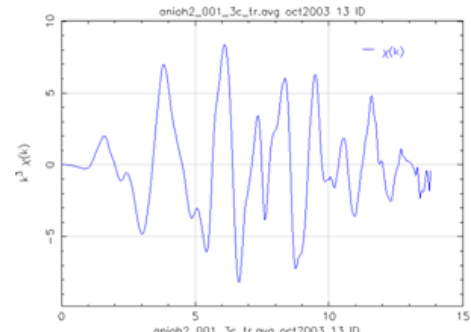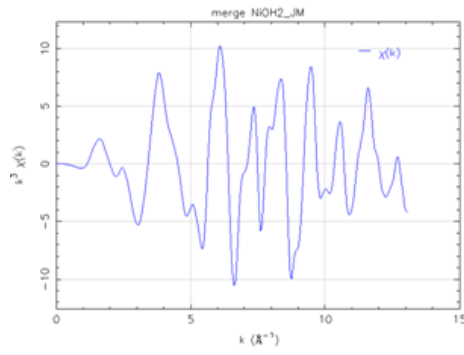
Ni(OH)$_2$ sample 1　　　　　Ni(OH)$_2$ sample 2

Figure 2.9　　　A

Figure 2.9   B

nickel-aluminum LDH,
silicate interlayer

nickel-aluminum LDH,
carbonate interlayer
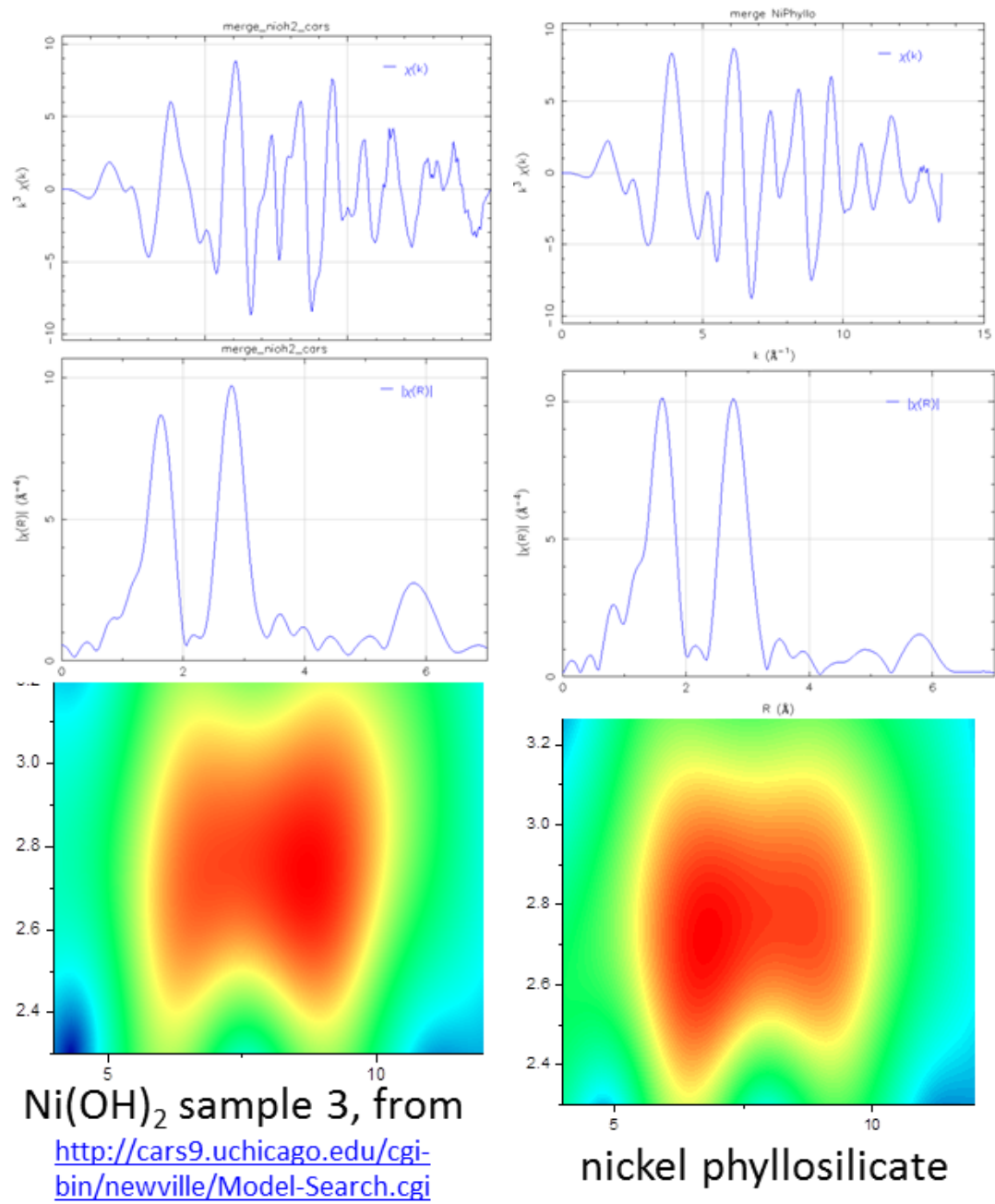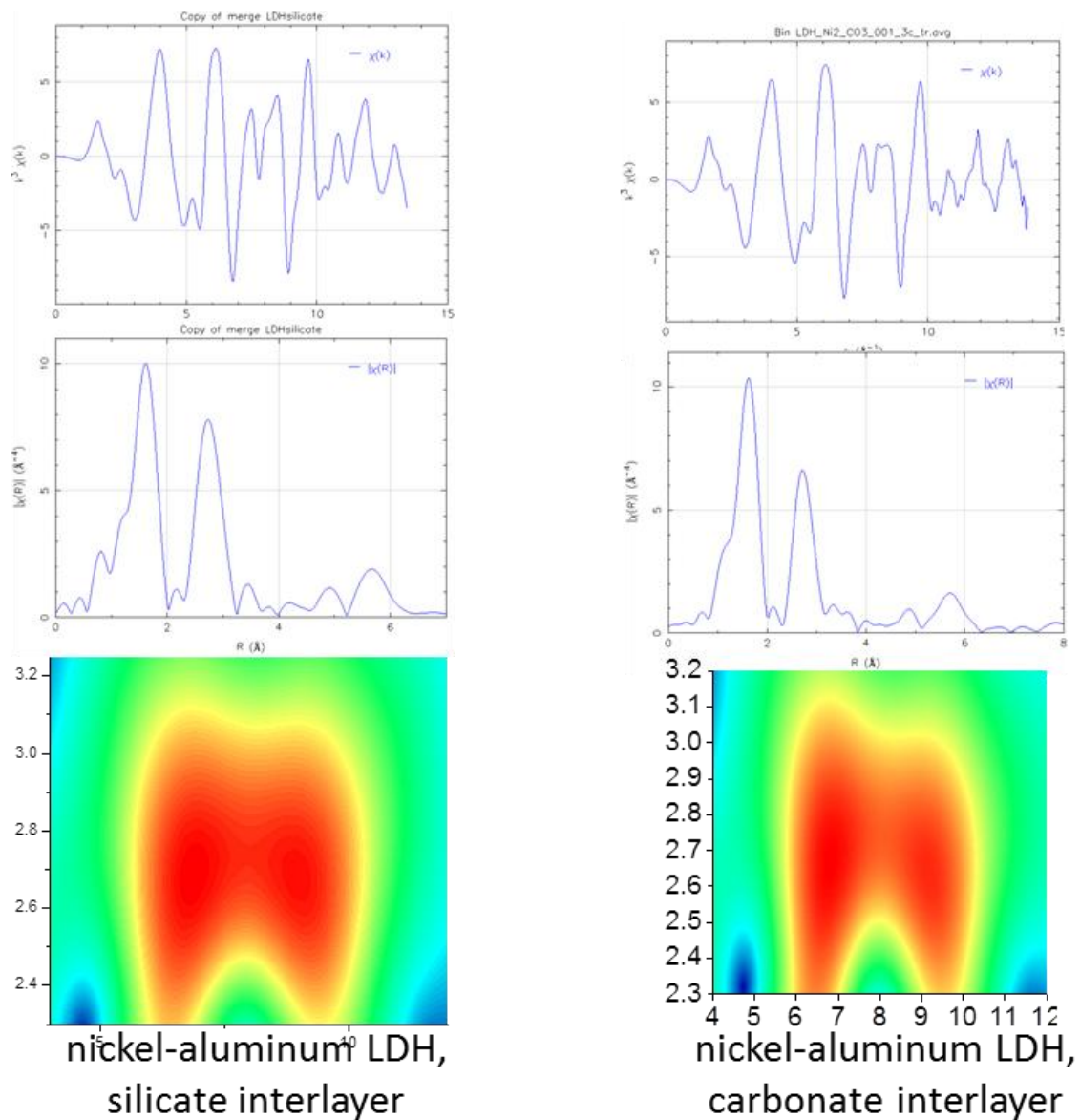
Figure 2.9   A,B, & C. The approximate k ranges for all FT and WT are 2.5 to 12 Å⁻¹,
with k weight of 3. The approximate R ranges for all WT are about 2.3 to
3.2 Å. The Morelet WT parameters ŋ*σ were set to equal approximately 2x
the second shell distance (6.14 and 1, respectively).

run 25_nr65to70min ni only

run 25_nr65to70min nisial isotropic
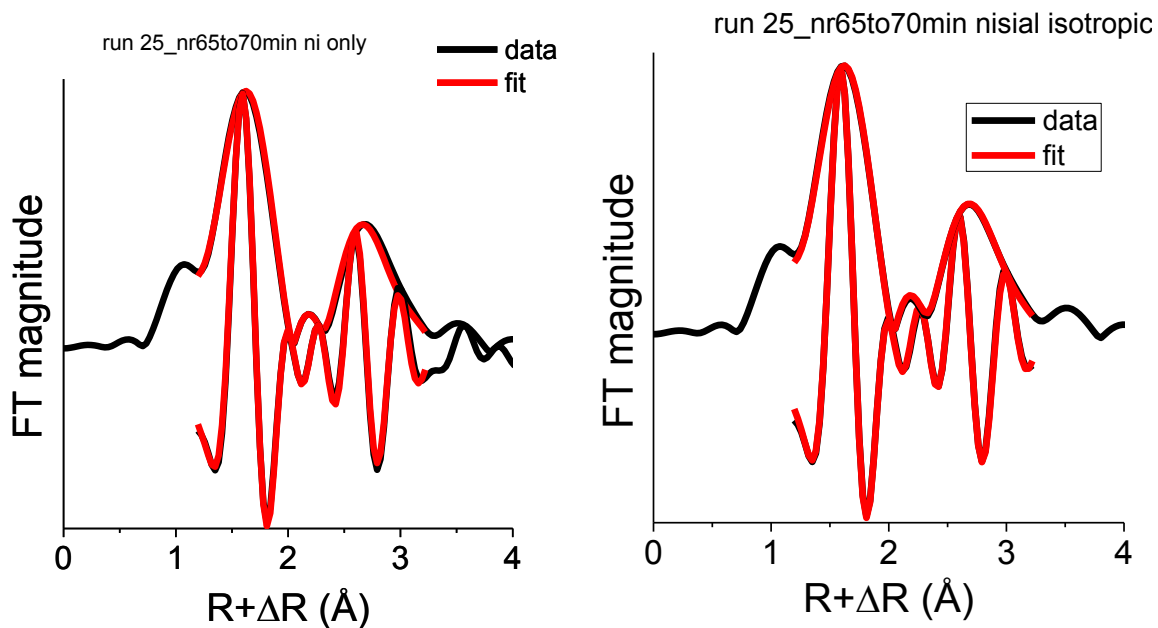
Figure 2.10   Shell fitting of Run 3 at 65-70 min NF. The first shells are similar in that they are only oxygen, however, for the second shell, Ni (left) and Ni, Al, and Si (right) are used. Visually there is a small enhancement of the fit when Ni, Al, and Si are included. Statistically the fit with Ni, Al, and Si is better (Table 2.3).

Table 2.2   Fitting Results Using Different Structural Fitting Models

Run 3, NF 65-70 min													
Fit Model [a]	R-factor	N_{idp} [b]	N_{var} [b]	Chi Square [b]	Reduced Chi Square [b]	Δk (Å^{-1}) [b]	ΔR (Å) [b]	Shell #	Path	CN	R (Å)	σ² (Å²)	ΔE (eV) [c]
1	0.001	10.6	6	82	18	2.5-11	1.2-3.2	1	Ni-O	6.2	2.056 (0.003)	0.006 (0.0002)	-0.294 (0.417)
								2	Ni-Ni	3	3.054 (0.004)	0.007 (0.0003)	-0.294 (0.417)
								2	Ni-Al	1.8	3.054 (0.004)	0.007 (0.0003)	-0.294 (0.417)
								2	Ni-Si	2	3.305 (0.016)	0.007 (0.0003)	-0.294 (0.417)
2	0.003	10.6	5	248	45	2.5-11	1.2-3.2	1	Ni-O	6.2	2.059 (0.004)	0.006 (0.0002)	0.351 (0.576)
								2	Ni-Ni	3	3.075 (0.005)	0.007 (0.0004)	0.351 (0.576)
3	0.0004	10.6	6	34	7.5	2.5-11	1.2-3.2	1	Ni-O	6.2	2.058 (0.002)	0.006 (0.0001)	0.003 (0.2409)
								2	Ni-Ni	5.5	3.085 (0.002)	0.0102 (0.0002)	0.003 (0.2409)
								2	Ni-MS	32	3.484 (0.011)	0.0102 (0.0002)	0.003 (0.2409)
4	0.003	10.6	5	235	42	2.5-11	1.2-3.2	1	Ni-O	6.2	2.095 (0.004)	0.006 (0.0002)	0.259 (0.576)
								2	Ni-Ni	4	3.072 (0.005)	0.008 (0.0004)	0.259 (0.576)
								2	Ni-Al	0.8	3.072 (0.005)	0.008 (0.0004)	0.259 (0.576)
5	0.0003	10.6	6	100	22	2.5-11	1.2-3.2	1	Ni-O	6.2	2.058 (0.003)	0.006 (0.0002)	0.046 (0.404)
								2	Ni-Ni	3.5	3.080 (0.003)	0.008 (0.0005)	0.046 (0.404)
								2	Ni-Al	0.8	3.238 (0.044)	0.008 (0.0005)	0.046 (0.404)
6	0.0009	10.6	6	76	17	2.5-11	1.2-3.2	1	Ni-O	6.2	2.056 (0.002)	0.006 (0.0002)	-0.267 (0.353)
								2	Ni-Ni	4.3	3.079 (0.005)	0.008 (0.0004)	-0.267 (0.353)
								2	Ni-Si	1.4	3.137 (0.029)	0.008 (0.0004)	-0.267 (0.353)
7	0.00079	10.6	5	64	11.5	2.5-11	1.2-3.2	1	Ni-O	6	2.091 (0.002)	0.005 (0.0001)	-0.357(0.291)
								2	Ni-Ni	4	3.085 (0.002)	0.009 (0.0002)	-0.357(0.291)
								2	Ni-Al	1.8	3.085 (0.002)	0.009 (0.0002)	-0.357(0.291)
								2	Ni-Si	1.8	3.292 (0.002)	0.009 (0.0002)	-0.357(0.291)

a - Fit Model 1: Ni, Al and Si in second shell. Ni and Al restricted to same distance. Ni, Al and Si sigma squared term constrained to a single value because each
   path had overlapping values within their uncertainties.
  - Fit Model 2: Ni only in the second shell
  - Fit Model 3: Ni and a Ni-multiple scattering path. Ni and MS sigma squared terms constrained to a single value.
  - Fit Model 4: Ni and Al in the second shell. Ni and Al restricted to same distance. Ni and Al sigma squared terms constrained to a single value.
  - Fit Model 5: Ni and Al in the second shell. Ni and Al not restricted to same distance. Ni and Al sigma squared terms constrained to a single value.
  - Fit Model 6: Ni and Si in the second shell. Ni and Si sigma squared term constrained to a single value.
  - Fit Model 7: Ni and Al and Si in the second shell, linked isostructurally (Kelly et al., 2008), and sharing deltaR, and SS values to decrease # of fitting variables
b - The best values from the two shell fit were fixed to examine the chi square values for a fit of just the second shell. The fitting range and chi square values
   for a fit of the isolated second shell are shown in italics for each Fit Type.
c - a single ΔE value was used for all fitting paths

Hanning windows were used for both Fourier and back-Fourier Transformations, with dk and dr values set to 1 and 0.3 , respectively. All spectra were analyzed with a k weighting of 3. An amplitude reduction factor of 0.91 as determined from a nickel hydroxide standard was fixed for all fitting paths.

REFERENCES

Aimoz, L., C. Taviot-Gueho, S.V. Churakov, M. Chukalina, R. Dahn, E. Curti, P. Bordet, and M. Vespa. 2012. Anion and cation order in iodide-bearing Mg/Zn-Al layered double hydroxides. Journal of Physical Chemistry C 116:5460-5475.

Bunker, G., and E.A. Stern. 1984. Experimental-study of multiple-scattering in X-ray-absorption near-edge structure. Physical Review Letters 52:1990-1993.

Charlet, L., and A. Manceau. 1994. Evidence for the neoformation of clays upon sorption of Co(II) and Ni(II) on silicates. Geochimica et Cosmochimica Acta 58:2577-2582.

Delacaillerie, J.B.D., M. Kermarec, and O. Clause. 1995. Impregnation of gamma-alumina with Ni(II) or Co(II) ions at neutral pH - hydrotalcite-type coprecipitate formation and characterization. Journal of the American Chemical Society 117:11471-11481.

Elzinga, E.J. 2012. Formation of layered Fe(II)-Al(III)-hydroxides during reaction of Fe(II) with aluminum oxide. Environmental Science & Technology 46:4894-4901.

Farley, K.J., R.F. Carbonaro, C.J. Fanelli, R. Costanzo, K.J. Rader, and D.M. Di Toro. 2011. Ticket-UWM: A coupled kinetic, equilibrium, and transport screening model for metals in lakes. Environmental Toxicology and Chemistry 30:1278-1287.

Ford, R.G., A.C. Scheinost, K.G. Scheckel, and D.L. Sparks. 1999. The link between clay mineral weathering and the stabilization of Ni surface precipitates. Environmental Science & Technology 33:3140-3144.

Funke, H., M. Chukalina, and A.C. Scheinost. 2007. A new FEFF-based wavelet for EXAFS data analysis. Journal of Synchrotron Radiation 14:426-432.

Ginder-Vogel, M., G. Landrot, J.S. Fischel, and D.L. Sparks. 2009. Quantification of rapid environmental redox processes with quick-scanning x-ray absorption spectroscopy (Q-XAS). Proceedings of the National Academy of Sciences of the United States of America 106:16124-16128.

Hochella, M.F., Jr., S.K. Lower, P.A. Maurice, R.L. Penn, N. Sahai, D.L. Sparks, and B.S. Twining. 2008. Nanominerals, mineral nanoparticles, and earth systems. Science 319:1631-1635.

Kelly, S.D., D. Hesterberg, and B. Ravel. 2008. Analysis of soils and minerals using X-ray absorption spectroscopy, *In* A. L. Ulery and L. R. Drees, eds. Methods of Soil Analysis. Part 5. Mineralogical Methods, Vol. 5. Soil Science Society of America, Madison, WI

Khalid, S., W. Caliebe, P. Siddons, I. So, B. Clay, T. Lenhard, J. Hanson, Q. Wang, A.I. Frenkel, N. Marinkovic, N. Hould, M. Ginder-Vogel, G.L. Landrot, D.L. Sparks, and A. Ganjoo. 2010. Quick extended X-ray absorption fine structure instrument with millisecond time scale, optimized for *in situ* applications. Review of Scientific Instruments 81:015105-7.

Landrot, G., M. Ginder-Vogel, and D.L. Sparks. 2010. Kinetics of chromium(III) oxidation by manganese(IV) oxides using quick scanning X-ray absorption fine structure spectroscopy (Q-XAFS). Environmental Science & Technology 44:143-149.

Li, W., K.J.T. Livi, W.Q. Xu, M.G. Siebecker, Y.J. Wang, B.L. Phillips, and D.L. Sparks. 2012. Formation of crystalline Zn-Al layered double hydroxide precipitates on gamma-alumina: the role of mineral dissolution. Environmental Science & Technology 46:11670-11677.

Livi, K.J.T., G.S. Senesi, A.C. Scheinost, and D.L. Sparks. 2009. Microscopic examination of nanosized mixed Ni-Al hydroxide surface precipitates on pyrophyllite. Environmental Science & Technology 43:1299-1304.

Manceau, A. 1990. Distribution of cations among the octahedra of phyllosilicates - insight from EXAFS. Canadian Mineralogist 28:321-328.

Manceau, A., and G. Calas. 1986. Nickel bearing clay minerals: 2. intracrystalline distribution of nickel - an X-ray absorption study. Clay Minerals 21:341-360.

Mellini, M., and C. Viti. 1994. Crystal-structure of lizardite-1t from Elba, Italy. American Mineralogist 79:1194-1198.

O'day, P.A., J.J. Rehr, S.I. Zabinsky, and G.E. Brown. 1994. Extended X-ray absorption fine structure (EXAFS) analysis of disorder and multiple-scattering in complex crystalline solids. Journal of the American Chemical Society 116:2938-2949.

Pandya, K.I., W.E. O'Grady, D.A. Corrigan, J. McBreen, and R.W. Hoffman. 1990. Extended x-ray absorption fine-structure investigations of nickel hydroxides. Journal of Physical Chemistry 94:21-26.

Peltier, E., R. Allada, A. Navrotsky, and D.L. Sparks. 2006. Nickel solubility and precipitation in soils: a thermodynamic study. Clays and Clay Minerals 54:153-164.

Ravel, B., and M. Newville. 2005. Athena, Artemis, Hephaestus: data analysis for X-ray absorption spectroscopy using IFEFFIT. Journal of Synchrotron Radiation 12:537-541.

Scheidegger, A.M., G.M. Lamble, and D.L. Sparks. 1996. Investigation of Ni sorption on pyrophyllite: An XAFS study. Environmental Science & Technology 30:548-554.

Scheidegger, A.M., G.M. Lamble, and D.L. Sparks. 1997. Spectroscopic evidence for the formation of mixed-cation hydroxide phases upon metal sorption on clays and aluminum oxides. Journal of Colloid and Interface Science 186:118-128.

Scheidegger, A.M., D.G. Strawn, G.M. Lamble, and D.L. Sparks. 1998. The kinetics of mixed Ni-Al hydroxide formation on clay and aluminum oxide minerals: a time-resolved XAFS study. Geochimica et Cosmochimica Acta 62:2233-2245.

Scheidegger, A.M., E. Wieland, A.C. Scheinost, R. Dahn, and P. Spieler. 2000. Spectroscopic evidence for the formation of layered Ni-Al double hydroxides in cement. Environmental Science & Technology 34:4545-4548.

Scheinost, A.C., and D.L. Sparks. 2000. Formation of layered single- and double-metal hydroxide precipitates at the mineral/water interface: a multiple-scattering XAFS analysis. Journal of Colloid and Interface Science 223:167-178.

Sparks, D.L. 2002. Environmental Soil Chemistry. 2nd. ed. Academic Press, San Diego.

Thompson, H.A., G.A. Parks, and G.E. Brown. 1999. Dynamic interactions of dissolution, surface adsorption, and precipitation in an aging cobalt(II)-clay-water system. Geochimica et Cosmochimica Acta 63:1767-1779.

Towle, S.N., J.R. Bargar, G.E. Brown, and G.A. Parks. 1997. Surface precipitation of $Co(II)_{(aq)}$ on Al_2O_3. Journal of Colloid and Interface Science 187:62-82.

Trainor, T.P., G.E. Brown, and G.A. Parks. 2000. Adsorption and precipitation of aqueous Zn(II) on alumina powders. Journal of Colloid and Interface Science 231:359-372.

Webb, S.M. 2005. SIXpack: a graphical user interface for XAS analysis using IFEFFIT. Physica Scripta T115:1011-1014.

Yamaguchi, N.U., A.C. Scheinost, and D.L. Sparks. 2002. Influence of gibbsite surface area and citrate on Ni sorption mechanisms at pH 7.5. Clays and Clay Minerals 50:784-790.

Zabinsky, S.I., J.J. Rehr, A. Ankudinov, R.C. Albers, and M.J. Eller. 1995. Multiple-scattering calculations of X-ray-absorption spectra. Physical Review B 52:2995-3009.

Zelmy, A.R., D.C. Girvin, and E.A. Jenne. 1984. MINTEQ. A computer program for calculating aqueous geochemical equilibrium NTIS PB 84-157148. (EPA-600/3-84-032). Nat. Tech. Inf. Ser., Springfield, VA.

Chapter 3

MOLECULAR STABILITY OF NICKEL-ALUMINUM LAYERED DOUBLE HYDROXIDES (Ni-Al LDHs): THE EFFECT OF METAL CATION RATIO IN THE HYDROXIDE SHEET

Introduction

LDHs in Soils: Geogenic and Anthropogenic Sources

The first naturally occurring (geogenic) LDH was discovered in 1842 and is hydrotalcite, which is a magnesium-aluminum LDH with carbonate anions in the interlayer (Rives, 2001). Another naturally occurring interstratified chrysotile-hydrotalcite is described by Drits et al. (1995). It consists of alternating serpentine-like layers and hydrotalcite with sulfate and chlorine anions in the interlayer. It was found in serpentinized peridotites. Non-geogenic (i.e., anthropogenically caused) LDHs have been found in zinc and nickel contaminated soils. Zinc and nickel LDHs are environmentally important in contaminated soils and sediments because they reduce metal (M) mobility by removing $M^{2+}_{(aq)}$ from the soil solution and into newly formed metal-rich solid phases. This process immobilizes the metal and prevents further transport (McNear et al., 2007; Nachtegaal et al., 2005; Sparks, 2003).

In the nickel refining process (e.g., smelting), particulates containing nickel are released into the air which later drift and fall to the ground (Hoflich et al., 2000). The chemical forms (species) of nickel emitted during this process are NiO and nickel metal

particles. McNear et al. (2007) carried out studies on soils contaminated by a nickel

refinery. Over time, Ni^{2+} dissolves and reacts with aluminum rich minerals present in

soils to form Ni-Al LDHs. The nickel contaminated soils treated with in situ stabilization

(i.e., raising the pH of the soil) formed more LDH and phyllosilicate-type minerals than

in unlimed, lower pH soils. This could have been caused by an increase in Si solubility at

higher pH. Aqueous modeling of Ni-Al LDHs based on empirical thermodynamic data

showed that at pH $\geq$ 6.5 the formation of Ni-Al LDH phases are favorable over $Ni(OH)_2$

phases in soils containing soluble aluminum (Peltier et al., 2006). The pH range for

formation of Ni-Al LDHs in the laboratory is pH 5-10 (deRoy et al., 1992). It should

therefore be possible that LDHs form at lower pH values in soils than observed. Perhaps

LDHs are not observed at lower pH in soils (e.g., 5-6.5) because of inhibition from

organic acids or humic substances. It has been shown that organic acids and humic

substances inhibit the formation of LDH on aluminum-rich minerals (Nachtegaal et al.,

2005; Yamaguchi et al., 2002). The interlayer anion and the metal ratio in the octahedral

layers also play roles in LDH stability.   In nature, carbonate is the most common anion

in the interlayer (Rives, 2001). The formation of LDHs in soils is affected by pH, soil

mineral type, and reaction time.

Ni-Al LDHs form on aluminum rich clay minerals like gibbsite, pyrophyllite,

kaolinite and montmorillonite. They do not form on aluminum deficient minerals.

Instead, alpha-type nickel hydroxides [α-$Ni(OH)_2$] or nickel phyllosilicates form on

aluminum deficient clay minerals (Scheinost and Sparks 2000). Aluminum availability

and solubility has been shown to be the dominant factor in the formation of LDHs on clay

minerals, with more soluble aluminum rich minerals forming Zn/Al-LDH faster than less soluble ones (Li et al., 2012). In soils, much of the LDH research has focused on Fe^{2+}, Ni^{2+}, Zn^{2+}, and Co^{2+} (Elzinga, 2012; O'Day et al., 1994; Roberts et al., 2002; Scheidegger et al., 1996a).

LDHs in the Laboratory

Although LDHs occur in soils and sediments both geogenically and anthropogenically, LDHs synthesized in the laboratory are a major research area. LDHs have a variety of applications including catalysts, adsorbents, anion scavengers, anion exchangers, polymer stabilizers, and "nanoreactors", e.g., the interlayer space provides a constrained region to perform chemical reactions (Rives, 2001). Many of these research areas focus on LDHs because of the unique characteristic that they are positively charged, which is opposite from most other clays which are negatively charged.

The general formula for a LDH is (deRoy et al., 2001; Reichle, 1986):

$$M_a^{2+}M_b^{3+}(OH)_{2a+2b}(X^-)_{2b}\cdot cH_2O \qquad\qquad 1$$
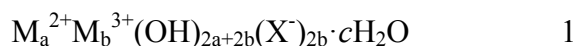
where M^{2+} (also written as M^{II}) can be Mg, Mn, Fe, Ni, Co, Zn or Cu and M^{3+} (also written as M^{III}) can be Al, Cr, Fe, Mn, Ga or Sc. The M^{II}/M^{III} ratio can be between 1-to-5. Anions present in the interlayer are represented by X^-. The subscripts a and b represent the quantity of metal cation in the hydroxide unit cell. Finally, c is structural water and equals 0-6. Ionic radius is the major limiting factor for metals that can be incorporated into the octahedral layers, with M^{II} ranging from 0.65-0.80 Å and M^{III}

ranging from 0.62-0.69 Å, with the exception of aluminum (0.50 Å). Octahedra are strongly flattened along the stacking direction, which changes the symmetry from O_h to D3d. Larger metal ionic radii yield more flattened octahedra and increased distance between metals (deRoy et al., 2001), e.g., LDHs with magnesium and aluminum have flatter octahedra and larger M^{II}-M^{III} distance than LDHs with nickel and aluminum.

In LDHs, a trivalent metal (M^{III}, e.g., Al^{3+}) substitutes for a divalent metal (M^{II}, e.g., Mg^{2+}) in the hydroxide sheet, which results in a net positive charge (Figure 3.1). The positive charge is balanced by anions that sorb to the M^{II}/M^{III} hydroxide sheets and/or move into the interlayer space between the sheets. The hydroxide sheet can be thought of as a solid solution of two metals. The LDH structure is based on metal octahedral units $[(M)(OH)_6]$ sharing edges to build $M(OH)_2$ brucite-like layers. Multiple layers of hydroxide sheets stack upon each other. The positive charge of the LDH is proportional to the value of x, where $x = M^{III}/(M^{II}+M^{III})$. The typical value of x is 0.2 to 0.4. This range, however, can extend from approximately 0.14 to 0.5 (deRoy et al., 2001). The upper limit of x is caused by electrostatic repulsion between neighboring trivalent metals. This repulsion is unavoidable if x > 0.333. At high degrees of substitution (x>0.333) there is also increased repulsion between the interlayer anions. According to the reported stability of Ni-Al LDH, pure LDH compounds are only achievable with 23-33% aluminum substitution. Above 33%, "islands" of $Al(OH)_3$ can form and below 23%, Ni^{2+} can form $Ni(OH)_2$ precipitates (Brindley, 1980).

The lower limit of what constitutes a LDH is somewhat controversial. With less M^{III} substitution, a smaller positive charge results. This causes fewer anions to be in the

interlayer. With too few anions in the interlayer, the space may expand and break down (deRoy et al., 2001). However, because single metal alpha-type hydroxides share a similar structure to LDHs (Figure 3.1), it is difficult to distinguish exactly when the interlayer structure breaks down. The precipitate can also contain impurity phases such as areas of single metal hydroxides or basic salts of the divalent/trivalent metal (deRoy et al., 2001). For example, nitrate (NO_3^-) anions from the soluble salt nickel nitrate can form covalent bonds as nitrato groups to the hydroxide layer (Delacaillerie et al., 1995).

Metal cation location and the M^{II}/M^{III} ratio are the focus of numerous studies; however, determining metal cation location in LDHs is difficult because of the low degree of crystallinity typically achieved during LDH syntheses. In the hydroxide layers, trivalent cations should avoid each other as nearest neighbors, so as to minimize electrostatic repulsion. In this manner a well ordered cation distribution should result. However, this high degree of order is often not observed via X-ray diffraction (Costa et al., 2010).

Synthetic Ni-Al LDHs can be made in the laboratory using two methods. They can be synthesized under induced/controlled hydrolysis conditions or co-precipitation (Reichle, 1986; Taylor, 1984). The induced hydrolysis method most likely imitates the reaction in soils. In this reaction, a fully hydrolyzed Al^{3+} cation [i.e., precipitated $Al(OH)_3$] is added to a solution of Ni^{2+} at the same pH, e.g., pH 6.9. The pH of the mixed metal slurry is maintained just below that at which Ni^{2+} hydroxide [$Ni(OH)_2$] would precipitate (pH≈6.9). The pH is maintained by, for example, adding sodium carbonate with a pH stat. As Ni^{2+} sorbs to the $Al(OH)_3$ surface, the Ni^{2+} hydrolyzes and

precipitates as a double-cation hydroxide (Taylor, 1984). Because of charge surplus, the hydroxide layer is positively charged. These steps are analogous to aluminum oxides or aluminum-rich clays in soil being exposed to Ni^{2+} in the soil solution, where Ni^{2+} hydrolyzes on aluminum-rich minerals in the soil to form Ni-Al LDHs. This reaction mechanism however does not describe how Al^{3+} moves from the $Al(OH)_3$ phase into the LDH phase.

In co-precipitation methods, the initial M^{II}/M^{III} ratio in solution should be retained in the LDH solid phase (deRoy et al., 2001). However, this is not the case for LHDs synthesized via the induced hydrolysis method, where the researcher controls when to terminate the synthesis reaction. If the reaction is stopped too soon the transformation from $Al(OH)_3$ to Ni-Al LDH may not be complete. The excess of M^{II} or M^{III} has not been studied under induced hydrolysis conditions. Excess M^{II} can result in the formation of $M(OH)_2$, while too little M^{II} can result in unreacted $M(OH)_3$. Unreacted $M(OH)_3$ can crystalize into other more stable forms, e.g., bayerite for Al^{3+} (deRoy et al., 2001).

Empirical thermodynamic data by Peltier et al. (2006) found that the most thermodynamically favorable x value is approximately 0.28. This value may be correct when neither M^{II} nor M^{III} are limiting factors as reactants but may not be reasonable if one reagent is limiting. For example, with excess Ni^{2+}(aq), sorption/precipitation of Ni^{2+} would lead to low x values and possibly $Ni(OH)_2$ phases mixed into the LDH. It was found that LDHs synthesized via induced hydrolysis (Taylor, 1984) tend to form with x values in the range of 0.13-0.15 when the reaction is carried out to completion (Centofanti et al., 2012). With such low values of x, the nickel content of the LDH is

very high, and perhaps a mixture of α-Ni(OH)$_2$ phases along with LDH are present. This low value of x indicates that when the reaction is carried to completion, the most stable product has a lower x value than predicted.

Apart from the metals present in the hydroxide sheet, the interlayer anions also affect LDH stability. It has been shown that the type of interlayer anion between the two hydroxide sheets greatly contributes to the stability of the LDH. In order of increasing stability, nitrate < sulfate < carbonate < silicate, where silicate has a more negative Gibbs free energy of formation than nitrate (Peltier et al., 2006). In the LDH structure, the interlayer can be occupied by water molecules, anions, or be vacant. Specific orientation of interlayer molecules can be thermodynamically favorable due to the attraction between opposing charges and enhancement of hydrogen bonding. The identity and orientation of the intercalated anion affect the hydroxide stacking sequence and mineral thermodynamic properties (Costa et al., 2010; Peltier et al., 2006).

LDH Precipitation Mechanisms in Soils

Layered double hydroxides that form in soils and sediments, or "environmental LDHs", form differently than LDHs synthesized by co-precipitation in the laboratory because the co-precipitation method is carried out in a batch reaction, where the final product is always limited by concentrations of the reactants. However, in the environment, there may be a long-term and large source of nickel slowly dissolving from nickel rich particles, e.g. nickel particles emitted from a nickel refinery. Even though environmental LDHs form differently, they are composed of material from both the

aqueous solution and the solid. Therefore they are still referred to in general as co-precipitates in soils (Sparks, 2002). Sparks (2002) and references therein outline how surface precipitation of LDHs occur in soils.

First, the solid surface (i.e., the adsorbent containing M^{III}) lowers the energy of nucleation necessary for the cation (M^{II}) by providing sterically similar sites for sorption (McBride, 1991). Second, the activity of the surface precipitate is less than one (Sposito, 1986). And third, because the dielectric constant of the solution near the surface is less than that of the bulk solution, the solubility of the surface precipitate also decreases (O'Day et al., 1994).

Yamaguchi et al. (2001) also elaborate on co-precipitation of Ni-Al LDHs in soils. They explain that first, nickel sorbs to an Al-rich surface, causing local super-saturation of nickel at the mineral – water interface, i.e., on the surface nickel is at a concentration above which $Ni(OH)_2$ precipitates. Second, the sorbent acts as a nucleation center to catalyze the precipitation process (McBride, 1994). Third, adsorbed water molecules cause a lower solubility of $Ni(OH)_2$ at the mineral water interface, causing $Ni(OH)_2$ to precipitate (Sposito, 1989). Lastly, over time, aluminum dissolves from the sorbent and diffuses into the octahedral layer of $Ni(OH)_2$ replacing nickel in some of the octahedral sites. As this procedure continues, a Ni-Al LDH, which is thermodynamically favored over $Ni(OH)_2$, is formed (Sparks, 2002). Another hypothesis for the formation of Ni-Al LDH is that as Ni^{2+} sorbs to the aluminum surface, aluminum dissolves from the surface and re-sorbs adjacent to the Ni^{2+} atom. In this fashion, the double metal octahedral layer grows.

These proposed mechanisms lead to a series of more fundamental questions:
Why would aluminum replace nickel in nickel hydroxide? Why are LDHs
thermodynamically favored over $Ni(OH)_2$? Does sorbed Ni^{2+} induce dissolution of
aluminum or silicon from the sorbent surface? How do we determine if aluminum
replaces nickel in surface precipitated $Ni(OH)_2$ or if dissolved aluminum resorbs adjacent
to Ni^{2+} already on the surface? What is the extent of nickel and aluminum intraparticle
diffusion into the adsorbent or $Ni(OH)_2$, respectively? In the controlled hydrolysis
method of LDH synthesis, what causes the rearrangement of atoms from amorphous
$Al(OH)_3$ into the layered structure? As aluminum dissolves, consequently creating
vacancy sites in the aluminum adsorbent, does/can Ni^{2+} replace the dissolved aluminum?
How do variations in the Ni-Al ratio affect LDH stability? What effects on mineral
stability do the d-orbitals electrons of nickel α-$Ni(OH)_2$ versus Ni-Al LDH have?
Although the hydrolysis and precipitation mechanisms outlined by Taylor (1984) and
Sparks (2002) are generally accepted, there are limited data to answer these fundamental
questions.

MOT Hypothesis for Ni-Al LDH Stability

To answer some of those fundamental questions, it would be helpful to discuss the
molecular orbital theory (MOT) of phyllosilicates and hydroxides to better comprehend
LDH formation and stability. The Ni-Al LDH structure is composed of sheets of
octahedra with either nickel or aluminum as the central atom (Figure 3.1). The electron
configuration of Al^{3+} is $[Ne]3s^2 2s^2 2p^6$, while the electron configuration of Ni^{2+} is

$[Ar]^3d^8$. Al^{3+} has no electrons in its d-orbitals while Ni^{2+} has eight electrons in its d-orbitals. Because both atoms have octahedral coordination geometry but Al^{3+} has no electrons in its d-orbitals, Al^{3+} has no d-orbital splitting while the d-orbitals in Ni^{2+} are split into the $t_{2g} - e_g$ energy levels. The split in the d-orbital energies (the ligand field splitting parameter) causes electrons to first fill the lower t_{2g} energy level and then the e_g energy level. For metals with weak-field ligands, like OH^-, the energy gap between the t_{2g} and e_g energy levels is smaller than for metals with strong field ligands. Nonetheless, this energy gap exists for the d-orbitals in Ni^{2+}. Because of this energy gap and preferential filling of the t_{2g} orbitals, more electrons in Ni^{2+} are in the d_{zx}, d_{yz} and d_{xy} orbitals. Therefore, more electron density will occur along these axes than in the d_{z2} or d_{x2-y2} orbitals.

In the hydroxide sheet of single (e.g., nickel) and double (e.g., nickel and aluminum) metal hydroxides, the octahedra are edge-sharing, i.e., the octahedra share both apex and equatorial O atoms. Because the d_{zx}, d_{yz} and d_{xy} orbitals of the central nickel and aluminum atoms are all between the vertices, these orbitals from diagonally neighboring octahedra may cause an overlapping of electron density and therefore increased electron densities between the octahedra. The overlap and increased electron density also increases repulsion between octahedra and mineral instability. This would be the case for nickel, which preferentially fills the d_{zx}, d_{yz} and d_{xy} orbitals.

If there were atoms with unoccupied d-orbitals (e.g., Al^{3+}) present in the lattice of a $Ni(OH)_2$ octahedral sheet (i.e., yielding a Ni-Al LDH), then the aluminum atoms would effectively give more space for the d_{zx}, d_{yz} and d_{xy} orbital electrons of the nickel atoms

and decrease the electron repulsion between neighboring octahedra. The decrease in electron repulsion between octahedra would reduce the energy necessary to stabilize the mineral, i.e., the overall stabilization energy of the mineral would be lower.

We hypothesize that increasing the aluminum content of layered α-Ni(OH)$_2$ would increase the mineral's stability because aluminum is lacking electrons in its d-orbitals while nickel has the d^8 electron configuration. We propose, based on these molecular orbital theory arguments, that if aluminum substitutes for nickel, the d-orbital electrons from nickel could enter the adjacent and empty d-orbitals of aluminum octahedra in the hydroxide layer. This could be one reason why the Ni-Al LDH is thermodynamically favored over α-Ni(OH)$_2$. However, as aluminum substitution increases to x >0.333 the electrostatic repulsion of neighboring trivalent Al^{3+} would also disrupt mineral stability (deRoy et al., 2001).

Motivation and Objectives

Although it is known that Ni-Al LDHs form in contaminated soils, it is not understood how they form or why they are more stable than single metal hydroxides. The reason why LDH formation is not understood is because of the difficulty in obtaining thermodynamic and structural information during their formation/precipitation. Thermodynamic and structural information are necessary to understand why LDHs are more stable than pure metal hydroxide precipitates. LDH precipitates in soils and on clay sorbents have been analyzed by a variety of techniques including X-ray Absorption Spectroscopy, Fourier Transformed Infrared Spectroscopy, Transmission Electron

Microscopy, calorimetry, diffuse reflectance spectroscopy and other techniques (Allada et al., 2002; Livi et al., 2009; Peltier et al., 2006; Scheinost et al., 1999). Additionally, synchrotron-based tools have demonstrated that LDHs are significant chemical species in zinc and nickel contaminated soils (McNear et al., 2007; Nachtegaal et al., 2005).

However, these tools have not explained why they form. For example, Quick-scanning Extended X-ray Absorption Fine Structure Spectroscopy (Q-XAS) can be used to obtain real time structural changes during LDH/metal precipitation reactions (see Chapter 1). However, this information is still limited in that it is observational. The researcher observes what is happening in real time but does not know why it happens. Additionally, EXAFS data analysis of mixed metal (heterogeneous) samples is complicated by overlapping backscattering photoelectric waves (see discussion in Chapter 1). To understand why LDHs form in soils, or even in synthetic laboratory reactions, one must obtain thermodynamic and structural information during the precipitation process at the atomic scale. Molecular modeling of LDH structures may be a tool to obtain thermodynamic and structural data at the atomic scale to understand why LDHs are more stable than single metal hydroxides. Good agreement between calculated and experimental values of enthalpies of formation for LHD systems was found by Costa et al. (2010) and (2011).

Energy minimized structures will provide complementary data to those obtained via EXAFS and calorimetry by providing theoretical inter-atomic distances and thermodynamic data, respectively. Using molecular modeling we will imitate the increase in aluminum substitution into the nickel hydroxide sheet that is hypothesized to

66

be the LDH formation mechanism. The results will help understand if heavily substituted aluminum for nickel is more stable than slightly substituted aluminum for nickel. Additionally, the most stable Ni/Al metal ratio in LDHs can be determined.

The objectives of this study are to 1) to calculate energy minimized structures of Ni-Al LDH with various Ni-Al ratios to determine if changing the aluminum content in the LDH structure increases or decreases the mineral's stability; 2) use the *ab initio* software IFEFFIT (Newville, 2001) to generate theoretical EXAFS spectra of energy minimized LDH compounds to compare them to empirical data and lastly, 3) employ Pair Distribution Function analysis on several LDH samples to better understand the long-range atomic ordering of metals. PDF analysis has been used to study the nano-crystallinity of various soil minerals (Michel et al., 2007), but has only recently been applied to LDHs to study their long range order (Aimoz et al., 2012). Lastly, it would be helpful to see what the electron densities look like between octahedra. The overall goal is to understand why Ni-Al LDHs form in soils versus the α-Ni(OH)$_2$ phases.

Methodology and Preliminary Results

Reactant Unit Cells

To carry out molecular modeling calculations, it is important to base the calculations off of a stoichiometrically balanced chemical reaction. This is not a mechanistic reaction but is necessary in order to calculate the energy of each of the reactants separately from the product. By knowing the energy of each reactant, that reactant can be added or subtracted from the product's energy multiple times in order to

compare products (e.g., LDH structures) with different numbers and types of atoms. For

our system we have written the following chemical reaction to represent the Ni-Al LDH:

$$6Ni^{2+}_{(aq)} + 2Al^{3+}_{(aq)} + 16OH^- + HCO_3^{2-}_{(aq)} + 12H_2O = Ni_6Al_2(OH)_{16}.HCO_3.12H_2O_{(s)} \qquad 2$$
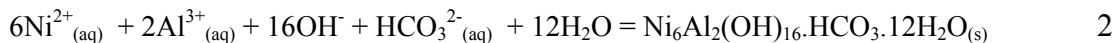
In this equation, all the elements and molecules represented in our systems are present.

For all the reactants and products, it is important to create their molecular structures to be

environmentally correct, i.e., they should be designed to be how they occur in nature. For

example, at pH 7.5, aluminum is tetrahedrally coordinated, so the aqueous model reactant

should also be tetrahedrally coordinated. Also at this pH, dissolved carbon dioxide

should be bicarbonate and not carbonate or carbonic acid.

The reactants created for the chemical reaction include: OH^-, $Ni^{2+}_{(aq)}$, $Al(OH)_4^+$,

and HCO_3^- (Figures 3.2-3.5). The reactants were designed and hydrated in a 10x10x10 Å

unit cell box was used using HyperChem. The unit cells were then submitted to

molecular dynamics (MD) simulations in Materials Studio using the module Forcite, with

the Universal force field (UFF; Rappe et al., 1992). The temperature for MD simulations

was set to 298K. A time step of 1 fs was used for several steps. After the MD

simulations of each reactant, the models were energy minimized using UFF. This was

done to ensure reasonable atomic coordinates (e.g., geometry optimized using MD)

before performing more intensive density functional theory (DFT) calculations.

Energy-minimized structures were then used as starting points for density

functional theory (DFT) energy minimization calculations in the Vienna Ab Initio

Simulation Package (VASP; Kresse and Furthmuller, 1996). VASP is a program for

performing quantum-mechanical calculations projector-augmented waves and a plane wave basis set (Kresse et al., 2011).

Product Unit Cells

In this study, calculations were carried out on Ni-Al LDHs with varying Ni-Al ratios to examine the mineral stability during various amounts aluminum for nickel substitution. Several systems were tested, ranging from 0% to 50% aluminum substitution. The starting structure was the naturally-occurring hydrotalcite mineral, Mg/Al-LDH-carbonate, with Mg substituted for Ni. The unit cell was large enough to allow for the desired amount of aluminum substitution to be achieved. The unit cells included three layers of mixed metal hydroxides with an anionic interlayer. Typically carbonate or silicate is the environmentally important interlayer anion. It has been shown that a silicate anion interlayer is more stable than carbonate (Peltier et al., 2006); however, this substitution takes time to occur and initial precipitates in soils most likely have carbonate in the interlayer. Additionally, carbonate is the most common interlayer anion found in the environment (Rives, 2001). Therefore, a carbonate interlayer will be used in this study.

The energies of the stoichiometrically-balanced chemical reaction discussed above (Equation 2) were calculated using VASP. These types of calculations are comparable to each other but do not yield absolute Gibbs free energies. Instead, potential energies can be compared to each other to determine the most stable atomic configurations of the components used not including entropic effects. The density of the

reactant unit cells, e.g., the density of nickel atoms and water molecules in the unit cell, should be close to 1. The density of the LDH product can be obtained by performing a MD simulation for geometry optimization in Materials Studio.

Five LDH products were designed to test Ni-Al LDH stability at various Ni/Al ratios (see Figures 3.6 and 3.7 for examples). The products are model compounds ranging from pure nickel systems to pure aluminum systems. Because LDHs form on aluminum-rich minerals, one of the products is be nickel-free, e.g. gibbsite. The gibbsite model is the 100% aluminum end member for these calculations for comparison basis. Other products to be studied will vary in x, where x = Al/(Ni+Al) in the hydroxide sheet. In the first system, x=0, and its results will represent the minimization energy for a pure $Ni(OH)_2$ system. The second, third, fourth, and fifth systems will vary as such: x= 0.14, 0.33, 0.5, and 1, respectively. These values have been chosen to represent the low, middle (ideal) and high end x values where the LDH structure is stable. In the ideal LDH formula, x=0.33, and no aluminum atoms have aluminum as second neighbors. The highest aluminum substitution ratio of x=0.5 is hypothesized to be the upper limit of LDH stability, and will provide good comparison to lower x values and some insight into the stability of LDHs with high aluminum substitution. In total, 36 atoms in the unit cell and 12 atoms per hydroxide layer were used.

In system 1, x=0. This system is $Ni(OH)_2$ (i.e., a pure alpha nickel hydroxide) in the hydrotalcite unit cell parameters. From the hydrotalcite crystallographic information file (CIF) (Allmann, 1970), which was downloaded from the American Mineralogist Crystal Structure Database (Downs and Hall-Wallace, 2003), it was found that the OH

bond distance was 0.85 Å, which is fundamentally wrong for OH bond distances. This

may have been a problem with the input CIF file. The DFT calculation in VASP changed

the OH bond distance to 0.97 Å during the calculation, which is an acceptable distance.

The Ni-O distance shrank from 2.026 Å to 1.979 Å during the VASP calculation;

however, the crystal structure was maintained with some disorder. The water molecules

in the interlayer moved around slightly. The cell volume was constrained so there was no

drastic reorientation or loss of structure. We attempted to keep magnetic ordering for all

five systems similar to the $Ni(OH)_2$ system, except for the aluminum atoms substituted

into the structure. It must be determined if aluminum has a net spin to consider for the

calculation. To determine this, further literature review is needed. This system finished

the VASP calculation successfully and was the only one to do so of the five systems.

System 2 had a Ni:Al ratio of 1/6, where 2 aluminum atoms and 10 nickel atoms

per the 12 atom hydroxide sheet were used. The $1/6 = 0.167$ ratio is this close to the

desired 0.14. There were problems with the magnetic ordering of the nickel atoms, so this

job could not complete in VASP.

In systems 3 and 4, there were 12 aluminum atoms and 24 nickel and 18 Al and

18 Ni atoms, respectively. This equates to 4 aluminum atoms and 8 nickel atoms per 12

atoms per sheet; x=1/3 and 6 Al and 6 Ni atoms per sheet for x = 1/2, respectively. At

four aluminum atoms per sheet, it is necessary to place two carbonate molecules per sheet

to balance the charge, or six carbonate molecules per unit cell. For system 4, three

carbonate molecules per sheet were necessary. The interlayer anions were energy

minimized with a force field calculation in Materials Studio prior to DFT calculations in VASP.

In System 5, all atoms were aluminum atoms; 12 aluminum atoms per sheet and 6 carbonate ions per sheet were used. Systems 3-5 were not submitted for VASP calculations because of problems obtaining stable electron density in System 2. Problems with System 2 should be worked out before continuing with the other systems.

Discussion

Cation Ordering and Unit Cell Dimensions

It has been determined that in a LDH with a magnesium to aluminum ratio of 3-to-1, the aluminum atoms are ordered in a honeycomb arrangement, keeping the aluminum atoms separate. Additionally, structures are fully ordered for Mg:Al ratios of 2:1 and at lower aluminum content a non-random distribution of cations persists, with no Al^{3+}-Al^{3+} in close contacts (Sideris et al., 2008). However, newer data (Cadars et al., 2011) suggest that there are occurrences of cation clustering. In general, though, the global structure of the LDH is maintained. For our calculations, it would be ideal to try to maintain the aluminum atoms apart from each other as much as possible, i.e., maintaining the honeycomb ordering and no close contact for aluminum cations seems most appropriate. However, it may be a good idea to test a system where there are clustering of like cations.

Lastly, each model with a different unit cell composition will have slightly different unit cell dimensions caused by differences in the ionic radii of nickel and

aluminum atoms. The dimensions for specific unit cell measurements can be predicted

for our systems using Almansa et al. (2008), Carteret et al. (2011), Kovanda et al. (2009),

and Rives and Kannan, (2000).

Interlayer Composition

A method for preparing LDH structures for MD is presented in Newman et al.

(2001), but doesn't specify how to determine the number of water molecules to place in

the interlayer region (pg. 97). They suggest using Dreiding force-field for Mg-Al LDH

CO_3, and determined carbonate and water molecules are generally midway between and

coplanar to the hydroxide layers. However, it is necessary to determine how much water

to put into the interlayer. Perhaps this can be done by looking at the molecular formulas

of several LDH structures in the literature (e.g., Allada et al., 2002; Peltier et al., 2006),

where the interlayer water content is calculated via thermogravimetric analysis. These

values however are determined from dry mineral samples and may not be realistic values

for hydrated LDHs in environmental conditions. The interlayer water amount and

distribution still needs a clarification.

Additionally, one important consideration is nitrato groups or other basic salts that

are covalently bonded to the hydroxide surface. It is very common for nitrato groups to

bond to the hydroxide sheet of nickel hydroxides during preparation (Delacaillerie et al.,

1995; Scheinost and Sparks, 2000). As it is common for hydroxides, it is reasonable to

assume it is also common for LDHs, and in fact this occurrence is mentioned by deRoy et

al. (2001). In the environment, it seems reasonable that a pure single metal hydroxide

phases with no covalently bonded anions would be uncommon. There would normally be some anions covalently bonded to the hydroxide sheet, whether they are carbonate or nitrato groups. It's important to make the molecules environmentally accurate to represent what one observes in natural systems.

Magnetic Properties

When writing the input files for VASP, it is important to consider, understand and label the magnetic ordering (magnetic state) and spin states of the unpaired valence electrons of the nickel atoms and of any other atoms with d-orbital electrons involved in the calculation, i.e., the magnetic ordering of nickel atoms in the LDH structure unit cell. The difficult part is to figure out the spin order of the 36 nickel atoms in the unit cell (e.g., 36 being the number of nickel atoms in system 1). To label the magnetic moment ordering, one must know the spin state of the atoms. Nickel is in +2 oxidation state with d^8 electronic configuration; it has 2 unpaired d-orbital electrons. The spins need to alternate to be either +2 or -2. In both Ni-Al LDHs and nickel hydroxide, nickel is in the high-spin state and has octahedral structure. In order to determine spin order, one needs to research literature that discuss the magnetic spin ordering of nickel atoms in nickel hydroxides, oxides or LDHs. Literature on the spin ordering of Fe in Fe-oxides may also be relevant information to consider; however, Coronado et al. (2008) determined it is important to consider only magnetic ordering of LDH models that do not include iron because or other transition metals can promote spin frustration. The goal is to identify the magnetic ordering of nickel atoms at low temperature, generally 5K. The magnetic

74

ordering of the atoms must be acceptable or the structures are not stable during the VASP calculations and will not represent their natural environmental states.

To label the magnetic moments of each atom in VASP, view the molecular structure (as seen in Materials Studio or other visualization software) and identify the atomic coordinates (e.g., xyz positions) of the specific atoms that need to be labeled with magnetic moments, e.g., all the nickel atoms. Then, with pen and paper, note positive or negative spins on each nickel atom, e.g., for each of the 36 nickel atoms in the $Ni(OH)_2$ structure unit cell. The magnetic moment labels are the most important and time consuming part of setting up the calculation – i.e., setting the values of each atom to positive or negative.

In labeling the magnetic moments of nickel in our LDH, we employed a ferromagnetic setup with alternating positive and negative columns for nickel atoms in the unit cell. Aluminum atoms that replaced nickel were designated to have zero spin or made to have spins that cancel out. In the Ni-Al LDH end-member that consisted of 100% nickel atoms (i.e., a pure nickel hydroxide), the magnetic ordering was hypothesized to alternate up and down – trying to minimize adjacent like spins. This worked well as the VASP calculation for this end member (System 1) successfully converged. However, as we moved away from the 100% nickel end-member and substituted in aluminum atoms, this alternation of up and down magnetic spins became trickier and several of our systems containing nickel and aluminum did not converge because there were problems obtaining a stable electron density. The spin ordering of the nickel atoms must be rearranged to try to stabilize the calculations. For System 2, we

tried to follow the magnetic moments used for the pure nickel hydroxide (System 1), but just change 1 nickel spin. This design however proved troublesome and several suggestions are presented below.

Magnetic studies performed on Ni-Al LDH-carbonate, Ni-Al LDH-nitrate, and Ni-hydroxide at nickel to aluminum ratios of 1.63, 2.8, and pure nickel hydroxide, respectively, demonstrate that Ni-Al LDHs and Ni-hydroxide are all ferromagnetic (Coronado et al., 2008; Perez-Ramirez et al., 2002; Taibi et al., 2002). That is to say, they have large domains of aligned magnetic moments; these domains can be sizes from 0.1 mm to a few mm (Nave, 2013). The magnetic ordering temperature, i.e. the Curie and Néel temperatures for ferromagnetic/ferrimagnetic and antiferromagnetic materials, respectively, is about 6-7 degrees K for Ni-Al LDH-carbonate (Perez-Ramirez et al., 2002). Above this temperature, the solids switch from being ferromagnetic (i.e., having aligned magnetic moments) to paramagnetic (i.e., random magnetic moments). For our DFT studies, which are performed computationally at zero K, all our models should be ferromagnetic.

For our models, all the previously tested hydroxide (except for pure Ni-hydroxide) structures failed to stabilize because they could not obtain a stable electron density (Kubicki, 2011). When the magnetic moments for each model (including pure Ni-hydroxide) were assigned, they were in supposedly done so a ferromagnetic fashion to make the overall magnetization close to zero. The magnetic ordering was performed by assigning neighboring rows of nickel atoms positive and negative magnetic moments in the same hydroxide layer. Perhaps these rows of opposing moments (where each row

represents a magnetic domain) were too small. That is to say, bigger domains of aligned magnetic moments should be tested. For example, align the magnetic moments for the entire hydroxide sheet.

As for models with lower Ni:Al ratios (e.g., 1-to-1), all the magnetic moments in the same hydroxide sheet should also be aligned. Arranging the magnetic moments in this order may help to stabilize the electron density. Lastly, since all of these compounds are ferromagnetic, perhaps all the magnetic moments should possibly be pointing in the same direction throughout the entire structure. The large d-spacing (about 7.5 Å) between hydroxide sheets reduces the effects of the interlayer hydrogen bonding on the magnetic properties of the hydroxide layer (Taibi et al., 2002). A technique for "in-plane" magnetic moment modeling for Ni-hydroxides of various d-spacing is also discussed by Taibi et al. (2002).

Importantly, superexchange between the Ni-O-Ni atoms (which is the oxo-bridge at about 90º) actually promotes ferromagnetic coupling between the two nickel atoms (Coronado et al., 2008; Taibi et al., 2002). Lastly, it is important to consider only magnetic ordering of LDH models that do not include iron because or other transition metals can promote spin frustration (Coronado et al., 2008), which shouldn't occur in our case as with diamagnetic aluminum atoms as neighbors. Taking this literature into account for new magnetic ordering of the nickel atoms may help fix and explain our electron density instabilities.

LDA+U

In terms of DFT calculations, there is the U-correction parameter that must be entered. This parameter is described in Rollmann et al., (2004). The "U" parameter in the DFT+U calculation is a correction parameter. It is a transition metal "self-correction" value. Dudarev et al., (1998) make some recommendations for U corrections (e.g. 4-5 eV), to use for the VASP input file. A reasonable starting value for U can be found in literature that uses the U-correction in similar calculations. Quantum Espresso (QE) is a free software available for DFT calculations. It "is an integrated suite of Open-Source computer codes for electronic-structure calculations and materials modeling at the nanoscale. It is based on density-functional theory, plane waves, and pseudopotentials." (http://www.quantum-espresso.org). QE has a LDA+U component described under "Ground-state calculations". A thorough discussion of the Hubbard U evaluation is provided by Dr. Heather Kulik and her tutorials (Kulik, 2013). Like the Hubbard U parameter, magnetization can also be constrained and implemented in QE (Mrozik, 2011).

Materials Studio

Materials Studio 5.5 is a software program for building molecular models. It was used in our research to create and save input files for the VASP program. In Materials studio, before creating the VASP input file, it is important to run a force field calculation to attempt to rearrange the atoms into semi-relaxed (or lower energy) positions before running the DFT calculations in VASP. MD tries to overcome activation energies in

order to push the structure to lower total energy. Force fields are not extremely accurate, but they are a fast start from the same molecular configuration and a good idea to perform on models before submitting them for DFT calculations. By performing a quick force field calculation on the structure, one can possibly remove considerable DFT computational time.

In molecular modeling in general, the final structure can be influence by the starting structure. To help minimize artifacts created by this, one can run multiple energy minimizations from different starting positions, and then use the structure that has the lowest energy. After a MD simulation, one can go through the intermediate files and perform force field calculations on these intermediate files to find structures with the lowest energies as well. Lastly, the structural model must be charge balanced (Kubicki, 2011).

Molecular Dynamics methods can vary as well. There are both classical and force field (clay FF) MD methods. Additionally, there are DFT force field methods (like in VASP). MD is different than straightforward energy minimization calculations because there is a force applied on the atoms to give them kinetic energy. Usually this force is applied via temperature. Many DFT calculations take place at 0K, while MD simulations are performed at higher temperatures, like room temperature (298K). During calculations, it is important to constrain thermodynamic variables experimentally, e.g., temperature and pressure, in the calculation (Mrozik, 2011). For force field calculations, one needs to know if an atom is bonded or not, for DFT this does no matter. VASP can perform both MD and DFT methods.

HyperChem

HyperChem was used to build the reactants of the LDH system (see Equation 2 and Figures 3.2-3.5). HyperChem is good for solvating atoms (i.e., adding water molecules). A neutral box (unit cell) for each component was charge balanced with Na^+ or Cl^-. In order to have accurate results, one must make chemically appropriate reactant systems. For example, at pH 7.5, aluminum is tetrahedral with 4 OH^- hydroxyl groups, not octahedral. To figure out what the correct species is under specific environmental conditions, one should use stability diagrams, a literature review, or aqueous speciation programs such as MINTEQ (Zelmy et al., 1984). It should be determined if aqueous nickel is octahedrally coordinated with water, if Na^+ is octahedrally coordinated with water, or if Na^+ only has 5 waters. These details are critical to the production of accurate results.

Lastly, it is important to represent bulk water as well in the reactants. However, it should be a reasonable calculation in terms of computational time, so a minimum number of water molecules to make adequate solvation should be used. HyperChem predicted about 35 water molecules would fit into our reactant unit cell boxes, but actually it only put in 23 water molecules. For the reactant to make physical sense, the density should be close to 1 (e.g., 0.9-1). So if the density is too low, one needs to go back to the original structure in HyperChem and add more water molecules into the unit cell.

Future Research

First, it may be difficult to balance out interlayer charge when using different Ni/Al ratios. This is because a change in Ni/Al ratio also requires the addition or subtraction of interlayer anions. The charge density of the mineral is proportional to the amount of aluminum substitution, so higher aluminum content causes a more positive charge and will require more anions to satisfy this charge. Adding or subtracting carbonate anions is a dramatic change in the unit cell. In order to compare data from the different systems, it is important to keep the systems as similar as possible while varying just the Ni/Al ratio. One of the overall goals of this study is to identify how the Ni/Al ratio affects the mineral stability, and if the interlayer properties (i.e., anions and water) cannot be accurately calculated then the results with respect to the Ni-Al ratio will also be compromised. Additionally, the choice of interlayer anion as carbonate or bicarbonate needs to be made. At pH 7.5, bicarbonate is the more abundant anion; however, most research discusses only carbonate interlayer anions.

Several other questions still need clarification as well: How much do several tenths of an Angstrom alter the calculation or affect the resulting energy? Can unit cell volume be held constant for different Ni/Al ratios? Or do they need to be altered for different Ni/Al ratios? How should the number of water molecules in the interlayer be determined?

Creating clusters that mimic nickel sorption to a vacancy or edge site of $Al(OH)_{3(s)}$ would help clarify what type of bonding is most stable at that site. This may help explain if nickel replaces aluminum or vice versa during LDH formation.

Additionally, to complement molecular modeling, Pair Distribution Function data (PDF) would be useful to provide information about the long range atomic ordering of the structures. PDF can be used to determine the long range structure of amorphous materials (Michel et al., 2007) and has been recently used in analysis of LDHs (Aimoz et al., 2012). Additionally, comparison of theoretical EXAFS spectra generated from DFT results for comparison to experimentally obtained EXAFS data would be useful to understand the effects of Ni/Al ratio and atomic placement on the EXAFS features. Lastly, a MOT analysis of phyllosilicates and hydroxides would also provide helpful insight as to why the addition of aluminum to single metal hydroxides is thermodynamically favorable.

α-Ni(OH)₂   LDH

Ni   Ni+Al

NO₃, Cl, CO₃, [SiO₂]ₙ   NO₃, Cl, CO₃, [SiO₂]ₙ

Ni   Ni+Al
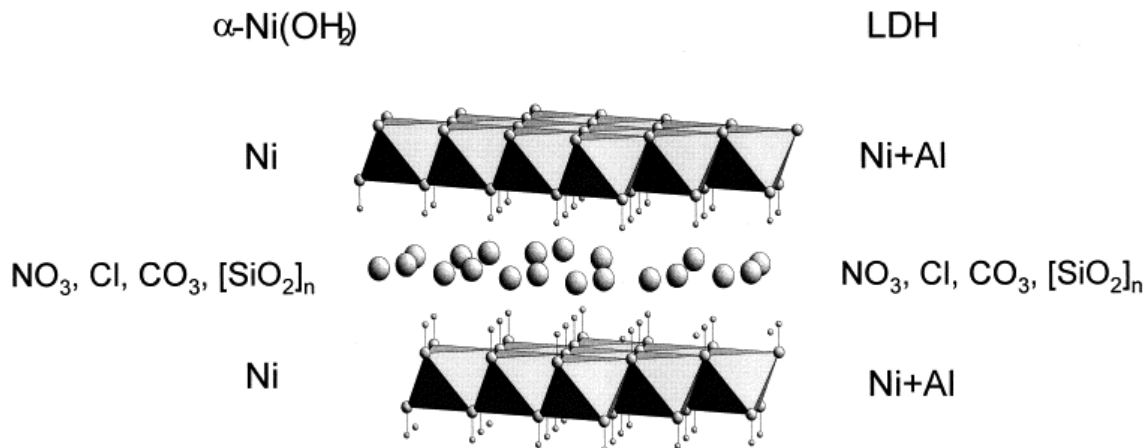
Figure 3.1   Alpha-type nickel hydroxide [α-Ni(OH)$_2$] and Ni-Al LDH are compared in
              the above figure. The M-M distances for alpha nickel hydroxide and Ni-Al
              LDH are 3.07-3.09 Å and 3.05–3.08 Å, respectively (Bellotto et al., 1996;
              Pandya et al., 1990). Both minerals are poorly crystallized and their d-
              spacing is about 8 Å, depending on the interlayer anion. Beta-type nickel
              hydroxides also have similar octahedral layers, however they are well
              crystallized, their interlayer space (d-spacing) is smaller, and the M-M
              distance is larger (c.a. 3.12 Å) (Génin et al., 1991, Pandya et al., 1990).
              Figure from Scheinost et al., 1999. "Reprinted from Geochimica et
              Cosmochimica Acta, 63 /19–20, Andreas C Scheinost, Robert G Ford,
              Donald L Sparks, The role of Al in the formation of secondary Ni
              precipitates on pyrophyllite, gibbsite, talc, and amorphous silica: a DRS
              study, 3193-3203, (1999), with permission from Elsevier."
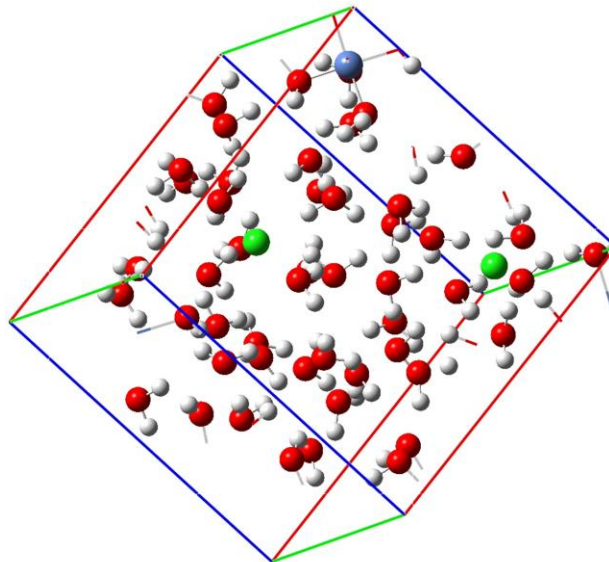
Figure 3.2   Reactant unit cell for aqueous nickel (Ni^{2+}_{aq}). Nickel is blue, and chlorine is green. Oxygen is red. Hydrogen is light gray. Chlorine was used to balance the positive nickel charges.
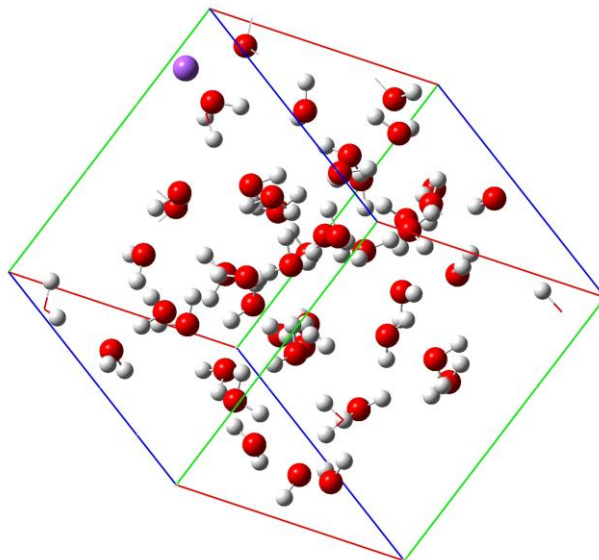
Figure 3.3   Reactant unit cell for hydroxide ion (OH⁻). Oxygen is red. Hydrogen is light gray. Sodium is purple and was used to balance the negative hydroxide charge.
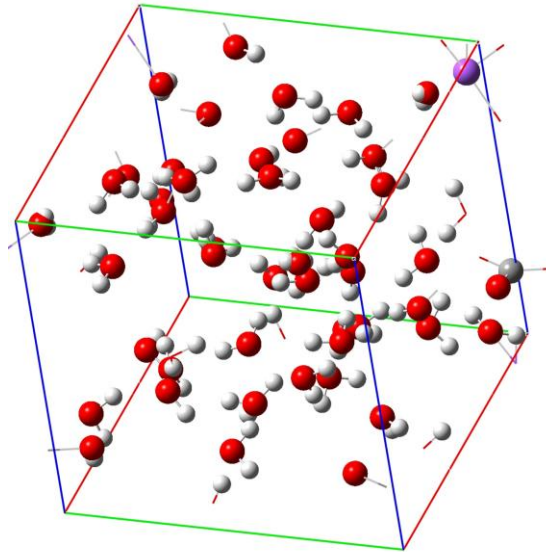
Figure 3.4   Reactant unit cell for bicarbonate (HCO_3^-). Carbon is gray. Sodium is
            purple. Oxygen is red. Hydrogen is light gray. At pH 7.5, the major
            dissolved carbon dioxide species is bicarbonate.
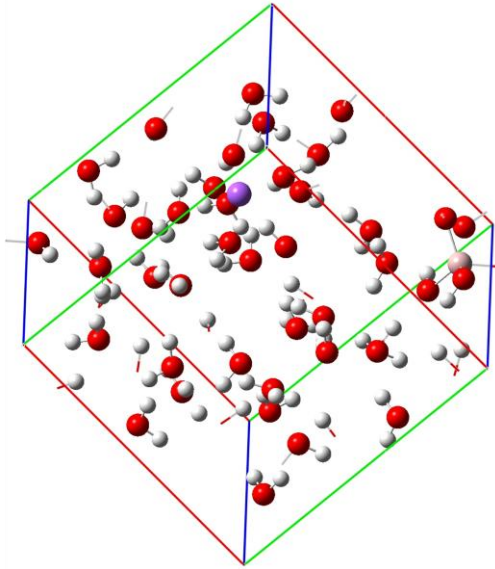
Figure 3.5   Reactant unit cell for aluminum ($AlOH_4^-$). Aluminum is cream. Sodium is purple. Oxygen is red. Hydrogen is light gray. Aluminum is tetrahedral in solution at pH 7.5.
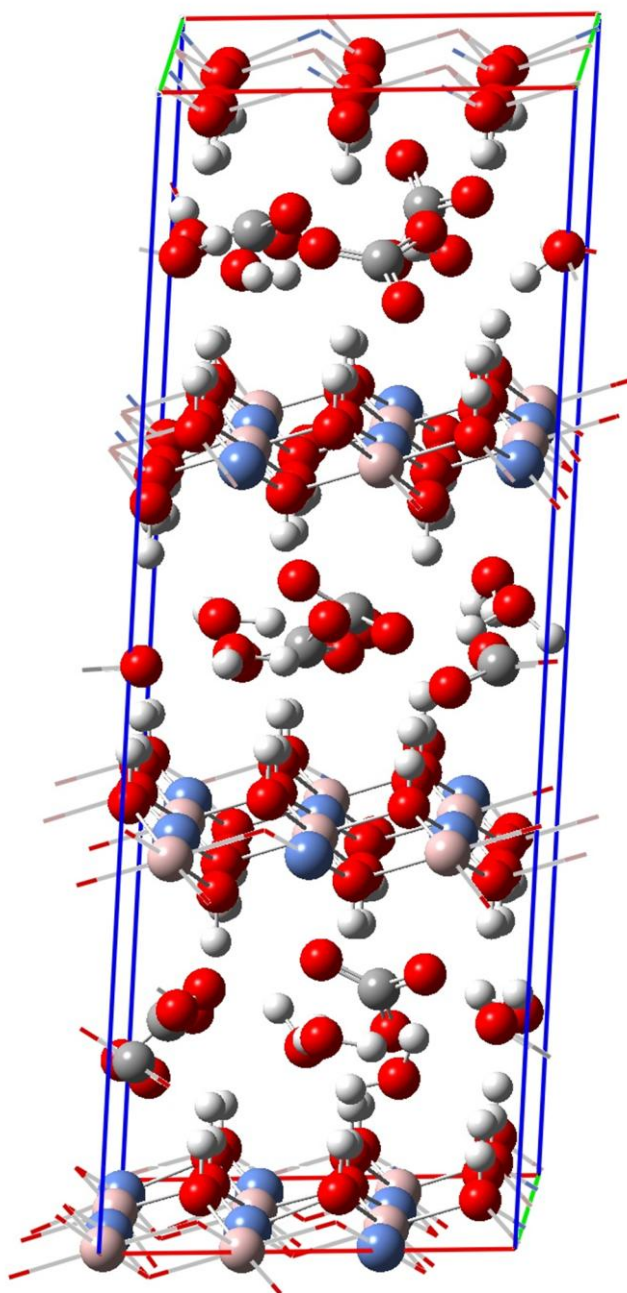
Figure 3.6   Product unit cell for Ni-Al LDH. Nickel is blue. Aluminum is cream.
Carbon is gray. Oxygen is red. Hydrogen is light gray. This is an example
of System 4, where x=0.5.
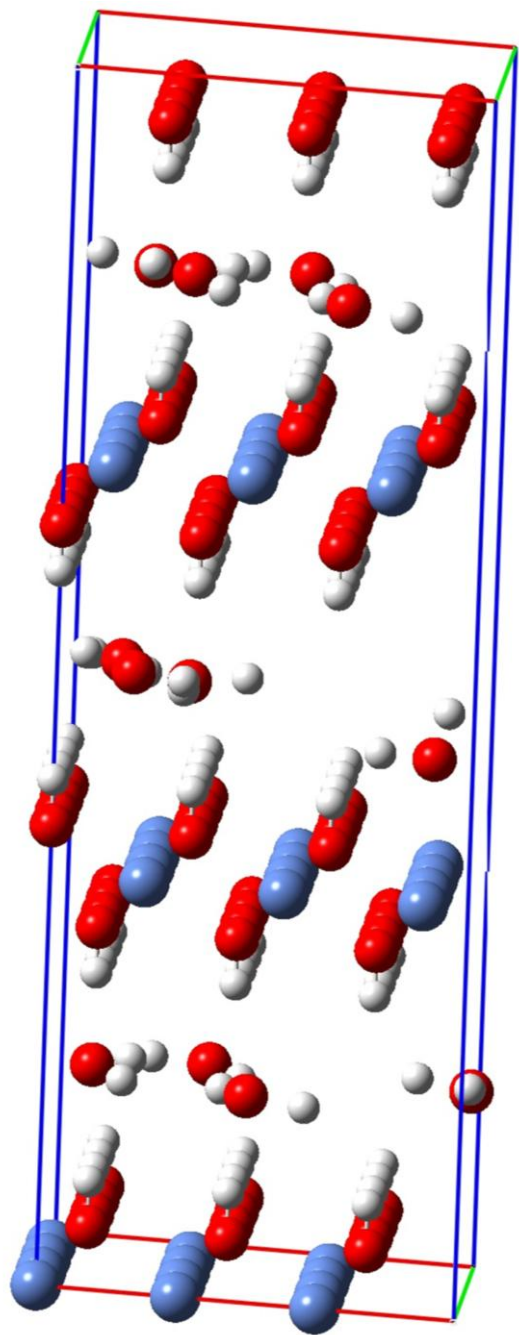
Figure 3.7   Product unit cell for nickel hydroxide. This is alpha-nickel hydroxide in the
unit cell of Ni-Al LDH. Nickel is blue. Oxygen is red. Hydrogen is light
gray. The bonds are not shown for clarity. This is System 1.

REFERENCES

Aimoz, L., C. Taviot-Gueho, S.V. Churakov, M. Chukalina, R. Dahn, E. Curti, P. Bordet, and M. Vespa. 2012. Anion and cation order in iodide-bearing Mg/Zn-Al layered double hydroxides. Journal of Physical Chemistry C 116:5460-5475.

Allada, R.K., A. Navrotsky, H.T. Berbeco, and W.H. Casey. 2002. Thermochemistry and aqueous solubilities of hydrotalcite-like solids. Science 296:721-723.

Allmann, R. 1970. Double layer structures with layer ions $[Me(II)_{1-X} Me(III)_X (OH)2]^{X+}$ of brucite type. Chimia 24:99-108.

Almansa, J.J., E. Coronado, C. Marti-Gastaldo, and A. Ribera. 2008. Magnetic properties of (NiCrIII)-Cr-II layered double hydroxide materials. European Journal of Inorganic Chemistry:5642-5648.

Bellotto, M., B. Rebours, O. Clause, J. Lynch, D. Bazin, and E. Elkaim. 1996. A reexamination of hydrotalcite crystal chemistry. Journal of Physical Chemistry 100:8527-8534.

Brindley, G.W. 1980. Lattice-parameters and composition limits of mixed Mg, aluminum hydroxy structures. Mineralogical Magazine 43:1047-1047.

Cadars, S., G. Layrac, C. Gerardin, M. Deschamps, J.R. Yates, D. Tichit, and D. Massiot. 2011. Identification and quantification of defects in the cation ordering in Mg/Al layered double hydroxides. Chemistry of Materials 23:2821-2831.

Carteret, C., B. Gregoire, and C. Ruby. 2011. Tunable composition of Ni-II-Al-III and Ni-II-Fe-III layered hydroxides within a wide range of layer charge. Solid State Sciences 13:146-150.

Centofanti, T., M.G. Siebecker, R.L. Chaney, A.P. Davis, and D.L. Sparks. 2012. Hyperaccumulation of nickel by *Alyssum corsicum* is related to solubility of nickel mineral species. Plant and Soil 359:71-83.

Coronado, E., J.R. Galan-Mascaros, C. Marti-Gastaldo, A. Ribera, E. Palacios, M. Castro, and R. Burriel. 2008. Spontaneous magnetization in Ni-Al and Ni-Fe layered double hydroxides. Inorganic Chemistry 47:9103-9110.

Costa, D.G., A.B. Rocha, W.F. Souza, S.S.X. Chiaro, and A.A. Leitao. 2011. Ab Initio simulation of changes in geometry, electronic structure, and Gibbs free energy caused by dehydration of hydrotalcites containing Cl^- and CO_3^{2-} counter anions. Journal of Physical Chemistry B 115:3531-3537.

Costa, D.G., A.B. Rocha, R. Diniz, W.F. Souza, S.S.X. Chiaro, and A.A. Leitao. 2010. Structural model proposition and thermodynamic and vibrational analysis of hydrotalcite-like compounds by DFT calculations. Journal of Physical Chemistry C 114:14133-14140.

Delacaillerie, J.B.D., M. Kermarec, and O. Clause. 1995. Impregnation of gamma-alumina with Ni(II) or Co(II) Ions at neutral pH - hydrotalcite-type coprecipitate formation and characterization. Journal of the American Chemical Society 117:11471-11481.

deRoy, A., C. Forano, and J.P. Besse. 2001. Layered double hydroxides: synthesis and post-synthesis modification, In V. Rives, ed. Layered Double Hydroxides: Present and Future. Nova Science Publishers, Inc., New York.

deRoy, A., C. Forano, M.K. El, and J.P. Besse. 1992. Anionc clays: trends in pillaring chemistry, p. 108-169, In M. L. Occelli and H. E. Robson, eds. Expanded Clays and Other Microporous Solids, Vol. II. Van Nostrand Reinhold, New York.

Downs, R.T., and M. Hall-Wallace. 2003. The American mineralogist crystal structure database. American Mineralogist 88:247-250.

Drits, V.A., A.I. Gorshkov, A.V. Mokhov, and E.V. Pokrovskaya. 1995. 201 (In Russian). Litol. Polez. Iskop. 3.

Dudarev, S.L., G.A. Botton, S.Y. Savrasov, C.J. Humphreys, and A.P. Sutton. 1998. Electron-energy-loss spectra and the structural stability of nickel oxide: An LSDA+U study. Physical Review B 57:1505-1509.

Elzinga, E.J. 2012. Formation of Layered Fe(II)-Al(III)-Hydroxides during reaction of Fe(II) with aluminum oxide. Environmental Science & Technology 46:4894-4901.

Genin, P., A. Delahayevidal, F. Portemer, K. Tekaiaelhsissen, and M. Figlarz. 1991. Preparation and characterization of alpha-type nickel hydroxides obtained by chemical precipitation - study of the anionic species. European Journal of Solid State and Inorganic Chemistry 28:505-518.

Han, J.G. 2003. A theoretical investigation on electronic properties and stability of IrSix(x=1-6) clusters. Chemical Physics 286:181-192.

Hoflich, B.L.W., M. Wentzel, H.M. Ortner, S. Weinbruch, A. Skogstad, S. Hetland, Y. Thomassen, V.P. Chaschin, and E. Nieboer. 2000. Chemical composition of individual aerosol particles from working areas in a nickel refinery. J. Environ.Monit. 2:213–217.

HyperChem. HyperChem (TM) Professional 7.51, Hypercube, Inc., 1115 NW 4th Street, Gainesville, Florida 32601, USA.

Kovanda, F., T. Rojka, P. Bezdicka, K. Jiratova, L. Obalova, K. Pacultova, Z. Bastl, and T. Grygar. 2009. Effect of hydrothermal treatment on properties of Ni-Al layered double hydroxides and related mixed oxides. Journal of Solid State Chemistry 182:27-36.

Kresse, G., M. Marsman, and J. Furthmüller. 2011. Vienna Ab Initio Simulation Package [Online] http://cms.mpi.univie.ac.at/vasp/.

Kresse, G., and J. Furthmuller. 1996. Efficient iterative schemes for *ab initio* total-energy calculations using a plane-wave basis set. Physical Review B 54:11169-11186.

Kubicki, J. 2011. Personal communication. The Pennsylvania State University.

Kulik, H. 2013. Quantum Chemistry with Quantum Espresso [Online] http://www.stanford.edu/~hkulik/www/Tutorials/Entries/2011/5/31_Calculating_the_Hubbard_U.html.

Li, W., K.J.T. Livi, W.Q. Xu, M.G. Siebecker, Y.J. Wang, B.L. Phillips, and D.L. Sparks. 2012. Formation of crystalline Zn-Al layered double hydroxide precipitates on gamma-alumina: the role of mineral dissolution. Environmental Science & Technology 46:11670-11677.

Livi, K.J.T., G.S. Senesi, A.C. Scheinost, and D.L. Sparks. 2009. Microscopic examination of nanosized mixed Ni-Al hydroxide surface precipitates on pyrophyllite. Environmental Science & Technology 43:1299-1304.

Materials Studio. Ref. Accelrys Software Inc., Discovery Studio Modeling Environment, Release 3.5, San Diego: Accelrys Software Inc., 2012.

McBride, M.B. 1991. Processes of heavy and transition metal sorption by soil minerals, p. 149-176, In G. H. Bolt, et al., eds. Interactions at the Soil Colloid-Soil Solution Interface, Vol. 190. Kluwer Academic Publishers, Dordrecht.

McBride, M.B. 1994. Environmental Chemistry of Soils Oxford University Press, New York.

McNear, D.H., R.L. Chaney, and D.L. Sparks. 2007. The effects of soil type and chemical treatment on nickel speciation in refinery enriched soils: A multi-technique investigation. Geochimica et Cosmochimica Acta 71:2190-2208.

Michel, F.M., L. Ehm, S.M. Antao, P.L. Lee, P.J. Chupas, G. Liu, D.R. Strongin, M.A.A. Schoonen, B.L. Phillips, and J.B. Parise. 2007. The structure of ferrihydrite, a nanocrystalline material. Science 316:1726-1729.

Mrozik, M.K. 2011. personal communication. The Pennsylvania State University.

Nachtegaal, M., M.A. Marcus, J.E. Sonke, J. Vangronsveld, K.J.T. Livi, D. Van der Lelie, and D.L. Sparks. 2005. Effects of in situ remediation on the speciation and bioavailability of zinc in a smelter contaminated soil. Geochimica et Cosmochimica Acta 69:4649-4664.

Nave, C.R. 2013. HyperPhysics [Online]. Available by Georgia State University http://hyperphysics.phy-astr.gsu.edu/hbase/solids/ferro.html.

Newman, S.P., H.C. Greenwell, P.V. Coveney, and J. W. 2001. Computer modelling of layered double hydroxides, p. 93–114, In V. Rives, ed. Layered Double Hydroxides.

Newville, M. 2001. IFEFFIT: interactive XAFS analysis and FEFF fitting. Journal of Synchrotron Radiation 8:322-324.

O'Day, P.A., G.E. Brown, Jr., and G.A. Parks. 1994. X-ray absorption spectroscopy of cobalt(II) multinuclear surface complexes and surface precipitates on kaolinite. Journal of Colloid and Interface Science 165:269-289.

Pandya, K.I., W.E. O'Grady, D.A. Corrigan, J. McBreen, and R.W. Hoffman. 1990. Extended X-ray absorption fine-structure investigations of nickel hydroxides. Journal of Physical Chemistry 94:21-26.

Peltier, E., R. Allada, A. Navrotsky, and D.L. Sparks. 2006. Nickel solubility and precipitation in soils: A thermodynamic study. Clays and Clay Minerals 54:153-164.

Perez-Ramirez, J., A. Ribera, F. Kapteijn, E. Coronado, and C.J. Gomez-Garcia. 2002. Magnetic properties of Co-Al, Ni-Al, and Mg-Al hydrotalcites and the oxides formed upon their thermal decomposition. Journal of Materials Chemistry 12:2370-2375.

Rappe, A.K., C.J. Casewit, K.S. Colwell, W.A. Goddard, and W.M. Skiff. 1992. UFF, a full periodic-table force-field for molecular mechanics and molecular-dynamics simulations. Journal of the American Chemical Society 114:10024-10035.

Reichle, W.T. 1986. Synthesis of anionic clay-minerals (mixed metal-hydroxides, hydrotalcite). Solid State Ionics 22:135-141.

Rives, V. 2001. Layered Double Hydroxides: Present and Future Nova Science Publishers, Inc., New York.

Rives, V., and S. Kannan. 2000. Layered double hydroxides with the hydrotalcite-type structure containing Cu^{2+}, Ni^{2+} and Al^{3+}. Journal of Materials Chemistry 10:489-495.

Roberts, D.R., A.C. Scheinost, and D.L. Sparks. 2002. Zinc speciation in a smelter-contaminated soil profile using bulk and microspectroscopic techniques. Environmental Science & Technology 36:1742-1750.

Rollmann, G., A. Rohrbach, P. Entel, and J. Hafner. 2004. First-principles calculation of the structure and magnetic phases of hematite. Physical Review B 69.

Scheidegger, A.M., M. Fendorf, and D.L. Sparks. 1996a. Mechanisms of nickel sorption on pyrophyllite: Macroscopic and microscopic approaches. Soil Science Society of America Journal 60:1763-1772.

Scheidegger, A.M., G.M. Lamble, and D.L. Sparks. 1996b. Investigation of nickel sorption on pyrophyllite: An XAFS study. Environmental Science & Technology 30:548-554.

Scheinost, A.C., and D.L. Sparks. 2000. Formation of layered single- and double-metal hydroxide precipitates at the mineral/water interface: A multiple-scattering XAFS analysis. Journal of Colloid and Interface Science 223:167-178.

Scheinost, A.C., R.G. Ford, and D.L. Sparks. 1999. The role of aluminum in the formation of secondary nickel precipitates on pyrophyllite, gibbsite, talc, and amorphous silica: A DRS study. Geochimica et Cosmochimica Acta 63:3193-3203.

Sideris, P.J., U.G. Nielsen, Z.H. Gan, and C.P. Grey. 2008. Mg/Al ordering in layered double hydroxides revealed by multinuclear NMR spectroscopy. Science 321:113-117.

Sparks, D.L. 2002. Environmental Soil Chemistry. 2nd. ed. Academic Press, San Diego.

Sposito, G. 1986. Distinguishing adsorption from surface precipitation, p. 217-229, In J. A. Davis and K. F. Hayes, eds. Geochemical processes at mineral surfaces, Vol. 323. American Chemical Society, Washington, DC.

Sposito, G. 1989. The Chemistry of Soils Oxford University Press, New York.

Taibi, M., S. Ammar, N. Jouini, F. Fievet, P. Molinie, and M. Drillon. 2002. Layered nickel hydroxide salts: synthesis, characterization and magnetic behavior in relation to the basal spacing. Journal of Materials Chemistry 12:3238-3244.

Yamaguchi, N.U., A.C. Scheinost, and D.L. Sparks. 2002. Influence of gibbsite surface area and citrate on Ni sorption mechanisms at pH 7.5. Clays and Clay Minerals 50:784-790.

Taylor, R.M. 1984. The rapid formation of crystalline double hydroxy salts and other compounds by controlled hydrolysis. Clay Minerals 19:591-603.

Zelmy, A.R., D.C. Girvin, and E.A. Jenne. 1984. MINTEQ. A computer program for calculating aqueous geochemical equilibrium NTIS PB 84-157148. (EPA-600/3-84-032). Nat. Tech. Inf. Ser., Springfield, VA.

Chapter 4

HYPERACCUMULATION OF NICKEL BY *ALYSSUM CORSICUM* IS RELATED TO SOLUBILITY OF NI MINERAL SPECIES
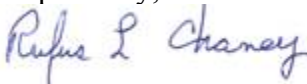
Tiziana Centofanti, Matthew G. Siebecker, Rufus L. Chaney,
Allen P. Davis & Donald L. Sparks

To Whom It May Concern:

The publication "Centofanti, T., M.G. Siebecker, R.L. Chaney, A.P. Davis and D.L. Sparks. 2012. Hyperaccumulation of nickel by *Alyssum* species is related to solubility of Ni mineral species. Plant Soil 359:71-83." was jointly planned and conducted by T. Centofanti and M.G. Siebecker. They should both be considered First Authors of this paper which required both of their creative contributions in order to conduct, interpret and report.

 Respectfully,

Rufus L. Chaney
Senior Research Agronomist
USDA-ARS-EMBUL
Beltsville, MD

Abstract

Aims: Past studies have demonstrated that hyperaccumulators absorb Ni from the same labile pools in soil as normal plant species. This study investigated whether the Ni hyperaccumulator plant *Alyssum corsicum* possesses distinct extraction mechanisms for different Ni species present in soils. Different Ni species have different solubilities and potential bioavailabilities to roots.

Methods: Uptake of Ni in shoots of *A. corsicum* was analyzed after four weeks of plant growth in nutrient solution with 17 different Ni compounds or soils.

Results: The results indicate that Ni uptake is related to Ni solubility and plant transpiration rate. The most soluble compounds had the highest Ni uptake, with the exception of $Ni_3(PO_4)_2$, Ni phyllosilicate, Ni-acid birnessite which showed a low solubility but a relatively high plant uptake and transpiration rate. In serpentine soils and insoluble NiO plant transpiration rate was high but uptake was very low and statistically comparable to the control.

Conclusions: It appears that Ni uptake is driven by convection, which depends on the initial concentration of Ni in solution and the plant transpiration rate.

Introduction

Several species of the genus *Alyssum* are capable of hyperaccumulating up to 30 g kg^{-1} Ni in their dry leaves when grown on serpentine soils (Reeves et al. 1983). Ni hyperaccumulating (Ni>1000 $\mu g\ g^{-1}$ DW) *Alyssum* species are endemic to serpentine soils. Ni hyperaccumulators can be used in phytomining, which is an economically

profitable method to produce Ni ore from the ash of the above-ground biomass (Chaney et al. 2007).

It has been shown that hyperaccumulators absorb metals from the same labile pools in soils as normal plant species (Hammer et al. 2006; Massoura et al. 2004; Shallari et al. 2001). However, Ni hyperaccumulators are able to accumulate 100 times more Ni in their shoots than normal crops. Despite recent advancements in understanding the physiological mechanisms of Ni uptake and translocation to shoots (Milner and Kochian 2008), several key hyperaccumulation mechanisms have still not been described.

Nolan et al. (2009) studied 13 urban soils contaminated with Ni smelter-waste from Australia and Canada. The isotopic exchangeability of Ni in these soils (E value), which is the labile Ni pool, ranged from 0.9– 32.4%(0.0009 to 60 mg kg^{-1}) of total Ni. Similarly, Bani et al. (2007) showed that the labile Ni pool in ultramafic soils from Albania which contains 3440 mg kg^{-1} was 119 mg kg^{-1} for the Ni exchangeable within 24 h and 3 months, and the water soluble Ni was only 0.25 mg L^{-1}. Similar low solubility of Ni in serpentine soils was reported by Kukier et al. (2004). Because the labile fraction of Ni is orders of magnitude lower than the total amount of Ni in the above-ground biomass in *Alyssum* species (10–30 g Ni kg dry biomass^{-1}), there must be other mechanisms that account for the high Ni uptake in hyperaccumulators.

Root-induced plant responses such as rhizosphere acidification and the release of organic acids that act as chelating agents have been suggested as mechanisms that increase Ni solubility in soil. Several authors (Bernal et al. 1994; McGrath et al. 1997; Zhao et al. 2001) have studied the modification of the rhizosphere soil by

hyperaccumulator plants and results indicate that the metal solubilization mechanism of hyperaccumulators does not involve rhizosphere acidification. Further, there is little evidence that hyperaccumulator plants secrete organic or amino acids which might increase Ni solubilization or uptake (Puschenreiter et al. 2003; Wenzel et al. 2003).

One other mechanism that has been suggested to cause the high metal acquisition by hyperaccumulator plants is the preferential root proliferation into soil patches containing elevated concentrations of the target metal. It is known that the spatial distribution of heavy metals in naturally or anthropogenically contaminated soils is heterogeneous. Roots of the Zn hyperaccumulator *Thlaspi caerulescens*, for example, preferentially grow toward substrate patches with elevated Zn concentrations (Schwartz et al. 1999; Whiting et al. 2000). However, Moradi et al. (2009) obtained the opposite results for Ni hyperaccumulator *Berkheya coddii*. They used a non-destructive method based on neutron radiography to observe root distribution inside a rhizobox filled with control soil and homogeneously or heterogeneously spiked soil with Ni. They demonstrated that roots of *Berkheya coddii*, in comparison to roots of the non-Ni-hyperaccumulator *Cicer arietinum* L., do not forage towards the Ni rich patches. Results of those studies are contradictory and more experiments are needed to better understand the mechanism.

Although hyperaccumulators deplete bioavailable pools of metals to extents where they change the chemical equilibria of that metal in the soil, no mechanism is yet known where plants attack the non-labile pool of Ni. Renewal of the labile pool from the nonlabile pool during equilibration over time is an indirect mechanism by which

hyperaccumulators deplete nonlabile pools of metal in soil. In this study we hypothesize that availability of Ni to roots of *Alyssum* hyperaccumulator plants may depend on the species of Ni in the soil.

Phytoavailability of individual Ni phases is unknown; some phases may be more phytoavailable than others. For example, Li et al. (2003) performed a hyperaccumulation study on soils surrounding a nickel refinery in Port Colborne, Ontario, Canada. These soils contained elevated concentrations of Ni and the authors were able to hyperaccumulate Ni from these soils using the Ni hyperaccumulators *A. corsicum* and *A. murale*. McNear et al. (2007) conducted a study on the same soils (Welland loam and Quarry muck) as in Li et al. (2003) to determine the effect of soil type and liming on the speciation of Ni. Their results showed that NiO was a common Ni species in both soils; this crystalline solid was likely emitted by the smelter and persisted in soils because of its low solubility and slow kinetics of dissolution (Fellet et al. 2009). Ni-fulvic acid dominated the speciation in the Quarry muck soils. In the loam soils, Ni/Al layered double hydroxides (LDH) were prevalent in both the limed and unlimed, and Ni phyllosilicates in the limed soil.

In this study we investigated which of the Ni species mentioned above are effectively available to *A. corsicum* roots. We tested whether *A. corsicum* grown in hydroponics can access Ni from 17 different Ni compounds and soils that are relatively insoluble at pH 7. Each compound was added separately to *A. corsicum* grown in nutrient solution under controlled conditions in a growth chamber. The solubility of each Ni species without plants was also tested for the same duration of the plant growth

experiment. The experimental methodology followed that used by Fellet et al. (2009) to test phytoavailability of NiO to *Alyssum* species.

Materials and Methods

Ni Uptake Experiment

Plant Material

Seeds of *A. corsicum* were collected from Turkey (Koycegiz) in 1998 and allowed to germinate on plastic seed plug flats filled with vermiculite. They were watered daily with deionized water until germination. Thereafter, the plants were watered with a 1:10 mixture of macronutrient solution (described below) and deionized water. Four weeks old seedlings were selected for homogenous and healthy growth then transplanted into 1250 mL beakers (3 plants per beaker) in a growth chamber and grown under controlled conditions (temperature: 24d/20n°C; relative humidity: 70d/50n%; PAR: 300 μmol m−2 s^{-1}, 16 h day^{-1}). The beakers contained 1250 mL of nutrient solution, and plants were grown for 12 days without Ni compounds to let the root systems recover from the transplanting process. Seventeen different forms of Ni were added to treatment beakers on day 12 at 73.36 mg of total Ni per beaker except for Ni sorbed to humic acid (12.81 mg), Ni/Al LDH with CO_3^{2-} interlayer (95.7 mg), α-$Ni(OH)_2$ (58 mg), β-$Ni(OH)_2$ (63.41 mg). Sufficient mixing in the jar was provided by continuous aeration. Each treatment was carried out in triplicate.

Because *A. corsicum* is a serpentine endemic species, the nutrient solution simulated the conditions of a typical serpentine soil solution for the macronutrients

(Brooks 1987). The Mg in the solutions was high (supplied as 2 mM MgSO$_4$) and Ca was low (1 mM Ca) compared with normal Hoagland solution (1 mM Mg and 4 mM Ca). The calcium and nitrogen sources were Ca(NO$_3$)$_2$ (1.0 mM) and KNO$_3$ (2.5 mM). K$_2$HPO$_4$ and KCl were supplied at 0.1 mM. In order to stabilize solution pH, the nutrient solution included 2 mM HEPES. Solution pH was set at 7.0±0.2 and was adjusted daily by KOH or HCl additions. The micronutrients were supplied at: 2.0 μM MnCl$_2$; 0.5 μM CuSO$_4$; 1.0 μM ZnSO$_4$; 0.2 μM CoSO$_4$; 15 μM H$_3$BO$_3$; 0.2 μM NaMoO$_4$; and 20 μM FeHBED chelate. The microelement cations were not chelator buffered but Fe was supplied as the stable chelate FeHBED; Ni dissolved in a nutrient solution cannot displace Fe from FeHBED (Parker et al. 1995).

Solution level was maintained by daily addition of DI water. Plants were harvested after 4 weeks of growth with Ni compounds. Roots of intact plants were inserted and kept in desorption solution (10 mM CaNO3) for 30 min at 4°C before separating roots from shoots. After harvest, three aliquots of nutrient solution from each beaker were sampled and filtered (0.2 μm) and analyzed for Ni and other nutrients (Ni in solution after plant harvest).

Soil Compounds and Minerals Used to Spike Hydroponic Nutrient Solution

Table 4.1 lists the compounds used in the experiment. The soils in this experiment were air dried and sieved to <2 mm. 18.2 megohm deionized water was always used. Seventeen Ni compounds that are relatively insoluble at pH 7 and occur in natural and anthropogenic contaminated soil (Li et al. 2003; McNear et al. 2007) were used in this

experiment, the names of some compounds have been abbreviated as follows: $Ni_3(PO_4)_2$ for $Ni_3(PO_4)_2 \cdot 11.8\ H_2O$; Ni - humate for Ni sorbed to humic acid; Ni-goethite for Ni sorbed to goethite; Ni-acid birnessite for Ni sorbed to acid birnessite; Ni/Al LDH, carbonate for Ni/Al LDH with CO_3^{2-} interlayer; Ni/Al LDH, nitrate for Ni/Al LDH with NO_3^- interlayer; Ni/Al LDH, silicate for Ni/Al LDH with $SiO_2(OH)_2^{2-}$ interlayer. Detailed information on the separation of the Ni species is provided in supplemental information.

Ni Solubility Experiment

Ni solubility in the serpentine nutrient solution was measured for each test material for the same duration of the plant uptake experiment. 73.36 mg Ni of each Ni compound except for Ni sorbed to humic acid (12.81 mg), Ni/Al LDH with CO3 2-interlayer (95.7 mg), α-Ni(OH)$_2$ (58.0 mg), β-Ni(OH)$_2$ (63.4 mg) was added to a 1250 mL beaker containing aerated serpentine-Hoagland nutrient solution and treated under the same conditions as the beaker containing plants. Three replications per Ni compound were used. Solution pH was set at 7±0.2. Water level and pH were adjusted daily. Solution was sampled and filtered (0.2 μm) at 24 h after addition of compounds and then every 7 days for 4 weeks.

Samples Analysis

Root and shoot tissues were oven dried at 70°C for 24 h, weighed and ashed at 480°C for 16 h, and then digested with concentrated HNO3. Once dry, the samples were dissolved in 10 mL of 3 M HCl, filtered (Whatman #40 filter paper) and diluted to 25 mL

with 0.1 M HCl in volumetric flasks. The Ni concentrations were determined using

atomic absorption spectrophotometry with deuterium background correction, and other

elements were determined by inductively coupled plasma atomic emission spectrometry

(ICP). Ni detection limit was 0.005 mg L^{-1}. An internal standard (Y) was used to improve

ICP analysis reliability, and standard reference materials and blanks were analyzed for

quality assurance.

Table 4.1   List of the seventeen Ni species used in the hydroponics uptake experiment,
along with the description and reference for the synthesis method or
manufacturer of the Ni compound. Detailed information on the preparation
methods is provided in the supplementary data.

	Abbreviated name	Amount added per jar (g)	Reference or Manufacturer	Additional Details
1	$NiSO_4$	0.09	Purchased from Acros	See supplementary data
2	α-$Ni(OH)_2$	0.12	(Genin et al. 1991)	Fresh alpha-$Ni(OH)_2$ was aged to beta-$Ni(OH)_2$
3	β-$Ni(OH)_2$	0.12	(Scheinost and Sparks 2000)	
4	$NiCO_3$	0.15	Purchased from Acros	
5	$Ni_3(PO_4)_2$	0.16	Purchased from Alfa Aesar	
6	Ni phyllosilicate	1.44	(Decarreau et al. 1987; Peltier et al. 2006)	See supplementary data
7	Ni - humate	8.89	Purchased from Sigma Aldrich	Washed similarly to Zhou et al. 2005
8	Ni - goethite	74.97	(Schwertmann and Cornell 2000)	Ni was sorbed to goethite at pH 7 in nutrient solution batch, then washed seven times with pH 7 nutrient solution via centrifugation and freeze dried
9	Ni - acid birnessite	12.99	(Feng et al. 2007; McKenzie 1971)	Ni was sorbed to acid birnessite at pH 7 in serpentine nutrient solution, then washed five times with pH7 nutrient solution and freeze dried
10	Ni/Al LDH, carbonate	1.49	(Taylor 1984)	See supplementary data
11	Ni/Al LDH, silicate	1.31	(Depege et al. 1996; Ford et al. 1999)	See supplementary data
12	Ni/Al LDH, nitrate	1.06	Taylor 1984	See supplementary data
13	Garnierite	24.11	Goiás, Brazil (Table 3)	Washed five times with serpentine nutrient solution and freeze dried
14	Limonite	56.84	Goiás, Brazil (Table 3)	Washed five times with serpentine nutrient solution and freeze dried
15	Serpentine soil 18	13.43	Southwest Oregon (Table 3)	Washed five times with serpentine nutrient solution and freeze dried
16	Serpentine soil 20	9.77	Southwest Oregon (Table 3)	Washed five times with serpentine nutrient solution and freeze dried
17	NiO	0.09	Purchased from Johnson Matthey	

Statistical Analysis

Data were analyzed using SAS PC version 6.0 (SAS Institute 1989). Data required log transformation to attain homogeneity; geometric means and standard errors are shown in the tables and figures. The PROC MIXED procedure was utilized for analysis of variance of plant yield and tissue metal concentration for differences of treatments. Significance was set at the 5% level.

Results

Yield and Uptake-Translocation to Shoots

The dry biomass of shoots at harvest ranged from 2.64 to 0.64 g. Differences among treatment compounds were not statistically significant (Table 4.2) except for garnierite and limonite soils which caused reduced plant growth. $NiSO_4$ caused Ni toxicity symptoms but no significant reduced growth (Fig. 4.3, supplementary data). Plants grown in solution with the garnierite and limonite soils manifested reduced shoots yield (Fig. 4.3, supplementary data) and in the garnierite soil the root system showed reduced growth (30% reduction relative to the other treatments, Table 4.2) possibly due to Cr toxicity (Table 4.3).

Yellowing and browning of some older leaves was observed for several treatments: α-$Ni(OH)_2$, β-$Ni(OH)_2$, Ni-goethite, and $NiCO_3$ (Fig. 4.3, supplementary data). However, the toxicity symptoms were not consistent among replicates, which may be due to higher variability amongst *A. corsicum* seeds collected from wild plants in the field.

At harvest both macro- and micro-nutrient levels were adequate for normal plant growth. Ni concentration in shoots was significantly different among treatments. No significant correlation between Ni concentration in shoots and shoot dry matter was observed, with some treatments having high shoot dry matter but low Ni concentration. Strong hyperaccumulation (>10 g kg^{-1} dry weight) was observed in decreasing order as follows: NiSO4$>\alpha$-Ni(OH)2$>$ Ni3(PO4)2$>$Ni phyllosilicate$>$Ni-goethite$>$NiCO3. Accumulation of Ni by plants grown in solution with β-Ni(OH)$_2$ was around 8000 mg kg^{-1} (Table 4.2).

Uptake of Ni was comparatively low (<5000 mg kg^{-1}) when plants were grown in solution with Ni-acid birnessite, Ni/Al LDH nitrate, carbonate, and silicate, the garnierite soil and the two serpentine soils. The lowest Ni uptake, similar to the control with 0 Ni, was observed for NiO and limonite. The results indicate that Ni uptake is related to the Ni solubility (Fig. 4.1) with the exception of Ni3(PO4)2, Ni-phyllosilicate and Ni-birnessite, which had low solubility yet relatively high uptake. The highest Ni uptake occurred when plants grew in solution with the most soluble Ni compounds.

Ni Solubility

As expected, the soluble salt NiSO4 had the highest solubility among all the Ni compounds. Solubility of the other compounds was in decreasing order as follows: NiCO3$>\alpha$-Ni(OH)2$>\beta$-Ni(OH)2$>$Ni-goethite$>$ Ni-humic acid$>$Ni-phyllosilicate$>$Ni3(PO4)2$>$Ni/Al LDH nitrate and carbonate$>$garnierite$>$Ni-birnessite $>$serpentine soil (S18)$>$Ni/Al LDH silicate$>$serpentine soil (S20)$>$Control$>$limonite

(Table 4.4 and Fig. 4.2a, b, c). The variation in solubility with time of many of the

compounds was not statistically significant (Fig. 4. 2a, b, c); only the increase in Ni

solubility from Ni-phyllosilicate was statistically significant.

Table 4.2   Mean and standard error (SE) of Ni uptake and dry weight of shoots and roots of *Alyssum corsicum*. The results of the statistical analysis are indicated, similar letters indicate no significant difference between mean values (p<0.05).

Treatment	Ni in shoots mg kg^{-1}	SE		Dry weight shoot g	SE		Dry weight root (g)	SE	
NiSO$_4$	23557	3496	a	1.51	0.11	a	0.51	0.02	a
α-Ni(OH)$_2$	17072	3288	ab	2.64	0.72	a	0.72	0.18	a
β-Ni(OH)$_2$	7856	1184	c	1.77	0.23	a	0.62	0.13	a
NiCO$_3$	10968	3989	ab	2.06	0.61	a	0.53	0.22	a
Ni$_3$(PO$_4$)$_2$	15101	641	ab	2.23	0.62	a	0.95	0.20	a
Ni phyllosilicate	11237	706	ab	2.54	0.07	a	0.94	0.04	a
Ni - humate	4142	170	cd	2.50	0.26	a	0.88	0.30	a
Ni - goethite	11161	1215	ab	1.32	0.11	a	0.79	0.08	a
Ni - acid birnessite	5195	298	cd	2.63	0.19	a	1.11	0.07	a
Ni/Al LDH, carbonate	3939	40	cd	2.64	0.18	a	1.20	0.15	a
Ni/Al LDH, silicate	234	74	f	2.31	0.18	a	0.80	0.13	a
Ni/Al LDH, nitrate	5112	424	cd	2.85	0.15	a	1.07	0.17	a
Garnierite	1147	258	e	0.85	0.08	b	0.32	0.12	b
Limonite	94	19	g	0.64	0.08	b	0.87	0.24	a
Serpentine soil (S18)	574	198	f	1.88	0.35	a	2.53	1.00	a
Serpentine soil (S20)	470	231	f	2.69	0.77	a	2.13	0.62	a
NiO	20	1.2	h	2.38	0.54	a	0.79	0.10	a
Control (0 Ni)	21	3.3	h	2.60	0.25	a	0.68	0.08	a

Table 4.3   Chemical composition of the two soils (Garnierite and Limonite) from the ultramafic sites of Goiás, Brazil (further details in Reeves et al. 2007) and the serpentine soils S18 and S20 from Southwest Oregon.

	pH	Organic Matter %	Ca g kg^{-1}	K	Mg	Fe	Cr	Cu	Co	Mn	Ni	Zn
Garnierite	6.6	4.5	3.1	0.1	19.3	180.7	11.3	4	0.7	2.8	18.5	0.1
Limonite	6.6	2.4	0.6	0.1	11.5	583.7	46.8	1.1	0.4	6.6	7.7	0.8
S20	6.9	3.6	0.4	0.3	13.8	138.6	1.6	0.1	0.2	3.1	5.9	1.4
S18	6.2	5.2	1.2	0.3	13.2	193	3.1	0.1	0.3	3.1	4.6	0.2

Desorption of Ni from roots was 3.9, 3.6, and 3.6 mg L^{-1} for Ni$_3$(PO$_4$)$_2$, NiSO$_4$, NiCO$_3$, respectively; it represented 2 mg L^{-1} for Ni-goethite and Ni-phyllosilicate, it was only 1 mg L^{-1} for α-Ni(OH)$_2$, Ni/Al LDH nitrate, and the Ni-birnessite, for the other compounds it was below 1 mg L^{-1}. The Ni desorption from roots grown in NiO and control was below detection limit (0.005 mg L^{-1}), and for limonite soil it was insignificant (0.01 mg L^{-1}).

The total amount of Ni in solution after harvest was highest for the NiCO$_3$ and NiSO4 (24 and 7 mg Ni, respectively) representing 26 and 19% of applied Ni (Table 4.5). Other compounds showed a lower amount (4–8 mg Ni) representing 7 to 2% of the applied Ni in the following order: α-Ni(OH)$_2$>Ni-goethite>β-Ni (OH)$_2$>Ni3(PO4)$_2$ >garnierite (Table 4.5). The total amount of Ni in solution after harvest for Ni phyllosilicate and Ni-acid birnessite was very low (0.4 and 0.2 mg Ni, respectively) representing only 0.5 and 0.3% of applied Ni. Negligible amount or no Ni was present in solution after harvest for the other Ni compounds (Table 4.5).

Ni Mass Analysis

Total Ni mass was calculated as the sum of: Ni concentration in solution after harvest, total Ni in shoot and in root (Table 4.5). The Ni compound solid residues present in the beakers at the end of the experiment were not collected; hence full recovery of Ni could not be calculated.

Because $NiSO_4$ was the most soluble compound the Ni was fully recovered in the shoots, roots and nutrient solution after plant harvest. The lower value of mass balance (61.5 mg of $NiSO_4$, which is the sum of Ni in shoot (mg), Ni in root (mg) and the soluble Ni measured in the nutrient solution after plant harvest (Table 4.5), compared with the soluble Ni in nutrient solution measured at the end of the experiment (28 days) is probably due to the loss and breakage of finer roots and of some senescenced leaves which fell off during the experiment and were not collected at harvest. The amount of Ni in solution after harvest and in the whole plant was about 68% of applied Ni for $Ni_3(PO_4)_2$, α-$Ni(OH)_2$, $NiCO_3$, Ni - phyllosilicate, and Ni-acid birnessite. It should be noted that the values of root Ni concentrations (Table 4.5) are not representative of the Ni uptake into the root because root epidermis was coated with Ni compounds sorbed onto the root surface. Washing off the root epidermis of the soil and mineral particles would have required considerable destruction and breakage of the roots. Desorption with $CaCO_3$ was carried out to desorb the exchangeable Ni present on the root epidermis, in our case most of the roots where coated with minerals and would have needed to be manually washed to detach the minerals from the epidermis.
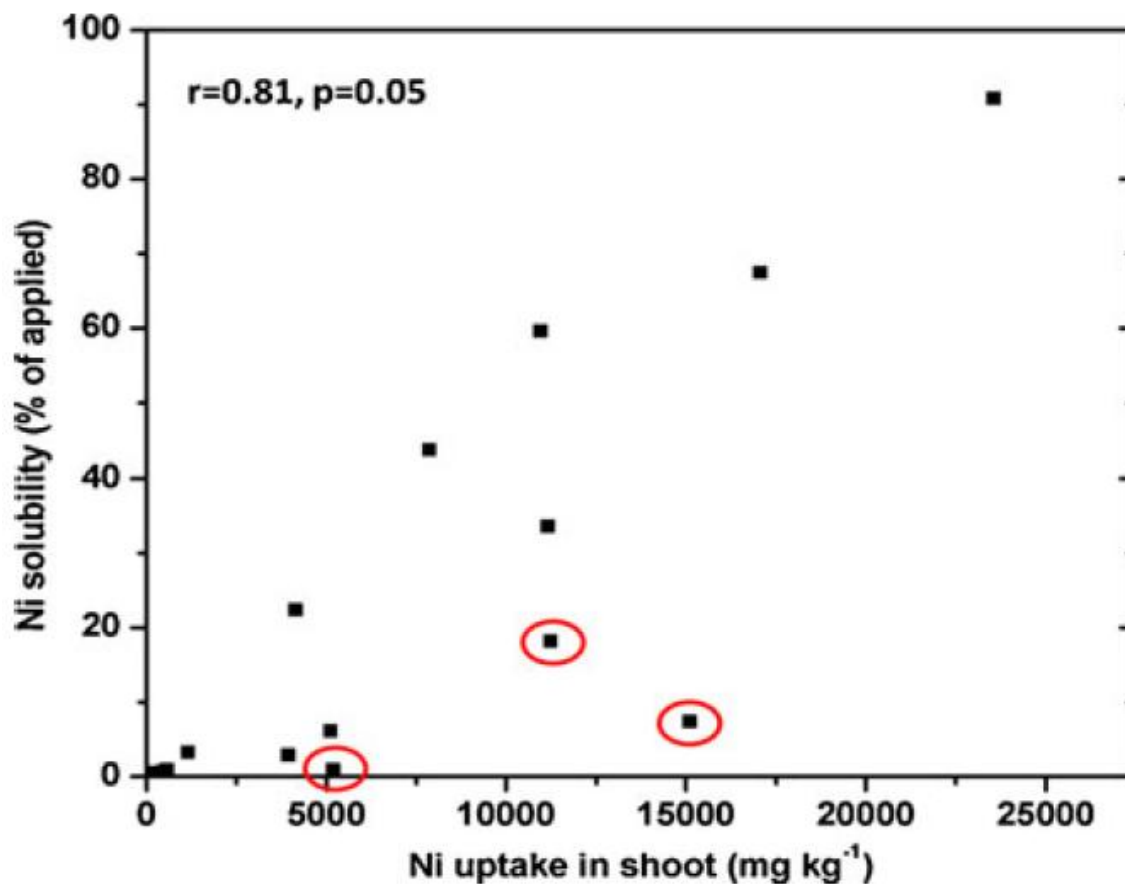
Figure 4.1   Ni uptake in shoot versus Ni solubility expressed as % of applied Ni (1 mM L^{-1}) to nutrient solution. The circles points refer to Ni-acid birnessite, Ni phyllosilicate, and $Ni_3(PO_4)_2$ (from left to right). The Pearson correlation coefficient (r) is reported on the left hand corner. In the Ni uptake experiment plants were grown for 28 days in serpentine-Hoagland solution with the addition of seventeen Ni species. Solubility of each Ni species was measured in a test with the same nutrient solution and for the same duration as for the uptake experiment. Values of Ni solubility reported here refer to the last sampling at 28 days after addition of the Ni species to the solution.

Table 4.4   Solubility of Ni in the nutrient solution without plants. Values of Ni solubility in each treatment are expressed as % of the applied Ni to each beaker (1 mM L^{-1}). Ni solubility has been measured at 5 different times after addition to Ni into solution.

	Ni solubility (% of applied Ni)				
	1 d	7 d	14 d	21 d	28 d
NiSO$_4$	100.00	96.13	92.40	90.66	90.80
α-Ni(OH)$_2$	42.17	75.57	67.48	70.57	67.49
β-Ni(OH)$_2$	28.29	43.29	45.79	48.26	43.63
NiCO$_3$	32.43	61.55	67.28	66.98	59.60
Ni$_3$(PO$_4$)$_2$	5.45	5.31	7.13	7.70	7.37
Ni phyllosilicate	3.98	7.83	13.98	20.33	18.18
Ni - humate	22.12	24.62	22.16	23.69	22.34
Ni - goethite	33.42	33.24	32.70	34.49	33.68
Ni - acid birnessite	0.50	0.68	0.71	0.85	0.92
Ni/Al LDH, carbonate	2.74	2.26	2.54	2.93	2.85
Ni/Al LDH, silicate	0.30	0.20	0.50	0.50	0.60
Ni/Al LDH, nitrate	4.49	5.11	5.41	6.11	6.14
Garnierite	4.05	3.62	3.70	3.50	3.30
Limonite	0.04	0.02	0.01	0.01	0.03
Serpentine soil (S18)	0.30	0.30	0.39	1.05	0.86
Serpentine soil (S20)	0.12	0.16	0.19	0.60	0.71
NiO	0.01	0.02	0.04	0.05	0.06
Control (0 Ni)	0.00	0.02	0.03	0.03	0.04

Discussion

The hydroponic Ni uptake study indicates that *A. corsicum* cannot access Ni from species that are insoluble at pH 7. These results agree with previous studies on Ni accessibility by *A. murale* (Massoura et al. 2004; Shallari et al. 2001), which showed that plants remove Ni exclusively from the exchangeable or labile pool in soil, and accumulation of Ni by *A. murale* is not due to the solubilization of non-labile forms of Ni in soils. Similarly, Hammer et al. (2006) showed that hyperaccumulation of Zn by *T. caerulescens* cannot be explained by the access to non-labile solid-phase pools of metals. Published data for the log of solubility constants (log K$_{sp}$) for several Ni minerals are: NiCO$_3$ (−6.78 to −11.2); amorphous α-Ni(OH)$_2$ (−15.11 or log Ksp 12.89, where Ksp

employs the hydrogen ion concentration versus the hydroxide ion concentration in the solubility product); β-Ni(OH)$_2$ (-17.2 to 17.3 or log Ksp 10.7 to 10.8); Ni$_3$(PO$_4$)$_2$ (-31.3); and a nickel phyllosilicate [Ni$_3$Si$_4$O$_{10}$(OH)$_2$] (-80.1) (Arai 2008; Peltier et al. 2006; Smith et al 2003). If dissolution of Ni and hence Ni uptake by the plant are directly related, Ni uptake should be in the order of NiCO$_3$>α- Ni(OH)$_2$>β-Ni(OH)$_2$ >>Ni$_3$(PO$_4$)$_2$>nickel phyllosilicate. However, we found that the order of Ni uptake by *A. corsicum* was α-Ni(OH)$_2$>Ni$_3$(PO$_4$)$_2$>nickel phyllosilicate> NiCO3>β-Ni(OH)$_2$. The difference in the order of uptake with respect to solubility, specifically Ni$_3$(PO$_4$)$_2$ and nickel phyllosilicate which are 16 and 65 folds less soluble than α-Ni(OH)$_2$, demonstrates that the plant plays a role in altering the uptake of aqueous Ni^{2+}.

The Ni compounds used in this experiment possessed inherent differences in that Ni was sorbed to several minerals whereas it was incorporated into the mineral/lattice structure in others. When one tries to apply aquatic speciation calculations for the Ni-rich minerals in an attempt to predict Ni solubility and consequently uptake into the plant, the results are inaccurate for several reasons. Firstly, the nutrient solutions containing the solid phase Ni compounds were constantly aerated; hence carbon dioxide was constantly being dissolved into the solution. This may have decreased the dissolution of NiCO3 due to the common ion effect of CO3 2-. Secondly, the nutrient solution contains pH buffer and may contain chelators secreted from roots for which the speciation analysis cannot account. Thirdly, many of the LDHs do not have published solubility product constants for the same Ni/Al ratios. Peltier et al. (2006) published solubility constants for LDHs with nitrate and carbonate interlayers along with a Ni-phyllosilicate and nickel hydroxide

similar to the ones used in this study. The amount of Al substitution for those calculations was 0.33 whereas Al substitution was 0.13–0.15 for the LDHs used in this study. Regardless, LDH with nitrate is predicted to be more soluble than LDH with carbonate interlayer, which was observed in our study. Thermodynamic data from Peltier et al. (2006) indicate that the order of stability of the LDH phases varies with interlayer anions, with silicate > carbonate > nitrate, from most to least stable. This result was followed in our dissolution experiment with LDH silicate interlayer being the least soluble and LDH nitrate interlayer being the most soluble and phytoavailable.

Uptake of Ni from α-Ni(OH)$_2$, Ni-goethite, NiCO$_3$, and β-Ni(OH)$_2$ was highest and corresponded to comparatively high Ni solubility. Ni desorption from goethite was expected to be high because the high PZC of goethite causes the mineral to have a positive surface at pH 7.5. High Ni uptake from Ni$_3$(PO$_4$)$_2$, which has comparably low solubility, may be due to phosphate depletion in solution. P levels of plants grown in solution with Ni$_3$(PO$_4$)$_2$ were slightly higher than in the other treatments, and the P uptake by the roots may have caused more P dissolution, and consequently Ni dissolution, from the mineral phase. The hypothesis of an experimental artifact that higher P uptake may have caused high Ni uptake is unlikely as demonstrated by Shallari et al. (2001) and Li et al. (2003) who studied the effect of P on Ni uptake by *A. murale* and showed no effect of increased P fertilization on Ni uptake. It is likely, however, that because P is a macronutrient for plants, as P in solution decreases, P from nickel phosphate dissolves into solution. The concentration of Ni will consequently also increase as P dissolves. The Ni in solution is then easily accumulated by *A. corsicum*.
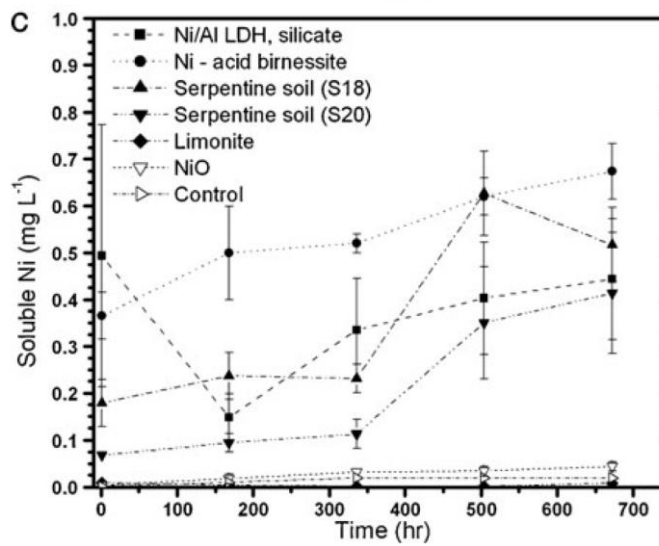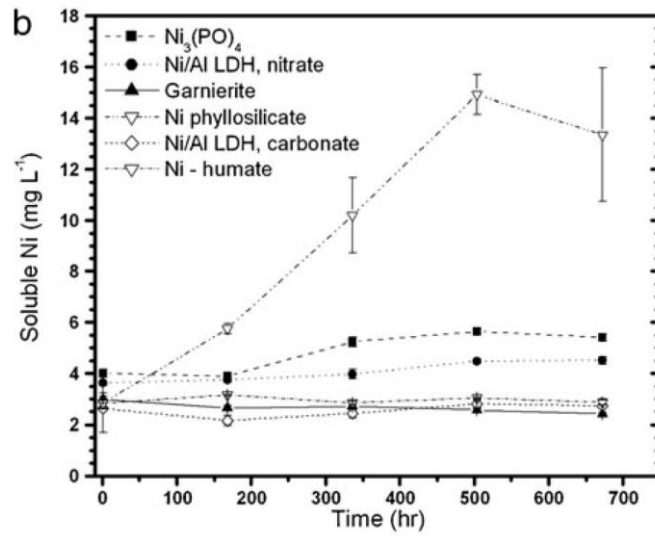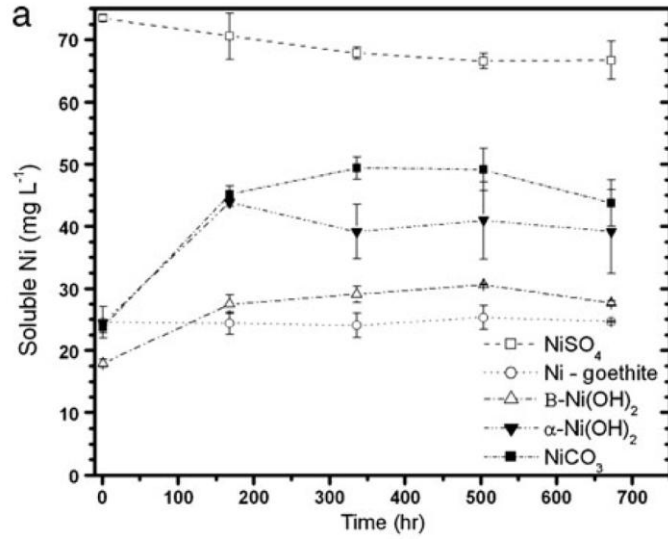
Figure 4.2   Solubility of Ni measured at different time after addition of Ni species in the beakers without plants (as in Figure a, b, and c) to the serpentine-Hoagland solution. Error bars indicate standard errors.

Table 4.5   Mass balance of Ni as the sum of Ni in shoot (mg), Ni in root (mg) and the soluble Ni measured in the nutrient solution after plant harvest. The mass balance of Ni is compared with the soluble Ni in nutrient solution measured at the end of the experiment (28 days) as reported in the second column.

Nickel Compound	Soluble Ni after 28 days in beakers without plants mg	Ni in solution after plant harvest mg	Ni in shoot mg	Ni in root mg	Total Ni mass balance at harvest mg
$NiSO_4$	66.7	17.4	35.5	8.6	61.5
α-$Ni(OH)_2$	39.2	7.1	45.0	3.8	55.9
β-$Ni(OH)_2$	27.7	4.9	13.9	11.8	30.6
$NiCO_3$	43.7	24.1	22.6	4.0	50.7
$Ni_3(PO_4)_2$	5.4	3.8	33.6	25.9	63.3
Ni phyllosilicate	13.3	0.4	28.5	13.4	42.3
Ni - humate	2.8	0.1	10.3	0.5	10.9
Ni - goethite	33.6	7.9	14.7	0.0	22.6
Ni - acid birnessite	0.7	0.2	13.6	6.0	19.8
Ni/Al LDH, carbonate	2.7	0.07	10.4	11.5	22.0
Ni/Al LDH, silicate	0.4	0.04	0.5	7.6	8.1
Ni/Al LDH, nitrate	4.5	0.05	14.6	14.5	29.1
Garnierite	2.4	2.1	1.0	0.3	3.4
Limonite	0.0	0.0	0.1	0.9	1.0
Serpentine soil (S18)	0.5	0.2	1.1	2.8	4.1
Serpentine soil (S20)	0.4	0.2	1.3	2.8	4.3
NiO	0.0	0.0	0.0	6.0	6.0
Control (0 Ni)	0.0	0.0	0.1	0.0	0.1

The concentration of aqueous Ni from Ni phyllosilicate increased with time and reached about 18% of the total applied Ni, much more than anticipated based off of previous solubility data (Peltier et al 2006). This may be due to the high desorption of Ni from the mineral's amorphous structure. Similarly, aqueous Ni from Ni-acid birnessite is very low but uptake is high (5000 mg kg^{-1}). When the fraction of Ni taken up by the plant is subtracted from the fraction of soluble Ni (Table 4.6), then several compounds are found to have higher uptake rates than should be indicated from their solubility. The plants grown in solution with compounds that have higher uptake rate than their solubility, showed a higher transpiration rate (calculated on a standard 200 ml g^{-1} dry matter, Table 4.6). Plants grown in solution with $Ni_3(PO_4)_2$, Ni phyllosilicate, Ni humate,

and Ni-acid birnessite, all show high transpiration rate and greater Ni uptake than should be possible considering the mineral's solubility.

The plants grown in solution with compounds with constantly low solubility ranging from 1 to 5% of applied Ni, such as the serpentine soils and NiO, showed low uptake of Ni by *A. corsicum* but relatively high transpiration rate (Table 4.6). Our results agree with Kukier et al. (2004), who measured the concentration of Ni in four consecutive water saturation extracts of Quarry, Welland, and Brockman soils which contained Ni/Al LDH, NiO, Ni bound to organic matter and Fe oxides (McNear et al. 2007). Their results indicated that the water soluble Ni at the neutral pH of these soils is low, seemingly too low to allow for hyperaccumulation. However, Li et al. (2003) were able to hyperaccumulate Ni from these soils using *Alyssum* plants, illustrating the importance of soil rhizosphere processes that occur when plants are grown in soils.

The two most important functional groups in humic acids are the carboxyl and phenol groups. The pK_a values of the carboxyl and phenol groups are approximately 3 and 9, respectively. Therefore, at pH 7, essentially all of the carboxyl groups will be deprotonated, and complexed with cations from solution (e.g., Ni). Chelation is predicted to take place at pH values above 4–5, and strength will increase gradually with pH (Tan 2003). It is expected that at neutral pH Ni desorption from humic acid is relatively low, as it was reported in this experiment. However, the amount of total Ni added to the beaker was significantly lower for Ni-humate than for the other compounds and plants showed high transpiration rate and greater Ni uptake than should be possible considering the mineral's solubility.

Table 4.6   Transpiration rate and the difference in % of total Ni taken up into the shoot from % soluble Ni at the end of the experiment. A negative number in column three (difference = soluble Ni – Ni taken up in shoot) indicates that Ni was taken up to a greater extent than its solubility should have indicated. [a] based in a standard value of 200 ml g^{-1}.

	Soluble Ni % of applied Ni	Total Ni in shoot	difference	Transpiration rate[a] ml g^{-1}
NiSO$_4$	90.80	48.35	42.45	302
α-Ni(OH)$_2$	67.49	77.69	−10.2	528
β-Ni(OH)$_2$	43.63	21.83	21.8	354
NiCO$_3$	59.60	30.73	28.87	412
Ni$_3$(PO$_4$)$_2$	7.37	45.77	−38.40	446
Ni phyllosilicate	18.18	38.89	−20.71	508
Ni - humate	22.34	80.83	−58.49	500
Ni - goethite	33.58	20.06	13.52	264
Ni - acid birnessite	0.92	18.59	−17.67	526
Ni/Al LDH, carbonate	2.85	10.86	−8.01	528
Ni/Al LDH, silicate	0.60	0.73	−0.13	462
Ni/Al LDH, nitrate	6.14	19.84	−13.70	570
Garnierite	3.30	1.32	1.89	170
Limonite	0.03	0.08	−0.05	128
Serpentine soil (S18)	0.86	1.8	−0.94	376
Serpentine soil (S20)	0.71	2.17	−1.46	538
NiO	0.06	0.07	−0.01	476
Control (0 Ni)	0.04	0.07	−0.03	520

The low solubility of, and uptake from NiO, which had similar Ni concentrations in the shoots as the control treatment, agrees with the results of Fellet et al. (2009), who reported that *A. corsicum* is not capable of dissolving and hyperaccumulating Ni from NiO which is kinetically inert.

Ni uptake and Ni solubility from the serpentine soils were very low. Interestingly, hyperaccumulation of Ni by *Alyssum* species was reached when plants were grown on

these soils in the field (Li et al. 2003). The contrasting results between Ni uptake from serpentine soils in hydroponic jars versus in the field illustrate the importance of soil rhizosphere processes, possibly including microbial processes, and their effect on Ni uptake. No rhizosphere was formed between the soil and root surfaces, which may account for the little Ni accumulated from the serpentine soils in this experiment. Additionally, in the field, plants obtain their nutrients from the soil whereas in our experiment all the nutrients, both micro and macro, were provided to the plant via nutrient solution. Hence, the plant had no need to scavenge mineral particles to obtain the required plant nutrients for growth. Abou-Shanab et al. (2003) clearly illustrate that bacteria facilitate the greater release of Ni from the labile pool in soil and enhance the availability of Ni to *A. murale*. A recent study by Ma et al. (2009) obtained similar results using Ni-resistant plant growth promoting bacteria.

These results support the convection model for Ni uptake, which comprises of both the concentration of soluble Ni in solution and the transpiration rate. Hyperaccumulators play a role in altering the concentration of soluble Ni in solution through depletion of bioavailable pools of metals to extents where they change the chemical equilibria of that metal in the soil.

Results by Moradi et al. (2010), who studied the dynamic spatial distribution of Ni(II) around the root of *Berkheya coddii* using magnetic resonance imaging in combination with numerical modeling, showed that metal concentration in the rhizosphere is dynamic and is controlled by the plant's transpiration rate, metal uptake rate, and the total concentration in the soil solution.

Conclusions

This study was designed to investigate which Ni species present naturally in serpentine soils and anthropogenically Ni contaminated soils are susceptible to absorption and hyperaccumulation by *A. corsicum*, using a hydroponic technique. It was demonstrated that Ni uptake to shoots is related to Ni solubility of the compounds with the exception of $Ni_3(PO_4)_2$, Ni phyllosilicate, and Ni-acid birnessite, which showed a low solubility but a relatively high plant uptake and transpiration rate. Strong hyperaccumulation (>10 g kg^{-1} dry weight) was obtained in decreasing order for the soluble salt $NiSO_4>\alpha$-$Ni(OH)_2> Ni_3(PO_4)_2>Ni$ phyllosilicate$>Ni$-goethite$>NiCO_3$. It appears that Ni uptake is driven by convection, which depends on the initial concentration of Ni in solution and the transpiration rate.

Acknowledgments

Supplementary Data

To produce alpha-Ni(OH)2, a methodology similar to Genin et al., 1991 was used. Under ambient conditions, 27.5 mL of 30% ammonium hydroxide solution was added to 250 mL of 1 M Ni(NO3)2. The slurry was then washed with water via centrifugation and freeze dried. A separate batch of fresh alpha-Ni(OH)$_2$ was aged to beta-Ni(OH)$_2$ in solution for one month in a N$_2$ atmosphere at room temperature (Scheinost and Sparks, 2000), washed five times with water via centrifugation and freeze dried. Before adding to

the nutrient solution, alpha -Ni(OH)$_2$ and beta -Ni(OH)$_2$ were washed four times with pH 7 nutrient solution and freeze dried and their structures confirmed by X-Ray Diffraction (XRD). Washing the minerals with nutrient solution prior to adding them to the hydroponic jars decreased their sorption capacity for nutrients in the hydroponic jars. NiCO$_3$, NiO, NiSO$_4$, Ni$_3$(PO$_4$)$_2$ were purchased from Acros, Johnson Matthey, Acros, and Alfa Aesar, respectively. NiCO$_3$, NiO, Ni$_3$(PO$_4$)$_2$ were washed four times via centrifugation at " 5000g for 5 minutes with pH 7 nutrient solution and then freeze dried prior to being added to the hydroponic jars.

Serpentine soils 18 and 20 from Southwest Oregon (Table 4.3) were washed five times with serpentine nutrient solution, then centrifuged at 10000 g for ten minutes and freeze dried. The high g was necessary in order to recover the clay fraction of the soils during washing. The soils were partially dried at 52°C overnight and then transferred to the freeze drier.

The nickel-aluminum layered double hydroxides (Ni/Al LDH) with various interlayer anions (carbonate, nitrate, or silicate) were synthesized according to Taylor, 1984; Depege et al., 1996; and Ford et al., 1999. Their structures were confirmed by XRD. Ni/Al LDH with carbonate interlayer was synthesized under ambient conditions. 800 mL of 25 mM Al-nitrate and 1000 mL of 100 mM Ni-nitrate solutions were separately adjusted to pH 6.9 with NaOH and HNO$_3$ and combined. 200 mL of water was used to rinse the bottle with precipitated Al hydroxide. The final volume was 2000mL of the combined metals. A Metrohm automatic titrator was used to add 1 M Na$_2$CO$_3$ to keep the pH constant at 6.9 until addition of Na$_2$CO$_3$ was less than 0.1 mL hr^{-1} or ceased

(about 20 to 46 hours). The pH electrode was periodically cleaned with 0.5 M HCl and calibrated throughout the synthesis. Ni/Al LDH with nitrate interlayer was synthesized under N_2 conditions in a glove box. 2.5 M NaOH was used in the automatic titrator to maintain a pH of 6.9. All water was purged with N_2 prior to being put in the glove box. To exchange silicate for nitrate in the interlayer, 1L of 0.08 M, N_2 purged, sodium metasilicate plus 3.5 g of nitrate interlayer LDH were mixed in the N_2 glove box (pH 12.6). The 1 bottle was sealed, removed from the glove box and placed in a 90°C water bath-shaker for 24 hours. The slurry was then transferred to an orbital shaker (170 rpm) at 60°C for three weeks. For one more week the slurry remained at room temperature until being washed four times with water and freeze dried. The Ni to Al ratio for the Ni/Al LDH was 5.49, 6.68, and 6.12 for the carbonate, nitrate, and silicate interlayer anions, respectively. Upon silicate substitution, the Ni to Al ratio changed from 6.75 to 6.12 with a 17.7% increase in total mass of the LDH. The percent of nitrogen and carbon in the Ni/Al LDH with carbonate, nitrate, and silicate interlayer anions was 0.145 and 1.792, 1.498 and 0.293, and 0.128 and 0.916, respectively. The percent of nitrogen and carbon in the Ni/Al LDH with nitrate interlayer used for silicate exchange was 1.541 and 0.538, respectively. The interlayer anions were also confirmed with Fourier Transformed Infrared Spectroscopy.

Goethite was synthesized according to Schwertmann and Cornell, 2000. Acid birnessite was synthesized according to McKenzie, 1971 and Feng et al., 2007. Goethite and acid birnessite were chosen as representative soil iron and manganese oxides because of their stability over time; their structures were confirmed by XRD. 3500 MWCO

dialysis tubing pretreated at 80°C with 10 mM EDTA, rinsed with 18.2 megohm water, and stored in 40% ethanol. Tubing was used for dialysis of goethite and acid birnessite until their electrical resistivity was twice that of water, 12 hours after changing the water. Approximately 110 g and 30 g of goethite and acid birnessite were added to 6 L and 2 L pH 7 serpentine nutrient solutions, respectively, for Ni sorption. The reason a considerably larger amount of goethite was needed is because the point of zero charge for goethite is very high compared to that of acid birnessite, about 7.8 versus 2.8 (Stumm and Morgan, 1981). At pH 7, the surface of the acid birnessite is negatively charged whereas the surface of goethite is slightly positive, so Ni^{2+} sorbs much more readily and strongly to acid birnessite than to goethite. Because of this surface charge difference, it would be much easier to desorb Ni cations from goethite than from acid birnessite. The pH of the 6 and 2 L vessels was then re-adjusted to 7 and Ni stock solution was added so the final concentration of Ni was 0.01 M in both mineral slurries. At the ionic strength (0.0134) and pH of the serpentine nutrient solution, amorphous $Ni(OH)_{2(s)}$ was calculated by the Visual MINTEQ program version 3.0 beta (Gustafsson, 2004) to be under saturated at 0.01 M Ni^{2+}. Visual MINTEQ is a chemical equilibrium model for predicting metal speciation and solubility in natural waters and is a MS31 Windows version of MINTEQ v. 4.0 (Allison et al., 1991). The acid birnessite and goethite slurries were constantly mixed open in the air by a stir plate and propeller, respectively, with their pH adjusted occasionally to 7 for approximately 11 days or until a constant pH was found. The goethite and acid birnessite slurries were washed seven and five times, respectively, with pH 7 nutrient solution to remove loosely sorbed Ni and then freeze dried.

Humic acid (HA) was purchased from Sigma Aldrich. HA was washed similarly to Zhou et al., 2005 to remove most of the commonly present Fe, which was initially about 9000 mg kg^{-1}. HA was washed three times with 6 M HCl for about 28 hours total on a shaker. Then it was washed twice with 11.25 M HCl for 36 hours total. Finally, the HA was rinsed once with 1 M HCl and twice with 0.1 M HCl to decrease the HCl concentration in the HA. HA was then added to 2 L of pH 7 nutrient solution, and the pH was adjusted to 7 with 10 M NaOH. Ni stock solution was added to make the final Ni concentration 0.01 M and the pH was adjusted to 7 with 10 M NaOH until a constant pH 7 was found (about two days). The HA slurry was then centrifuged and washed five times with pH 7 nutrient solution and freeze dried. About 85% weight loss of HA occurred as much of the HA remained in solution at pH 7 and could not be retrieved via centrifugation. The final Ni and Fe concentrations were 9450 and 160 mg kg^{-1} dry weight, respectively. Garnierite and limonite samples were obtained from Goiás, Brazil (Table 4.2). Garnierite is a Ni-silicate rich ore and limonite is highly weathered, iron mineral rich top soil.

Ni phyllosilicate was synthesized at room temperature according to Decarreau et al., 1987 and Peltier et al., 2006. A solution of 0.08 moles of sodium metasilicate was added to a solution of 0.06 moles of nickel sulfate and 0.02 moles of sulfuric acid. Upon the rapid addition and mixing of sodium metasilicate, a nickel phyllosilicate of to approximate structure $Si_4Ni_3O_{11}$ precipitated. This precipitate was settled for four hours, washed three times with water, then dispersed at approximately 12g L^{-1} in water for seven weeks. Finally, it was centrifuged and freeze-dried. Ni-phyllosilicate, and all the

LDH phases were washed four times with pH 7 nutrient solution and freeze dried prior to

being added to the hydroponic jars.
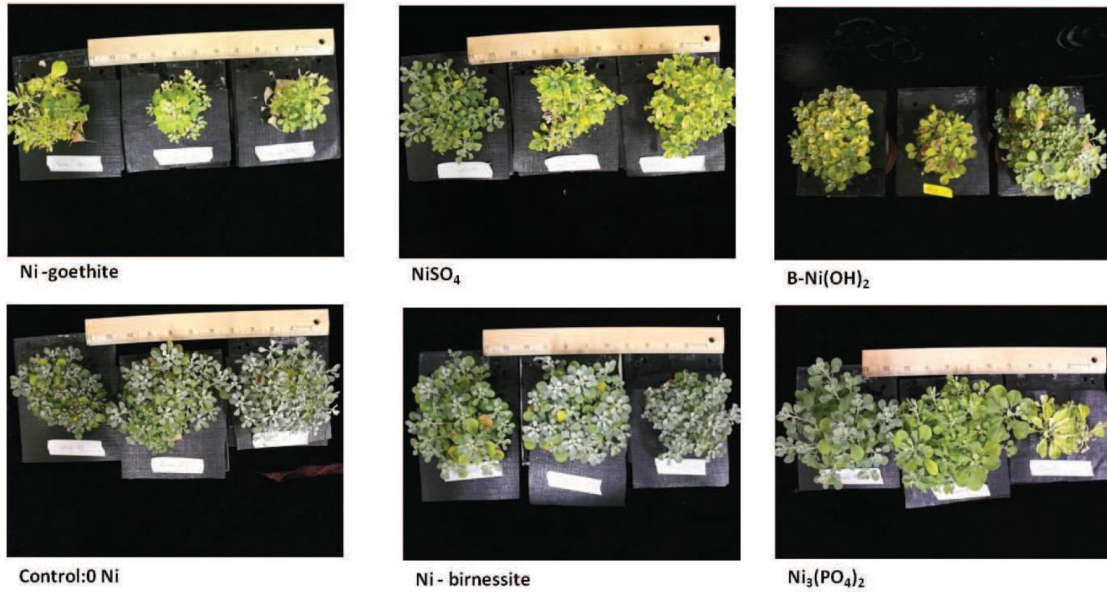
Figure 4.3   Plant shoot biomass after 28 days of growth in serpentine-Hoagland solution
with the addition of various Ni species (indicated at the bottom of each
picture). Plants grown in solution with the garnierite and limonite soils
manifested reduced shoots yield as plants grown in solution containing Ni-
goethite.

REFERENCES

Abou-Shanab RA, Angle JS, Delorme TA, Chaney RL, Van Berkum P, Moawad H, Ghanem K, Ghozlan HA (2003) Rhizobacterial effects on nickel extraction from soil and uptake by *Alyssum murale*. New Phytol 158:219–224

Allison JD, Brown DS, Novo-Gradac KJ (1991) MINTEQA2/ PRODEFA2, a geochemical assessment model for environmental systems. U.S. Environmental Protection Agency

Arai Y (2008) Spectroscopic evidence for Ni(II) surface speciation at the iron oxyhydroxides - Water interface. Environ Sci Technol 42:1151–1156

Bani A, Echevarria G, Sulce S, Morel JL, Mullai A (2007) In-situ phytoextraction of Ni by a native population of *Alyssum murale* on an ultramafic site (Albania). Plant Soil 293:79–89

Bernal MP, McGrath SP, Miller AJ, Baker AJM (1994) Comparison of the chemical changes in the rhizosphere of the nickel hyperaccumulator *Alyssum murale* with the non-accumulator *Raphanus sativus*. Plant Soil 164:251–259

Brooks RR (1987) Serpentine and its vegetation. A multidisciplinary approach. Dioscorides, Portland

Chaney RL, Angle JS, Broadhurst CL, Peters CA, Tappero RV, Sparks DL (2007) Improved understanding of hyperaccumulation yields commercial phytoextraction and phytomining technologies. J Environ Qual 36:1429–1433

Decarreau A, Bonnin D, Badauttrauth D, Couty R, Kaiser P (1987) Synthesis and crystallogenesis of ferric smectite by evolution of the Si-Fe coprecipitates in oxidizing conditions. Clay Miner 22:207–223

Depege C, ElMetoui FZ, Forano C, deRoy A, Dupuis J, Besse JP (1996) Polymerization of silicates in layered double hydroxides. Chem Mater 8:952–960

Fellet G, Centofanti T, Chaney RL, Green CE (2009) NiO(s) (bunsenite) is not available to *Alyssum* species. Plant Soil 319:219–223

Feng XH, Zhai LM, Tan WF, Liu F, He JZ (2007) Adsorption and redox reactions of heavy metals on synthesized Mn oxide minerals. Environ Pollut 147:366–373

Ford RG, Scheinost AC, Scheckel KG, Sparks DL (1999) The link between clay mineral weathering and the stabilization of Ni surface precipitates. Environ Sci Technol 33:3140– 3144

Genin P, Delahayevidal A, Portemer F, Tekaiaelhsissen K, Figlarz M (1991) Preparation and characterization of alpha-type nickel hydroxides obtained by chemical precipitation – Study of the anionic species. Eur J Solid State Inorg Chem 28:505–518

Gustafsson JP (2004) Visual MINTEQ v 2.30. Swedish Royal Institute of Technology (KTH)

Hammer D, Keller C, McLaughlin MJ, Hamon RE (2006) Fixation of metals in soil constituents and potential remobilization by hyperaccumulating and non-hyperaccumulating plants: Results from an isotopic dilution study. Environ Pollut 143:407–415 Institute S (1989) SAS procedures guide, Version 6, 3rd edn. SAS Institute, Cary

Kukier U, Peters CA, Chaney RL, Angle JS, Roseberg RJ (2004) The effect of pH on metal accumulation in two *Alyssum* species. J Environ Qual 33:2090–2102

Li YM, Chaney RL, Brewer EP, Angle JS, Nelkin J (2003) Phytoextraction of nickel and cobalt by hyperaccumulator *Alyssum* species grown on nickel-contaminated soils. Environ Sci Technol 37:1463–1468

Ma Y, Rajkumar M, Freitas H (2009) Improvement of plant growth and nickel uptake by nickel resistant-plant-growth promoting bacteria. J Hazard Mater 166:1154–1161

Massoura ST, Echevarria G, Leclerc-Cessac E, Morel JL (2004) Response of excluder, indicator, and hyperaccumulator plants to nickel availability in soils. Aust J Soil Res 42:933–938

Massoura ST, Echevarria G, Becquer T, Ghanbaja J, Leclerc- Cessac E, Morel J-L (2006) Control of nickel availability by nickel bearing minerals in natural and anthropogenic soils. Geoderma 136:28–37

McGrath SP, Shen ZG, Zhao FJ (1997) Heavy metal uptake and chemical changes in the rhizosphere of *Thlaspi caerulescens* and *Thlaspi ochroleucum* grown in contaminated soils. Plant Soil 188:153–159

McKenzie RM (1971) Synthesis of birnessite, cryptomelane, and some other oxides and hydroxides of manganese. Mineral Mag 38:493–502

McNear DH Jr, Chaney RL, Sparks DL (2007) The effects of soil type and chemical treatment on nickel speciation in refinery enriched soils: A multi-technique investigation. Geochimica et Cosmochimica Acta 71:2190–2208

Milner MJ, Kochian LV (2008) Investigating heavy-metal hyperaccumulation using *Thlaspi caerulescens* as a model system. Ann Bot 102:3–13

Moradi AB, Conesa HM, Robinson BH, Lehmann E, Kaestner A, Schulin R (2009) Root responses to soil Ni heterogeneity in a hyperaccumulator and a non-accumulator species. Environ Pollut 157:2189–2196

Moradi AB, Oswald SE, Nordmeyer-Massner JA, Pruessmann KP, Robinson BH, Schulin R (2010) Analysis of nickel concentration profiles around the roots of the hyperaccumulator plant *Berkheya coddii* using MRI and numerical simulations. Plant Soil 328:291–302

Nolan AL, Ma Y, Lombi E, McLaughlin MJ (2009) Speciation and isotopic exchangeability of nickel in soil solution. J Environ Qual 38:485–492

Parker DR, Chaney RL, Norvell WA (1995) Chemical equilibrium models: applications to plant nutrition research. Chemical equilibrium models: applications to plant nutrition research. In: Loeppert RH, Schwab AP, Goldberg S (eds) Chemical equilibrium and reaction models. Soil Science Society of America Special Publ. No. 42. Soil Sci. Soc. Am./Am. Soc. Agron., Madison, WI, pp 163–200

Peltier E, Allada R, Navrotsky A, Sparks DL (2006) Nickel solubility and precipitation in soils: a thermodynamic study. Clays Clay Miner 54:153–164

Puschenreiter M, Wieczorek S, Horak O, Wenzel WW (2003) Chemical changes in the rhizosphere of metal hyperaccumulator and excluder *Thlaspi* species. J Plant Nutr Soil Sci 166:579–584

Reeves RD, Brooks RR, Dudley TR (1983) Uptake of nickel by species of *Alyssum*, *Bornmuellera*, and other genera of Old World *Tribus Alysseae*. Taxon 32:184–192

Reeves RD, Baker AJM, Becquer T, Echevarria G, Miranda ZJG (2007) The flora and biogeochemistry of the ultramafic soils of Goiás state, Brazil. Plant Soil 293:107–119

Scheinost AC, Sparks DL (2000) Formation of layered single and double-metal hydroxide precipitates at the mineral/ water interface: a multiple-scattering XAFS analysis. J Colloid Interface Sci 223:167–178

Schwartz C, Morel JL, Saumier S, Whiting SN, Baker AJM (1999) Root development of the zinc-hyperaccumulator plant *Thlaspi caerulescens* as affected by metal origin, content and localization in soil. Plant Soil 208:103–115

Schwertmann U, Cornell RM (2000) Iron oxides in the laboratory: preparation and characterization, 2nd edn. Wiley- VCH

Shallari S, Echevarria G, Schwartz C, Morel JL (2001) Availability of nickel in soils for the hyperaccumulator *Alyssum murale* Waldst. & Kit. S Afr J Sci 97:568–570

Smith RM, Martell AE, Motekaitis RJ (2003) NIST critically selected stability constants of metal complexes database. NIST standard reference database 46, version 7.0. NIST, Gaithersburg, MD, USA

Stumm W, Morgan JJ (1981) Aquatic chemistry, 2nd edn. Wiley, New York

Tan HK (2003) Humic matter in soil and the environment: principles and controversies. Marcel Dekker, Inc., New York

Taylor RM (1984) The rapid formation of crystalline double hydroxy salts and other compounds by controlled hydrolysis. Clay Miner 19:591–603

Wenzel WW, Bunkowski M, Puschenreiter M, Horak O (2003) Rhizosphere characteristics of indigenously growing nickel hyperaccumulator and excluder plants on serpentine soil. Environ Pollut 123:131–138

Whiting SN, Leake JR, McGrath SP, Baker AJM (2000) Positive responses to Zn and Cd by roots of the Zn and Cd hyperaccumulator *Thlaspi caerulescens*. New Phytol 145:199–210

Zhao FJ, Hamon RE, McLaughlin MJ (2001) Root exudates of the hyperaccumulator *Thlaspi caerulescens* do not enhance metal mobilization. New Phytol 151:613–620

Zhou P, Yan H, Gu BH (2005) Competitive complexation of metal ions with humic substances. Chemosphere 58:1327–1337

Chapter 5

NICKEL SPECIATION IN SEVERAL SERPENTINE TOPSOILS USING SYNCHROTRON-BASED TECHNIQUES

Abstract

Although ultramafic laterite profiles and serpentine soils have been extensively studied, nickel speciation in these soils using direct methods such as synchrotron-based techniques has not.   Using multiple techniques, we improve the understanding of nickel speciation in several serpentine topsoils from the USA. Our findings help predict nickel bioavailability and transport from serpentine soils by directly describing the chemical phases of nickel. Additionally, our results help better understand how nickel hyperaccumulating plants access nickel from serpentine soils.

We find the literature comprehensively describes how nickel speciation is directly related to local climate, weathering, topography, and bedrock of the specific serpentine soil site. Primary serpentine minerals like peridotite and serpentinite break down because magnesium preferentially leaches out of the soil profile, consequently enriching other elements like iron. The secondary minerals formed from peridotite and serpentinite include vermiculite and smectites. Smectites tend to form when the soil has poor drainage. Eventually, in heavily weathered soils, iron oxides form. In deep profiles of nickel laterites it is even possible for supergene processes to occur and serpentine minerals may precipitate out again.

In terms of how this sequence of weathering is related to the speciation of nickel, the nickel is removed from the octahedral position in the primary silicates and becomes part of the octahedral layer of smectites or incorporates with amorphous iron oxides or manganese oxides. Our synchrotron based-data show that nickel is associated in this fashion in several serpentine soils from Oregon, California and Maryland. Nickel is present with iron oxides like goethite, and XRF mapping indicates it also can accumulate with manganese oxides. Additionally, however, even in the clay fraction we find nickel present in primary serpentine minerals such as lizardite. Using linear combination fitting of synchrotron data, we determine that nickel associates with phyllosilicates such as lizardite and also with iron and manganese oxides.

Introduction

Serpentine Weathering and Mineralogy

Serpentine soils result from the weathering of ultramafic rocks. Ultramafic rocks are formed from magma located deeper in the earth's mantle than magma that forms most of the rocks of the continental crust. Because the magma comes from deeper in the earth's mantle, it contains increased proportions of elements with smaller cationic radii (e.g. Mg, Cr, Co, Fe, and Ni) versus larger cations that are typically found in lighter crustal rocks (e.g., Ca, Na, Li, Al) that compose the continental crust (Alexander et al.,

2007). Because ultramafic rocks have elevated amounts of heavier, often transition metals, the soils that form also possess similar characteristics. These chemical differences have direct implications for the soil chemistry and weathering products of ultramafic rocks versus those from soils of non-ultramafic origin.

There are three serpentine minerals: antigorite, chrysotile and lizardite. For clarity, the term "serpentine" refers to these minerals. The term "serpentinite" refers to the parent bedrock material, principally the magnesium-iron silicate minerals like olivine and pyroxene. Serpentine minerals form during the process of "serpentinization", where serpentine rock reacts with water to form, for example, lizardite. The reaction: olivine + water = serpentine mineral + brucite is a common formation mechanism of serpentine. The term "serpentine soil" refers to soils that develop from serpentinite or contain its weathering products. Nickel substitutes for magnesium in the octahedral layer of serpentine minerals, and during geochemical weathering, nickel is removed from the octahedral layer and accumulates with iron and manganese oxides (Alexander et al., 2007b).

Harzburgite is a rock, and is common variety of peridotite rock in terrestrial environments. The olivine and pyroxenes in harzburgite weather more readily than serpentine minerals. Serpentine soils that form from dunite rock contain large amounts of brucite. Dunite is nearly all olivine (Alexander, 2004). Most of the ultramafic rock of eastern North America consists of peridotite and serpentinite which are derived from oceanic mantle. Serpentinite is hydrothermally altered peridotite (Alexander, 2009).

The term "serpentine" was coined because of the dark, serpent-like waves present in the parent bedrock. The term "serpentine soil" refers to soils that develop on serpentinite and contain its weathering products. The geochemistry of serpentine soils has been extensively studied [e.g., (Alexander et al., 2007; Cheng et al., 2009; Oze et al., 2004a)]. The weathering of serpentinite rock by biotic processes has been studied, and secondary magnesium oxalate crystals containing both iron and nickel were found (Adamo et al., 1993; Alibhai et al., 1993; Wilson et al., 1980)

The main chemical feature that separates serpentine soils is very high magnesium and first row transition metals, specifically chromium, cobalt, and nickel. The major soil-forming processes are weathering, leaching of basic cations and silica and the oxidation of iron (Alexander, 2009).

Drainage of serpentine soil is a major factor in mineralogy. Yongue-Fouateu et al. (2009) found in lateritic soil profiles developed on ultramafic rock that goethite was the main mineral in the profile with silicate clays less abundant but generally occurring at the top of the profile. Smectites were found where water accumulated in the downslope and bottom of the soil profile, and this smectite transformed to kaolinite in the well-drained upper portions of the profile. Gibbsite was also more common at the summit.

In a series of studies by Gasser and Dahlgren (1994) and Gasser et al. (1994; 1995) colloids were found to be important in the transport of Cr, Fe, Mg, and Ni in serpentine soils. Less than 40% of nickel in the soil water was found in dissolved form, indicating that colloidal transport may be an important factor for nickel translocation from the soil. Serpentine minerals and iron oxides were the major soil mineral

components, along with a small amount of quartz. Gibbsite and smectite were not detected. Iron oxides were rich with non-iron elements like aluminum, chromium, nickel, and silicon. They found that nickel can substitute for Mg in serpentine minerals, and that manganese oxides also incorporated nickel into their structure. In batch and stirred-flow experiments, they showed that nickel release increased with decreasing solution pH. Most serpentine soils are pH 6.0 and higher and only a few below 6.0 except in highly leached situations, or where fertilizers have caused acidification. The pH of serpentine soils can vary generally between (4.5 very uncommon) 5.5 and 7.5 (Alexander et al., 1989; Gasser et al., 1995; Rabenhorst et al., 1982, Chaney 2013).

Iron and aluminum released from serpentines during weathering is incorporated with silica and forms dioctahedral iron-rich montmorillonite (nontronite) in well-drained serpentine soils (Wildman et al., 1968b). The formation of dioctahedral sheets of iron rich montmorillonite rather than saponite (the trioctahedral end member) is common in soils formed from serpentinite. In well drained soils, iron or aluminum montmorillonite will form before any saponite forms (Wildman et al., 1971). The solubility of Mg may explain why iron rich montmorillonite forms in high Mg soils rather than trioctahedral saponite. In soils of well drained environments, iron and aluminum montmorillonite is stable before the soil pore water contains enough Mg to crystallize saponite (Ece et al., 1999; Wildman et al., 1968a). Because magnesium is lost faster than silicon from the surface of serpentine, incongruent dissolution of the serpentine mineral takes place and silicon is enriched at the mineral surface. Serpentine with silicon rich surfaces will have

a low isoelectric point, meaning that they will be negatively charged at a neutral pH (Tartaj et al., 2000).

Caillaud et al., (2004) found similar results in that the leaching of magnesium and silicon causes enrichment of lesser mobile elements like iron and aluminum, which produced dioctahedral smectites. The smectites were mostly of two classes, one iron-rich montmorillonite with little tetrahedral charge and another that had tetrahedral charge. These smectites were mixed in the lower horizon of the weathering profile, but increasingly more segregated in the surface horizons. Based on chemical composition, clays were iron rich in the lower profile and aluminum rich in the surface horizon.

In the saprolite zone that developed from serpentinized peridotites in a study by Gaudin et al. (2005), saponite and Mg,Ni saponite in addition to two dioctahedral smectites (iron nontronite and montmorillonite) formed. In the smectite zone, there were no serpentine minerals or saponite, but dioctahedral smectites, magnetite and goethite were common.

In the clay fraction of an Entisol and Inceptisol of a serpentine soil catena, Bonifacio et al. (1997) found serpentine to be the main mineral along with small amounts of low charged vermiculites. More developed soils in the catena contained higher amounts of vermiculites and smectites. The weathering of the serpentine minerals yielded low charged vermiculite in the upper, drier soil horizons, and smectite in the poorly drained soils. They also found that vermiculite can transform to smectite under moist conditions. They propose that low charge vermiculite is the first weathering product of serpentine under free drainage conditions. Smectites are found in the soil

horizons with lower porosity, indicating that smectite formation occurs only under restricted drainage. Smectite formation in the deeper horizons may form via two mechanisms, precipitation from the soil water or transformation from vermiculites translocated down through the soil profile. Under wet conditions, smectite seemed to form directly from serpentine minerals (Bonifacio et al., 1997).

Iron smectites form from serpentinite where much of the Mg is lost more rapidly than Si. Mg dissolves more rapidly than Si, thereby leaching much faster from the soil. The remaining silica slowly dissolves and saturates the soil solution, which then can crystallize as iron-rich montmorillonite (Ece et al., 1999). Several other authors have also come to similar findings with respect to the weathering of serpentine soils. Weathering of the serpentine minerals produced smectite and vermiculite, which eventually transformed into goethite and hematite (Cheng et al., 2011). Smectite is the ultimate weathering product under impeded drainage conditions (Buurman et al., 1988; Istok and Harward, 1982; Wildman et al., 1968b; Wildman et al., 1971).

In Niquelandia, Goiás, Brazil, pyroxene is the parent material, not serpentine minerals. The pyroxenes transform to goethite and kaolinite via several nickel bearing phyllosilicates. Nickel rich smectite and pimelite are especially enriched with nickel and trioctahedral smectites (saponite) formed in highly fractured rocks (Colin et al., 1990). Colin et al., (1990) developed a profile model with five layers. The top layer was a clayey ferruginous layer with kaolinite and goethite and hematite. The second layer was clayey with lots of smectite and lesser amounts of kaolinite and goethite. The third layer was saprolitic with lots of smectite, kerolite, enstatite, diopside, chromite and quartz. The

fourth layer contained enstatite, diopside chromite and lesser amounts of smectite, and the fifth layer consisted of parent rock (pyroxene) containing enstatite, diopside, and chromite.

Younger soils studied by Hseu et al. (2007) contained smectite and serpentine minerals on the summit and shoulder. Older soils in the back slope and foot slope contained more vermiculite. Chlorite and serpentine present in the young soils at the summit weather to smectite and interstratified chlorite-vermiculite in older soils via strong leaching and oxidizing conditions. Vermiculite along with kaolinite and quartz formed in the foot slope.

Several primary minerals, e.g. olivine, serpentine and chlorite, which typically are not stable in soil environments, were still present in the A horizon of a soil in a temperate climate (Kierczak et al., 2007). Additionally, several authors have concluded metal speciation is directly affected by climatic conditions which influence soil mineralogy. For example, iron and manganese oxides precipitate in humid tropical climates or other clays form in cold continental or temperate climates (Antic-Mladenovic et al., 2011; Kierczak et al., 2007).

Nickel in Serpentine Soils

In a study of Ni-bearing laterites in Southern Oregon and Northern California, it was found that the laterites were composed principally of serpentine, chlorite, goethite, and maghemite. Minor amounts of smectite, quartz, talc, hornblend and tremolite were found (Foose, 1992). This contradicts older data stating that serpentine minerals were

mostly weathered (Hotz, 1964). In the saprolitic zone, Ni occurs as a solid solution, replacing Mg in several Mg-silicates (e.g. serpentine, talc or chlorite). In the limonitic zone, Ni occurs mostly in goethite at about 2% (Foose, 1992). The garnierite group can reach approximately 2-3% Ni (Faust, 1966).

Nickel speciation depends on the type of primary mineral and the climatic conditions. For example the leaching of silicon and magnesium and accumulation of iron and manganese in highly weathered soils increases nickel retention. Slightly weathered soils have more iron in primary silicate minerals while more weathered soils have more iron oxides (Massoura et al., 2006). This was the case for Bani et al. (2009) where nickel was associated with amorphous iron oxides. In those soils more than two thirds of total soil nickel was in the clay fraction. However, nickel was less associated with well crystalline iron oxides, and crystallization during pedogenesis was a process that separated nickel from goethite particles (Bani et al., 2007; Bani et al., 2009). In terms of nickel availability, the soils with the highest amount of amorphous iron oxide also had the highest amounts of available nickel. In Ferralsols from New Caledonia, most of the nickel was associated with iron oxides (e.g. goethite). Manganese oxides similar to interstratified lithiophorite-asbolane were a minor sink for nickel as was talc (Becquer et al., 2006).

Alves et al. (2011) found that surface-bound nickel is primarily adsorbed, and that most of the variability in nickel bioavailability in the soil was linked to manganese oxides, which determined the nickel sorption capacity. The concentration of Ni in

serpentine soils increase as other elements weather and leach out over time (Oze et al., 2004b).

Antic-Mladenvoic et al. (2011) carried out a study on the impact of redox conditions on nickel in a serpentine soil. They found that the residual fraction of the soil, when analyzed by sequential fractionation, contained more than 90% of the nickel. It was difficult to compare studies on nickel solubility because often different sequential extraction procedures were used in each study. Additionally, they identified several important transformation mechanisms that affect nickel solubility during redox change, including dissolution and precipitation of iron and manganese oxides, and organic matter transformations. Dissolved organic carbon can potentially be an important ligand for nickel. They found the silt and clay fractions were important nickel sources.

In a sulfide deposit, lizardite and clinochlore were important scavengers of nickel, and nickel was found mostly in the octahedral sites of lizardite. In this case, serpentine is a secondary mineral enriched with nickel and formed via a supergene process where nickel dissolves from the sulfide ore and then precipitates as lizardite down the soil profile (Suarez et al., 2011). Gleeson et al. (2004) found a similar process occurring in a nickel laterite deposit where nickel leached from the upper portion of the profile down into the saprolite portion where it is fixed in silicate minerals.

Bani et al. (2007) carried out a study on nickel phytoextractability from serpentine soils and found phytoextractability was mainly influenced by the nickel bearing minerals and not by pH. For example, nickel from primary serpentine clay minerals was not phytoextractable because nickel is present in the crystal lattice of the mineral. However

140

secondary nickel rich minerals like iron oxides or smectites probably have nickel as a

sorbed species on the mineral surface or internal exchangeable sites, therefore making it

more phytoextractable. Bani et al. (2009) found that the highest levels of nickel

phytoavailability were associated with amorphous iron oxides.   This is directly related to

weathering in that slightly weathered soils have iron almost entirely as primary silicate

minerals, whereas increasingly weathered soils have more free iron oxides, including

both amorphous and crystalline iron oxides. Clay minerals such as smectites or poorly

crystalline iron oxides are the main contributors to nickel phytoavailability in serpentine

soils, however, nickel phytoavailability is very low when present in well crystalline iron

oxides, such as in ultramafic laterites (Massoura et al., 2006). These results are similar to

a study on nickel phytoavailability and extractability in an ultramafic toposequence,

where iron geochemistry determined the fate of nickel (Chardot et al., 2007). Nickel in

the crystal lattice of goethite is not phytoavailable and extractable (Echevarria et al.,

2006). Massoura et al. (2006) also conclude that nickel is generally more available when

associated with phyllosilicates than with well crystallized iron oxides (Massoura et al.,

2006). Because peridotite derived serpentine soils have more free iron oxides than

serpentine soils formed from serpentinite (Alexander et al., 2004), soils that form from

peridotite should have more plant available nickel.

Apart from iron oxides, nickel can also associate with manganese oxides. About

60% of nickel was associated with phyllomanganates and 40% with goethite in the upper

limonite layer of a Philippine ultramafic laterite. In the lower saprolite layer, about 90%

nickel substitutes for magnesium in serpentine minerals with the rest associated with phyllomanganates (Fan and Gerson, 2011).

A summary of nickel availability consists of two situations, one in moderately weathered soils where plant available nickel is controlled by amorphous iron oxides and a second where more weathered soil have higher nickel accumulation in charged, secondary phyllosilicates (Bani et al., 2009).

Other minerals that contain nickel were found by Kierczak et al. (2007) and include Cr-magnetite, forsterite, iddingsite and serpentine. Nickel-rich primary minerals were more susceptible to weathering and releasing nickel versus Cr-magnetite. Smectite was important for trapping nickel in the soil, and nickel concentrations increased down the soil profile (Kierczak et al., 2007). Similarly, nickel mainly remained in silicates during initial weathering stages and concentrated in secondary clays like iron-montmorillonite, which was derived from serpentine minerals (Caillaud et al., 2009). In another toposequence study, nickel was again mainly concentrated in silicates; most of the nickel was found in the residual fraction based on the sequential extraction sequence, indicating that the major source of nickel was nickel-bearing silicates such as serpentines, smectites and vermiculites (Becquer et al., 2006).

In more intensely weathered soil, Echevarria et al. (2006) found goethite, serpentine and talc were the most frequent nickel-bearing minerals in the soils. Nickel concentrations were always higher in goethite than in other minerals, with up to 6.1% nickel. Iron or manganese oxyhydroxides scavenge nickel during intense weathering.

Geogenic nickel in soils is mainly influenced by the nickel-bearing minerals, and nickel is more available when it is associated with poorly crystalline phyllosilicates than with crystalline iron or manganese-iron oxides. This is probably due to high amounts of adsorbed nickel on the phyllosilicates that can be exchanged easily versus nickel sequestered in the mineral lattice (Echevarria et al., 2006).

Nickel is a heavy metal commonly found in soils from both geogenic and anthropogenic sources. Serpentine soils serve as an example of soils with high levels of geogenic nickel. As a commodity, 60% of land based nickel resources come from nickel laterites and 40% from sulfide deposits. Stainless steel and alloy production, nonferrous alloys and super-alloys, and electroplating are important industrial processes that consume nickel. End uses for products containing nickel include transportation, fabricated metals, electrical equipment, the petroleum and chemical industries, construction, household appliances and industrial machinery. Stainless steel traditionally accounts for 2/3 of nickel use worldwide, with ½ of steel going into the construction, food processing and transportation sectors (USGS, 2012).

Nickel Species Identified by Spectroscopy

Using infrared techniques, it was determined that nickel-rich kerolites have nickel distributed as domains in the octahedral sheet, versus a random distribution found in nickel-talc (Gerard and Herbillon, 1983). Decarreau et al. (1987) determined that nickel and iron separated into distinct domains in a smectite derived from the weathering of pyroxenes. In the smectite, nickel clustered into nickel-rich (pimelite-like) domains in

the octahedral layer, while iron similarly clusters into nontronite-like domains. The Ni-Fe-Mg smectite was not homogeneously distributed with these cations but was a mixture of trioctahedral and dioctahedral domains (Decarreau et al., 1987).

Nickel speciation in ultramafic ore minerals was characterized by EXAFS, again with the results that there is a non-random distribution of nickel atoms in the octahedral layer of nickel-rich phyllosilicates (Manceau and Calas, 1986; Manceau et al., 1985). The authors note that nickel and iron have similar backscattering phases and amplitudes and cannot be distinguished by EXAFS, and nickel can substitute for magnesium because they have similar atomic radii. The presence of magnesium with nickel in the second shell however, decreases the amplitude of the wave backscattered by the surrounding atoms in such a way that EXAFS cannot separate the contributions of nickel from magnesium. Additionally, because of the limited mean free path of the photoelectron, structural problems involving atomic ordering between 5 and 15A are impossible by EXAFS (Manceau and Calas, 1985).

Nickel in chromite is tetrahedrally coordinated and has very distinct pre-edge and edge features not seen in many serpentine soils. Lizardite is a primary mineral, and in it nickel is not distributed randomly but again segregated into domains (Manceau and Calas, 1986).

Manceau (1987) found that nickel builds partial nickel-hydroxide layers in asbolane and is not incorporated into the manganese octahedral layers. In general, nickel speciation has a large variability. It can be present in phyllosilicates where it substitutes for Mg, 2.) associated with goethite, 3.) substitutes for Al in lithiophorite or 4.) in nickel

hydroxide layers in asbolane. The multiple species of nickel allow it to be present more commonly in the environment than other elements e.g., cobalt (Manceau et al., 1987).

In a study of nickel incorporation into natural goethite, Ni was found to be in a tetragonal dipyramid of oxygen, indicating that nickel preserves its usual local symmetry, but locally distorts the goethite structure. However, the long range structure of goethite is preserved (Carvalho-E-Silva et al., 2003). The maximum amount of Ni that can be incorporated into goethite should be about 5.5 mol% Ni. This low amount of nickel that can be incorporated into the goethite structure allows only a fraction of total nickel in the soil profile to be retained in the oxidized horizon. The remaining nickel migrates downward and results in nickel enriched silicate phases (or garnierite) at the bottom of the weathering profile. This enrichment process at the bottom of the profile is a supergene process (Carvalho-E-Silva et al., 2003) similar to what occurs in other nickel sulfide and laterite deposits (Suarez et al., 2011; Gleeson et al., 2004).

In ferric smectites from lateritic nickel ore of Murrin Murrin, Western Australia, nickel was located in the octahedral sheets of the smectite and not present as a separate clay mineral. Additionally, nickel was not randomly distributed but again ordered into small clusters in the octahedral layer. The nickel-rich clusters resemble small trioctahedral clusters distributed with the dioctahedral smectite. The dioctahedral structure of smectite layers limits the formation of larger nickel-rich domains as seen in other trioctahedral smectites. However, large nickel cluster tri-dioctahedral (Fe-Mg-Ni)-phyllosilicates formed at low temperature lateritic weathering (Gaudin et al., 2004).

Nickel is located in small trioctahedral clusters within the dioctahedral sheets of ferric smectites (Gaudin et al., 2004). This is different from smectites in Ni-Mg phyllosilicates in New Caledonia (Manceau and Calas 1985) or in weathering profiles in Brazil (Colin 1990, Decarreau 1987), where there are large trioctahedral clusters of nickel even in smectites low in nickel content (Gaudin et al., 2005).

Nickel Hyperaccumulating Plants

Several nickel hyperaccumulator plants are native to serpentine soils. In the genus *Alyssum*, some species can hyperaccumulate up to 30 g kg^{-1} in their dry leaves when they are grown on serpentine soils (Reeves et al., 1983). The nickel content can reach up to 5% in some hyperaccumulating plants (Reeves et al., 1999). However, it is not clear how plants remove the nickel from the soil, i.e., how plants solubilize nickel for subsequent uptake.

Several of the native serpentine plants have nickel contents that would be toxic to other plants; however, it is mainly the low calcium to magnesium ratio in serpentine soils that inhibits plant growth more than low potassium or phosphorous levels or high nickel, cobalt, and chromium levels. The soil organic carbon content is similar to non-serpentine soils of similar climate (Alexander et al., 2007, p 42). Other researchers have found that there are some organic soils of serpentine nature where seasonal flooding and high OM input allow accumulation of OM, but otherwise, OM is low. Additionally, nitrogen, phosphorous, potassium, calcium, and sometimes molybdenum and boron are deficient for plants (Chaney, 2013). The soil chemistry is a direct result of the serpentine parent

material and has the greatest impact on vegetation and plant species. Serpentine soils are not particularly low in nitrogen (Alexander et al., 2007; Alexander, 2009).

A low cost, long-term soil remediation option for several heavy metals commonly found in polluted soils is phytoremediation. Phytoremediation, specifically phytoextraction and phytomining, use plants to remove toxic metals from the soil and transport them to above ground where the plant can then be safely harvested and the metal recycled. Additionally, phytoremediation can be incorporated into natural attenuation remediation strategies. Nickel hyperaccumulating plants have unique characteristics that make them good candidates for the remediation of large areas of soils polluted with Ni and phytomining of serpentine soils (Chaney et al., 2007).

Research Objectives

Although hyperaccumulation is well documented, the mechanisms of it, for example the metal dissolution processes in soil, are not understood (Centofanti et al., 2012). Identifying the nickel bearing phases and their fate during soil weathering will allow for prediction of the potential mobility and bioavailability of nickel over the long term (Massoura et al., 2006). Echevarria et al. (2006) also emphasized the importance of identification of nickel-bearing minerals in the soil because these minerals also strongly affect nickel solubility and hence mobility and bioavailability. The mechanisms of the soil-plant transfer of soluble nickel need to be identified (Antic-Mladenvoic et al., 2011). Our studies employ a variety of techniques to characterize the major and minor nickel species that naturally occur in selected serpentine soils. We speciate nickel using

physical separation methods, bulk XRD, and synchrotron radiation. We use μ-SXRF, μ-SXRD, and μ-EXAFS in conjunction with bulk-EXAFS and bulk-XRD to elucidate the major Ni species in the sand, silt, and clay fraction of several serpentine soils.

Few studies on nickel speciation in serpentine topsoils have been published using micron-scale X-ray techniques (e.g., synchrotron based micro-XRD (μ-SXRD), synchrotron based micro-X-ray fluorescence mapping (μ-SXRF), and synchrotron based micro-Extended X-ray Absorption Fine Structure spectroscopy (μ-EXAFS). There is little information on the direct speciation of nickel naturally present in serpentine topsoils using synchrotron-based XAS.

Traditionally, sequential chemical extractions were used to identify soil metal species which involved repeated extractions with increasingly aggressive reagents. Sequential extractions were effective in determining that nickel accumulates partly in magnesium silicates but mostly with manganese and iron oxides (Alexander et al. 2007). However, these techniques are limited by the possibility of sample alteration, and it is difficult to compare studies on nickel solubility because often different sequential extraction procedures are used in each study (Antic-Mladenvoic et al., 2011). XAS is capable of determining *in situ* metal speciation with minimal chemical sample treatment.

Another focus of this study is to identify if any nickel-aluminum layered double hydroxides (LDH) form during weathering of serpentine soils. For example, takovite is a naturally occurring Ni/Al LDH formed in metamorphosed serpentinite. Also, a naturally occurring mixed-layer chrysotile-hydrotalcite was found by Drits et al. (1995). The mineral is an interstratified chrysotile-hydrotalcite, consisting of alternating hydrotalcite

and serpentine-like layers with sulfate and chlorine anions. It was found in serpentinized peridotites.

Particle size fractionation was implemented to identify unique Ni species from the sand, silt, and clay fractions. Ni concentration increased in the clay fraction (Oze et al., 2004b), where particle size ranged from two micrometers to the nano-scale. Particles in this size fraction possess different physical and chemical characteristics than those in the larger silt and sand fractions, such as surface area and solubility. It is important to keep in mind that Ni in serpentine soils is geogenic, not anthropogenic. This inherent difference means that apart from being sorbed to clay mineral surfaces, Ni can also be incorporated into the crystal lattice structures of silt and sand-size particles. In terms of XAS, this means that Ni fluorescence emits not only from Ni species sorbed to clay surfaces (e.g., Fe and Mn oxides), but also from the bulk mineral. In order to separate these differences, a sonication method was used.

The objective of this study is to characterize the major and minor nickel species that naturally occur in selected serpentine topsoils to better understand what nickel species plants can naturally hyperaccumulate. The results will improve our understanding of phytoextraction and phytomining and their use to remediate and mine metal rich soil and help understand the fate of nickel released from the soils.

Materials and Methods

Sampling Locations

Samples from three different serpentine soils, all within the United States, were obtained for this study. The first and largest set of samples is from the Klamath Mountains, specifically the Cave Junction area of Josephine County in Southwest Oregon. The second set of samples is from the Jasper Ridge Biological Preserve, which is part of the Franciscan Complex of California. The California soils are some of the same ones characterized by Oze et al. (2004). The last soil sample is from a serpentine soil site near Baltimore, Maryland. Notations for these three soils will be Oregon, California and Maryland soil, respectively. Multiple samples were selected to study how nickel speciation changes in relation to pH, organic matter, clay content, particle size, depth, and location.

Sonication of Soil Samples

Because nickel is geogenic in ultramafic rocks and their derived soils, and not introduced from outside, human sources, e.g., aerosols from smelters, nickel is not only sorbed to the surface of clay minerals, but also located in the lattice structures of clay and larger minerals. In order to discern between sorbed nickel phases and mineral nickel phases, a sonication technique was employed to remove clay coatings from the silt and sand fractions of the soils. This method also served to disperse the clay fraction and separate the mineral by particle size.

A modified sonication method has was used to disperse the clay fraction and separate the minerals by particle size (Amelung and Zech, 1999; Amelung et al., 1998; Doelsch et al., 2006; Gimbert et al., 2005; Kahle et al., 2003; North, 1976; Oorts et al., 2005; Raine and So, 1994; Schmidt et al., 1999; Sohi et al., 2001; Solomon et al., 2002; Yang et al., 2009). Briefly, the probe sonicator was calibrated (North, 1976) using a 250 mL glass beaker. A slurry of 20 g of soil in 80 ml of 18.2 megohm water (1:4 soil:water ratio) was placed in the beaker for sonication. The probe was always placed 20 mm below the surface of the slurry. A Branson DIGITAL Sonifier® UNITS Model S-450D was used with a flat tip on the horn. Initially, 60 J/mL were applied to the slurry. Then the slurry was wet sieved with a 250 μm sieve, using 70 mL of water from a fine mist, calibrated hand-pump spray bottle. Another 440 J/mL were applied to the 150 mL sub-250 μm fraction slurry (Amelung et al., 1998). After the second sonication, the slurry was wet sieved using the spray bottle with a 45 μm sieve until the effluent was clear. The sub-2 μm clay fraction and then sub-5 μm clay/fine silt fraction were sequentially separated from the sub-45 μm fraction via centrifugation. The 5-25 μm fraction (fine silt) was separated from the 25-45 μm fraction via wet sieving using a 25 μm sieve and again the spray bottle until the effluent was clear. The wet sieved and centrifuged samples were dried with warm air at 35 C in typically less than 36 hours.

During every sonication the slurry was placed in an ice bath to maintain a slurry temperature of less than 37 C. A swing bucket rotor was used to centrifuge the samples. Particle density was assumed to be 2.65 g cm^{-1}. This methodology is a compilation of methodologies designed to minimize the breakdown of particulate organic matter (i.e.,

sand-size OM) into smaller particles. Centrifuge speed and time were calculated using a

Sorvall RC 6 centrifuge with a HS-4 rotor, taking into account the R1 and R2 distances

from the axis of rotation for sedimentation time. 50 mL conical centrifuge tubes were

used. Centrifugation times were calculated from formulas in Soil Chemical Analysis

Advanced Course (Jackson, 1985) pages 113 and 127 and Methods of Soil Analysis Part

4, Physical Methods (Gee and Or, 2002). The published methodologies using sonication

for clay fraction separation do not provide the specific details mentioned above, hence the

sonication times, centrifuge times, and decantation distances are all calculated using the

materials and equipment available in our lab.

Sample Physicochemical Properties

Soil elemental compositions were determined via a combination of digestion

procedures including: microwave digestion with nitric acid (EPA method 3051), EPA

method 3050B hot nitric, and Aqua Regia method, all followed by ICP-OES.

Additionally, particle size analysis was carried out by the hydrometer method, and

citrate-dithionite extraction were used in soil characterization (Holmgren, 1967; Loeppert

and Inskeep, 1996). Soil pH was determined by mixing the soil with distilled water in a

1:1 ratio and measuring the pH. Percent organic matter was determined by the loss-on-

ignition (LOI) method.

X-Ray Diffraction: Soils, Minerals, and Standards

Bulk synchrotron XRD was carried out to determine the major minerals in the <2

mm fraction of the Oregon and Maryland soils. Bulk diffractometer XRD analysis was

carried out on serpentine mineral standards obtained from the University of Delaware's mineralogical supply (Serpentine minerals 96, 185, 186, 5811) and on the sub-2 mm and clay fractions of serpentine soils from Oregon and Maryland. Several soil clay fractions were treated with sodium dithionite (Holmgren, 1967; Loeppert and Inskeep, 1996) to remove the iron oxides present, and then additional XRD spectra were collected. Elemental data were obtained from the dithionite extract to determine Ni content in the Fe oxide fractions of the clays. To obtain the nickel concentrations of the serpentine mineral standards, complete dissolution of the mineral was accomplished using a Katanax Fusion machine with a mix of lithium tetraborate, metaborate and bromide.

Bulk synchrotron XRD analyses were carried out at SSRL beamline11-3 and bulk diffractometer-based XRD was carried out at the University of Delaware on a Philips/Norelco powder diffraction system using Bragg-Brentano parafocusing optics with a graphite monochromator. Copper k-alpha radiation (8.04 keV) was used, operating at 35 kV and 20 mA.

In addition to diffractograms of serpentine mineral standards and soil fractions from Oregon and Maryland, several other diffractograms were taken of synthetic nickel standards prepared in the laboratory and of bedrock from the California soils. Specifically diffractograms of the bed rock JR3 and COII sites were taken. Naturally occurring takovite diffractogram was also measured. For synthetic minerals, nickel oxalate, magnesium oxalate @ 60% nickel substitution, magnesium oxalate @ 5% nickel substitution, pure magnesium oxalate, cryptomelane doped with nickel, acid birnessite doped with nickel, and magnetite, hematite, goethite, ferrihydrite all doped with nickel,

and Ni-Fe LDH (10:1), and Ni-Fe LDH (2:1) were made in the lab and characterized by XRD and EXAFS.

Bulk XAFS: Soils, Minerals, Standards, and Linear Combination Fitting

Table 5.1 describes the synchrotron beamline characteristics used in this study. The electron beam storage ring energy was 2.5–2.8 GeV with a maximum beam current of 300 mA at the National Synchrotron Light Source (NSLS). The electron beam energy was 3 GeV with a maximum beam current of 300mA at the Stanford Synchrotron Radiation Lightsource (SSRL). The gas ionization chambers (where used) were filled with either nitrogen or argon or a mix of both gases to obtain c.a. 10-20% beam absorption in I0, and 50-70% absorption in I_1 and I_2. The Lytle detector was filled with argon gas. Harmonic X-ray elimination was achieved by detuning the monochromators c.a. 30-35%, unless KB mirrors were used where typically beam energy >24KeV does not pass through the mirror setup. Additionally, beamline 4-1 at SSRL is equipped with a harmonic rejection mirror at 22keV. Z-1 X-ray filters were always used when collecting data in fluorescence mode (i.e., either 3 or 6 absorption length Co filters for Ni K-edge EXAFS data collection). Where iron was prevalent in the sample, 1-5 layers of aluminum foil were used to preferentially attenuate Fe fluorescence and reduce the Fe K-beta fluorescence peak.

For bulk-EXAFS, the sub-2 mm fraction of serpentine soil was powdered via mortar and pestle and placed in sample plastic holders of c.a. 1.5 mm thickness. Samples were placed in the beam path at 45° to the beam and 45° to the detector. The detector

154

was a 13, 30 or 100 element solid state Ge, Lytle, or PIPS detector. Nickel K-edge EXAFS spectra were collected from c.a. 200 eV below the absorption edge to c.a. 12.5 k-space. Sufficient scans were taken to obtain reasonable signal to noise, generally 5-15 scans depending on nickel and iron concentrations. Scans were calibrated with a nickel foil using the peak of its first derivative at 8333 eV.

Synthetic and natural mineral standards were made or purchased to analyze the soils by Linear Combination Fitting (LCF) to determine the most dominant Ni species. EXAFS spectra from previous research and collaborators was also used and cited where used. X-ray diffraction and elemental data were used in conjunction with LCF to assist in selecting the most reasonable standards to fit the soils. Data were processed either using Sixpack (Webb, 2005) or Athena/Artemis package (Ravel and Newville, 2005).

Micro-XAS: µ-SXRF, µ-EXAFS, µ-XRD and Linear Combination Fitting

For sonicated samples, µ-XRF mapping, µ-XRD and µ-EXAFS were carried out on the clay, coarse silt and medium sand fractions (i.e., the sub-2 µm, the 25-45 µm, and the 250-500 µm fractions, respectively), hereafter referred to as clay, silt and sand fractions. It is recommended to not grind samples in a mortar/pestle for micro-XRF experiments because this process can decrease the particle size smaller than the beam itself, effectively homogenizing the sample and preventing higher quality correlations of different elements. The sonicated fractions were mounted on Kapton® tape and are roughly different from each other by one order of magnitude. For petrographic thin sectioned samples, whole soil fractions (air dried, <2 mm) were embedded in Scotchcast®

electrical resin, adhered to a trace element free quartz slide with a cyanoacrylate-based adhesive and ground to 30 micrometer thickness. For μ-XRF mapping, sufficient incident energy (e.g., 10-17 keV) to simultaneously excite fluorescence from Ni, Co, Fe, and Mn was used. These energies enable determination of elemental associations and distributions.

Fluorescence data were collected with either a Ge detector or Vortex Si-drift detector positioned 90° to the incident beam (45° to the sample). When acquiring fluorescence data, special attention was paid to selecting the fluorescence of the Ni K-alpha peak on the multi-channel analyzer display so that the resulting spectra excluded as much fluorescence from the Fe K-beta peak as possible. In some samples, coarse XRF maps (1-3 mm^2) were created to observe metal correlations in a larger area to identify regions of interest (i.e., "hotspots") for μ-EXAFS and μ-XRD analysis. Fine XRF maps were generated where necessary within coarse maps on regions of interest. Scanning rates varied depending on the specific beamline detector, sample stage motors, and beam size. The different technologies at each beamline drastically affected time necessary to create μ-XRF maps. At beamlines with fast scanning rates fine maps were sometimes not necessary.

With the monochromator calibrated at the Ni K-edge (8333eV), μ-EXAFS spectra were collected from approximately 200 eV below the absorption edge energy to k values of 10-12.5 Å^{-1} in the EXAFS region. Multiple scans were collected until satisfactory signal to noise ratios were achieved (typically 15-30 scans). EXAFS spectra were analyzed by Linear Combination Fitting (LCF) to determine the dominant Ni species

using the same reference spectra as those that were used for bulk EXAFS analysis. A combination of both Sixpack (Webb, 2005) and Athena/Artemis package (Ravel and Newville, 2005) were used for data processing.

Micro-XRD data also were collected with CCD detectors at microprobe beamlines, and the data were calibrated with reference diffraction patterns and analyzed using Fit2D (Hammersley, 1998; Hammersley et al., 1996) and Match! (Crystal-Impact, 2012) , which uses the Crystallography Open Database (Grazulis et al., 2009; Grazulis et al., 2012) and The American Mineralogist Crystal Structure Database (Downs and Hall-Wallace, 2003).

Results and Discussion

Sampling Locations

The ultramafic Oregon soils have been previously studied (Alexander, 2004; Alexander and DuShey, 2011; Alexander et al., 2007a; Borine, 1983; Burt et al., 2001; Hotz, 1964; Istok and Harward, 1982). Soil redness in the Klamath Mountains is related to the mineralogical differences between peridotite and serpentinite. Peridotite, which is composed of mostly olivine and pyroxene, contains fewer serpentine minerals than serpentinite, which is the metamorphic product of peridotite. The redder soils contain higher amounts of free iron (oxy,hydro)oxides. Most of the iron in peridotite is in olivine, which weathers relatively easily compared to pyroxene. The iron released oxidizes rapidly and imparts a reddish color to the soils. However, most of the iron in serpentinized peridotite is in magnetite and serpentine minerals, which are both

considerably more resistant to weathering than olivine and pyroxene. Soil parent material is the dominant factor that determines the amount of iron oxides that form, with peridotite-derived soils containing more iron oxides than serpentinite-derived soils. In the Klamath Mountains, the well-drained soils formed from peridotite form more free iron oxides than the soils formed from serpentinite (Alexander, 2004).

Smectite formation only occurred in poorly drained landscape positions in other samples from the Klamath Mountains. Smectite formation is promoted in soils in wetter landscape positions and concentrates in the foot slopes versus higher landscape positions (Bulmer and Lavkulich, 1994; Burt et al., 2001; Istok and Harward, 1982).

Harzburgite is the dominant type of peridotite in the Klamath Mountains. The olivine in harzburgite weathers more rapidly than the pyroxene, which can lead to an increase in the pyroxene minerals in the soils. Enstatite is an orthopyroxene mineral that is found in similar serpentine soils derived from harzburgite (Alexander, 2004). In a soil chronosequence in the Klamath Mountains, weathering eliminated olivine from the oldest soils and greatly diminished serpentine from both sand and clay fractions (Alexander et al., 2007a). Additionally, slopes were steeper and soils were redder on peridotite parent material than on serpentinite. Peridotite is a common rock at the top of the upper mantel, and much of it is altered to serpentinite (Alexander and DuShey, 2011).

In this region, serpentine soils have developed over mostly peridotite. Geochemical weathering of the parent rock has left ferrunginous nickeliferous lateritic soils (Hotz, 1964). Nickel Mountain is the only area where Ni has been found as part of silicate minerals (collectively called garnierite). Olivine, orthopyroxenes and serpentine

minerals in this area have been weathered away. Ferric oxides (e.g., goethite) and some

montmorillonite, chlorite and talc are common soil minerals where Ni may be present

(Hotz, 1964). Ni can substitute for Mg in the octahedral layers of silicates because its

ionic radius is similar to that of magnesium (0.69 Å vs. 0.66 Å, respectively). Unaltered

serpentine minerals may account for some Ni (Montoya and Baur, 1963) and much of the

Ni may occur with goethite (Fisher and Dressel, 1959). Iron, aluminum, and Ni

concentrations are greatest in the weathered zone.

Serpentine soils have characteristically low calcium-to-magnesium ratios,

generally below one (Burt et al., 2001), and serpentine minerals were found to be

dominant in the clay fraction of several serpentine soils from the Klamath Mountains.

The amount of serpentine mineral decreased with depth, indicating its susceptibility of

weathering in the upper horizons. Burt et al (2001) also determined that vermiculite and

smectite were the weathering products of serpentine minerals in the clay and coarse silt

fractions of the soil. Because the soils were well drained, smectite may have limited

stability. Gibbsite and kaolinite were not present in the serpentine pedons, probably due

to low amounts of silica and alumina in the parent rocks (Burt et al., 2001).

The soils at the Jasper Ridge site are some of the same samples from Oze et al.

(2004). These soils are dominantly Mollisols formed on top of serpentinized peridotite.

The serpentinite at Jasper Ridge is composed of mainly lizardite and antigorite (70%),

chlorite (15%), talc (10%), magnetite (4%), and chromite (1%). Other minerals include

olivine, augite and enstatite. Sites JR3 and COII were used in our study. Nickel in these

samples was found in three phases in the JR3 bedrock, including olivine, serpentine, and

a nickel-iron metal alloy, probably awaruite. In both sites, nickel concentrations in the soil were less than in the bedrock, with nickel concentrations ranging from 3510 ppm to 2400 ppm in the COII site. The pH of the soils is near neutral and slightly increases with depth, ranging from 6.71 to 6.98.

The clay fraction of the JR3 site had the highest concentration of nickel, and the silt fraction the lowest, with about 2900 ppm and 1800 ppm, respectively. The clay size fraction of the JR3 site is composed of smectite, vermiculite, lizardite, antigorite, clinochlore and Cr-clinochlorite, with smectite being the most abundant mineral. This mineralogy did not vary significantly at different depths. Site COII was treated with sequential extractions, and the vast majority of nickel remained in the solid phase, and was not dissolved by this procedure. Most of the nickel in the Jasper Ridge site originated from olivine. During serpentinization, the resulting serpentine mineral also contained nickel, and small grains of a nickel-iron alloy were produced. Oze et al (2004) state nickel is more possibly more bioavailable (to bacteria and vegetation) than chromium in serpentine soils because nickel-rich olivine weathers more easily than chromite.

The third and final sample is the Maryland serpentine soil. Other serpentine soils from Maryland have been characterized by Rabenhorst et al. (1982). The pH values general increased with depth from pH 6.6 at the surface to pH 6.8 in the subsurface. The pH gradient differed from nearby non-serpentine soils where pH decreased with depth. Serpentine minerals were found in the coarse clay and silt fractions but not in the fine clay fraction. Smectites dominated the clay fraction, along with chlorite interstratified

with smectite and vermiculite. The serpentine mineral weathering products included

smectite and vermiculite, which dominated the clay fractions. However, the vermiculite

may have been a weathering product of non-serpentine mica and chlorite. Iron release

from the serpentine structure or other iron-rich minerals remained in the oxide form.

Sample Physicochemical Properties

Physicochemical properties of the soils are listed in Table 5.2. The Oregon soils

varied in terms of elemental concentration and particle size. The pH range of the soils is

between 5.8 and 6.9. The clay fraction of the soils ranged between 16% - 39%. The Ni

concentration ranged from 100 ppm to 6000 ppm. Physicochemical properties and XRD

data of the Jasper Ridge soils can be found in Oze et al. (2004b).

X-Ray Diffraction: Soils, Minerals, and Standards

Figure 5.1 contains the XRD diffractograms of clay, silt and sand from several of

the serpentine soils. Additionally, some clay spectra from citrate-dithionite treated

samples are also shown. In Figure 5.1, five soils are analyzed: S20UNT, S11UNT,

S10T2, S9T2, and S5T2. All these soils are from Oregon, except S5T2 which is from

Maryland. The major minerals identified in the sand fraction of S20UNT are quartz,

clinochlore, lizardite, enstatite, and magnetite. In the silt fraction, clinochlore, cordierite,

lizardite, quartz, enstatite, and magnetite were identified. The clay fraction contained

antigorite, goethite, hematite, quartz, enstatite, and magnetite. When the clay fraction

was treated with dithionite, the peaks for goethite and hematite were reduced

significantly and more of the phyllosilicate peaks, like talc, clinochlore, and lizardite are

161

clearer. Alexander, (2004) stated that enstatite is an orthopyroxene mineral that is found in similar serpentine soils derived from harzburgite.

Soil S11UNT has three diffractograms; the first of which is the sand. In the sand fraction, clinochlore, cordierite, quartz, enstatite, magnetite are found. The clay fraction contains lizardite, some goethite, quartz, and hematite. After treatment with dithionite, the lizardite/antigorite peaks are clearer and several small wide peaks from goethite and hematite are gone.

The S10T2 sand fraction contains some talc, lizardite, magnetite, quartz, enstatite, hematite and some goethite. The sand fraction was ground in a mortar and pestle from which the clay fraction was retrieved via the centrifugation method outlined above. This fraction has peaks for lizardite, quartz, goethite, enstatite, and hematite. The clay fraction of S10t2 contains lizardite, goethite, trace amounts of quartz and enstatite, and hematite. When the clay fraction is treated with dithionite, the lizardite/antigorite peaks are much clearer, as well as some peaks for clinochlore and quartz. Hotz (1964) stated that serpentine minerals in this area had weathered away, but here commonly we find them. Actually, this is not surprising because Burt et al. (2001) also found serpentine minerals to be the dominant mineral in the clay fraction of several serpentine soils from the Klamath Mountains.

The S9T2 sand contains clinochlore, talc, quartz, enstatite and pargasite, while the clay fraction contains mostly clinochlore and some hematite and goethite. When treated with dithionite, mostly the clinochlore peaks come through with broad small iron oxide peaks disappearing.

The Maryland soil, S5T2, contained mostly talc, antigorite, and quartz in the sand fraction. The clay fraction showed peaks for antigorite, brucite, goethite, and quartz. In the dithionite treated clay fraction, the peaks for antigorite, brucite, talc, and quartz are clearer as the goethite peaks have disappeared. Serpentine minerals were also found in the coarse clay and silt fractions from other Maryland soils (Rabenhorst et al. 1982).

Figure 5.2 is a collection of mineral standards, both natural and synthetic. Some of these minerals were used as standards for LCF of EXAFS data, so their XRD diffractograms are shown here to illustrate their mineralogy. Two types of Ni-Fe LDHs were synthesized and their peaks are typical for an LDH. Other minerals such a nickel-doped goethite, hematite, magnetite, ferrihydrite (not shown), acid birnessite, cryptomelane, and magnesium oxalate are shown. The peaks for the iron, manganese and magnesium minerals all correspond to their correct phases. Several other ultramafic related diffractograms are also shown, including takovite, picrolite, several serpentine minerals, and the bedrock from California sites JR3 and COII. Several of these minerals served as useful standards for LCF of the bulk EXAFS data.

Bulk EXAFS: Literature, New Data, and Data Analysis

Literature: Spectroscopic Studies on Ultramafic Materials

In a natural goethite sample, the Ni-O distance was 1.98 Å and 2.12 Å with coordination numbers (CN) of 2.2 and 4.3. The Ni-Fe distances were 3.05 Å (CN 1.7), 3.21 Å (CN 1.9), and Ni-Fe 3.73 Å (CN 0.8). In a synthetic goethite, the Ni-O distance was 1.98 Å (CN 2.8) and 2.12 Å (CN 4) and the Ni-Fe distances were 3.00 Å (CN 2.8),

3.17 Å (CN-3.2), and lastly 3.60 Å (CN-0.5) (Carvalho-E-Silva et al., 2003). Singh et al. (2002) found nickel-iron distances similar to or shorter than those for iron in goethite: Ni-O 2.06 Å, Ni-Fe 2.99 Å -3.02 Å, Ni-Fe 3.16 Å -3.19 Å, and Ni-Fe 4.03 Å.

For nickel synthetic hematite the distances of Ni-Fe were 2.90-2.92 Å, Ni-Fe 3.41 Å -3.42 Å and Ni-Fe 3.66 Å -3.67 Å. Nickel replaced iron in hematite and no separate nickel phases like NiO or $Ni(OH)_2$. The first shell has 2 oxygen paths each with 3 CN: one at 1.97 Å -1.98 Å and the other at 2.09 Å -2.1 Å (Singh et al., 2000).

In a study on nickel complexation to amorphous HFO, nickel formed mononuclear bidentate edge-sharing surface complexes with interatomic distances of Ni-O 2.05 Å -2.07 Å and Ni-Fe 3.07 Å -3.11 Å (Xu et al., 2007). This mechanism did not change as a function of ionic strength, pH, loading, or times used in this study. There was no evidence for nickel substitution for iron in sorption samples or in coprecipitation. Nickel forms inner sphere mononuclear bidentate complexes along edges of iron octahedra. Metastable α-$Ni(OH)_2$ formed during coprecipitation of nickel-HFO. The absence of multiple Fe shells indicates surface complexes and no precipitates for sorption samples. Ni substitution requires crystal growth of iron oxides where Ni octahedra would have to be buried into the Fe octahedral network (Xu et al., 2007).

Several studies on nickel surface speciation at the iron oxyhydroxide interface and distribution in lateritic nickel ores showed that nickel surface complexes on iron oxides are sensitive to iron oxide crystallinity and nickel may inhibit the crystallinity of the oxide itself. Goethite had two different edge-sharing complexes (Ni-Fe 3.03 Å and Ni-Fe 3.18 Å) and a corner sharing surface complex of Ni-Fe 4.06 Å. Hematite had a face

164

sharing complex of Ni-Fe 2.92 Å and a corner sharing complex of 4.07 Å. Ferrihydrite

had an edge sharing complex in chains (Ni-Fe 3.05 Å -3.08 Å) and in rows (Ni-Fe 3.19 Å

-3.21 Å). Nickel was uniformly incorporated into goethite and hematite structures (Arai,

2008; Landers and Gilkes, 2007; Landers et al., 2009; Landers et al., 2011).

Another study on the crystal chemistry of trace elements in natural and synthetic

goethite found Ni-O distance of 2.07 Å, Ni-Fe of 3.0 Å -3.07 Å, and Ni-Fe of 3.18 Å, and

Ni-Fe of 3.62 Å -3.65 Å. In Ni-asbolane, nickel hydroxide is present as a separate but

mixed layer in the MnO_2 mineral. Ni, Cu and Zn are incorporated into the gibbsitic layer

of lithiophorite (Manceau et al., 1987; Manceau, 1990).

The unique structural feature cause by the "light" Al atoms in the second

coordination shell of Ni lithiophorite instead of heavy Fe atoms in goethite and Mn atoms

in birnessite produces a split of the first oscillation at 3.8 $Å^{-1}$. Magnesium is also a light

cation, and when it is present in the second shell of neighboring nickel atoms in edge-

sharing octahedral layers, it also produces a similar split in Ni k-edge EXAFS (Manceau

et al., 2000). This feature is identifiable in some of the serpentine minerals standards and

soils in our study. Moreover, limitations in EXAFS for studying trioctahedral

phyllosilicates is discussed by Manceau (1990). There are in and out of phase

oscillations for Mg and Ni atoms in the second shell, and the addition of Si at about 3.24

Å may be necessary to fit the second shell data. However, Si is in phase with Ni

oscillations; however, Mg is out of phase. These in and out of phase oscillations

significantly complicate shell fitting analysis of phyllosilicates. Si, Al, and Mg as a group

and Fe and Ni in another group have nearly equal scattering factors and prevent the

distinction between atoms in each group based on scattering intensity and phase. Silicon interferes constructively with nickel at low k and increases the total amplitude; however, magnesium interferes destructively and its contribution to the EXAFS spectrum is "subtracted" from that of Ni and Si atoms. Nickel atoms are never randomly distributed but clustered into nickel-rich domains (Manceau and Calas, 1986).

Some Zn-phyllosilicates have a very similar spectral feature (i.e., a split in the first oscillation) to the nickel rich serpentine minerals (Ni-phyllosilicates) in our study. Manceau et al. (2003) shows Zn-surrounded by light Mg atoms, which he describes as causing the split in the first oscillation. Both the phyllosilicate and lithiophorite have similar spectra because they are surrounded by light atoms; hence the large indentation in the first oscillation is caused by light elements as first neighbors. A shift towards shorter R values versus pure $Ni(OH)_2$ may indicate an actual reduction in interatomic distance and/or a second shell filled with light atoms, e.g. Al. (Manceau, 1987).

However, Fan and Gerson (2011) show spectra for nickel in lizardite, and there is no break in the first oscillation. Nickel is also identified as a second neighbor via EXAFS. This indicates that perhaps in the saprolite layer, Ni is forming domains. For goethite EXAFS there were two main peaks, one at 2.03 Å for O and the second for Fe at 3.03 Å and 3.28 Å (just 1 peak for both Fe atoms).

With respect to the formation of LDH in serpentine soils, Fan and Gerson (2011) identify at 8 Å^{-1} a strong double oscillation for Ni adsorbed to phyllomanganates. This perhaps could explain why the LDH fits well into LCF. Burt et al. (2001) found low amounts of gibbsite and kaolinite, two minerals known to form layered double

166

hydroxides when reacted with nickel, a low amount of alumina in the soil would also decrease the possibility of forming nickel-aluminum layered double hydroxides as weathering products. Additionally, the EXAFS spectra from S20UNT (Figure 5.3) appears to be very similar to a Ni-Al LDH spectra, however, its XRD spectra in Figure 5.1 shows that other phyllosilicates are dominant.

New Data: Bulk EXAFS of Soils, Minerals, and Standards

Figure 5.3 is the bulk Ni K-edge EXAFS data for the serpentine soils. In general, all the soils have the same major oscillations with slight differences with respect to locations of shoulders and beat patterns. Some spectra have a slight indentation on the first oscillation, which would indicate the presence of a light element (Mg, Al) as a neighbor to the central nickel atom in a phyllosilicate environment. The samples from JR3, COII, S15T2, S14T2, S11UNT sand, STT2 and S5T2 have this feature.

Figures 5.4 to 5.10 are the standards used in LCF of the bulk EXAFS.

Data Analysis: LCF of Soil Bulk EXAFS.

Oregon soil S20U is broken down into separate particle sizes by sonication the RDF spectra show the second neighbor to Ni is much larger in both the sand and silt fraction, whereas it is smaller in the clay fraction (Figure 5.11). This is possibly caused by the presence of a regularly occurring second neighbor in the crystal lattice of larger minerals present in the silt and sand fractions versus a more random distribution of second neighbors found in a mix of sorbed/precipitated complexes typical on clay surfaces.

Figure 5.12 shows a LCF of S20UNT whole fraction soil using EXAFS spectra taken from each of its particle size fractions. It is evident that the clay fraction dominates the EXAFS spectrum as it accounts for 77% of the nickel signal. A significant portion of nickel is located in the clay fraction. Ni has been shown to accumulate in the clay fraction of serpentine soils (Oze et al., 2004b).

Figure 5.13 is LCF of Ni K-edge bulk EXAFS of the clay fraction of Oregon soil S20U. Three major species 1.) Ni adsorbed to goethite, 2.) nickel incorporated into structural goethite, and 3.) Ni-bound to manganese oxides were found as the major species, with each contributing 24%, 27% and 49% to the spectrum, respectively. This indicates that iron and manganese oxides play a critical role in the clay fraction of nickel speciation in this serpentine soil.

Micro-XAS: μ-SXRF, μ-XRD, and Data Analysis

μ-SXRF and μ-XRD

Figure 5.14 is an example of a petrographic thin section 30 μm thick (left), and a close up photo of the area raster scanned by the synchrotron micro-beam at SSRL BL 2-3. This figure illustrates on an eye-level scale the procedure and information obtained from micro-fluorescence. Photos taken with microscope camera at NSLS X27A.

Figures 5.15-5.17 are μ-SXRF maps of COII 0-2 cm from a thin section of the <2 mm soil. Each map shows a different distribution of Ni versus Mn and Fe. In Figure 5.15, one large mineral particle (approx. 150x70 microns) is highly correlated with Ni and Mn. Fe is also present but not distributed in the same manner as Ni or Mn. Cr is not

correlated with other metals except Zn (not shown). Lower amounts of Ni are also present in the large Fe bearing minerals, indicating that Ni has a low level, ubiquitous abundance in some of the larger Fe rich minerals.

Figure 5.16 illustrates another distinct Ni distribution pattern. Here Fe and Mn accumulate together in the veins of larger minerals, however, Ni concentration sharply decreases in these veins and is concentrated more homogeneously in the bulk mineral. Lastly, Figure 5.17 demonstrates an example where Ni and Mn accumulate together in what appears to be veins of the larger mineral. Fe is independently distributed from Mn and Ni.

Figures 5.18-5.22 show the elemental fluorescence and μ-SXRD spectra from the sand, silt and clay fractions of the Oregon soil S10T2. The removal of secondary mineral coatings via sonication allowed for strong elemental fluorescence (e.g., Ni) from bulk minerals. The minerals identified via micro-XRD on specific elemental hotspots are listed in the Mineralogical Key along with a table of elements at present at each spot [Figures 5.19 and 5.21].

Figure 5.18 shows the elemental maps and correlations in Oregon Soil S10T2 sand fraction. The fluorescence maps in Figure 5.18 in conjunction with the micro-XRD diffractograms obtained from this map shown in Figure 5.19 illustrate that magnesium silicate minerals like lizardite commonly contain Mn and Ni. Additionally, discrete Ni fluorescence also occurs in these minerals. At other nickel hotspots, the diffractograms showing both lizardite and goethite indicate these two minerals exist very intimately [spot 5, Figures 5.18 and 5.19]. Iron hotspots show diffraction patterns for goethite and

hematite [spot 13, Figures 5.18 and 5.19]. Spots where Ni was the predominant element gave diffraction patterns for various magnesium silicate minerals like lizardite and pyroxene [spots 2 and 9]. Even though few peaks are obtained for this particle, they match lizardite. It is common in micro-diffraction to not obtain diffraction peaks from all the surfaces of a mineral because the beam size is very small compared to a bulk diffractometer. In a hotspot of Mn and Ni, a pyroxene magnesium silicate mineral was found, though the diffraction peaks are weak. Quartz was also detected in the sand fraction. Hotspots for Zn and Cr showed zincochromite and chromite peaks [spots 11 and 12]. On pure Fe spots, goethite gave the predominant diffraction peaks with some additional peaks attributed to zincochromite, which probably resulted from the 10 μm rocking during spectrum collection [spot 14]. Spot 15, with high Ca and low Ni fluorescence, showed peaks for a magnesium silicate pyroxene. Spot 16 gave hematite peaks.

The fluorescence data collected from the medium sand particles show several areas where nickel and iron are correlated. In the correlation plots [Figures 5.18], there are several areas where Ni has a different relationship with iron. In at least one area, Ni and Fe appear to be heavily correlated, while in two other areas, Ni fluorescence is independent of Fe, indicating a variety of Ni species are present. Ni and Mn, in general, are not highly correlated in the sand fraction. There are two spots where the two elements co-occur [spots 15 and 7, Figure 5.18]. Ni and Cr are not correlated in the sand fraction, while Ni and Si appear to have several clusters of a linear relationship, indicating that the Ni and Si are correlated.

Figures 5.20 and 5.21 show the fluorescence and diffraction from the silt fraction of Oregon Soil S10T2. In the silt fraction, Ni and Fe correlation is much less than in the sand fraction. From the fluorescence map, however, there are several particles were Ni and Fe do appear together [spot 5 and 7]. Ni and Mn have several particles of high correlation in the silt fraction [spots19, 12, 13, 14]. Ni and Cr are not associated in the silt fraction. Ni and Si have less correlation in the silt fraction than in the sand fraction, with little evidence of correlation from the plots or maps.

In the silt fraction, high Ni and Fe spots showed diffraction peaks for magnesium silicate and iron oxide minerals. Spot 6, high in Ni, showed clear peaks for lizardite, one of the three serpentine minerals. Quartz and another magnesium silicate, chlorite, were found at spot 7, which is high in both Fe and Ni. Hot iron spots [8, 9, and 11] gave diffraction peaks for hematite, magnesioferrite and manganosite, indicating Mg accumulation in Fe particles. A pure Mn spot gave very clear diffraction peaks of lizardite, indicating the presence of Mn in this mineral [spot 12]. A hot spot of Ti [17] revealed anatase and ilmenite.

The clay fraction demonstrates a completely different relationship than particles sizes 10-100 times larger. The sub 2 micron particle sizes show complete elemental co-occurrence in the fluorescence map and hence in the correlation plots. Micro-XRD from the clay fraction revealed very similar spectra, which is in agreement with the correlation data and the fluorescence maps. The peaks on spot 3 were matched with very good agreement to the minerals phlogopite, lizardite, goethite, and hematite. Phlogopite is common to ultramafic igneous rocks.

Conclusion

The heterogeneity of nickel in our serpentine soil samples was identified using micro-synchrotron based techniques. Nickel is distributed in many forms, including with iron and manganese and as discrete particles on the micron scale. The bulk EXAFS provided an average of the nickel speciation in each soil sample, with nickel heavily distributed in the clay fractions of several soils. Also, in the speciation of nickel changes depending on particle size, in the sand, silt or clay.

The extensive literature available on serpentine soils over the past 50 years gives good predictions of nickel speciation based on four of the five soil formation factors: parent material, climate, topography, and time. The uniqueness of the parent material hampers the biological factor so many plants cannot grow in the extreme soil chemical conditions. Based on LCF of bulk EXAFS data, (Figure 5.13), iron and manganese oxides are the principle compounds for nickel accumulation in S20UNT clay fraction serpentine topsoil.

Table 5.1   List of Synchrotron Beamlines Used in This Study.

Beamline	Technique	Monochromator	X-ray detector types	approximate spot size (horizontal x vertical)
NSLS X11A	Bulk EXAFS	Si (111)	Lytle	5x1mm
NSLS X11B	Bulk EXAFS	Si (111)	Lytle	5x1mm
NSLS X26A	Microprobe	Si (111)	9-element germanium array	11x5μm
NSLS X27A	Microprobe	Si(111)	13-element germanium array	15x10μm
SSRL 2-3	Microprobe	Si(111); Si(220)	Vortex detector	2x2μm
SSRL 4-1	Bulk EXAFS	Si(220)	13-element germanium array	5x1mm
SSRL 9-3	Bulk EXAFS	Si(220)	100 - element germanium array	5x1mm
SSRL 10-2	Microprobe	Si(111)	Ge array detector	50x50μm
SSRL 11-2	Bulk EXAFS	Si(220)	30 - element germanium array	5x1mm
SSRL 11-3	Bulk XRD	Bent cube-root I_beam Si(311), Side deflecting	MAR345 Imaging Plate	150x150μm

Table 5.2   Physicochemical Data of the Oregon and Maryland Soils

Sample ID	pH	Sand (%)	Silt (%)	Clay (%)	OM (%)	Ni (mg/kg)	Fe (mg/kg)	Co (mg/kg)	Cr (mg/kg)	Mn (mg/kg)
OR Series S3 Untreated	6.5	-	-	-	4.8	2627	41623	181	1555	2111
OR Series S5 T2	6.0	25	49	27	5.1	1514	67880	87	580	1342
OR Series S6 T2	6.1	42	37	21	5.1	544	29013	49	398	1065
OR Series S7 T2	5.6	57	25	18	5.5	736	32171	64	493	1147
OR Series S8 T2	5.8	35	36	29	5.8	1070	54945	63	540	987
OR Series S9 T2	6.4	28	33	39	4.0	2329	38726	229	2913	2870
OR Series S10 T2	6.3	57	23	20	5.4	4711	46365	243	2296	2970
OR Series S11 T2	5.8	49	29	22	5.3	1783	35875	95	1106	1516
OR Series S11 Untreated	5.6	45	31	25	5.4	1661	73759	100	1866	1620
OR Series S12 T2	6.3	50	21	29	6.3	2579	38302	156	634	1673
OR Series S13 T2	6.4	37	30	33	6.5	4164	46319	311	1791	3359
OR Series S14 T2,sieved	6.1	43	31	26	6.1	3698	111000	211	2284	2937
OR Series S15 T2	6.2	56	24	20	3.2	2474	38202	119	1015	1404
OR Series S16 T2	6.0	38	41	21	3.6	500	31697	54	185	900
OR Series S16 Untreated	6.3	39	43	18	2.7	558	27711	66	501	1100
s17unt,sieved	6.2	62	22	16	2.8	2042	60620	188	1696	2506
OR Series S18 T2	6.2	39	31	31	5.2	4634	193042	294	3086	3122
s19t2,new,sieved	5.7	45	31	24	3.6	118	34039	28	175	1370
s19unt,new,again	5.2	45	31	24	2.8	110	31826	28	93	1472
OR Series S20 T2	6.5	32	29	39	3.7	8065	48710	284	1763	3614
OR Series S20 Untreated	6.9	34	27	39	3.6	5974	138606	242	1608	3098

Figure 5.1   A – antigorite, B – brucite, Ch – chromite, Cl – clinochlore, Co – cordierite, Ct – chlorite, E – enstatite, F – forsterite, Fr – ferrosilite, G – goethite, H – hematite, L – lizardite, L2 - Lizardite 2H1, M – magnetite, P – pyroxene, Pg – pargasite, Q – quartz, T – talc. The sand, silt and clay fraction diffractograms are shown in this figure. DT signifies "Dithionite Treated" clay fractions that were treated with the citrate dithionite method to remove iron oxides. In the DT samples, the disappearance of peaks associated with hematite, magnetite and goethite can be noted when compared to the non-treated samples. Enstatite is a common mineral found in many serpentine soils. Quartz and clinochlore are also common. The clay fraction is commonly composed of serpentine minerals, iron oxides and clinochlore.
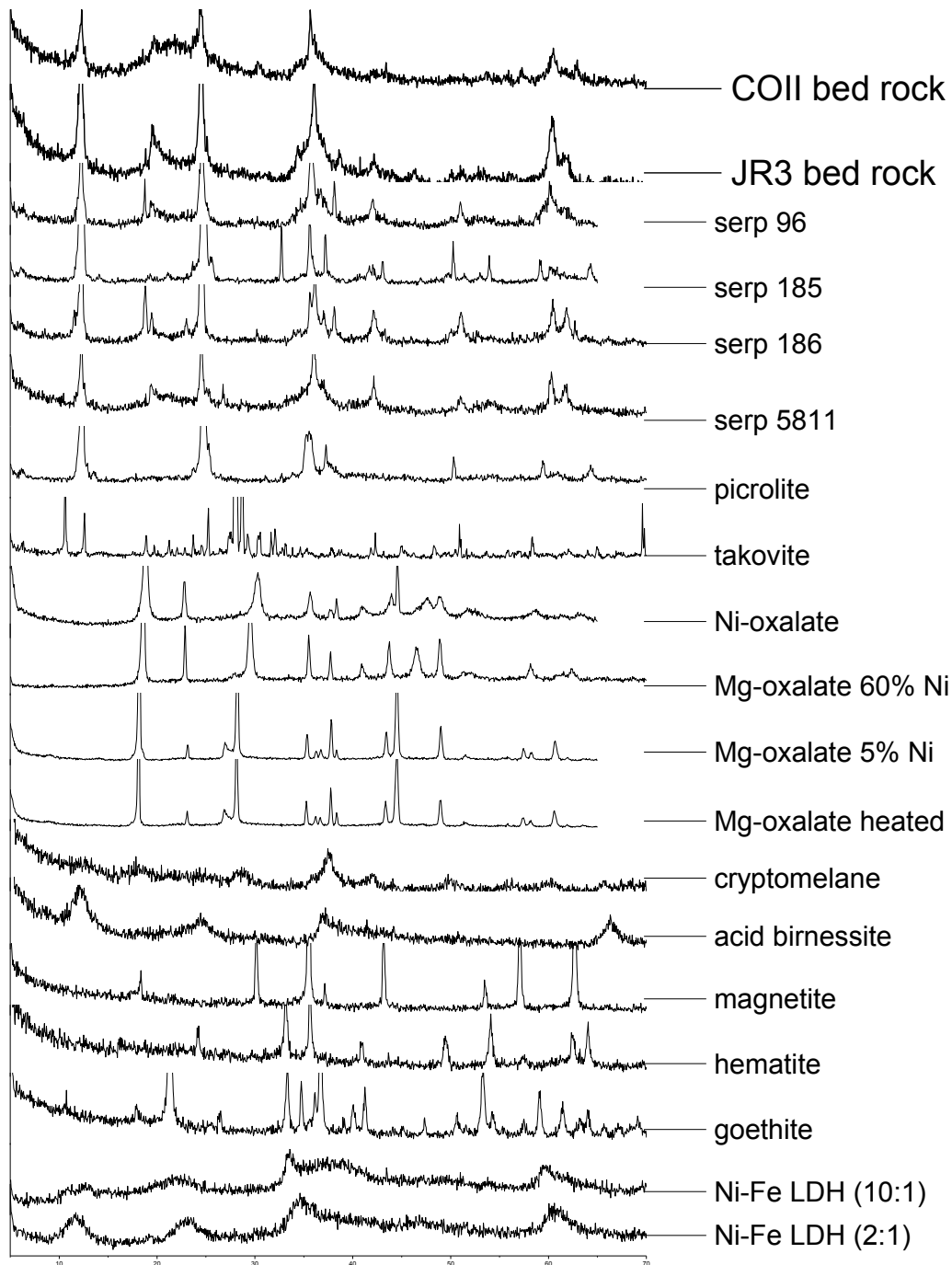
Figure 5.2   XRD spectra of nickel enriched and serpentine minerals, some used as standards for EXAFS LCF. A comparison of JR3 bedrock and serpentine 96 indicates the bedrock is mostly serpentine mineral.

177
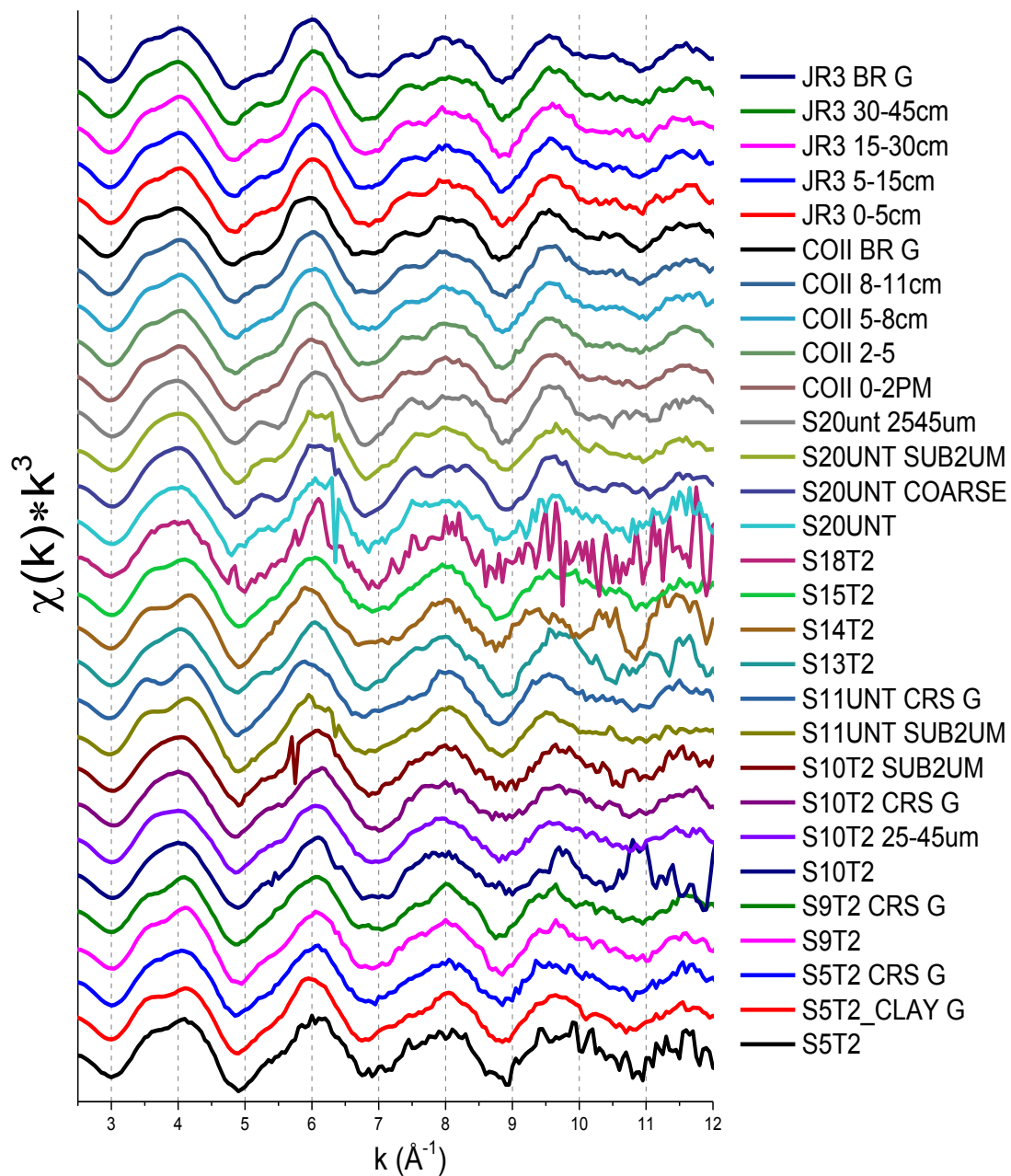
Figure 5.3   Bulk EXAFS of Oregon, California, and Maryland soils and Soil Fractions.
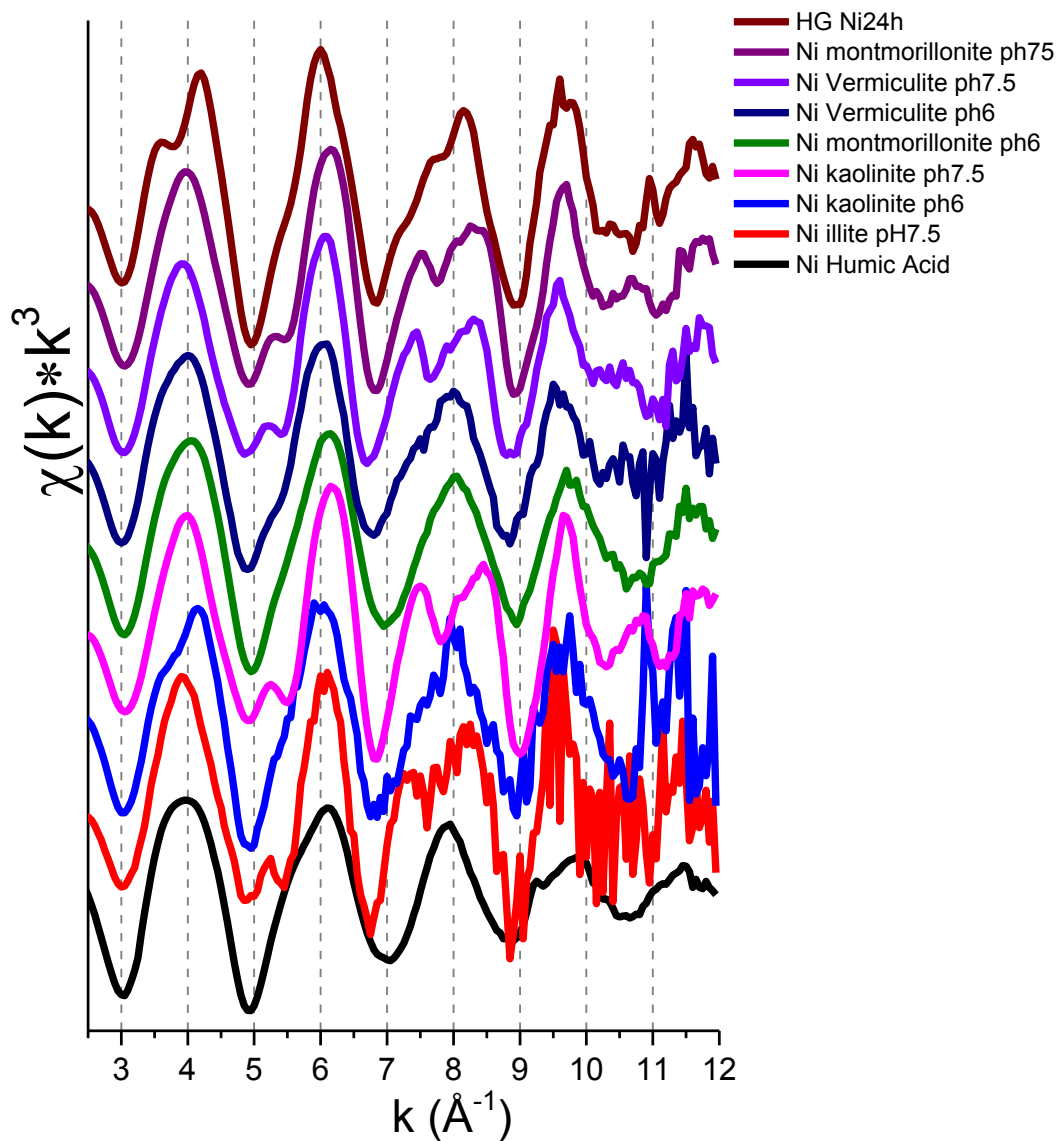
Figure 5.4   Set 1 of Standards Used in Linear Combination Fitting of Serpentine Soils[a].
[a]Some raw spectra presented in this figure were originally published in one
of the following sources: Arai, 2008; Ford et al., 1999; McNear et al., 2007;
Peltier et al., 2006; Scheinost and Sparks, 2000; Yamaguchi et al., 2002; or
Zhu et al., 2010.
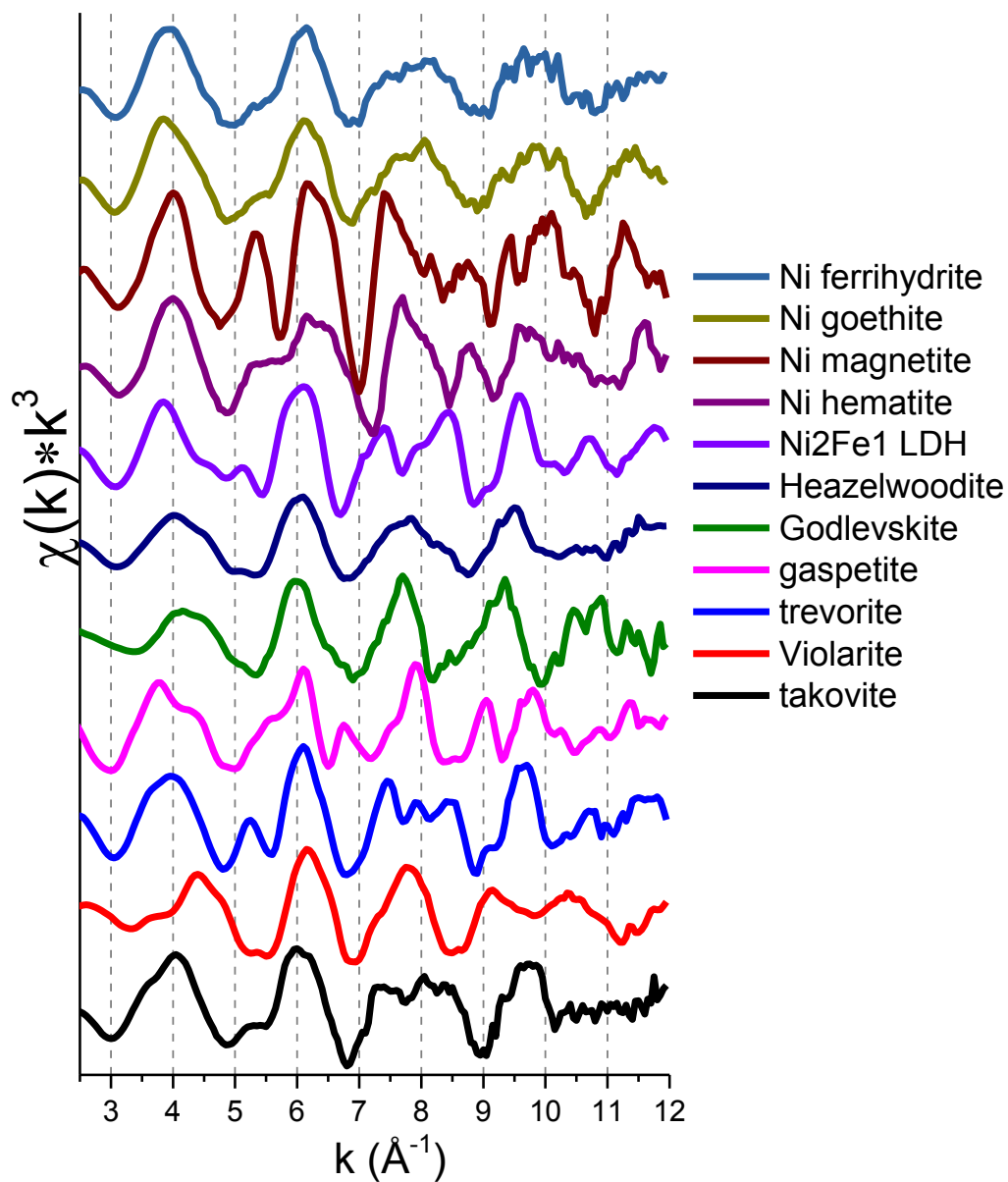
Figure 5.5   Set 2 of Standards Used in Linear Combination Fitting of Serpentine Soils[a].
[a]Some raw spectra presented in this figure were originally published in one of the following sources: Arai, 2008; Ford et al., 1999; McNear et al., 2007; Peltier et al., 2006; Scheinost and Sparks, 2000; Yamaguchi et al., 2002; or Zhu et al., 2010.
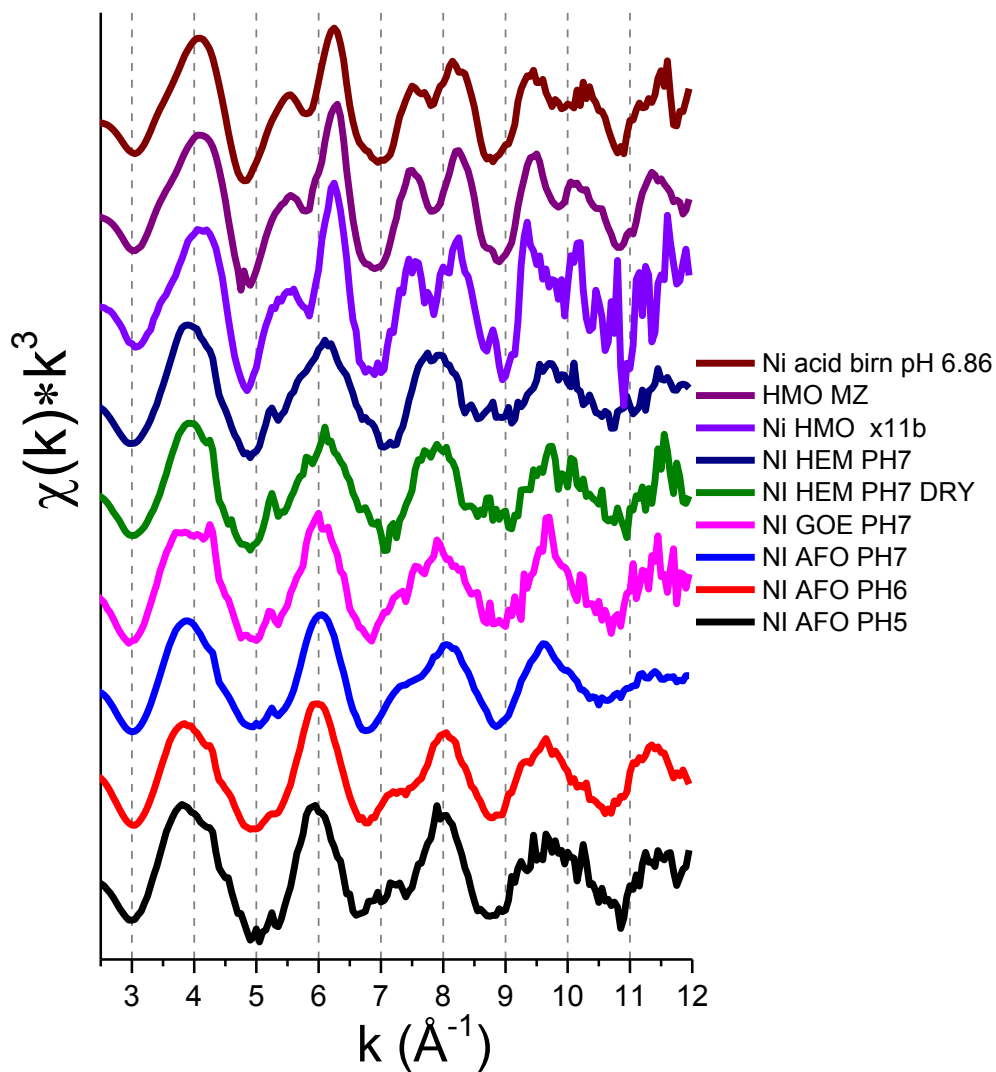
Figure 5.6   Set 3 of Standards Used in Linear Combination Fitting of Serpentine Soils[a].
[a]Some raw spectra presented in this figure were originally published in one of the following sources: Arai, 2008; Ford et al., 1999; McNear et al., 2007; Peltier et al., 2006; Scheinost and Sparks, 2000; Yamaguchi et al., 2002; or Zhu et al., 2010.
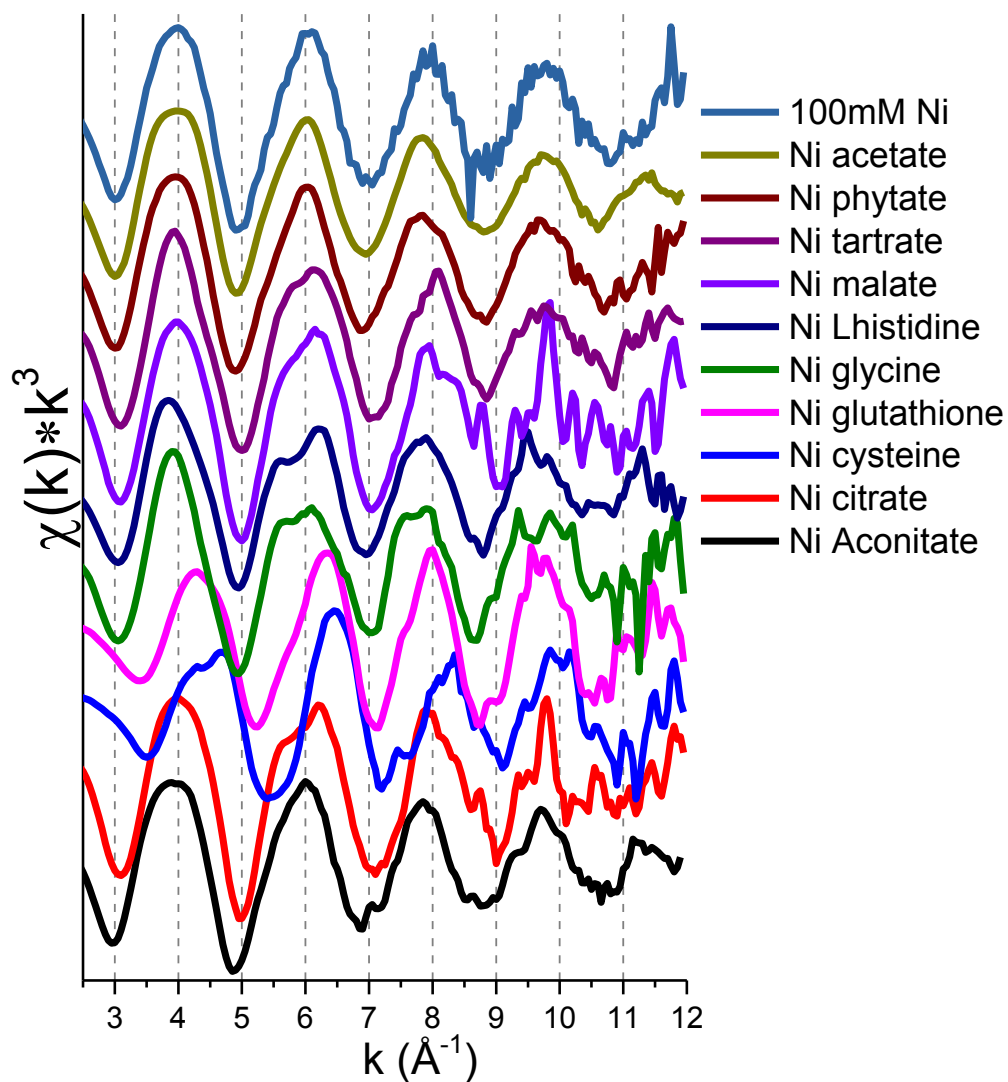
Figure 5.7   Set 4 of Standards Used in Linear Combination Fitting of Serpentine Soils[a].
[a]Some raw spectra presented in this figure were originally published in one of the following sources: Arai, 2008; Ford et al., 1999; McNear et al., 2007; Peltier et al., 2006; Scheinost and Sparks, 2000; Yamaguchi et al., 2002; or Zhu et al., 2010.
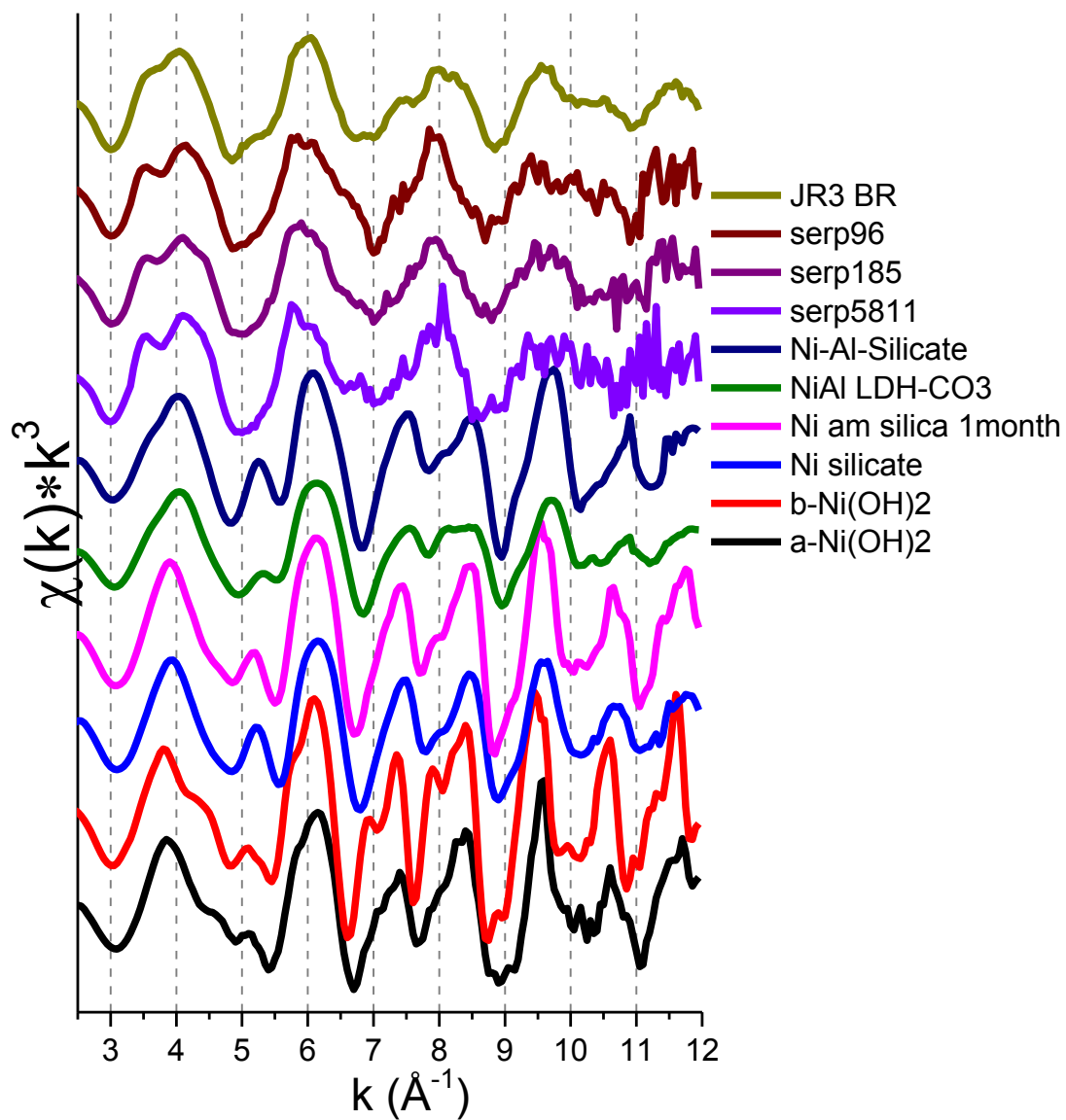
Figure 5.8   Set 5 of Standards Used in Linear Combination Fitting of Serpentine Soils[a].
[a]Some raw spectra presented in this figure were originally published in one of the following sources: Arai, 2008; Ford et al., 1999; McNear et al., 2007; Peltier et al., 2006; Scheinost and Sparks, 2000; Yamaguchi et al., 2002; or Zhu et al., 2010.
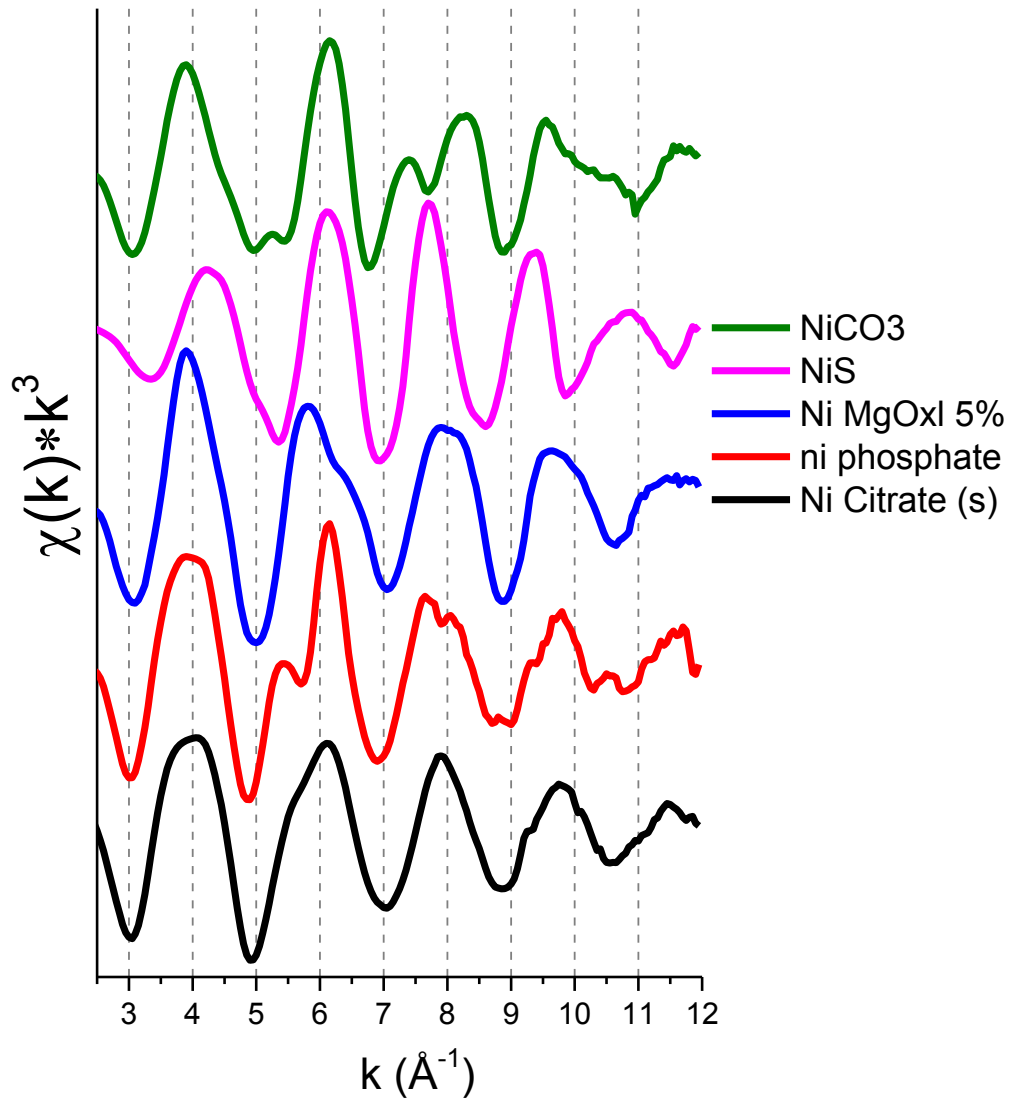
Figure 5.9   Set 6 of Standards Used in Linear Combination Fitting of Serpentine Soils[a].
[a]Some raw spectra presented in this figure were originally published in one of the following sources: Arai, 2008; Ford et al., 1999; McNear et al., 2007; Peltier et al., 2006; Scheinost and Sparks, 2000; Yamaguchi et al., 2002; or Zhu et al., 2010.
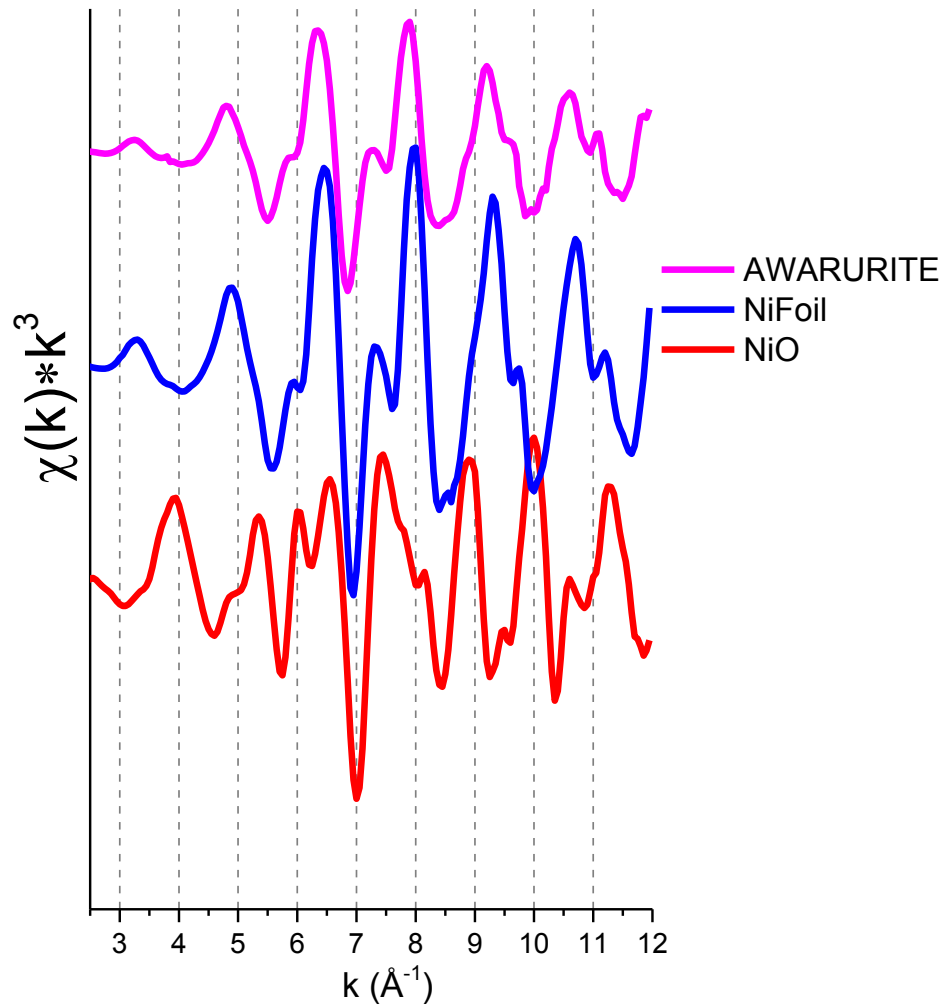
Figure 5.10   Set 7 of Standards Used in Linear Combination Fitting of Serpentine Soils[a].
[a]Some raw spectra presented in this figure were originally published in one
of the following sources: Arai, 2008; Ford et al., 1999; McNear et al., 2007;
Peltier et al., 2006; Scheinost and Sparks, 2000; Yamaguchi et al., 2002; or
Zhu et al., 2010.
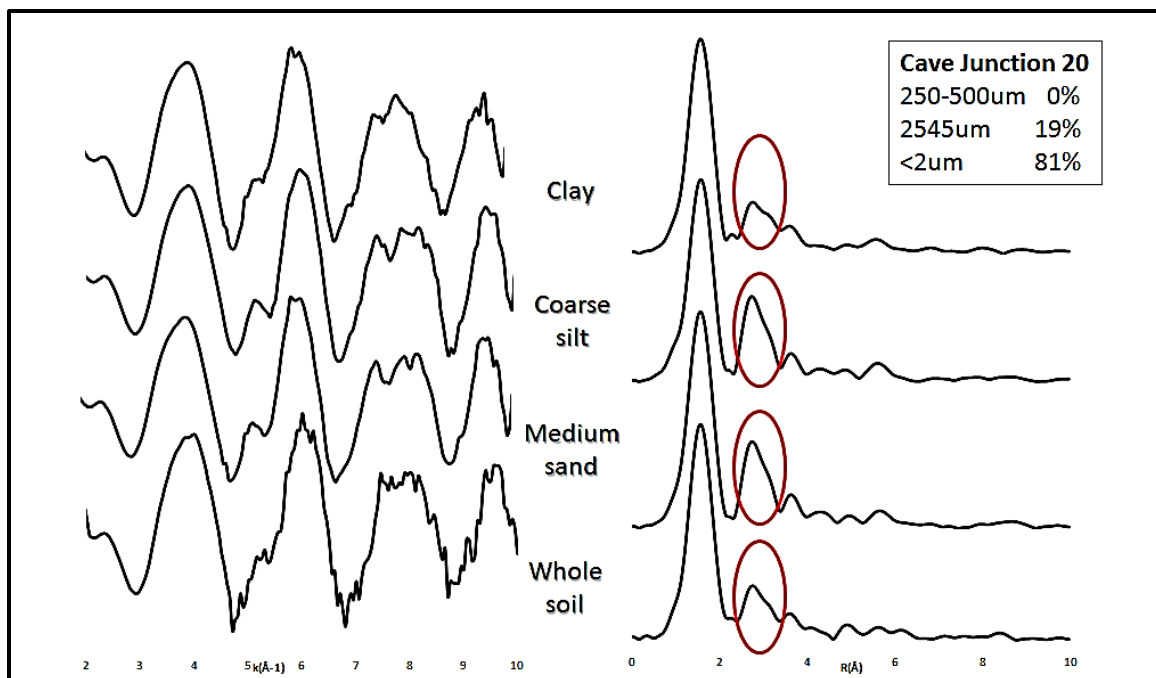
Figure 5.11 Bulk Ni K-edge EXAFS spectra of Oregon S20U sample. The four spectra represent the different particle size fractions. The left side of the figure is the data in k-space and the right side of the figure are the Fourier Transformed Radial Structure Function spectra. Spectra from the clay, silt, sand and whole soil are shown (top to bottom). The clay fraction and whole soil fraction have smaller second shell peaks as compared to the silt and sand fractions. This is due to the difference in nickel speciation in each size fraction. A linear combination fit of the whole fraction spectra (bottom) using the other three spectra determine that the clay portion (sub-2 μm fraction) contribute to more than 80% of the whole soil fraction, showing the dominance of the clay fraction in terms of nickel speciation in this sample.

186
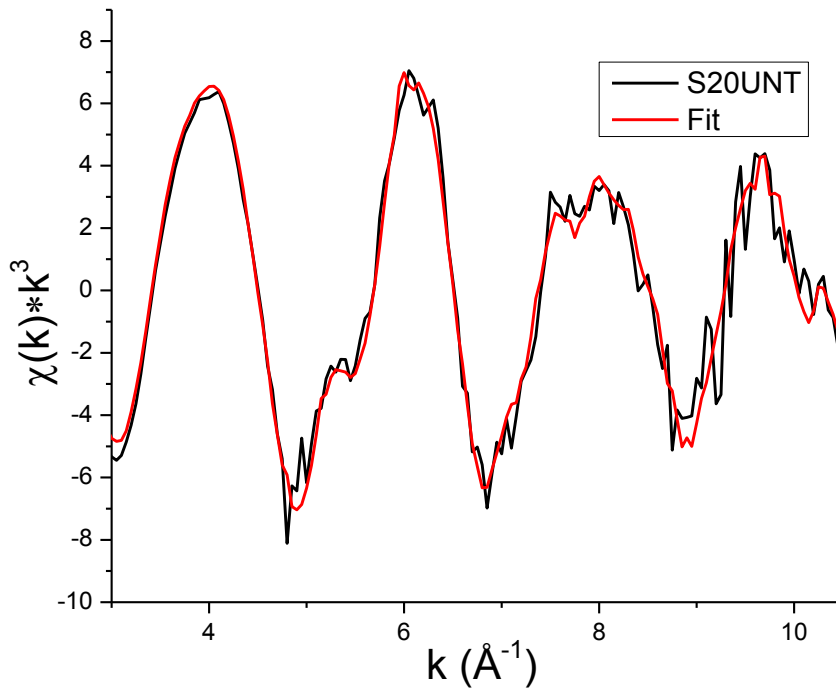
Figure 5.12 This LCF of S20UNT whole fraction soil using EXAFS spectra taken from each of its particle size fractions shows that the clay fraction accounts for 77% of the nickel signal. A significant portion of nickel is located in the clay fraction.
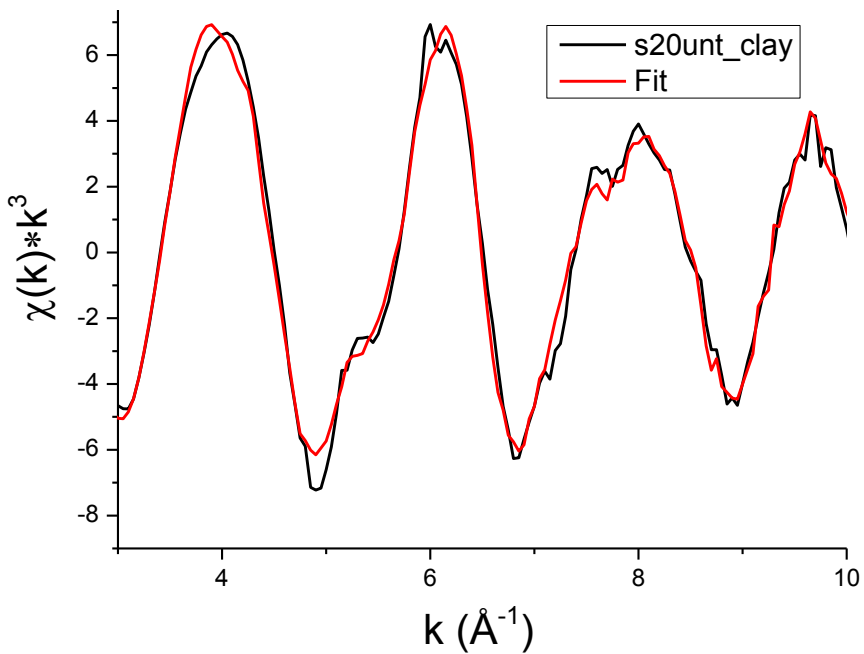
Figure 5.13 A LCF of Ni K-edge bulk EXAFS of the clay fraction of Oregon soil S20U. Three major species 1.) Ni adsorbed to goethite, 2.) nickel incorporated into structural goethite, and 3.) Ni-bound to manganese oxides were found as the major species, with each contributing 24%, 27% and 49% to the spectrum, respectively. This indicates that iron and manganese oxides play a critical role in the clay fraction of nickel speciation in this serpentine soil.

petrographic thin
section photo

2.5cm

photo   iron   nickel
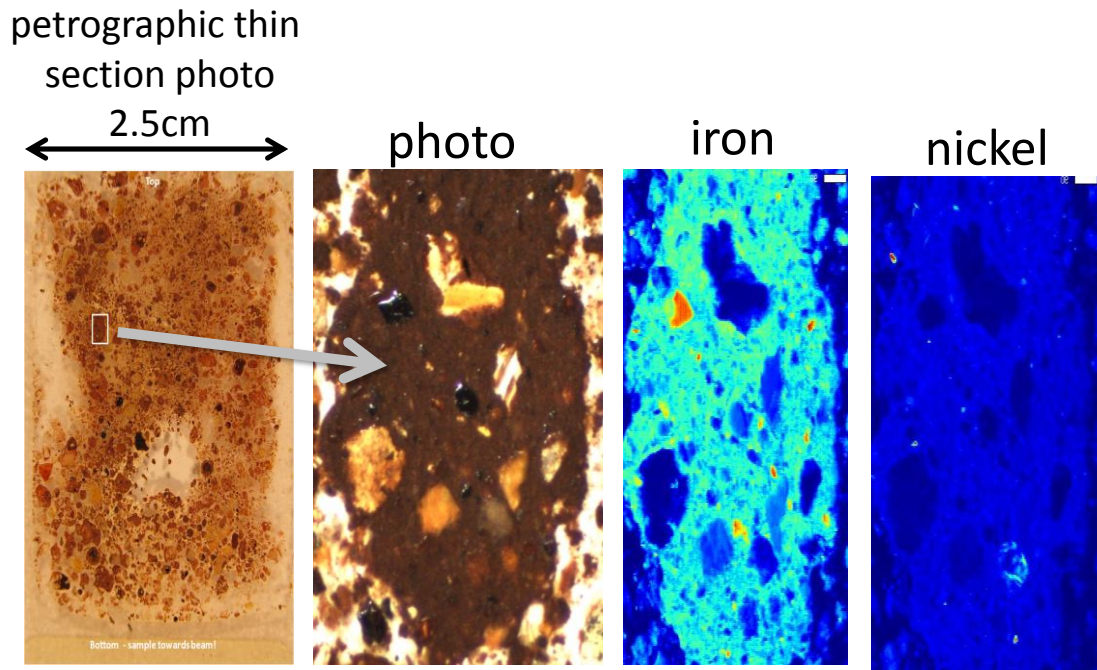
Figure 5.14   An example of a petrographic thin section 30 μm thick (left), and a
close up photo of the area raster scanned by the synchrotron micro-
beam at SSRL BL 2-3. This figure illustrates on an eye-level scale
the procedure and information obtained from micro-fluorescence.
Photos taken with microscope camera at NSLS X27A.
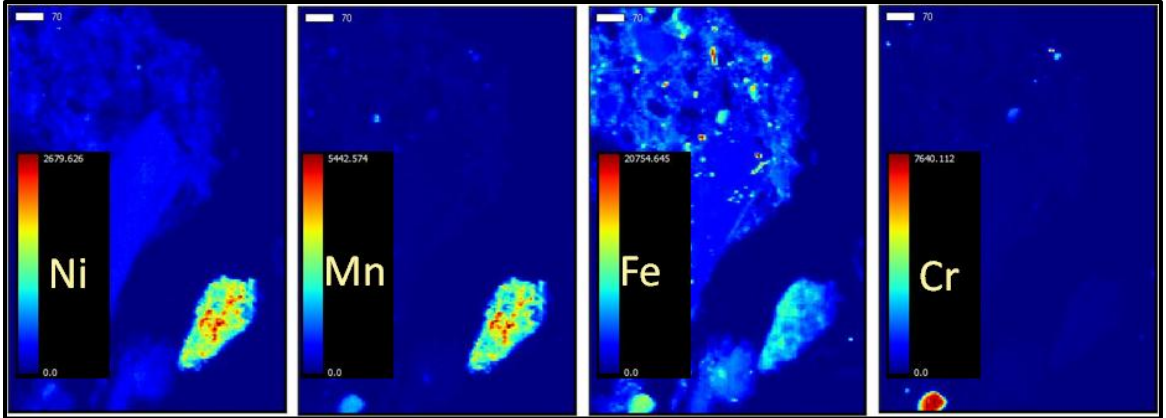
Figure 5.15   This micro-XRF map is of California soil COII 0-2cm. Elemental fluorescence of Ni, Mn, Fe, and Cr is shown. In these maps, nickel is highly correlated with manganese in a particle in the lower left of the map. Iron is also present but distributed differently. Additionally, iron is present in a larger particle along with lower concentrations of nickel in the upper central/left portion of the map. Chromium is not associated with other elements shown here, which is common for chromite particles typically found in serpentine soils.
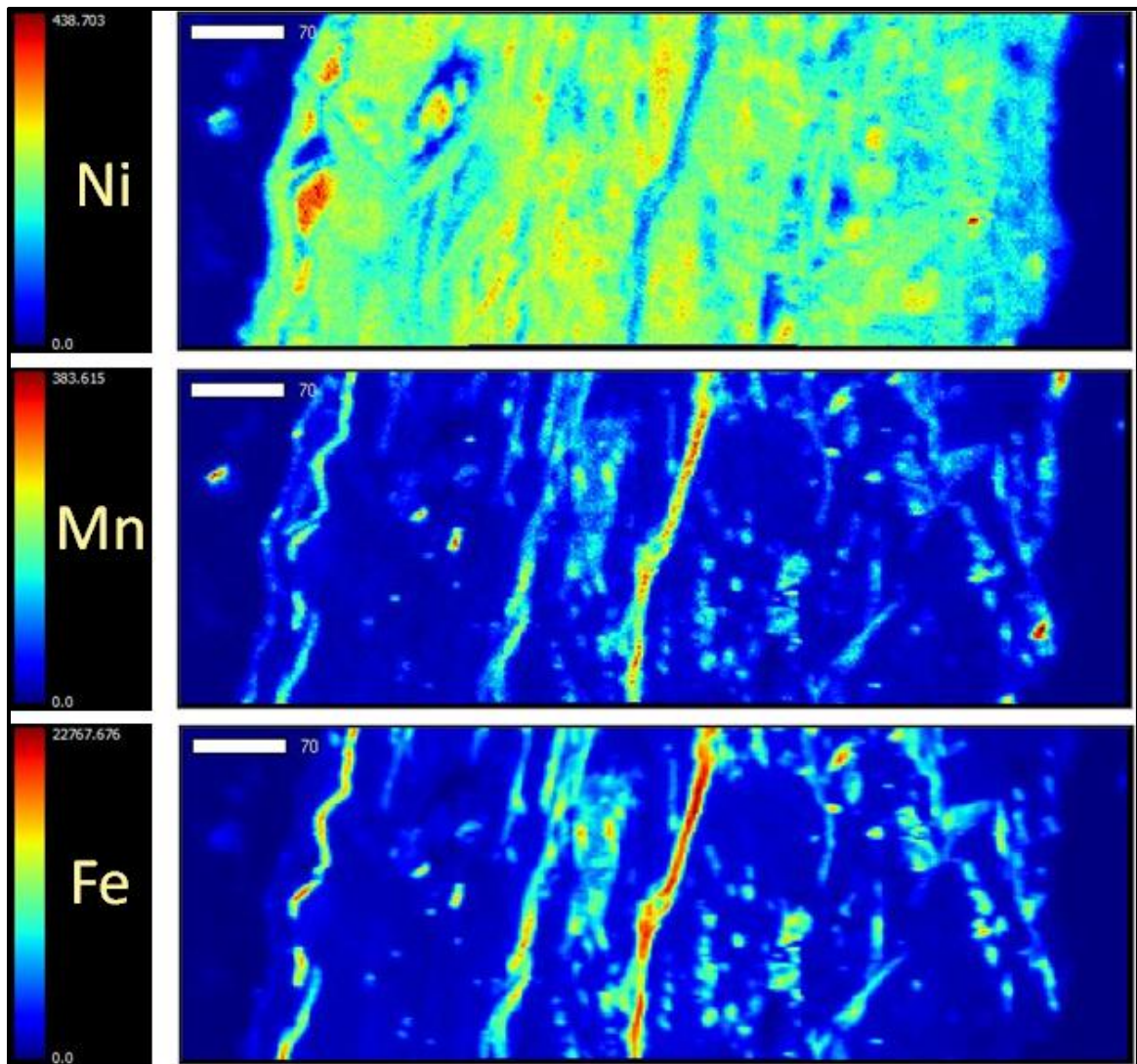
Figure 5.16 This micro-XRF map is of California soil COII 0-2cm. Elemental fluorescence of Ni, Mn, and Fe is shown. Here nickel is abundant in the majority of the particle, but there appears a vein in the middle of the particle where iron and manganese accumulate together and nickel concentration decreases.
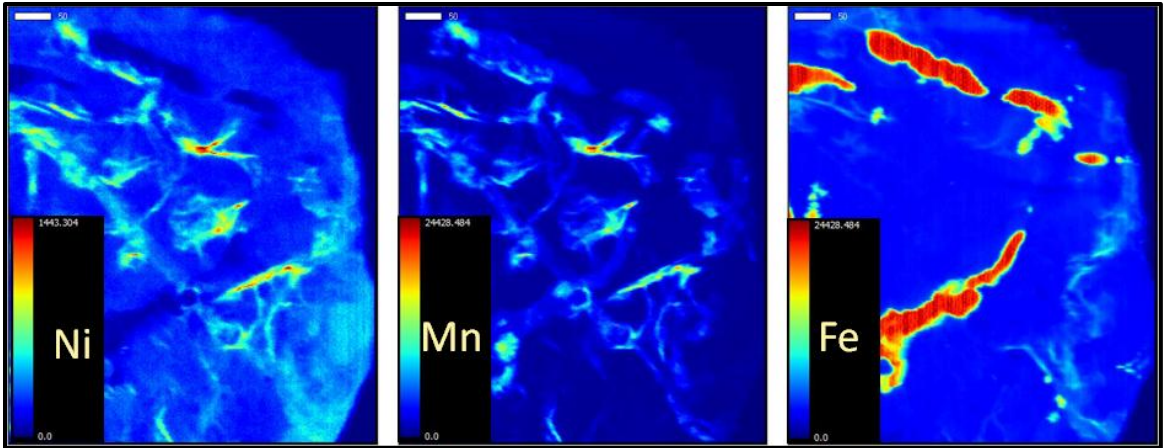
Figure 5.17   Micro-XRF map of California soil COII 0-2cm. Elemental fluorescence of Ni, Mn and Fe is shown separately. In this particle the distribution of nickel appears to be similar is several areas to this distribution of manganese. While iron is distributed throughout the particle, there are several areas significantly higher in iron concentration. Those areas are not associated with an increase in nickel or manganese.
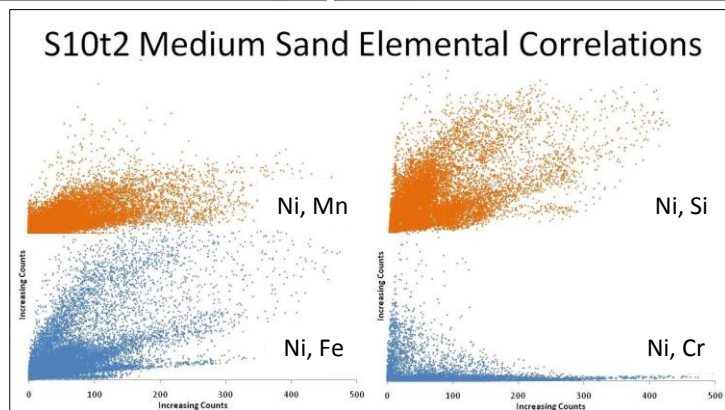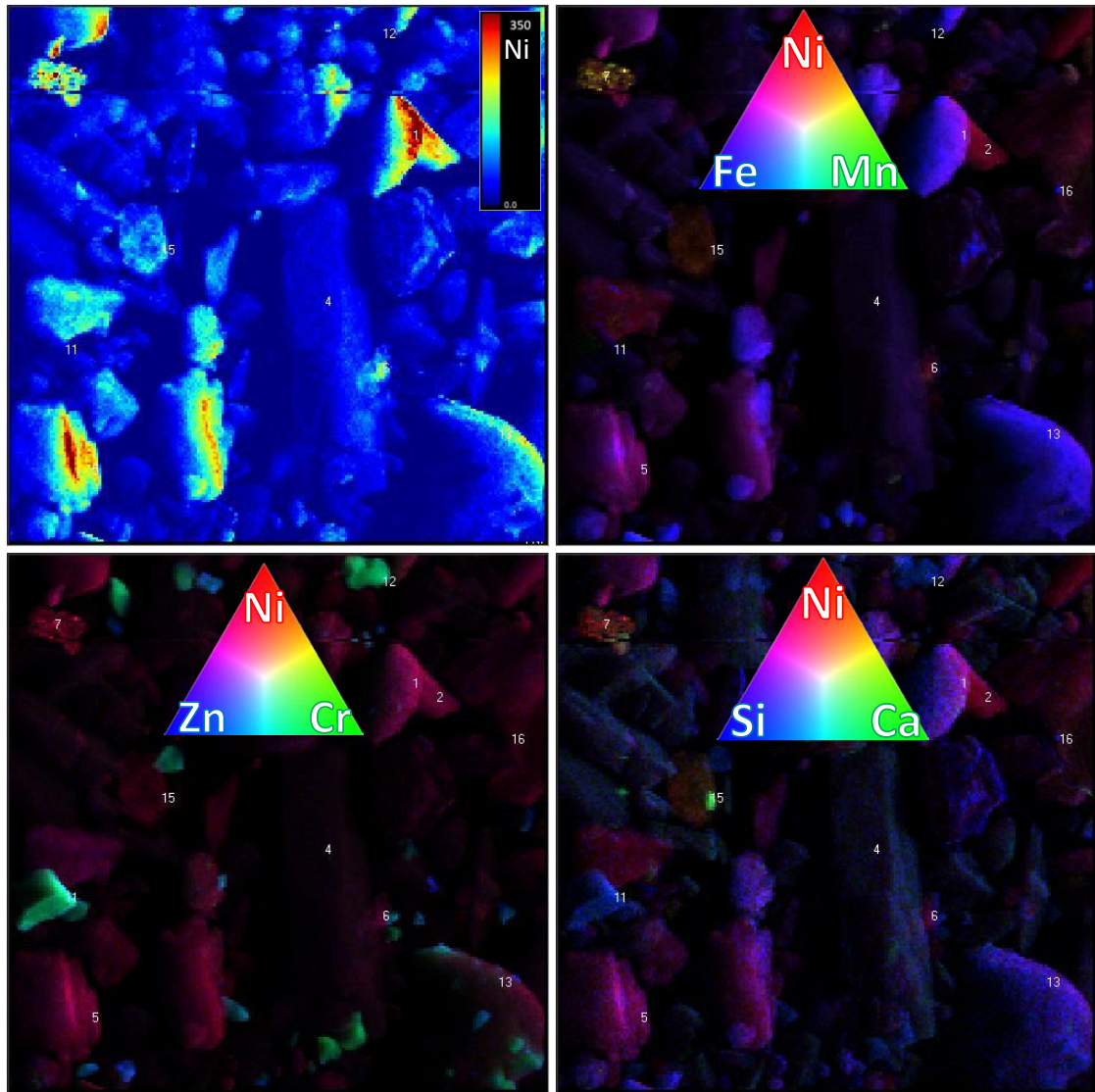
Figure 5.18   Elemental Maps in Oregon Soil S10T2 Sand Fraction.

Mineralogical Key:
Lizardite (L)
Goethite (G)
Clinochlore (C)
Quartz (Q)
Zincochromite (Zc)
Chromite (Cr)
Pyroxene (P)
Chlorite (Ch)
Magnesioferrite (MgF)
Anatase (Ti)
Ilmenite (I)
Clay Fraction:
Phlogopite (P)
Hematite (H)

Spot	Elements
1	Ni Fe
2	Ni
3	same as 2
4	Si Fe
5	Ni Fe Si
6	Zn Cr
7	Mn Ni Ca
8	same as 2
9	same as 2
10	same as 7
11	Zn Cr
12	Cr
13	Ni Fe Si
14	same as 4
15	Ca Mn Ni
16	Fe Si
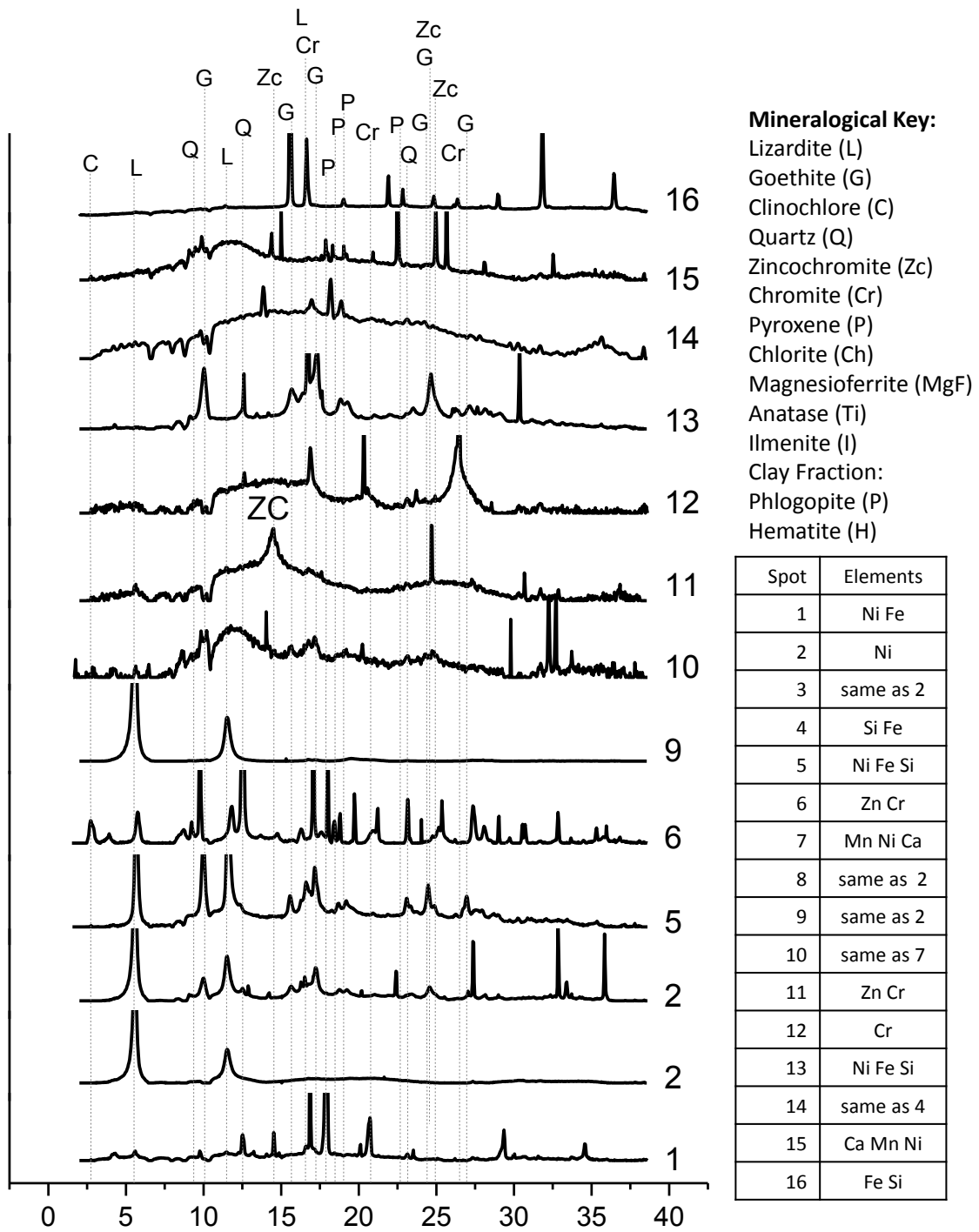
Figure 5.19   Micro-XRD Diffractograms from Oregon Soil S10T2 Sand Fraction.

194
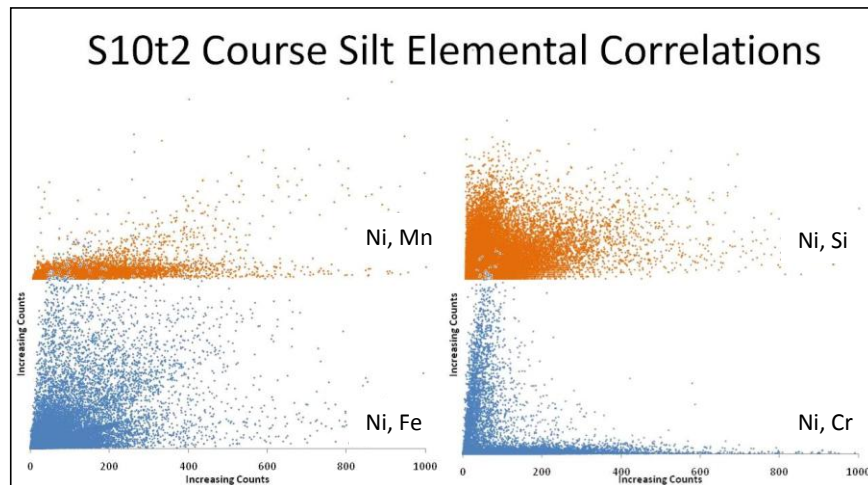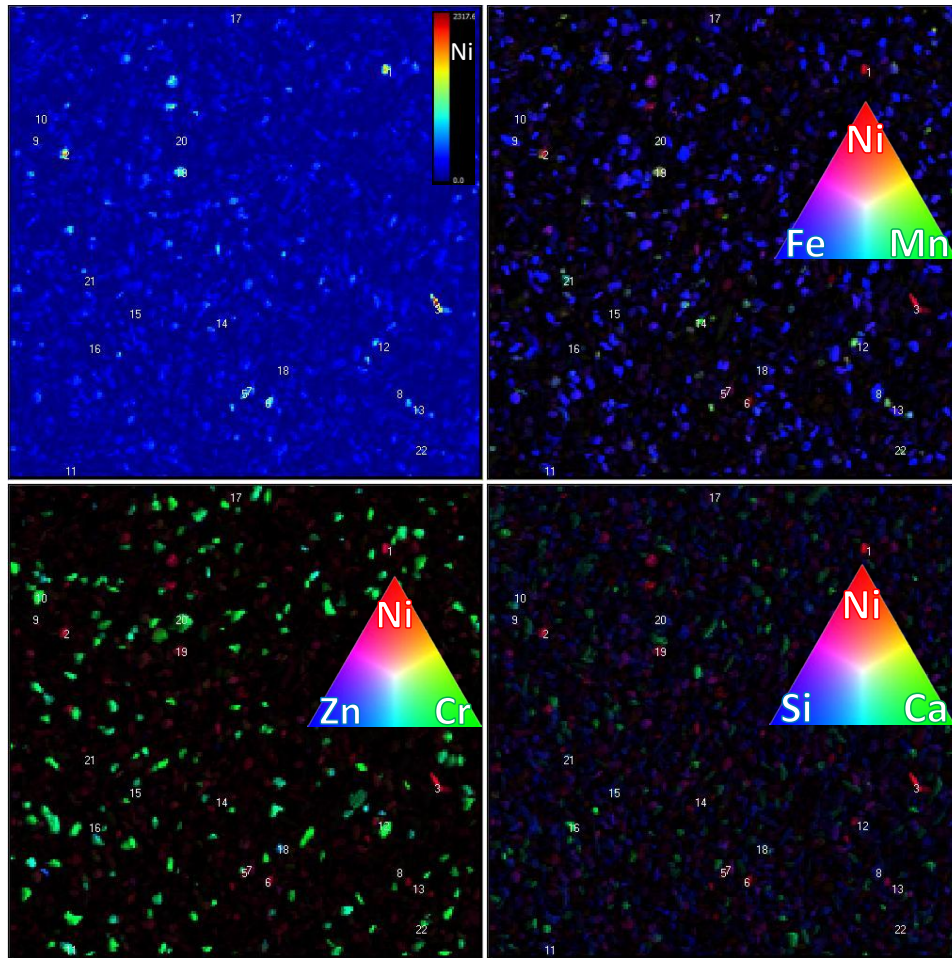
Figure 5.20   Elemental Maps and Correlations in Oregon Soil S10T2 Silt Fraction.
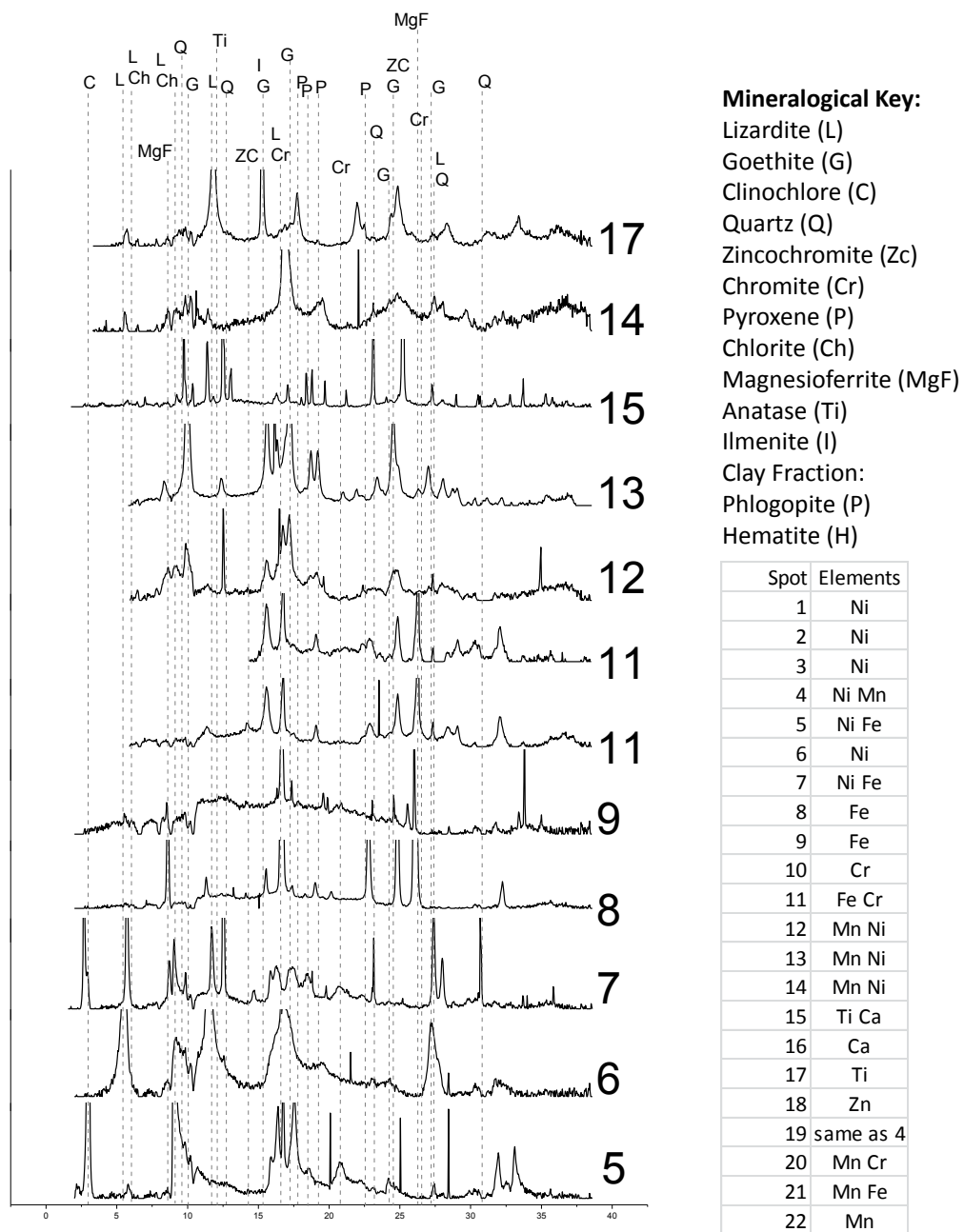
Figure 5.21   Micro-XRD Spectra from Oregon Soil S10T2 Silt Faction.
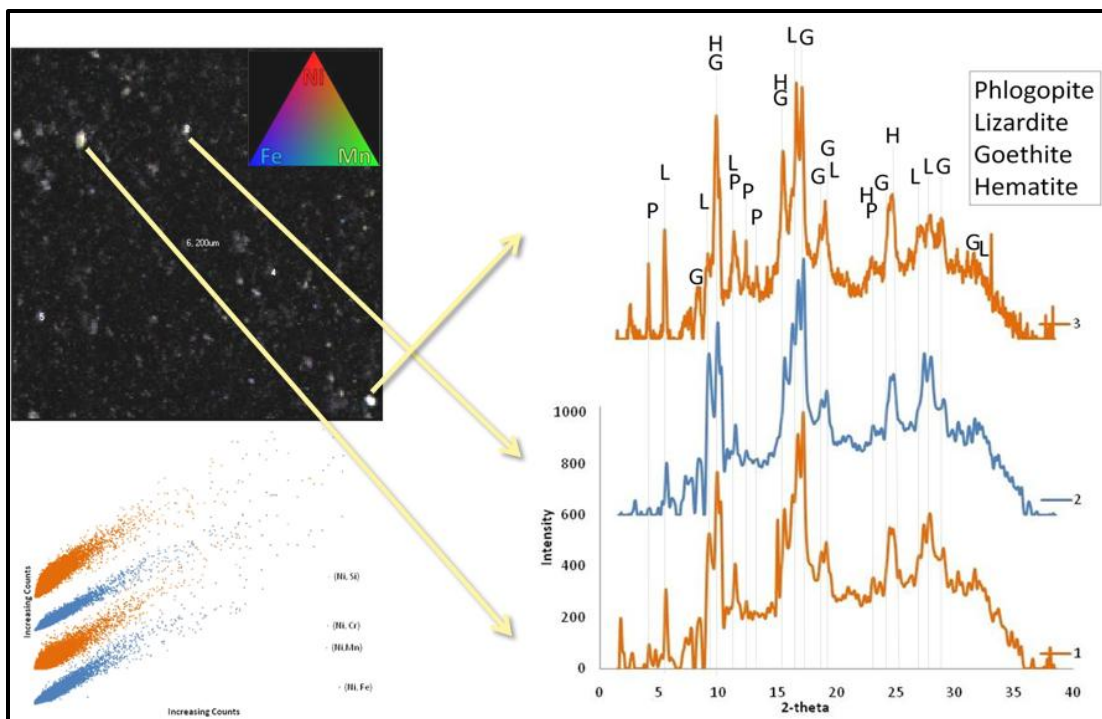
Figure 5.22 This figure contains μ-SXRF maps and μ-SXRD spectra of Oregon soil S10T2 - Clay fraction. The XRF map is gray because this is the clay fraction (sub-2 μm), which is the same size and smaller than the beam itself at SSRL BL 2-3. Because the sample particle sizes are the same and smaller than the beam the elements are homogeneously distributed throughout the map, making any meaningful correlations between different elements (e.g., Fe, Ni, Mn, Cr) impossible. The inability to find heterogeneity in the sample is highlighted by the correlation plot in the lower left corner, where Ni correlates with all elements. μ-SXRD was carried out on several hotspots, and the arrows indicate the corresponding integrated, background subtracted diffractograms in 2-theta. The three diffractograms also are very similar, indicating the homogeneity of the clay fraction. Several iron oxides, a serpentine mineral, and a phyllosilicate are identified via peak matching.

REFERENCES

Adamo, P., A. Marchetiello, and P. Violante. 1993. The weathering of mafic rocks by lichens. Lichenologist 25:285-297.

Alibhai, K.A.K., A.W.L. Dudeney, D.J. Leak, S. Agatzini, and P. Tzeferis. 1993. Bioleaching and bioprecipitation of nickel and iron from laterites. Fems Microbiology Reviews 11:87-96.

Alexander, E.B. 2009. Serpentine geoecology of the eastern and southeastern margins of North America. Northeastern Naturalist 16:223-252.

Alexander, E.B., C. Adamson, P.J. Zinke, and R.C. Graham. 1989. Soils and conifer forest productivity on serpentinized peridotite of the trinity ophiolite, California. Soil Science 148:412-423.

Alexander, E.B. 2004. Serpentine soil redness, differences among peridotite and serpentinite materials, Klamath Mountains, California. International Geology Review 46:754-764.

Alexander, E.B., and J. DuShey. 2011. Topographic and soil differences from peridotite to serpentinite. Geomorphology 135:271-276.

Alexander, E.B., C.C. Ellis, and R. Burke. 2007a. A chronosequence of soils and vegetation on serpentine terraces in the Klamath Mountains, USA. Soil Science 172:565-576.

Alexander, E.B., R.G. Coleman, T. Keeler-Wolf, and S.P. Harrison. 2007b. Serpentine geoecology of western North America: soils, geology, and vegetation. Oxford University Press.

Alves, S., M.A. Trancoso, M.D.S. Goncalves, and M.M.C. dos Santos. 2011. A nickel availability study in serpentinized areas of Portugal. Geoderma 164:155-163.

Amelung, W., and W. Zech. 1999. Minimization of organic matter disruption during particle-size fractionation of grassland epipedons. Geoderma 92:73-85.

Amelung, W., W. Zech, X. Zhang, R.F. Follett, H. Tiessen, E. Knox, and K.W. Flach. 1998. Carbon, nitrogen, and sulfur pools in particle-size fractions as influenced by climate. Soil Science Society of America Journal 62:172-181.

Antic-Mladenovic, S., J. Rinklebe, T. Frohne, H.J. Stark, R. Wennrich, Z. Tomic, and V. Licina. 2011. Impact of controlled redox conditions on nickel in a serpentine soil. Journal of Soils and Sediments 11:406-415.

Arai, Y. 2008. Spectroscopic evidence for Ni(II) surface speciation at the iron oxyhydroxides - water interface. Environmental Science & Technology 42:1151-1156.

Bani, A., G. Echevarria, S. Sulce, J.L. Morel, and A. Mullai. 2007. In-situ phytoextraction of Ni by a native population of *Alyssum murale* on an ultramafic site (Albania). Plant and Soil 293:79-89.

Bani, A., G. Echevarria, A. Mullaj, R. Reeves, J.L. Morel, and S. Sulce. 2009. Nickel hyperaccumulation by *brassicaceae* in serpentine soils of Albania and northwestern Greece. Northeastern Naturalist 16:385-404.

Becquer, T., C. Quantin, S. Rotte-Capet, J. Ghanbaja, C. Mustin, and A.J. Herbillon. 2006. Sources of trace metals in Ferralsols in New Caledonia. European Journal of Soil Science 57:200-213.

Bonifacio, E., E. Zanini, V. Boero, and M. FranchiniAngela. 1997. Pedogenesis in a soil catena on serpentinite in north-western Italy. Geoderma 75:33-51.

Borine, R. 1983. Soil Survey of Josephine County, Oregon. State Soil Scientist, Natural Resources Conservation Service (formerly Soil Conservation Service).

Bulmer, C.E., and L.M. Lavkulich. 1994. Pedogenic and geochemical processes of ultramafic soils along a climatic gradient in southwestern British-Columbia. Canadian Journal of Soil Science 74:165-177.

Burt, R., M. Fillmore, M.A. Wilson, E.R. Gross, R.W. Langridge, and D.A. Lammers. 2001. Soil properties of selected pedons on ultramafic rocks in Klamath Mountains, Oregon. Communications in Soil Science and Plant Analysis 32:2145-2175.

Buurman, P., E.L. Meijer, and J.H. Vanwijck. 1988. Weathering of chlorite and vermiculite in ultramafic rocks of Cabo Ortegal, northwestern Spain. Clays and Clay Minerals 36:263-269.

Caillaud, J., D. Proust, D. Righi, and F. Martin. 2004. Fe-rich clays in a weathering profile developed from serpentinite. Clays and Clay Minerals 52:779-791.

Caillaud, J., D. Proust, S. Philippe, C. Fontaine, and M. Fialin. 2009. Trace metals distribution from a serpentinite weathering at the scales of the weathering profile and its related weathering microsystems and clay minerals. Geoderma 149:199-208.

Carvalho-E-Silva, M.L., A.Y. Ramos, H.C.N. Tolentino, J. Enzweiler, S.M. Netto, and M. Alves. 2003. Incorporation of Ni into natural goethite: An investigation by X-ray absorption spectroscopy. American Mineralogist 88:876-882.

Centofanti, T., M.G. Siebecker, R.L. Chaney, A.P. Davis, and D.L. Sparks. 2012. Hyperaccumulation of nickel by *Alyssum corsicum* is related to solubility of Ni mineral species. Plant and Soil 359:71-83.

Chaney, R.L., J.S. Angle, C.L. Broadhurst, C.A. Peters, R.V. Tappero, and D.L. Sparks. 2007. Improved understanding of hyperaccumulation yields commercial phytoextraction and phytomining technologies. Journal of Environmental Quality 36:1429-1443.

Chaney, R.L. 2013 Personal communication.

Chardot, V., G. Echevarria, M. Gury, S. Massoura, and J.L. Morel. 2007. Nickel bioavailability in an ultramafic toposequence in the Vosges Mountains (France). Plant and Soil 293:7-21.

Cheng, C.H., S.H. Jien, H. Tsai, Y.H. Chang, Y.C. Chen, and Z.Y. Hseu. 2009. Geochemical element differentiation in serpentine soils from the ophiolite complexes, Eastern Taiwan. Soil Science 174:283-291.

Cheng, C.H., S.H. Jien, Y. Izuka, H. Tsai, Y.H. Chang, and Z.Y. Hseu. 2011. Pedogenic chromium and nickel partitioning in serpentine soils along a toposequence. Soil Science Society of America Journal 75:659-668.

Colin, F., D. Nahon, J.J. Trescases, and A.J. Melfi. 1990. Lateritic weathering of pyroxenites at Niquelandia, Goiás, Brazil - the supergene behavior of nickel. Economic Geology and the Bulletin of the Society of Economic Geologists 85:1010-1023.

Crystal-Impact. 2012. Match! 1.11d, Crystal Impact GbR, http://www.crystalimpact.com/match/Default.htm, info@crystalimpact.com.

Decarreau, A., F. Colin, A. Herbillon, A. Manceau, D. Nahon, H. Paquet, D. Trauthbadaud, and J.J. Trescases. 1987. Domain segregation in Ni-Fe-Mg-smectites. Clays and Clay Minerals 35:1-10.

Doelsch, E., I. Basile-Doelsch, J. Rose, A. Masion, D. Borschneck, J.L. Hazemann, H. Saint Macary, and J.Y. Borrero. 2006. New combination of EXAFS spectroscopy and density fractionation for the speciation of chromium within an Andosol. Environmental Science & Technology 40:7602-7608.

Downs, R.T., and M. Hall-Wallace. 2003. The American mineralogist crystal structure database. American Mineralogist 88:247-250.

Drits, V.A., A.I. Gorshkov, A.V. Mokhov, and E.V. Pokrovskaya. 1995. 201 (In Russian). Litol. Polez. Iskop. 3.

Ece, O.I., F. Coban, N. Gungor, and F. Suner. 1999. Clay mineralogy and occurrence of ferrian smectites between serpentinite saprolites and basalts in Biga Peninsula, northwest Turkey. Clays and Clay Minerals 47:241-251.

Echevarria, G., S.T. Massoura, T. Sterckeman, T. Becquer, C. Schwartz, and J.L. Morel. 2006. Assessment and control of the bioavailability of nickel in soils. Environmental Toxicology and Chemistry 25:643-651.

Fan, R., and A.R. Gerson. 2011. Nickel geochemistry of a Philippine laterite examined by bulk and microprobe synchrotron analyses. Geochimica et Cosmochimica Acta 75:6400-6415.

Faust, G.T. 1966. The hydrous nickel-magnesium silicates -the garnierite group. American Mineralogist 51:279-298.

Fisher, R.B., and W.M. Dressel. 1959. The Nicaro (Cuba) nickel ores : basic studies, including differential thermal analysis in controlled atmospheres U.S. Dept. of the Interior, Bureau of Mines, Washington, D.C.

Foose, M.P. 1992. Nickel - mineralogy and chemical composition of some nickel-bearing laterites in southern Oregon and northern California. U.S. Geological Survey Bulletin 1877:E1-E24.

Gasser, U.G., and R.A. Dahlgren. 1994. Solid-phase speciation and surface association of metals in serpentinitic soils. Soil Science 158:409-420.

Gasser, U.G., S.J. Juchler, and H. Sticher. 1994. Chemistry and speciation of soil-water from serpentinitic soils - importance of colloids in the transport of Cr, Fe, Mg, and Ni. Soil Science 158:314-322.

Gasser, U.G., R.A. Dahlgren, C. Ludwig, and A.E. Lauchli. 1995. Release kinetics of surface-associated Mn and Ni in serpentinitic soils - pH effects. Soil Science 160:273-280.

Gaudin, A., A. Decarreau, Y. Noack, and O. Grauby. 2005. Clay mineralogy of the nickel laterite ore developed from serpentinized peridotites at Murrin Murrin, Western Australia. Australian Journal of Earth Sciences 52:231-241.

Gaudin, A., S. Petit, J. Rose, F. Martin, A. Decarreau, Y. Noack, and D. Borschneck. 2004. The accurate crystal chemistry of ferric smectites from the lateritic nickel ore of Murrin Murrin (Western Australia). II. Spectroscopic (IR and EXAFS) approaches. Clay Minerals 39:453-467.

Gee, G.W., and D. Or. 2002. Particle-Size Analysis, In J. H. a. T. Dane, C., ed. Methods of Soil Analysis Part 4 Physical Methods. Soil Science Society of America Book Series, Madison, Wisconsin, USA.

Gerard, P., and A.J. Herbillon. 1983. Infrared studies of Ni-bearing clay-minerals of the kerolite-pimelite series. Clays and Clay Minerals 31:143-151.

Gimbert, L.J., P.M. Haygarth, R. Beckett, and P.J. Worsfold. 2005. Comparison of centrifugation and filtration techniques for the size fractionation of colloidal material in soil suspensions using sedimentation field-flow fractionation. Environmental Science & Technology 39:1731-1735.

Gleeson, S.A., R.J. Herrington, J. Durango, C.A. Velasquez, and G. Koll. 2004. The mineralogy and geochemistry of the Cerro Matoso SA Ni laterite deposit, Montelibano, Colombia. Economic Geology 99:1197-1213.

Grazulis, S., D. Chateigner, R.T. Downs, A.F.T. Yokochi, M. Quiros, L. Lutterotti, E. Manakova, J. Butkus, P. Moeck, and A. Le Bail. 2009. Crystallography Open Database - an open-access collection of crystal structures. Journal of Applied Crystallography 42:726-729.

Grazulis, S., A. Daskevic, A. Merkys, D. Chateigner, L. Lutterotti, M. Quiros, N.R. Serebryanaya, P. Moeck, R.T. Downs, and A. Le Bail. 2012. Crystallography Open Database (COD): an open-access collection of crystal structures and platform for world-wide collaboration. Nucleic Acids Research 40:D420-D427.

Hammersley, A.P. 1998. FIT2D V9.129 Reference Manual V3.1. ESRF Internal Report ESRF98HA01T.

Hammersley, A.P., S.O. Svensson, M. Hanfland, A.N. Fitch, and D. Hausermann. 1996. Two-dimensional detector software: From real detector to idealized image or two-theta scan. High Pressure Research 14:235-248.

He, J., M. Wei, B. Li, Y. Kang, D.G. Evans, and X. Duan. 2006. Preparation of layered double hydroxides, p. 89-119 Layered Double Hydroxides, Vol. 119. Springer-Verlag Berlin, Berlin.

Holmgren, G.G. 1967. A rapid citrate-dithionite extractable iron procedure. Soil Science Society of America Proceedings 31:210.

Hotz, P.E. 1964. Nickeliferous laterites in southwestern Oregon and northwestern California. Economic Geology 59:355–396.

Hseu, Z.Y., H. Tsai, H.C. Hsi, and Y.C. Chen. 2007. Weathering sequences of clay minerals in soils along a serpentinitic toposequence. Clays and Clay Minerals 55:389-401.

Istok, J.D., and M.E. Harward. 1982. Influence of soil-moisture on smectite formation in soils derived from serpentinite. Soil Science Society of America Journal 46:1106-1108.

Jackson, M.L. 1985. Soil chemical analysis - Advanced course. 2nd ed. University of Wisconsin, Madison, WI.

Kahle, M., M. Kleber, M.S. Torn, and R. Jahn. 2003. Carbon storage in coarse and fine clay fractions of illitic soils. Soil Science Society of America Journal 67:1732-1739.

Kierczak, J., C. Neel, H. Bril, and J. Puziewicz. 2007. Effect of mineralogy and pedoclimatic variations on Ni and Cr distribution in serpentine soils under temperate climate. Geoderma 142:165-177.

Landers, M., and R.J. Gilkes. 2007. Dehydroxylation and dissolution of nickeliferous goethite in New Caledonian lateritic Ni ore. Applied Clay Science 35:162-172.

Landers, M., R.J. Gilkes, and M. Wells. 2009. Dissolution kinetics of dehydroxylated nickeliferous goethite from limonitic lateritic nickel ore. Applied Clay Science 42:615-624.

Landers, M., M. Grafe, R.J. Gilkes, M. Saunders, and M.A. Wells. 2011. Nickel distribution and speciation in rapidly dehydroxylated goethite in oxide-type lateritic nickel ores: XAS and TEM spectroscopic (EELS and EFTEM) investigation. Australian Journal of Earth Sciences 58:745-765.

Loeppert, R.P., and W.P. Inskeep. 1996. Iron, In J. M. Bigham, ed. Methods of Soil Analysis. Part 3. Chemical Methods. Soil Science Society of America and American Society of Agronomy, 677 S. Segoe Rd., Madison, WI 53711, USA.

Manceau, A., and G. Calas. 1986. Nickel bearing clay minerals: 2. Intracrystalline distribution of nickel - an x-ray absorption study. Clay Minerals 21:341-360.

Manceau, A. 1990. Distribution of cations among the octahedra of phyllosilicates - insight from EXAFS. Canadian Mineralogist 28:321-328.

Manceau, A., and G. Calas. 1985. Heterogeneous distribution of nickel in hydrous silicates from New Caledonia ore-deposits. American Mineralogist 70:549-558.

Manceau, A., S. Llorca, and G. Calas. 1987. Crystal-chemistry of cobalt and nickel in lithiophorite and asbolane from New-Caledonia. Geochimica et Cosmochimica Acta 51:105-113.

Manceau, A., M.L. Schlegel, M. Musso, V.A. Sole, C. Gauthier, P.E. Petit, and F. Trolard. 2000. Crystal chemistry of trace elements in natural and synthetic goethite. Geochimica et Cosmochimica Acta 64:3643-3661.

Manceau, A., N. Tamura, R.S. Celestre, A.A. MacDowell, N. Geoffroy, G. Sposito, and H.A. Padmore. 2003. Molecular-scale speciation of Zn and Ni in soil ferromanganese nodules from loess soils of the Mississippi Basin. Environmental Science & Technology 37:75-80.

Manceau, A., N. Tamura, M.A. Marcus, A.A. MacDowell, R.S. Celestre, R.E. Sublett, G. Sposito, and H.A. Padmore. 2002. Deciphering Ni sequestration in soil ferromanganese nodules by combining X-ray fluorescence, absorption, and diffraction at micrometer scales of resolution. American Mineralogist 87:1494-1499.

Manceau, A., G. Calas, and A. Decarreau. 1985. Nickel bearing clay minerals: 1. Optical spectroscopic study of nickel crystal chemistry. Clay Minerals 20:367-387.

Massoura, S.T., G. Echevarria, T. Becquer, J. Ghanbaja, E. Leclere-Cessac, and J.L. Morel. 2006. Control of nickel availability by nickel bearing minerals in natural and anthropogenic soils. Geoderma 136:28-37.

McNear, D.H., R.L. Chaney, and D.L. Sparks. 2007. The effects of soil type and chemical treatment on nickel speciation in refinery enriched soils: A multi-technique investigation. Geochimica et Cosmochimica Acta 71:2190-2208.

Montoya, J.W., and G.S. Baur. 1963. Nickeliferous serpentines, chlorites, and related minerals found in two lateritic ores. The American Mineralogist 48:1227-1238.

North, P.F. 1976. Towards an absolute measurement of soil structural stability using ultrasound. Journal of Soil Science 27:451-459.

Oorts, K., B. Vanlauwe, S. Recous, and R. Merckx. 2005. Redistribution of particulate organic matter during ultrasonic dispersion of highly weathered soils. European Journal of Soil Science 56:77-91.

Oze, C., S. Fendorf, D.K. Bird, and R.G. Coleman. 2004a. Chromium geochemistry of serpentine soils. International Geology Review 46:97-126.

Oze, C., S. Fendorf, D.K. Bird, and R.G. Coleman. 2004b. Chromium geochemistry in serpentinized ultramafic rocks and serpentine soils from the Franciscan Complex of California. American Journal of Science 304:67-101.

Rabenhorst, M.C., J.E. Foss, and D.S. Fanning. 1982. Genesis of Maryland soils formed from serpentinite. Soil Science Society of America Journal 46:607-616.

Raine, S.R., and H.B. So. 1994. Ultrasonic dispersion of soil in water - the effect of suspension properties on energy-dissipation and soil dispersion. Australian Journal of Soil Research 32:1157-1174.

Ravel, B., and M. Newville. 2005. Athena, Artemis, Hephaestus: data analysis for X-ray absorption spectroscopy using IFEFFIT. Journal of Synchrotron Radiation 12:537-541.

Reeves, R.D., R.R. Brooks, and T.R. Dudley. 1983. Uptake of nickel by species of *Alyssum, Bornmuellera*, and other genera of old-world *Tribus Alysseae*. Taxon 32:184-192.

Reeves, R.D., A.J.M. Baker, A. Borhidi, and R. Berazain. 1999. Nickel hyperaccumulation in the serpentine flora of Cuba. Annals of Botany 83:29-38.

Reichle, W.T. 1986. Synthesis of anionic clay-minerals (mixed metal-hydroxides, hydrotalcite). Solid State Ionics 22:135-141.

Schmidt, M.W.I., C. Rumpel, and I. Kogel-Knabner. 1999. Evaluation of an ultrasonic dispersion procedure to isolate primary organomineral complexes from soils. European Journal of Soil Science 50:87-94.

Singh, B., D.M. Sherman, R.J. Gilkes, M. Wells, and J.F.W. Mosselmans. 2000. Structural chemistry of Fe, Mn, and Ni in synthetic hematites as determined by extended X-ray absorption fine structure spectroscopy. Clays and Clay Minerals 48:521-527.

Singh, B., D.M. Sherman, R.J. Gilkes, M.A. Wells, and J.F.W. Mosselmans. 2002. Incorporation of Cr, Mn and Ni into goethite (alpha-FeOOH): mechanism from extended X-ray absorption fine structure spectroscopy. Clay Minerals 37:639-649.

Sohi, S.P., N. Mahieu, J.R.M. Arah, D.S. Powlson, B. Madari, and J.L. Gaunt. 2001. A procedure for isolating soil organic matter fractions suitable for modeling. Soil Science Society of America Journal 65:1121-1128.

Solomon, D., F. Fritzsche, M. Tekalign, J. Lehmann, and W. Zech. 2002. Soil organic matter composition in the sub-humid Ethiopian highlands as influenced by deforestation and agricultural management. Soil Science Society of America Journal 66:68-82.

Suarez, S., F. Nieto, F. Velasco, and F.J. Martin. 2011. Serpentine and chlorite as effective Ni-Cu sinks during weathering of the Aguablanca sulphide deposit (SW Spain). TEM evidence for metal-retention mechanisms in sheet silicates. European Journal of Mineralogy 23:179-196.

Tartaj, P., A. Cerpa, M.T. Garcia-Gonzalez, and C.J. Serna. 2000. Surface instability of serpentine in aqueous suspensions. Journal of Colloid and Interface Science 231:176-181.

USGS. 2012. U.S. Geological Survey. Mineral Commodity Summaries.

Webb, S.M. 2005. SIXpack: a graphical user interface for XAS analysis using IFEFFIT. Physica Scripta T115:1011-1014.

Wildman, W.E., M.L. Jackson, and L.D. Whittig. 1968a. Serpentinite rock dissolution as a function of carbon dioxide pressure in aqueous solution. American Mineralogist 53:1252.

Wildman, W.E., M.L. Jackson, and L.D. Whittig. 1968b. Iron-rich montmorillonite formation in soils derived from serpentinite. Soil Science Society of America Proceedings 32:787.

Wildman, W.E., L.D. Whittig, and M.L. Jackson. 1971. Serpentine stability in relation to formation of iron-rich montmorillonite in some California soils. American Mineralogist 56:587.

Wilson, M.J., D. Jones, and J.D. Russell. 1980. Glushinskite, a naturally occurring magnesium oxalate. Mineralogical magazine 43:837-840.

Xu, Y., L. Axe, T. Boonfueng, T.A. Tyson, P. Trivedi, and K. Pandya. 2007. Ni(II) complexation to amorphous hydrous ferric oxide: An X-ray absorption spectroscopy study. Journal of Colloid and Interface Science 314:10-17.

Yang, X.M., C.F. Drury, W.D. Reynolds, and D.C. MacTavish. 2009. Use of sonication to determine the size distributions of soil particles and organic matter. Canadian Journal of Soil Science 89:413-419.

Yongue-Fouateu, R., M. Yemefack, A.S.L. Wouatong, P.D. Ndjigui, and P. Bilong. 2009. Contrasted mineralogical composition of the laterite cover on serpentinites of Nkamouna-Kongo, southeast Cameroon. Clay Minerals 44:221-237.

Zhu, M.Q., M. Ginder-Vogel, and D.L. Sparks. 2010. Ni(II) Sorption on Biogenic Mn-Oxides with Varying Mn Octahedral Layer Structure. Environmental Science & Technology 44:4472-4478.

Appendix A

PERMISSION FOR FORD ET AL. (1999)

"Reprinted 2013 with permission from The Link between Clay Mineral Weathering and the Stabilization of Ni Surface Precipitates Author: Robert G. Ford, , Andreas C. Scheinost, Kirk G. Scheckel, and Donald L. Sparks. Environmental Science &Technology. Copyright (1999) American Chemical Society."

208

Appendix B

PERMISSION FOR SCHEINOST ET AL. (1999)

"Reprinted from Geochimica et Cosmochimica Acta, 63 /19–20, Andreas C Scheinost, Robert G Ford, Donald L Sparks, The role of Al in the formation of secondary Ni precipitates on pyrophyllite, gibbsite, talc, and amorphous silica: a DRS study, 3193-3203, (1999), with permission from Elsevier."

209

Estimated size (number of pages)	250
Elsevier VAT number	GB 494 6272 12
Permissions price	0.00 USD
VAT/Local Sales Tax	0.00 USD / 0.00 GBP
Total	0.00 USD
Terms and Conditions	

INTRODUCTION

1. The publisher for this copyrighted material is Elsevier. By clicking "accept" in connection with completing this licensing transaction, you agree that the following terms and conditions apply to this transaction (along with the Billing and Payment terms and conditions established by Copyright Clearance Center, Inc. ("CCC"), at the time that you opened your Rightslink account and that are available at any time at http://myaccount.copyright.com).

GENERAL TERMS

2. Elsevier hereby grants you permission to reproduce the aforementioned material subject to the terms and conditions indicated.

3. Acknowledgement: If any part of the material to be used (for example, figures) has appeared in our publication with credit or acknowledgement to another source, permission must also be sought from that source. If such permission is not obtained then that material may not be included in your publication/copies. Suitable acknowledgement to the source must be made, either as a footnote or in a reference list at the end of your publication, as follows:

"Reprinted from Publication title, Vol /edition number, Author(s), Title of article / title of chapter, Pages No., Copyright (Year), with permission from Elsevier [OR APPLICABLE SOCIETY COPYRIGHT OWNER]." Also Lancet special credit - "Reprinted from The Lancet, Vol. number, Author(s), Title of article, Pages No., Copyright (Year), with permission from Elsevier."

4. Reproduction of this material is confined to the purpose and/or media for which permission is hereby given.

5. Altering/Modifying Material: Not Permitted. However figures and illustrations may be altered/adapted minimally to serve your work. Any other abbreviations, additions, deletions and/or any other alterations shall be made only with prior written authorization of Elsevier Ltd. (Please contact Elsevier at permissions@elsevier.com)

6. If the permission fee for the requested use of our material is waived in this instance, please be advised that your future requests for Elsevier materials may attract a fee.

7. Reservation of Rights: Publisher reserves all rights not specifically granted in the combination of (i) the license details provided by you and accepted in the course of this licensing transaction, (ii) these terms and conditions and (iii) CCC's Billing and Payment terms and conditions.

8. License Contingent Upon Payment: While you may exercise the rights licensed

---

immediately upon issuance of the license at the end of the licensing process for the transaction, provided that you have disclosed complete and accurate details of your proposed use, no license is finally effective unless and until full payment is received from you (either by publisher or by CCC) as provided in CCC's Billing and Payment terms and conditions. If full payment is not received on a timely basis, then any license preliminarily granted shall be deemed automatically revoked and shall be void as if never granted. Further, in the event that you breach any of these terms and conditions or any of CCC's Billing and Payment terms and conditions, the license is automatically revoked and shall be void as if never granted. Use of materials as described in a revoked license, as well as any use of the materials beyond the scope of an unrevoked license, may constitute copyright infringement and publisher reserves the right to take any and all action to protect its copyright in the materials.

9. Warranties: Publisher makes no representations or warranties with respect to the licensed material.

10. Indemnity: You hereby indemnify and agree to hold harmless publisher and CCC, and their respective officers, directors, employees and agents, from and against any and all claims arising out of your use of the licensed material other than as specifically authorized pursuant to this license.

11. No Transfer of License: This license is personal to you and may not be sublicensed, assigned, or transferred by you to any other person without publisher's written permission.

12. No Amendment Except in Writing: This license may not be amended except in a writing signed by both parties (or, in the case of publisher, by CCC on publisher's behalf).

13. Objection to Contrary Terms: Publisher hereby objects to any terms contained in any purchase order, acknowledgment, check endorsement or other writing prepared by you, which terms are inconsistent with these terms and conditions or CCC's Billing and Payment terms and conditions. These terms and conditions, together with CCC's Billing and Payment terms and conditions (which are incorporated herein), comprise the entire agreement between you and publisher (and CCC) concerning this licensing transaction. In the event of any conflict between your obligations established by these terms and conditions and those established by CCC's Billing and Payment terms and conditions, these terms and conditions shall control.

14. Revocation: Elsevier or Copyright Clearance Center may deny the permissions described in this License at their sole discretion, for any reason or no reason, with a full refund payable to you. Notice of such denial will be made using the contact information provided by you. Failure to receive such notice will not alter or invalidate the denial. In no event will Elsevier or Copyright Clearance Center be responsible or liable for any costs, expenses or damage incurred by you as a result of a denial of your permission request, other than a refund of the amount(s) paid by you to Elsevier and/or Copyright Clearance Center for denied permissions.

LIMITED LICENSE

The following terms and conditions apply only to specific license types:

15. Translation: This permission is granted for non-exclusive world **English** rights only unless your license was granted for translation rights. If you licensed translation rights you

210

may only translate this content into the languages you requested. A professional translator must perform all translations and reproduce the content word for word preserving the integrity of the article. If this license is to re-use 1 or 2 figures then permission is granted for non-exclusive world rights in all languages.

16. **Website**: The following terms and conditions apply to electronic reserve and author websites:

Electronic reserve: If licensed material is to be posted to website, the web site is to be password-protected and made available only to bona fide students registered on a relevant course if:

This license was made in connection with a course,

This permission is granted for 1 year only. You may obtain a license for future website posting,

All content posted to the web site must maintain the copyright information line on the bottom of each image,

A hyper-text must be included to the Homepage of the journal from which you are licensing at http://www.sciencedirect.com/science/journal/xxxxx or the Elsevier homepage for books at http://www.elsevier.com , and

Central Storage: This license does not include permission for a scanned version of the material to be stored in a central repository such as that provided by Heron/XanEdu.

17. **Author website** for journals with the following additional clauses:

All content posted to the web site must maintain the copyright information line on the bottom of each image, and the permission granted is limited to the personal version of your paper. You are not allowed to download and post the published electronic version of your article (whether PDF or HTML, proof or final version), nor may you scan the printed edition to create an electronic version. A hyper-text must be included to the Homepage of the journal from which you are licensing at http://www.sciencedirect.com/science/journal/xxxxx . As part of our normal production process, you will receive an e-mail notice when your article appears on Elsevier's online service ScienceDirect (www.sciencedirect.com). That e-mail will include the article's Digital Object Identifier (DOI). This number provides the electronic link to the published article and should be included in the posting of your personal version. We ask that you wait until you receive this e-mail and have the DOI to do any posting.

Central Storage: This license does not include permission for a scanned version of the material to be stored in a central repository such as that provided by Heron/XanEdu.

18. **Author website** for books with the following additional clauses:
Authors are permitted to place a brief summary of their work online only.
A hyper-text must be included to the Elsevier homepage at http://www.elsevier.com . All content posted to the web site must maintain the copyright information line on the bottom of each image. You are not allowed to download and post the published electronic version of your chapter, nor may you scan the printed edition to create an electronic version.

Central Storage: This license does not include permission for a scanned version of the material to be stored in a central repository such as that provided by Heron/XanEdu.

19. **Website** (regular and for author): A hyper-text must be included to the Homepage of the journal from which you are licensing at http://www.sciencedirect.com/science/journal

---

/xxxxx . or for books to the Elsevier homepage at http://www.elsevier.com

20. **Thesis/Dissertation**: If your license is for use in a thesis/dissertation your thesis may be submitted to your institution in either print or electronic form. Should your thesis be published commercially, please reapply for permission. These requirements include permission for the Library and Archives of Canada to supply single copies, on demand, of the complete thesis and include permission for UMI to supply single copies, on demand, of the complete thesis. Should your thesis be published commercially, please reapply for permission.

21. **Other Conditions**:

v1.6

If you would like to pay for this license now, please remit this license along with your payment made payable to "COPYRIGHT CLEARANCE CENTER" otherwise you will be invoiced within 48 hours of the license date. Payment should be in the form of a check or money order referencing your account number and this invoice number RLNK501167524.
Once you receive your invoice for this order, you may pay your invoice by credit card. Please follow instructions provided at that time.

Make Payment To:
Copyright Clearance Center
Dept 001
P.O. Box 843006
Boston, MA 02284-3006

For suggestions or comments regarding this order, contact RightsLink Customer Support: customercare@copyright.com or +1-877-622-5543 (toll free in the US) or +1-978-646-2777.

Gratis licenses (referencing $0 in the Total field) are free. Please retain this printable license for your reference. No payment is required.

211

Appendix C

PERMISSIONS FOR CENTOFANTI ET AL. (2012)

Springer and the original publisher Plant and Soil, 359:71–83, 2012,

Hyperaccumulation of nickel by Alyssum corsicum is related to solubility of Ni mineral

species, Tiziana Centofanti, Matthew G. Siebecker, Rufus L. Chaney, Allen P. Davis,

and Donald L. Sparks, **Abstract License Number 3276090407483, Figures License**

Number 3276090323389 , Full text License Number 3276090156095 is given to the

publication in which the material was originally published, by adding; with kind

permission from Springer Science and Business Media"

Indemnity

You hereby indemnify and agree to hold harmless Springer Science + Business Media and CCC, and their respective officers, directors, employees and agents, from and against any and all claims arising out of your use of the licensed material other than as specifically authorized pursuant to this license.

No Transfer of License

This license is personal to you and may not be sublicensed, assigned, or transferred by you to any other person without Springer Science + Business Media's written permission.

No Amendment Except in Writing

This license may not be amended except in a writing signed by both parties (or, in the case of Springer Science + Business Media, by CCC on Springer Science + Business Media's behalf).

Objection to Contrary Terms

Springer Science + Business Media hereby objects to any terms contained in any purchase order, acknowledgment, check endorsement or other writing prepared by you, which terms are inconsistent with these terms and conditions or CCC's Billing and Payment terms and conditions. These terms and conditions, together with CCC's Billing and Payment terms and conditions (which are incorporated herein), comprise the entire agreement between you and Springer Science + Business Media (and CCC) concerning this licensing transaction. In the event of any conflict between your obligations established by these terms and conditions and those established by CCC's Billing and Payment terms and conditions, these terms and conditions shall control.

Jurisdiction

All disputes that may arise in connection with this present License, or the breach thereof, shall be settled exclusively by arbitration, to be held in The Netherlands, in accordance with Dutch law, and to be conducted under the Rules of the 'Netherlands Arbitrage Instituut' (Netherlands Institute of Arbitration). *OR*:

All disputes that may arise in connection with this present License, or the breach thereof, shall be settled exclusively by arbitration, to be held in the Federal Republic of Germany, in accordance with German law.

Other terms and conditions:

v1.3

If you would like to pay for this license now, please remit this license along with your payment made payable to "COPYRIGHT CLEARANCE CENTER" otherwise you will be invoiced within 48 hours of the license date. Payment should be in the form of a check or money order referencing your account number and this invoice number RLNK501167532.
Once you receive your invoice for this order, you may pay your invoice by credit card. Please follow instructions provided at that time.

Make Payment To:
Copyright Clearance Center
Dept 001
P.O. Box 843006
Boston, MA 02284-3006

indicated in your enquiry.

Licenses are for one-time use only with a maximum distribution equal to the number that you identified in the licensing process.

This License includes use in an electronic form, provided its password protected or on the university's intranet or repository, including UMI (according to the definition at the Sherpa website: http://www.sherpa.ac.uk/romeo/). For any other electronic use, please contact Springer at (permissions.dordrecht@springer.com or permissions.heidelberg@springer.com).

The material can only be used for the purpose of defending your thesis, and with a maximum of 100 extra copies in paper.

Although Springer holds copyright to the material and is entitled to negotiate on rights, this license is only valid, subject to a courtesy information to the author (address is given with the article/chapter) and provided it concerns original material which does not carry references to other sources (if material in question appears with credit to another source, authorization from that source is required as well).

Permission free of charge on this occasion does not prejudice any rights we might have to charge for reproduction of our copyrighted material in the future.

Altering/Modifying Material: Not Permitted
You may not alter or modify the material in any manner. Abbreviations, additions, deletions and/or any other alterations shall be made only with prior written authorization of the author(s) and/or Springer Science + Business Media. (Please contact Springer at (permissions.dordrecht@springer.com or permissions.heidelberg@springer.com)

Reservation of Rights
Springer Science + Business Media reserves all rights not specifically granted in the combination of (i) the license details provided by you and accepted in the course of this licensing transaction, (ii) these terms and conditions and (iii) CCC's Billing and Payment terms and conditions.

Copyright Notice:Disclaimer
You must include the following copyright and permission notice in connection with any reproduction of the licensed material: "Springer and the original publisher /journal title, volume, year of publication, page, chapter/article title, name(s) of author(s), figure number(s), original copyright notice) is given to the publication in which the material was originally published, by adding; with kind permission from Springer Science and Business Media"

Warranties: None

Example 1: Springer Science + Business Media makes no representations or warranties with respect to the licensed material.

Example 2: Springer Science + Business Media makes no representations or warranties with respect to the licensed material and adopts on its own behalf the limitations and disclaimers established by CCC on its behalf in its Billing and Payment terms and conditions for this licensing transaction.

213

SPRINGER LICENSE
TERMS AND CONDITIONS

Nov 25, 2013

This is a License Agreement between Matthew Siebecker ("You") and Springer ("Springer")
provided by Copyright Clearance Center ("CCC"). The license consists of your order details,
the terms and conditions provided by Springer, and the payment terms and conditions.

**All payments must be made in full to CCC. For payment instructions, please see
information listed at the bottom of this form.**

License Number	3276090323389
License date	Nov 25, 2013
Licensed content publisher	Springer
Licensed content publication	Plant and Soil
Licensed content title	Hyperaccumulation of nickel by Alyssum corsicum is related to solubility of Ni mineral species
Licensed content author	Tiziana Centofanti
Licensed content date	Jan 1, 2012
Volume number	359
Issue number	1
Type of Use	Thesis/Dissertation
Portion	Figures
Author of this Springer article	Yes and you are a contributor of the new work
Order reference number	
Title of your thesis / dissertation	Environmental Speciation, Chemistry, Stability and Kinetics of Nickel in Soils, Mineral Systems and Plants
Expected completion date	Dec 2013
Estimated size(pages)	250
Total	0.00 USD
Terms and Conditions	

Introduction

The publisher for this copyrighted material is Springer Science + Business Media. By clicking
"accept" in connection with completing this licensing transaction, you agree that the
following terms and conditions apply to this transaction (along with the Billing and Payment
terms and conditions established by Copyright Clearance Center, Inc. ("CCC"), at the time
that you opened your Rightslink account and that are available at any time at
http://myaccount.copyright.com).

Limited License

With reference to your request to reprint in your thesis material on which Springer Science
and Business Media control the copyright, permission is granted, free of charge, for the use
indicated in your enquiry.

**For suggestions or comments regarding this order, contact RightsLink Customer
Support: customercare@copyright.com or +1-877-622-5543 (toll free in the US) or
+1-978-646-2777.**

Gratis licenses (referencing $0 in the Total field) are free. Please retain this printable
license for your reference. No payment is required.

214

Licenses are for one-time use only with a maximum distribution equal to the number that you identified in the licensing process.

This License includes use in an electronic form, provided its password protected or on the university's intranet or repository, including UMI (according to the definition at the Sherpa website: http://www.sherpa.ac.uk/romeo/). For any other electronic use, please contact Springer at (permissions.dordrecht@springer.com or permissions.heidelberg@springer.com).

The material can only be used for the purpose of defending your thesis, and with a maximum of 100 extra copies in paper.

Although Springer holds copyright to the material and is entitled to negotiate on rights, this license is only valid, subject to a courtesy information to the author (address is given with the article/chapter) and provided it concerns original material which does not carry references to other sources (if material in question appears with credit to another source, authorization from that source is required as well).

Permission free of charge on this occasion does not prejudice any rights we might have to charge for reproduction of our copyrighted material in the future.

Altering/Modifying Material: Not Permitted
You may not alter or modify the material in any manner. Abbreviations, additions, deletions and or any other alterations shall be made only with prior written authorization of the author(s) and/or Springer Science + Business Media. (Please contact Springer at (permissions.dordrecht@springer.com or permissions.heidelberg@springer.com).

Reservation of Rights
Springer Science + Business Media reserves all rights not specifically granted in the combination of (i) the license details provided by you and accepted in the course of this licensing transaction, (ii) these terms and conditions and (iii) CCC's Billing and Payment terms and conditions.

Copyright Notice:Disclaimer
You must include the following copyright and permission notice in connection with any reproduction of the licensed material: "Springer and the original publisher /journal title, volume, year of publication, page, chapter/article title, name(s) of author(s), figure number(s), original copyright notice) is given to the publication in which the material was originally published, by adding; with kind permission from Springer Science and Business Media"

Warranties: None

Example 1: Springer Science + Business Media makes no representations or warranties with respect to the licensed material.

Example 2: Springer Science + Business Media makes no representations or warranties with respect to the licensed material and adopts on its own behalf the limitations and disclaimers established by CCC on its behalf in its Billing and Payment terms and conditions for this licensing transaction.

Indemnity

You hereby indemnify and agree to hold harmless Springer Science + Business Media and CCC, and their respective officers, directors, employees and agents, from and against any and all claims arising out of your use of the licensed material other than as specifically authorized pursuant to this license.

No Transfer of License
This license is personal to you and may not be sublicensed, assigned, or transferred by you to any other person without Springer Science + Business Media's written permission.

No Amendment Except in Writing
This license may not be amended except in a writing signed by both parties (or, in the case of Springer Science + Business Media, by CCC on Springer Science + Business Media's behalf).

Objection to Contrary Terms
Springer Science + Business Media hereby objects to any terms contained in any purchase order, acknowledgment, check endorsement or other writing prepared by you, which terms are inconsistent with these terms and conditions or CCC's Billing and Payment terms and conditions. These terms and conditions, together with CCC's Billing and Payment terms and conditions (which are incorporated herein), comprise the entire agreement between you and Springer Science + Business Media (and CCC) concerning this licensing transaction. In the event of any conflict between your obligations established by these terms and conditions and those established by CCC's Billing and Payment terms and conditions, these terms and conditions shall control.

Jurisdiction
All disputes that may arise in connection with this present License, or the breach thereof, shall be settled exclusively by arbitration, to be held in The Netherlands, in accordance with Dutch law, and to be conducted under the Rules of the 'Netherlands Arbitrage Instituut' (Netherlands Institute of Arbitration).OR:

All disputes that may arise in connection with this present License, or the breach thereof, shall be settled exclusively by arbitration, to be held in the Federal Republic of Germany, in accordance with German law.

Other terms and conditions:

v1.3

If you would like to pay for this license now, please remit this license along with your payment made payable to "COPYRIGHT CLEARANCE CENTER" otherwise you will be invoiced within 48 hours of the license date. Payment should be in the form of a check or money order referencing your account number and this invoice number RLNK501167535.
Once you receive your invoice for this order, you may pay your invoice by credit card. Please follow instructions provided at that time.

Make Payment To:
Copyright Clearance Center
Dept 001
P.O. Box 843006
Boston, MA 02284-3006

For suggestions or comments regarding this order, contact RightsLink Customer Support: customercare@copyright.com or +1-877-622-5543 (toll free in the US) or

215

SPRINGER LICENSE
TERMS AND CONDITIONS

Nov 25, 2013

This is a License Agreement between Matthew Siebecker ("You") and Springer ("Springer") provided by Copyright Clearance Center ("CCC"). The license consists of your order details, the terms and conditions provided by Springer, and the payment terms and conditions.

All payments must be made in full to CCC. For payment instructions, please see information listed at the bottom of this form.

License Number	3276090407483
License date	Nov 25, 2013
Licensed content publisher	Springer
Licensed content publication	Plant and Soil
Licensed content title	Hyperaccumulation of nickel by Alyssum corsicum is related to solubility of Ni mineral species
Licensed content author	Tiziana Centofanti
Licensed content date	Jan 1, 2012
Volume number	359
Issue number	1
Type of Use	Thesis/Dissertation
Portion	Abstract
Author of this Springer article	Yes and you are a contributor of the new work
Order reference number	
Title of your thesis / dissertation	Environmental Speciation, Chemistry, Stability and Kinetics of Nickel in Soils, Mineral Systems and Plants
Expected completion date	Dec 2013
Estimated size(pages)	250
Total	0.00 USD
Terms and Conditions	

Introduction

The publisher for this copyrighted material is Springer Science + Business Media. By clicking "accept" in connection with completing this licensing transaction, you agree that the following terms and conditions apply to this transaction (along with the Billing and Payment terms and conditions established by Copyright Clearance Center, Inc. ("CCC"), at the time that you opened your Rightslink account and that are available at any time at http://myaccount.copyright.com).

Limited License

With reference to your request to reprint in your thesis material on which Springer Science and Business Media control the copyright, permission is granted, free of charge, for the use indicated in your enquiry.

+1-978-646-2777.

Gratis licenses (referencing $0 in the Total field) are free. Please retain this printable license for your reference. No payment is required.

216

You hereby indemnify and agree to hold harmless Springer Science + Business Media and CCC, and their respective officers, directors, employees and agents, from and against any and all claims arising out of your use of the licensed material other than as specifically authorized pursuant to this license.

No Transfer of License

This license is personal to you and may not be sublicensed, assigned, or transferred by you to any other person without Springer Science + Business Media's written permission.

No Amendment Except in Writing

This license may not be amended except in a writing signed by both parties (or, in the case of Springer Science + Business Media, by CCC on Springer Science + Business Media's behalf).

Objection to Contrary Terms

Springer Science + Business Media hereby objects to any terms contained in any purchase order, acknowledgment, check endorsement or other writing prepared by you, which terms are inconsistent with these terms and conditions or CCC's Billing and Payment terms and conditions. These terms and conditions, together with CCC's Billing and Payment terms and conditions (which are incorporated herein), comprise the entire agreement between you and Springer Science + Business Media (and CCC) concerning this licensing transaction. In the event of any conflict between your obligations established by these terms and conditions and those established by CCC's Billing and Payment terms and conditions, these terms and conditions shall control.

Jurisdiction

All disputes that may arise in connection with this present License, or the breach thereof, shall be settled exclusively by arbitration, to be held in The Netherlands, in accordance with Dutch law, and to be conducted under the Rules of the 'Netherlands Arbitrage Instituut' (Netherlands Institute of Arbitration).*OR*

All disputes that may arise in connection with this present License, or the breach thereof, shall be settled exclusively by arbitration, to be held in the Federal Republic of Germany, in accordance with German law.

Other terms and conditions:

v1.3

If you would like to pay for this license now, please remit this license along with your payment made payable to "COPYRIGHT CLEARANCE CENTER" otherwise you will be invoiced within 48 hours of the license date. Payment should be in the form of a check or money order referencing your account number and this invoice number RLNK501167537.
Once you receive your invoice for this order, you may pay your invoice by credit card. Please follow instructions provided at that time.

Make Payment To:
Copyright Clearance Center
Dept 001
P.O. Box 843006
Boston, MA 02284-3006

For suggestions or comments regarding this order, contact RightsLink Customer Support: customercare@copyright.com or +1-877-622-5543 (toll free in the US) or

---

Licenses are for one-time use only with a maximum distribution equal to the number that you identified in the licensing process.

This License includes use in an electronic form, provided its password protected or on the university's intranet or repository, including UMI (according to the definition at the Sherpa website: http://www.sherpa.ac.uk/romeo/). For any other electronic use, please contact Springer at (permissions.dordrecht@springer.com or permissions.heidelberg@springer.com).

The material can only be used for the purpose of defending your thesis, and with a maximum of 100 extra copies in paper.

Although Springer holds copyright to the material and is entitled to negotiate on rights, this license is only valid, subject to a courtesy information to the author (address is given with the article/chapter) and provided it concerns original material which does not carry references to other sources (if material in question appears with credit to another source, authorization from that source is required as well).

Permission free of charge on this occasion does not prejudice any rights we might have to charge for reproduction of our copyrighted material in the future.

Altering/Modifying Material: Not Permitted
You may not alter or modify the material in any manner. Abbreviations, additions, deletions and/or any other alterations shall be made only with prior written authorization of the author(s) and/or Springer Science + Business Media. (Please contact Springer at (permissions.dordrecht@springer.com or permissions.heidelberg@springer.com)

Reservation of Rights
Springer Science + Business Media reserves all rights not specifically granted in the combination of (i) the license details provided by you and accepted in the course of this licensing transaction, (ii) these terms and conditions and (iii) CCC's Billing and Payment terms and conditions.

Copyright Notice:Disclaimer
You must include the following copyright and permission notice in connection with any reproduction of the licensed material: "Springer and the original publisher /journal title, volume, year of publication, page, chapter/article title, name(s) of author(s), figure number(s), original copyright notice) is given to the publication in which the material was originally published, by adding; with kind permission from Springer Science and Business Media"

Warranties: None

Example 1: Springer Science + Business Media makes no representations or warranties with respect to the licensed material.

Example 2: Springer Science + Business Media makes no representations or warranties with respect to the licensed material and adopts on its own behalf the limitations and disclaimers established by CCC on its behalf in its Billing and Payment terms and conditions for this licensing transaction.

Indemnity

217

+1-978-646-2777.

Gratis licenses (referencing $0 in the Total field) are free. Please retain this printable license for your reference. No payment is required.